



FAKULTÄT FÜR VERFAHRENS-
UND SYSTEMTECHNIK

Direct Numerical Simulations of Turbulent Flow and Spray Combustion

Dissertation
for the award of the degree

Doktoringenieur
(Dr.-Ing.)

by M.Sc. Abouelmagd Abdelsamie

Date of birth: 28. March 1985

Place of birth: Cairo, Egypt

Accepted by the Faculty of Process and System Engineering
of the Otto-von-Guericke-University of Magdeburg

Reviewer:

Prof. Dr.-Ing. Dominique Thévenin

Prof. Dr. rer. nat. habil. Ulrich Maas

Prof. Dr.-Ing. Christian Hasse

Submitted on : 02.12.2016

Graduation Colloquium on : 16.05.2017

To my family

Acknowledgments

The road has been rather long, yet wonderful, somewhat winding and often paved with overwhelming experiences. Nevertheless, it has been my good fortune to encounter many people who have patiently given me their time, companionship, and professional and personal help. First and foremost, I would like to thank my supervisor, Prof. Dominique Thévenin, who gave me scientific support and supervision, which were always more than a graduate student can expect from his professor. He has also been extremely encouraging, with a fatherly ear. Without his guidances, this work would never have gone this far. Thank you! There are several fellow researchers and countless individuals whom I would specifically like to thank for the support they have given me throughout my time as a graduate student: Dr. Gábor Janiga, who helped me a lot with his excellent computer science background. He has been instrumental in helping some of the numerical developments and software extensions described in this thesis come to life. Dr. Gordon Fru who first helped me understand combustion numerics and solvers in the early days of my Ph.D. work. Thank you! I would like to thank Dr. Mohammed Hassan from the Helwan University in Egypt for introducing and recommending me to Prof. Dominique Thévenin, and for his continued social support. Special thanks go to Prof. Mohammed Fatouh from Helwan University in Egypt for encouraging me since I was an undergraduate student and all the way through today. He is a second father to me. Thank you! I would like to express my appreciation to the Egyptian government and Helwan University for their support during my scientific journey, since they allowed me to travel out of the country for years. A list that has far too many names on it to mention separately is that of all the co-workers, group members, and mates that I have worked with and talked to over the years. My gratitude goes out to all the colleagues at the Institute of Fluid Dynamics and Thermodynamics at the University of Magdeburg (Germany). I am, of course, particularly indebted to my family for their monumental, unwavering support and encouragement on all fronts. They have truly always been there for me and without them, none of this would have been even remotely possible. Last but not the least, special thanks goes to my office-mate, Mr. Nils Lichtenberg, who was like a brother to me, for all of his support and help with my social life in Germany. The financial support of the DFG (Deutsche Forschungsgemeinschaft) within the project FOR1447 “Physicochemical-based models for the prediction of safety-relevant ignition processes” which was the main financial support during my Ph.D. work, is gratefully acknowledged.

Magdeburg,
16.05.2017

Abouelmagd Abdelsamie

Declaration

I hereby declare that I prepared the submitted work without inadmissible assistance and without the use of any aids other than those indicated. Facts or ideas taken from other sources, either directly or indirectly have been marked as such.

In particular, I did not use the services of a commercial graduation consultation. Furthermore, I have not made payments to third parties either directly or indirectly for any work connected with the content of the submitted dissertation.

This work has so far not been submitted either in Germany or abroad in same or similar form as a dissertation and has also not yet been published as a whole.

Magdeburg,
16.05.2017

Abouelmagd Abdelsamie

Abstract

This dissertation aims at developing tools to investigate the behavior and mechanisms of spray dispersion, evaporation, and ignition in turbulent reactive flow at near-practical conditions. One of these tools is a direct numerical simulation (DNS) code which is able to resolve the physical scales of interest. This DNS tool was validated with different reactive and non-reactive flows before using it in the main investigations. Spray combustion itself is a type of two-phase flow, which includes both a continuous phase (gas) and a discrete phase (liquid droplets). The numerics of both phases should first be well-established and resolved before any deep analysis, as will be seen in this dissertation. Furthermore, the following numerical reduction models have been examined as well, in order to either reduce the required computational resources or to perform post-processing of the turbulent flow: (1) one dimensional turbulence model, (2) tabulation chemistry, and (3) modal decomposition techniques. The dissertation includes seven chapters which can be summarized as follows.

In the first chapter, a general introduction to spray combustion and turbulent reactive flow is given. The literature on direct numerical simulation of sprays is reviewed. This chapter also discusses the physical spatial resolution, which is required in turbulent spray flow simulation in order to resolve all possible spatial scales. The complete plan for this dissertation is also summarized in this chapter.

The second chapter reviews most of the fundamentals and the equations of turbulent reactive flow and spray combustion, starting from the governing equations of different flow regimes (incompressible, low Mach number, fully compressible), then reviewing the related thermodynamic, transport, and kinetic relations. Afterwards, some important definitions, scales, and non-dimensional numbers in different combustion modes (premixed, non-premixed) are presented for laminar and turbulent flows, respectively. Finally, the fundamentals of the discrete phase (spray) and its governing equations are reviewed.

The developed DNS tool (DINO) is discussed in detail in Chapter 3. The numerical algorithms, computational efficiency, and scaling are presented. DINO's verification and validation are examined by comparison with different analytical, experimental, and numerical benchmarks. Some examples and applications are given at the end of this chapter.

The fourth chapter investigates the behavior and mechanisms of spray dispersion, evaporation, burning, and ignition in turbulent jet flow. The role of scalar dissipation rate and shear impact are examined, highlighting the importance of DNS in understanding spray combustion and developing models thereof. Furthermore, two numerical settings are suggested, as benchmarks, which would help in numerical study to investigate different phenomena in spray turbulent combustion: spray-turbulence-flame interactions, turbulent mixing, trans-

port, evaporation, ignition, etc.

A tool to quantify the flow state is developed in Chapter 5. This tool is based on the spectral entropy obtained from solving an eigenvalue problem, which kernel is the auto-correlation function of the flow velocity. This tool is first derived and then calibrated with a well-defined flow benchmark: homogeneous isotropic turbulence. After the calibration, two different applications is tested using this tool. (1) DNS results obtained for the Taylor-Green vortex benchmark at $Re = 1600$ as well as (2) results obtained through Large Eddy Simulations (LES) in a blood nozzle, revealing in both cases a perfect agreement with a traditional, user-based analysis of the flow conditions.

In the sixth chapter, different approaches for reductions are presented to optimize the computational resources required for DNS of turbulent reactive flows. Since the numerical methods employed in this dissertation for the discrete phase (spray) are already considered as a reduced model (Discrete Particles Simulation, DPS), the techniques described in this chapter are only applied to the continuous phase (gas mixture). These techniques can be categorized into three categories based on their nature and application: (1) dimension reduction: one-dimensional turbulence model, (2) chemistry/kinetic reduction: DNS with tabulation chemistry, (3) analysis: modal decomposition methods. These three techniques have been tested and validated, highlighting their ability to analyze the turbulent flow or make significant reductions in the required computational resources compared to standard DNS.

This dissertation is concluded with a summary, recommendations, and outlook which are presented in Chapter 6. The main contributions and novelties contained in this work are listed below.

Novelties and main contributions:

- Development of a new DNS tool which can accurately handle many different physical phenomena in reactive and non-reactive two-phase turbulent flows;
- Development of a method to quantify the flow state and detect transition to turbulence;
- Using of the temporally-evolving jet configuration for the first time in 3D DNS of spray combustion;
- Proving for the first time that the one-dimensional turbulence model can be used to test the occurrence of auto-ignition in premixed propane/air mixtures;
- Development of a new tool which can perform modal decomposition (SPOD and DMD) as a post-processing technique to reduce the required disk storage space and to quantify the turbulence dynamics and scales.

Zusammenfassung

Ziel dieser Dissertation ist es, unterschiedliche Tools zu entwickeln, um das Verhalten und die Mechanismen der Spray-Dispersion, Verdunstung und Zündung in turbulenter reaktiver Strömung unter praxisnahen Bedingungen zu untersuchen. Eines dieser Tools ist ein Direkte Numerische Simulations (DNS) Code, welcher in der Lage ist, die physikalischen Skalen, die von Interesse sind, aufzulösen. Dieses DNS-Tool wurde für verschiedene reaktive und nicht-reaktive Strömungen validiert, bevor es bei den Untersuchungen zum Einsatz kam. Sprühverbrennung an sich ist eine Form der Zweiphasenströmung, welche sowohl eine kontinuierliche Phase (Gas) als auch eine diskrete Phase (flüssige Tröpfchen) beinhaltet. Die Numerik dieser beiden Phasen sollte bevor jegliche tiefere Analyse stattfindet, völlig bestimmt und aufgelöst sein, wie in dieser Dissertation zu sehen sein wird. Außerdem wurden die nachfolgenden vereinfachten numerischen Modelle ebenso untersucht, um entweder die notwendigen Rechenressourcen oder ein Post-processing der turbulenten Strömung durchzuführen: (1) eindimensionales Turbulenzmodell, (2) tabellarische Chemie und (3) Methoden der modalen Zersetzung.

Die Dissertation beinhaltet sieben Kapitel, welche wie folgt zusammengefasst werden können. Im ersten Kapitel wird eine generelle Einführung zur Sprühverbrennung und turbulenter reaktiver Strömung gegeben. Die Literatur zu Direkter Numerischer Simulation wird besprochen. Dieses Kapitel behandelt auch die physikalisch-räumliche Auflösung, die in der turbulenten Sprühströmungssimulation benötigt wird, um alle möglichen räumlichen Skalen aufzulösen. Der gesamte Plan dieser Dissertation ist ebenfalls in diesem Kapitel zusammengefasst.

Das zweite Kapitel wiederholt die meisten Grundlagen und die Gleichungen für turbulente reaktive Strömungen und Sprühverbrennung, ausgehend von den Erhaltungsgleichungen verschiedener Strömungsregime (inkompressible, niedrige Machzahl, vollständig kompressibel) und anschließend die damit verbundenen thermodynamischen, transport- und kinetischen Beziehungen. Danach werden einige wichtige Definitionen, Skalen und dimensionslose Kennzahlen in verschiedenen Verbrennungsmoden (vorgemischt und nicht-vorgemischt) für laminare und turbulente Strömungen vorgestellt. Zum Schluss wird auf die Grundlagen der diskreten Phase (Spray) und deren Erhaltungsgleichungen eingegangen.

Das entwickelte DNS-Tool (DINO) ist in Kapitel 3 im Detail diskutiert. Die numerischen Algorithmen, Rechenleistung und Skalierung werden vorgestellt. Das Verifizieren und Validieren von DINO werden durch Vergleiche mit verschiedenen analytischen, experimentellen und numerischen Benchmarks überprüft. Einige Beispiele und Anwendungen sind am Ende dieses Kapitels enthalten.

Das vierte Kapitel untersucht das Verhalten und die Mechanismen der Spray-Dispersion, Verdunstung, Verbrennung und Zündung in turbulenter Strahlströmung. Die Rolle der skalaren Dissipationsrate und des Scheraufpralls werden untersucht und stellen die Bedeutung der DNS für das Verständnis der Spray-Verbrennung und die dafür entwickelten Modelle dar. Außerdem werden zwei numerische Einstellungen, in Form von Benchmarks, vorgeschlagen, welche in der numerischen Untersuchung hilfreich wären, zur Ermittlung verschiedener Phänomene in turbulenter Sprühverbrennung: Spray-Turbulenz-Flammen-Interaktionen, turbulentes Mischen, Transport, Verdunstung, Zündung, usw.

Ein weiteres Tool zur Quantifizierung des Strömungszustandes wird in Kapitel 5 entwickelt. Dieses Tool basiert auf der spektralen Entropie, die durch das Lösen eines Eigenwert-Problems erhalten wird und wiederum die Autokorrelationsfunktion der Strömungsgeschwindigkeit als Grundlage hat. Dieses Tool wird zuerst hergeleitet und dann mit einem gut definierten Strömungs-Benchmark kalibriert: homogene isotrope Turbulenz. Nach der Kalibrierung werden zwei unterschiedliche Anwendungen mit diesem Tool untersucht: (1) Taylor-Green-Vortex-Benchmark mit den DNS Ergebnissen bei $Re = 1600$, sowie (2) Ergebnisse einer Large-Eddy-Simulation (LES) in einer Blutdüse, wobei in beiden Fällen eine perfekte Übereinstimmung mit einer traditionellen, bedienbasierten Analyse der Strömungsbedingungen gezeigt wird.

Im sechsten Kapitel werden verschiedene Reduzierungsansätze vorgestellt, um die Rechenressourcen zu optimieren, welche für die DNS turbulenter reaktiver Strömungen benötigt werden. Während die, in dieser Dissertation, angewandten numerischen Methoden für die diskrete Phase (Spray) bereits als reduziertes Modell berücksichtigt werden (diskrete Partikelsimulation, DPS), sind die Methoden, die in diesem Kapitel beschrieben werden, nur für die kontinuierliche Phase angewendet (Gasmischung). Diese Methoden können basierend auf ihre Natur und Anwendung in drei Kategorien eingeteilt werden: (1) Dimensionsreduktion: ein-dimensionales Turbulenzmodell, (2) chemische/kinetische Reduktion: DNS mit tabellarischer Chemie, (3) Analyse: modale Zersetzungsmethoden. Diese drei Methoden wurden bereits getestet und validiert, welches ihre Fähigkeit unterstreicht, die turbulente Strömung zu analysieren oder signifikante Reduktionen der erforderlichen Rechenressourcen im Vergleich zu Standard-DNS zu erreichen.

Diese Dissertation wird abgeschlossen mit einer Zusammenfassung, Empfehlungen und einem Ausblick im Kapitel 6. Die wichtigsten Beiträge und Neuheiten in dieser Arbeit sind nachfolgend aufgelistet.

Neuheiten und Hauptbeiträge:

- Entwicklung eines neuen DNS-Tools, welches viele verschiedene physikalische Phänomene bei reaktiven und nicht-reaktiven turbulenten Zweiphasenströmungen korrekt bewältigen kann;
- Entwicklung einer Methode zur Quantifizierung des Strömungszustands und Ermittlung des Übergangs zur Turbulenz;
- Einsatz, der sich zeitlich entwickelnden Strahlkonfiguration zum ersten Mal in 3D-DNS für die Sprühverbrennung;
- Erstmaliger Beweis, dass das eindimensionale Turbulenzmodell verwendet werden kann, um das Auftreten von Selbstzündung in vorgemischten Propan/Luft-Gemischen zu testen;
- Entwicklung eines neuen Tools zur modalen Zersetzung (SPOD und DMD) als post-processing Technik zur Reduzierung des benötigten Speicherplatzes und zur Quantifizierung der Turbulenzdynamik und -skalen.

Contents

Abstract	v
Contents	xii
List of Tables	xiii
List of Figures	xix
Nomenclatures	xx
1 Introduction	1
1.1 Practical Importance of Spray Combustion	1
1.2 Spray	1
1.3 Challenges for Numerics of Spray Combustion	2
1.4 History of DNS of Spray Combustion	3
1.5 Spatial Resolution of DNS-DPS	5
1.5.1 Resolution of Turbulence Scales	5
1.5.2 Resolution of Chemical Scales	6
1.5.3 Resolution of the spray	7
1.6 Motivation and Dissertation Plan	8
2 Fundamentals and Governing Equations of DNS-DPS	10
2.1 DNS for Different Flow Regimes	10
2.1.1 Compressible Flow Equations	10
2.1.2 Low Mach Number Flow Equations	13
2.1.3 Incompressible Flow Equations	14
2.2 Thermodynamic Relations	15
2.3 Transport Relations	17
2.4 Chemical Kinetic Relations	18
2.5 Combustion Modes	19
2.5.1 Premixed Combustion	19
2.5.2 Non-Premixed (Diffusion) Combustion	22
2.6 Turbulent Combustion	24
2.6.1 Characterization of Turbulent Premixed Combustion	25
2.6.2 Characterization of Turbulent non-Premixed Combustion	27

2.7	Fundamentals of Droplet and Spray Combustion	29
2.7.1	Injection	29
2.7.2	Atomization	29
2.7.3	Dispersion and Evaporation	31
2.7.4	Spray Combustion	31
2.8	Modeling the Evaporation of Fuel Droplets	33
2.8.1	Existing Evaporation Models	34
2.8.2	Evaporation Model for a Single Isolated Droplet	35
2.8.3	DNS-DPS Coupling Equation	38
3	A New DNS Solver: DINO	40
3.1	Introduction	40
3.2	DINO Challenges and Important Features	40
3.3	Governing Equations	42
3.4	Low-Mach Number Formulation for Reacting Flows	42
3.4.1	Available Diffusion Velocity Models	44
3.4.2	Further Transport Coefficients	46
3.4.3	Thermodynamic Parameters	46
3.4.4	Chemical Kinetics	46
3.5	Incompressible Formulation for Non-Reacting Flows	46
3.6	Parallelization Strategy	47
3.7	Time Integration Schemes	47
3.8	Spatial Discretization	50
3.9	Solving the Poisson Equation in Parallel	50
3.10	Boundary Conditions in Time and Space	53
3.11	Grid Stretching	53
3.12	Immersed Boundaries	54
3.12.1	DNS in Complex Geometries: DB-IBM	54
3.12.2	DF-IBM	55
3.13	Multiphase Flows	56
3.14	Code Performance and Verification	58
3.14.1	Parallel Efficiency	58
3.14.2	Accuracy and Order	59
3.15	Validation	63
3.15.1	Lid-Driven Cavity	63
3.15.2	Homogeneous Isotropic Turbulence (HIT)	63
3.15.3	3D Taylor-Green Vortex (TGV)	64
3.15.4	Turbulent Channel Flow	67
3.15.5	IBM Validation: flow past a circular cylinder	68
3.15.6	Chemistry and Transport	69
3.16	First Application Examples	73
3.16.1	Spatially-Evolving Jet	73
3.16.2	Temporally-Evolving Jet	73

4	Spray and Droplets	78
4.1	Introduction	78
4.2	Validation Evaporation Model	78
4.3	Temporally-Evolving Jet	79
4.3.1	Numerical Setups	80
4.3.2	Results and Discussion	81
4.3.3	Conclusions on the Temporally Evolving Jet	88
4.4	Spatially-Evolving Jet	89
4.4.1	Numerical Settings	89
4.4.2	Conclusion on Spatially-Evolving Jet	91
4.5	General Conclusion	91
5	A Tool to Quantify the Flow State: Spectral Entropy	93
5.1	Introduction	93
5.2	History and Literature Survey	94
5.3	Governing Equations	95
5.3.1	Eigenvalue Problem	95
5.3.2	Spectral Entropy	97
5.4	Numerical Approaches and Algorithms	97
5.5	Results and Discussion	98
5.5.1	Suitable Time Scales for the Entropy Analysis	99
5.5.2	Using Spectral Entropy as a Measure of Turbulence Intensity	101
5.5.3	Impact of Spatial Resolution	102
5.5.4	Impact of Temporal Resolution	103
5.5.5	2D vs. 3D Analysis	105
5.5.6	First Benchmark: Three-Dimensional Taylor-Green Vortex (3D-TGV)	107
5.5.7	Second Benchmark: LES of Transitional Flow Within the FDA Nozzle	108
5.6	Conclusions	110
6	Model Reduction and Modal Decomposition	112
6.1	Introduction	112
6.2	Spatial Reduction: ODT	112
6.2.1	Objectives	112
6.2.2	State of The Art	113
6.2.3	Governing Equations	115
6.2.4	Numerical Settings	117
6.2.5	Results	118
6.2.6	Advantages and Drawbacks of ODT	127
6.2.7	Conclusions on ODT	132
6.3	Tabulation Chemistry: FPI	133
6.3.1	Objectives	133
6.3.2	State of The Art	133
6.3.3	FPI Principle	133
6.3.4	Numerics	134

6.3.5	Results	134
6.3.6	Conclusions on FPI	137
6.4	Post-Processing Analysis: DMD vs SPOD	140
6.4.1	Objectives	140
6.4.2	Fundamentals of SPOD and DMD	140
6.4.3	Numerical Settings	142
6.4.4	Results and Analysis	143
6.4.5	Conclusions on Modal Decomposition	145
6.5	Conclusion	147
7	Conclusions and Outlook	148
7.1	Conclusion	148
7.2	Outlook and Recommendations	150
	Bibliography	165

List of Tables

3.1	Coefficients for third-order additive semi-implicit Runge-Kutta integration. . .	50
3.2	Turbulence properties at time $t = 11.2\tau_\eta$	64
3.3	Parameters of the turbulent channel flow. Note that the mesh sizes Δx^+ , Δy^+ , Δz^+ are in wall units, and that Δy^+ represents the grid size at the center, the grid being refined close to the walls.	68
3.4	Comparison of the drag coefficient C_d obtained by IBM in DINO with literature values.	70
3.5	Reaction mechanisms employed to compute ignition delays.	70
5.1	Initial turbulence parameters employed for the ten DNS computations. Please keep in mind that a fixed grid (equidistant grid points $N = 512^3$, needed to resolve properly the most turbulent case) has been used for all conditions. . .	100
5.2	Spectral entropy S_d computed with all modes.	103
5.3	Minimum number of snapshots $N_{m,min}$ needed for analyzing the flow state. The bold values in the second column are obtained from the exact DNS scales using Eq. (5.20). In the last column, the estimate values deduced from Eq. (5.19) are presented.	106
5.4	Evolution of spectral entropy values for 3D-TGV as function of the number of snapshots N_m	109
6.1	Initial properties of the four cases considered to investigate autoignition with both DNS and ODT	119

List of Figures

1.1	Spray combustion applications.	1
1.2	Typical spray atomization and dispersion [4].	2
1.3	Schematic diagram showing the spray combustion process [5].	3
1.4	Rate of publications of DNS spray combustion since 1996, collected from google-scholar.	4
2.1	Combustion modes: (a) premixed, (b) non-premixed [35].	20
2.2	Typical color of the flame of different combustion modes: (a) premixed [36], (b) non-premixed [37].	20
2.3	Diffusion flame structure in the mixture fraction ζ diagram, for an infinitely-fast and irreversible reaction.	25
2.4	Modified turbulent combustion diagram: combustion regimes are identified in terms of length (l_t/δ) and velocity (u'/s_L) ratios (log-log scale) [11].	27
2.5	Regimes for turbulent non-premixed combustion as a function of the Damköhler number $Da = \tau_t/\tau_c$ (based on the turbulence integral time scale τ_t and the chemical time τ_c) and the turbulent Reynolds number Re_t [11].	29
2.6	Phenomenology of the atomization of a spray [39].	31
2.7	Group combustion diagram [17].	33
2.8	Classification of different spray combustion regimes [17].	33
3.1	2D domain decomposition with x-pencil orientation.	47
3.2	Sketch of imposing boundaries into the regular mesh in DB-IBM: stepwise geometry [77].	54
3.3	Representation of domains with a complex geometry in DINO using DB-IBM. Left: patient-specific cerebral aneurysm [79]. Right: Streamlines colored by velocity magnitude at peak systole.	55
3.4	Schematic diagram showing the location of the surface force [78].	55
3.5	Particles in initially homogeneous isotropic turbulence (HIT). (a) Non-resolved spherical particles (ratio diameter/Kolmogorov length scale of 0.1), the color field shows vorticity. (b) Fully resolved solid spherical particles (ratio diameter/Kolmogorov length scale of 20.6), the iso-surface shows the enstrophy of turbulence.	58
3.6	Schematic diagram showing the collision mechanism and model ranges [82].	59
3.7	Parallel efficiency (strong scaling) of DINO on SuperMUC.	59

3.8	Verification and spatial order obtained by solving the one-dimensional Burgers' equation. Left: time-dependent solution for a case with $N = 1025$ grid points. Right: error norms and resulting spatial order of DINO.	60
3.9	Verification and spatial order obtained by solving the 2D Taylor-Green vortex problem. Left: L_2 of velocity field. Right: L_∞ and L_2 of pressure field.	61
3.10	Verification and temporal order obtained by solving the one-dimensional wave equation. Left: time-dependent solution. Right: error norms and resulting temporal order of DINO.	62
3.11	Steady-state solution for the two-dimensional lid-driven cavity at $Re = 1000$. (a) horizontal velocity along the vertical centerline of the cavity. (b) vertical velocity along the horizontal centerline of the cavity.	63
3.12	Homogeneous isotropic turbulence decaying in time. (a) Q-criterion isosurface (value of $6 \times 10^5 \text{ 1/s}^2$) at time $t = 11.2\tau_\eta$. (b) energy spectrum obtained by DINO compared with experimental results of [86].	65
3.13	isosurface of z-vorticity of 3D-TGV at initial conditions.	65
3.14	Time evolution of isosurfaces of z-vorticity for 3D-TGV using 512^3 grid points at times: (a) $t/T_c = 5.46$ (vortex roll-up), (b) $t/T_c = 8.0$ (coherent structure breakdown), (c) $t/T_c = 12.11$ (turbulence), (d) $t/T_c = 18.55$ (decay), respectively.	66
3.15	Temporal evolution of (a) normalized kinetic energy, and (b) its dissipation rate.	67
3.16	Comparison between DINO, Moser et al. (MKM) and Vreman and Kuerten (VK) concerning the turbulent channel flow at $Re_\tau \simeq 180$. (a) mean velocity. (b) velocity fluctuations and correlations.	69
3.17	Streamlines of flow past a circular cylinder using DB-IBM at (a) $Re = 20$, and (b) $Re = 40$	69
3.18	Ignition delay obtained with DINO compared with experimental results. (a) C_2H_4/Air . (b) C_7H_{16}/Air . Note that the data have been scaled by the oxygen concentration in the left figure.	71
3.19	Comparison of numerically obtained laminar flame speeds with experimental measurements for ethylene/air flames.	72
3.20	Time evolution of spatially-evolving jet of H_2/air mixture. Red and gray isosurfaces represent the heat release and Q-criterion, respectively. The color 2D-cut plane shows the mixture temperature.	74
3.21	Time evolution of spatially-evolving jet of C_2H_4/air mixture. Red and gray iso-surfaces represent the heat release and Q-criterion, respectively. The color 2D-cut plane shows the mixture temperature.	75
3.22	Time evolution of temperature of H_2/air mixture for initial jet temperature of 1300 K.	76
3.23	Time evolution of temperature of H_2/air mixture for initial jet temperature of 1500 K.	77

4.1	Time evolution of diameter of single n-heptane droplet: validation of the evaporation model. The symbols represent the experimental work of Chauveau et al. (2008) [111]; dashed lines represent the simulation result computed by Sierra (2012) [39]; the solid lines represent DINO simulations.	79
4.2	Numerical configuration.	80
4.3	Isosurface of temperature ($T = 1800$ K) at time $t = \tau_g$ for both configurations: (a) Case A, (b) Case B. The spheres represent the droplets (size multiplied by factor 10 for visualization purpose). The windows enclosed within blue dashed lines are discussed in the next figure.	83
4.4	Two-dimensional cuts through Fig. 4.3 (blue dashed rectangles): (a) Case A, (b) Case B. The thin isolevels show the temperature with values between 1800 K and 2600 K at time $t = \tau_g$. The background represents the mixture fraction, increasing from white ($\zeta_z = 0$) to blue ($\zeta_z = 0.2$). Solid thick gray lines represent premixed flames ($\xi_p \simeq 1$), while dashed thick gray lines represent nonpremixed flames ($\xi_p \simeq 0$).	83
4.5	Normalized probability density function of mixture fraction at ignition time, $t = \tau_g$	84
4.6	Scatter plot of temperature versus mixture fraction at ignition time, $t = \tau_g$: (a) Case A, (b) Case B. Black and white dots represent nonpremixed ($\xi_p \simeq 0$), and premixed ($\xi_p \simeq 1$) flames, respectively.	84
4.7	Scatter plot of heat release versus mixture fraction at ignition time, $t = \tau_g$. (a) Case A, (b) Case B. Black and white dots represent nonpremixed ($\xi_p \simeq 0$), and premixed ($\xi_p \simeq 1$) flames, respectively.	85
4.8	Scatter plot of scalar dissipation rate versus mixture fraction at ignition time, $t = \tau_g$. (a) Case A, (b) Case B. Black and white dots represent nonpremixed ($\xi_p \simeq 0$), and premixed ($\xi_p \simeq 1$) flames, respectively.	85
4.9	Time evolution for conditional mean of scalar dissipation rate versus mixture fraction; where the solid lines and dashed lines represent Case A and B, respectively.	86
4.10	Volume-averaged gas temperature versus time for different values of the local equivalence ratio ϕ	87
4.11	Volume-averaged values versus time for different values of the droplet diameter a . (a) Gas temperature. (b) n-heptane mass fraction in the gas.	88
4.12	Conditional mean of scalar dissipation rate versus mixture fraction at ignition time for different jet velocities. The case with $U_j^* = 100$ m/s is a repetition of $U_j = 100$ m/s, doubling the domain length with same grid resolution.	88
4.13	Temporal-evolution of 2D-cut plane of gas temperature and droplets for Case I. The size of each droplet is multiplied by 2 for visualization.	90
4.14	Temporal-evolution of 2D-cut plane of gas temperature and droplets for Case II. The size of each droplet is multiplied by 2 for visualization.	90
4.15	Temporal-evolution of 2D-cut plane of gas temperature and droplets for Case III. The size of each droplet is multiplied by 2 for visualization.	91
4.16	Temporal-evolution of iso-volume of gas temperature (value $T = 2000$ K) with droplets for Case III. The size of each droplet is multiplied by 4 for visualization.	92

5.1	Evolution of the Taylor Reynolds number vs. time for all time-decaying DNS simulations. The time interval used for the analysis of the DNS results starts at $t = \tau_\Lambda$ and stops at $t = 3\tau_\Lambda$ for all cases. Values of τ_Λ listed in Table 5.1 are used for normalization.	101
5.2	Spectral entropy versus average Taylor Reynolds number for all DNS simulations, computed with all modes ($M = N_m = 50$). The dashed line with black dots represents the entropy computed directly from the DNS data. The solid line represents the best curve fitting, with coefficients $A = 1.089$ and $B = 0.0431$. The vertical and horizontal gray regions represent the transitional region in terms of Re_λ and of the corresponding entropy values.	102
5.3	Spectral entropy versus average Taylor Reynolds number for all 3D DNS simulations, as a function of the spatial resolution used during post-processing.	104
5.4	Spectral entropy versus average Taylor Reynolds number for all 3D DNS simulations, as a function of the number of snapshots N_m involved in the analysis while keeping the overall time constant, $\Delta t_{\text{overall}}^s = 2\tau_\Lambda$	106
5.5	Spectral entropy versus average Taylor Reynolds number for all 3D DNS simulations using different 2D slices, compared to the 3D analysis (solid line).	107
5.6	Time statistics of 3D-TGV benchmark. (a) Evolution of the spectral entropy S_d computed for increasing values of $\Delta t_{\text{overall}}^s \in [3t/T_c, 18t/T_c]$ starting from initialization, the resulting value of S_d being plotted at the end of the corresponding time interval. (b) Dissipation rate of the kinetic energy computed using DINO simulation.	108
5.7	Analysis results for the FDA nozzle, with flow from left to right. Top: instantaneous velocity magnitude in a central 2D plane, as obtained by LES; the blue lines with the labels refer to the locations of the analyzed cross-sections. Bottom: spectral entropy S_d obtained at the different cross-sections, the numbers from 1 to 9 corresponding to the labels in the top figure.	110
6.1	A schematic illustration of the triplet map in ODT [179].	115
6.2	Numerical settings; (a) Schematic distribution of initial temperature and major species mass fractions for autoignition tests. (b) Instantaneous DNS result in the 3D domain, showing the temperature field as color contours. The white thick line along the crosswise direction, with a profile plotted along it, represents a typical 1D ODT simulation.	119
6.3	Time-evolution of ensemble-averaged temperature of Case I	120
6.4	Time-evolution of ensemble-averaged temperature of Case II	121
6.5	Time-evolution of ensemble-averaged temperature of Case III	121
6.6	Time-evolution of ensemble-averaged temperature of Case IV	121
6.7	Time-evolution of ensemble-averaged temperature of Case I	122
6.8	Time-evolution of ensemble-averaged temperature of Case II	122
6.9	Time-evolution of ensemble-averaged temperature of Case III	123
6.10	Time-evolution of ensemble-averaged temperature of Case IV	123
6.11	Time-evolution of ensemble-averaged temperature of Case I	124
6.12	Time-evolution of ensemble-averaged temperature of Case II	124

6.13	Time-evolution of ensemble-averaged temperature of Case III	124
6.14	Time-evolution of ensemble-averaged temperature of Case IV	125
6.15	Instantaneous temperature profile at $t = 32.6\tau_j$ for Case I: (a) Contours of DNS, (b) line taken along the crosswise direction of DNS domain, (c) An ODT realization selected randomly.	125
6.16	Instantaneous temperature profile at $t = 37.5\tau_j$ for Case II: (a) Contours of DNS, (b) line taken along the crosswise direction of DNS domain, (c) An ODT realization selected randomly.	126
6.17	Instantaneous temperature profile at $t = 27.27\tau_j$ for Case III: (a) Contours of DNS, (b) line taken along the crosswise direction of DNS domain, (c) An ODT realization selected randomly.	126
6.18	Instantaneous temperature profile at $t = 20.69\tau_j$ for Case IV: (a) Contours of DNS, (b) line taken along the crosswise direction of DNS domain, (c) An ODT realization selected randomly.	126
6.19	Time-evolution of scatter plot of heat release versus temperature for Case I. Left column represents the DNS. Right column represents ODT. Time from top to bottom: $t = 6.5\tau_j, 10.8\tau_j, 15.2\tau_j,$ and $19.5\tau_j$	128
6.20	Time-evolution of scatter plot of heat release versus temperature for Case II. Left column represents the DNS. Right column represents ODT. Time from top to bottom: $t = 7.5\tau_j, 10.0\tau_j, 15.0\tau_j,$ and $20.0\tau_j$	129
6.21	Time-evolution of scatter plot of heat release versus temperature for Case III. Left column represents the DNS. Right column represents ODT. Time from top to bottom: $t = 9.0\tau_j, 12.0\tau_j, 15.0\tau_j,$ and $21.0\tau_j$	130
6.22	Time-evolution of scatter plot of heat release versus temperature for Case IV. Left column represents the DNS. Second column represents ODT with $\beta = 1.2$. Last column represents ODT with $\beta = 1.5$. Time from top to bottom: $t = 10.0\tau_j, 13.3\tau_j, 16.7\tau_j,$ and $20.0\tau_j$	131
6.23	Temperature versus different possible progress variables.	135
6.24	Comparison of FPI with detailed chemistry: temperature.	135
6.25	Comparison of FPI with detailed chemistry: heat release.	136
6.26	Schematic diagram shows the burned gases escape from combustion system and illustrate the considered DNS domain. The iso-surfaces in the right-hand side figure represents the temperature at different levels.	136
6.27	Temporal revolution of temperature iso-surface for both detailed (Det.) chemistry simulation (Top) and FPI one (bottom).	137
6.28	Schematic diagram showing the places where the averages are computed. Average is computed over spanwise direction at 4 different locations along the streamwise direction; $y/H = 10, 15, 29,$ and 25 . H is the jet width, and y is the length along the streamwise direction.	138
6.29	Ensemble-average temperature collected over spanwise direction at 4 different location along the streamwise direction.	139
6.30	Ensemble-averaged streamwise velocity collected over spanwise direction at 4 different location along the streamwise direction.	139

6.31	(a) 2D cuts showing instantaneous velocity magnitude in the highly turbulent channel flow. (b) Iso-volume of instantaneous mixture fraction in the turbulent jet.	142
6.32	Modal spectrum of the mixing jet case. (a) eigenvalue of SPOD. (b) spectrum of DMD.	143
6.33	Iso-surfaces of the spatial modes in the mixing jet, colored by the sign of streamwise velocity (positive or negative); each mode is normalized by its local maximum. Red and blue iso-surfaces represent the values of 0.5 and -0.5 , respectively. Top: SPOD. Bottom: DMD.	144
6.34	Modal spectrum of the channel flow case. (a) eigenvalue of SPOD. (b) spectrum of DMD	145
6.35	Iso-surfaces of the spatial modes in the channel flow close to the wall (part of the domain), colored by the sign of streamwise velocity (positive or negative); each mode is normalized by its local maximum value. Red and blue iso-surfaces represent the values of 0.5 and -0.5 , respectively. Top: POD. Bottom: DMD.	146

Nomenclatures

Roman Letters

Symbol	Description	Units
a_{ij}	Number of atoms of element j in a molecule of species i	[-]
a_k	Diameter of non-resolved droplets	[m]
A_{fj}	Arrhenius law pre-exponential constant	[varies]
c	Speed of sound	[m/s]
C_d	Drag coefficient	[-]
C_{ij}	Correlation matrix	
C_p	Specific heat of mixture at constant pressure	[J/kg/K]
$C_{p,f}^F$	Specific heats of fuel vapor in the film region	[J/kg/K]
$C_{p,f}$	Specific heats of gas mixture in the film region	[J/kg/K]
$C_{p,k}$	Specific heat of specie k at constant pressure	[J/kg/K]
D_k	Molecular diffusion coefficient of species k	[m ² /s]
D_{kT}	Thermodiffusion coefficient (Soret effect)	[m ² /s]
D_{th}	Thermal diffusion coefficient	[m ² /s]
e_t	Total energy per unit mass	[m ² /s ²] \equiv (J/kg)
E_j	Arrhenius law activation energy	[J/mole]
$E(\kappa)$	Energy spectrum of turbulent kinetic energy	[m ² /s ²]
f_k	Volume force	[N/kg]
h_t	Total energy	[J/kg]
h_s	Sensible enthalpy	[J/kg]
H	Jet width	[m]
l_t	Integral length scale	[m]
J	Jacobian matrix	
k	Turbulent kinetic energy	[m ² /s ²]
L	Length	[m]
$L_{v,s}$	Molar latent heat at reference temperature	[J/mole]
L_2	Second error-norm	
L_∞	Infinity error-norm	
m	Total mass of mixture	[kg]
m_j	Mass of element j	[kg]
m_k	Mass of species k	[kg]
\dot{m}_F	Fuel mass flux gained by the gas mixture	[kg/s]

\dot{m}_k	Liquid mass flux leaving the droplet surface	[kg/s]
N	Number of grid points	[-]
N_e	Number of elements	[-]
N_k	Number of droplets	[-]
N_s	Number of species	[-]
p	Hydrodynamic pressure	[Pa]
p_0	Ambient thermodynamic pressure	[Pa]
P_∞	Pressure in far-field gas mixture	[Pa]
P_{ref}	Reference pressure	[Pa]
$P_{\text{sat},k}$	Saturated vapor pressure	[Pa]
\tilde{p}	Perturbational pressure field	[Pa]
q_i	Heat energy flux	[W/m ²]
Q	Number of grid points across a flame front	[-]
Q_k	Total heat rate leaving the droplet k	[W]
Re	Reynolds number	[-]
Re _t	Reynolds based on integral length scale	[-]
Re _λ	Reynolds number based on Taylor length scale	[-]
Re _τ	Friction Reynolds number	[-]
s_d	spectral entropy	[-]
S_{ij}	Shear stress tensor	[s ⁻¹]
s_L	Laminar flame speed	[m/s]
s_m	Mass-based stoichiometric ratio	[-]
s_n	Molar-based stoichiometric ratio	[-]
t	Time	[s]
T	Temperature of mixture	[K]
T_{cr}	Critical temperature	[K]
T_{ref}	Reference temperature	[K]
u	Flow velocity	[m/s]
u_f	Fame velocity	[m/s]
u^+	Mean flow velocity in wall unit	[-]
U_{co}	Co-flow flow velocity	[m/s]
U_j	Jet flow velocity	[m/s]
\mathbf{U}	Velocity vector of fluid at the surface of the immersed body	[m/s]
\mathbf{U}_d	Desired velocity vector of immersed body	[m/s]
U^{ex}	Exact analytical solution	
u'	Turbulent fluctuation velocity	[m/s]
u'_k	Kolmogorov turbulent fluctuation velocity	[m/s]
$V_{i,k}$	Diffusion velocity of species K	[m/s]
\mathbf{V}_k	Velocity vector of discrete phase	[m/s]
W	Molar weight of mixture	[kg/mole]
W'_j	Molar weight of element j	[kg/mole]
W_k	Molar weight of species k	[kg/mole]
\mathbf{x}	Position vector	[m]
X_k	Mole fraction of species k	[-]

Y_c	Mass fraction of progress variable	[-]
Y_k	Mass fraction of species k	[-]
$Y_{s,k}$	Vapor surface mass fraction (saturated vapor mass fraction)	[-]
$Y_{F,\infty}$	Fuel mass fraction in far-field gas mixture	[-]
Y_z	Mixture fraction	[-]
Z_j	Mass fraction of element j	[-]

Greek Letters

Symbol	Description	Units
β_j	Arrhenius law temperature-dependent exponent	[-]
Γ_e	Source term of energy flux per unit volume	[J/m ³ /s]
Γ_m	Source term of mass flux per unit volume	[kg/m ³ /s]
Γ_{u_i}	Source term of momentum flux per unit volume	[kg/m ² /s ²]
δ_d	Diffusive flame thickness	[m]
δ_i	Initial flame thickness	[m]
δ_{ij}	Kronecker delta function	[-]
δ_L	Laminar flame thickness	[m]
δ_t	Total flame thickness	[m]
δ_{th}	Thermal flame thickness	[m]
δ_ν	Flame thickness based on transport properties	[m]
$\Delta h_{f,k}^o$	Mass enthalpy of formation of species k at a reference temperature T_0	[J/kg]
Δt	Time step	[s]
Δx	Grid resolution	[m]
Δy^+	Grid resolution in wall unit	[-]
ΔH_j^0	Change in enthalpy from reactants to products	[J/kg]
ΔS_j^0	Change in entropy from reactants to products	[J/kg/K]
ϵ	Dissipation rate of turbulence kinetic energy	[m ² /s ³]
ζ	Mixture fraction	[-]
ζ_{st}	Mixture fraction at stoichiometric conditions	[-]
η_k	Kolmogorov length scale	[m]
κ	spatial wave number	[m ⁻¹]
λ	Eigenvalue	
λ'	The local rate of occurrence (per square length) of each eddy in ODT model	[m ⁻² .s ⁻¹]
λ_t	Taylor length scale	[m]
λ	Thermal conductivity of mixture	[W/K/m]
Λ	Longitudinal integral length scale of turbulence	[m]
Λ'	The total rate of occurrence of each eddy in the ODT model	[s ⁻¹]
μ	Dynamic viscosity of mixture	[kg/m/s] \equiv (Pa.s)
ν	kinematic viscosity	[m ² /s]

ν'_{kj}	Molar stoichiometric coefficient of species k in reaction j in reactants	[-]
ν''_{kj}	Molar stoichiometric coefficient of species k in reaction j in products	[-]
ξ	Stretching function	[m]
ρ	Density of mixture	[kg/m ³]
ρ_L	Density of liquid droplet	[kg/m ³]
σ_{ij}	Total stress tensor	[kg/m/s ²] \equiv (Pa)
τ	The eddy time scale	[s]
$\tau_{a,k}$	Evaporation delay time scale of non-resolved droplet	[s]
τ_c	Chemical time scale	[s]
τ_{ij}	Viscous stress tensor	[kg/m/s ²] \equiv (Pa)
$\tau_f(r)$	Flow time scale of eddy of size r	[s]
τ_g	Autoignition delay time	[s]
τ_t	Turbulent time scale	[s]
$\tau_{t,k}$	Heating delay time scale of non-resolved droplet	[s]
$\tau_{v,k}$	Momentum relaxation time scale of non-resolved droplet	[s]
τ_η	Kolmogorov times scale	[s]
ϕ	Equivalence ratio of mixture	[-]
ϕ_g	Global equivalence ratio of mixture	[-]
ϕ	POD spatial modes	
χ	Scalar dissipation rate	[s ⁻¹]
χ_q	Scalar dissipation rate at quenching	[s ⁻¹]
χ_{st}	Scalar dissipation rate at the stoichiometric condition	[s ⁻¹]
$\dot{\omega}_k$	Mass reaction rate of species k	[kg/m ³ /s]

Non-dimensional Numbers

Symbol	Description
B_m	Spalding number for mass transfer
B_T	Spalding number for heat transfer
Da	Damköhler number
G	Group number of droplet
Ka	Karlovitz number
Le_k	Lewis number
Ma	Mach number
Nu	Nusselt number
Re_c	Acoustic Reynolds number
Re_k	Droplet Reynolds number
Sc_k	Schmidt number of species k
Sh	Sherwood number
Pr	Prandtl number

Operators

Symbol	Description
\sum_i	Einstein summation convention
∇	Differential operator
$\hat{\cdot}$	Fourier transform

Miscellaneous

Symbol	Description	Units
\mathcal{C}	Progress variable	[-]
\mathcal{D}_{jk}	Binary diffusion coefficients	[m ² /s]
\mathcal{J}_j	Progress rate of reaction j	[varies]
\mathcal{K}_{fj}	Forward rates of reaction j	[varies]
\mathcal{K}_{rj}	Reverse rates of reaction j	[varies]
$\mathcal{O}(\cdot)$	Order of (\cdot)	[-]
\dot{Q}_s	Heat source rate	[J/m ³ /s]
\mathcal{R}	Universal gas constant	[J/mol/k]
\mathcal{V}	Unit volume	[m ³]

Subscripts

Symbol	Description
0	Thermodynamic reference state
1	Refers to properties on the fresh gas side
2	Refers to properties on the burned gas side
∞	Refers to state in far field gas mixture
f	Refers to state in liquid film
F	Refers to Fuel
g	Refers to gas
max	Refers to maximum value
O	Refers to Oxidizer
O_2	Refers to Oxygen
ref	Stands for reference value

Abbreviations

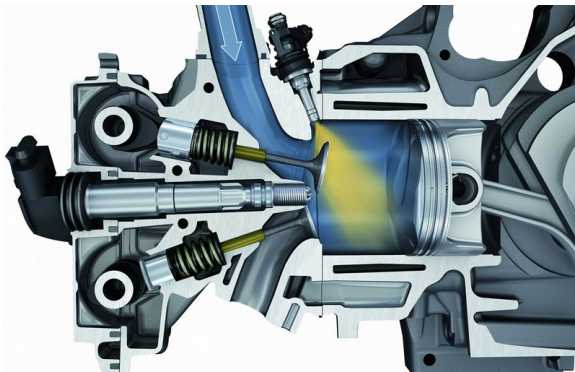
Acronym	Description
CFD	Computational fluid dynamics
CFL	Courant-Friedrichs-Lewy number
CG	Conjugate gradient
DMD	Dynamic mode decomposition
DNS	Direct numerical simulation
DCT	Discrete cosine transform
DD	Dirichlet-Dirichlet boundary conditions
DST	Discrete sine transform
FDA	Food and drug administration
FFT	Fast Fourier transform
FPI	Flame prolongation of intrinsic low-dimensional manifold
HIT	Homogeneous isotropic turbulence
HR	Heat release
IFFT	Inverse fast Fourier transform
ILDm	Intrinsic low-dimensional manifold
LES	Large eddy simulation
NN	Neumann-Neumann boundary conditions
ODT	One-dimensional turbulence model
PDF	Probability density function
RANS	Reynolds-averaged Navier-Stokes simulation
REDIM	Reaction-diffusion manifold
RHS	Right hand side
SuperMUC	Supercomputer at Leibniz Supercomputing Center in Munich
SPOD	Snapshot proper orthogonal decomposition
TGV	Taylor-Green vortex
VKP	Von Karman-Pao analytical spectrum of turbulence kinetic energy

Chapter 1

Introduction

1.1 Practical Importance of Spray Combustion

Spray combustion is found in many practical energy systems such as diesel engines, direct injection engines (Fig. 1.1(a)), gas turbines, industrial furnaces, thermal coating processes (Fig. 1.1(b)), etc. Many physical processes are involved in the spray combustion such as injection, atomization, dispersion, evaporation, and burning. Understanding the physics of spray combustion is very important for safety, energy efficiency, pollution reduction, health, etc.



(a) Porsche 911 (997) engine with direct fuel injection [1].



(b) Coating process using thermal spraying technique [2].

Figure 1.1: Spray combustion applications.

1.2 Spray

A spray is one type of two-phase flow. It involves a liquid as the dispersed phase in the form of droplets and a gas as the continuous phase. Challenging and complex fluid transport and fluid dynamic phenomena can occur with sprays in many different ways. On the scale of an individual droplet size in a spray, boundary layers and wakes develop due to relative

motion between the droplet center and the ambient gas. Other complicated and coupled fluid dynamic factors can be listed as follows: shear-driven internal circulation of the liquid in the droplet, flow modifications due to closely neighboring droplets in the spray, hydrodynamic interfacial instabilities leading to droplet shape distortion and perhaps droplet shattering, as well as droplet interactions with vortical structures in the gas flow. On a much larger and coarser scale, integrated exchanges of mass, momentum, and energy between many droplets take place with the surrounding gas flow. The problem is further complicated by the strong coupling of the phenomena on the different scales; one cannot accurately describe the mass, momentum, and energy exchanges on the large scale without detailed knowledge of the fine-scale phenomena. In some practical applications, these scales can differ by several orders of magnitude which results in a challenging sub-grid modeling problem [3]. Figure 1.2 shows the complexity of the spray dynamics even in a simple practical application.



Figure 1.2: Typical spray atomization and dispersion [4].

1.3 Challenges for Numerics of Spray Combustion

The spray combustion problem is a challenging, multidisciplinary problem. It involves many physical processes, including atomization, droplet collision and agglomeration, vaporization, heat and mass transfer, droplet dispersion, ignition, turbulence, pollutant production and flame extinction, as it can be illustrated in Fig. 1.3. In general, there is a relative motion between a droplet and its ambient gas. The aerodynamic characteristics of viscous boundary layers, pressure gradients, separated flows, and wakes can appear in the gas flow around the liquid droplet. Internal liquid circulation, driven by surface shear forces, is another important fluid dynamic feature of the liquid droplet problem. These flow features have a critical impact on the exchanges of mass, momentum, and energy between the gas and the liquid phases. They are important for both vaporizing and non-vaporizing situations. In developing the numerical study of the gas flow field surrounding the droplet and of the liquid flow in the droplet, certain assumptions are made. A small Mach number is considered so that kinetic energy and viscous dissipation are negligible. Droplet deformation, effect of gravity, radiation, and mass

1.4. History of DNS of Spray Combustion

diffusion due to pressure and temperature gradients are all neglected. The multicomponent gas phase mixture is assumed to behave as an ideal gas. Phase equilibrium is stated at the droplet-gas interface. Gas phase density and thermophysical parameters are generally considered variable, unless stated otherwise [3]. It is also common to assume that the droplet size is smaller than the grid cells (non-resolved droplets). Such DNS with non-resolved spray resolves the turbulence and flame structure scales only, as will be discussed later in this dissertation.

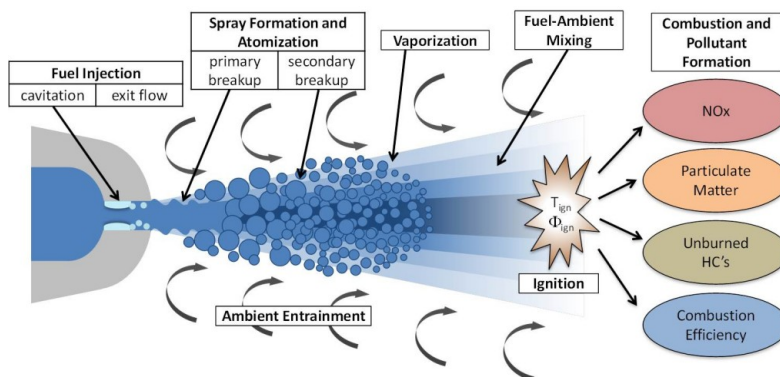


Figure 1.3: Schematic diagram showing the spray combustion process [5].

1.4 History of DNS of Spray Combustion

Numerical modeling of the phenomena in the combustion chamber is a necessary stage nowadays when developing or improving engines. Model development is based on the understanding of the basic physical phenomena. For this purpose, experimental measurements may be of great help. However, most often they contribute only incomplete information. Indeed, the simultaneous presence of a turbulent flow, an evaporating spray, and a combustion process in a confined geometry limits the capability of experimental techniques. On the other hand, direct numerical simulations (DNS) of the flow offer essential information, although such simulations have severe limitations in terms of Reynolds number. Therefore, an ideal research project would be to simultaneously carry out numerical and experimental studies on some basic configurations in order to understand all of the underlying phenomena, especially for two-phase (spray) flow in turbulent combustion.

A DNS consists of resolving the full set of partial differential equations describing the physics of the tested case. Despite claiming the resolution of the entire physics, these equations often result from a closure at a given level of the physics. The Navier-Stokes equations or Fick's law in scalar transport equations are themselves models issued from the analysis of the motion of the various molecules of the flow. However, as far as low or medium range Mach number flow is considered, the Navier-Stokes equations are regarded to be an exact representation of reality [6]. DNS offers a unique description of the physical phenomena with a direct access to all the flow parameters. However, considering two-phase flow, good intentions have to face reality: the presence of an interface between the continuous phase (gas)

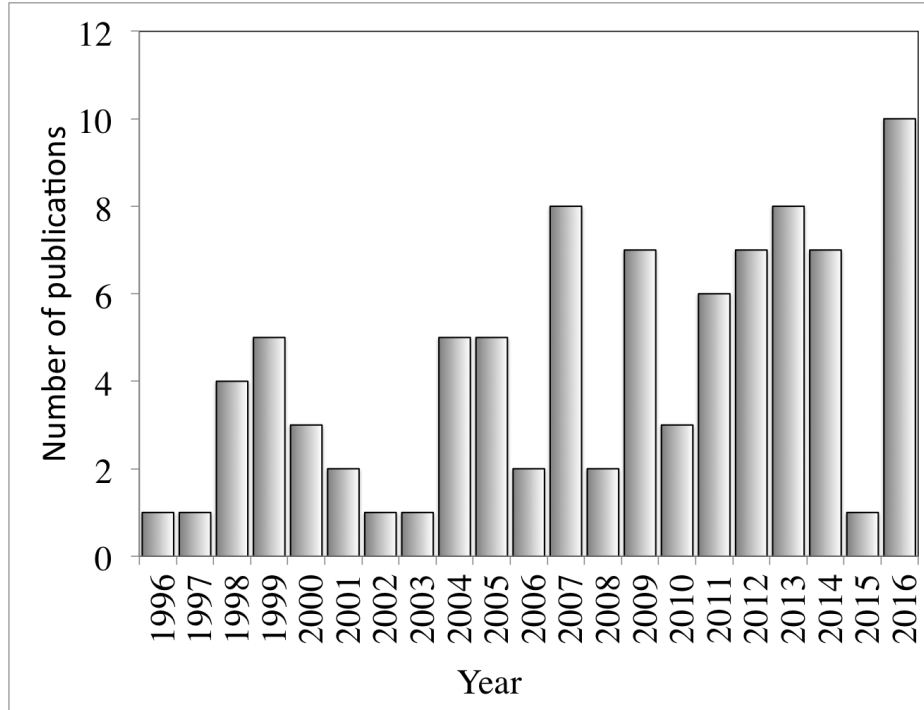


Figure 1.4: Rate of publications of DNS spray combustion since 1996, collected from google-scholar.

and the discrete phase (liquid) leads to characteristic scales and gradients far too extreme to be resolved without sacrificing accuracy. The most common alternative is the introduction of some Lagrangian models to account for the spray. This leads to **DNS-DPS** (Discrete Particle Simulation), results of which are correct enough to help in the understanding of many physical phenomena [6].

DNS was first introduced 44 years ago by Orszag and Patterson [7] and then Rogallo [8] for the simulation of inert gaseous flows. It has been used in a variety of applications since. During the last two decades, DNS of reactive flows have been carried out to study non-premixed, partially premixed, and premixed turbulent combustion of purely gaseous states [9–11]. DNS has been extended to two-phase flows since the pioneering work of Riley and Patterson [12]. Most of the first numerical studies were limited to solid particle dispersions. More recently, Mashayek et al. [13] and Miller and Bellan [14] have conducted the first DNS with evaporating droplets in turbulent flows. Since then, DNS of two-phase flows have been extended to incorporate two-way coupling effects, multicomponent fuels, etc. DNS also have been extended to deal with spray evaporation and combustion phenomena [14–17]. The rate of publications of DNS spray combustion can be presented in Fig.1.4.

In total, the literature on DNS with spray combustion can be divided into three different categories based on the kinetic scheme and numerical complexity: (1) DNS with single-step mechanisms [17–25]; (2) detailed kinetics in 2D simulations [6, 26, 27]; (3) more recently, detailed chemistry in 3D simulations [28–32]. It is also possible to divide the literature into three groups based on the numerical configurations: (1) spray dispersion and ignition in

homogeneous conditions and/or in flow with zero mean-flow velocity [6, 18, 20, 25, 26, 28–31], (2) spatially-evolving jets [17, 19, 23, 24, 32], and (3) temporally-evolving jets [27]. Frequent and common conclusions of all of these literature sources state that the equivalence ratio and droplet size are the most critical parameters controlling spray combustion mode and ignition. Although these studies answered many questions, the impact of different operation conditions and configurations has not yet been sufficiently clarified [23]; more specifically, the effect of shear and scalar dissipation rate are not completely clear. This issue will therefore be considered here.

1.5 Spatial Resolution of DNS-DPS

Direct numerical simulation grids must ensure that: (1) the calculation is performed in the largest possible domain to resolve the large scales, (2) the mesh is fine enough to resolve the smallest scales (usually Kolmogorov scale), (3) the mesh is fine enough to resolve the inner structure of the flame [11], (4) the mesh is larger than the droplet size.

1.5.1 Resolution of Turbulence Scales

Turbulence scales are well-resolved when the largest and smallest eddies are captured by the grid mesh. This leads to a standard condition which is derived as follows [11]. Consider a computational domain with a typical size L . The mesh with total number of grid points N in each dimension leads to a typical cell size $\Delta x = L/N$. The turbulent flow can be characterized by the large scale velocity fluctuations u' and integral length scale l_t . The size of the full domain should be at least of the order of one integral scale l_t ; $L = N \Delta x \geq l_t$. The smallest scale of turbulent eddies η_k (Kolmogorov length scale) is estimated from the Kolmogorov cascade arguments as:

$$\eta_k \simeq l_t / (\text{Re}_t)^{3/4} \quad \text{or} \quad \frac{\eta_k}{l_t} \simeq \text{Re}_t^{-3/4}, \quad (1.1)$$

where l_t is computed as a function of turbulent kinetic energy k and its dissipation rate ϵ ,

$$l_t = \frac{k^{3/2}}{\epsilon}, \quad (1.2)$$

and Kolmogorov length scale,

$$\eta_k = \left(\frac{\nu^3}{\epsilon} \right)^{1/4}. \quad (1.3)$$

The turbulent kinetic energy and dissipation rate can be defined, respectively, as:

$$k = \frac{3}{2}u'^2, \quad (1.4)$$

$$\epsilon = 2\nu \langle S_{ij}S_{ij} \rangle, \quad (1.5)$$

where ν is the kinematic viscosity of the gas and S_{ij} is the shear stress second-order tensor,

$$S_{ij} = 0.5 \left(\frac{\partial u_i}{\partial x_j} + \frac{\partial u_j}{\partial x_i} \right). \quad (1.6)$$

The Kolmogorov length scale is resolved by the computation if it is larger than the mesh size:

$$\eta_k > \Delta x, \quad (1.7)$$

or if, in wave space, the computation has a sufficiently large maximum wavenumber $\kappa_{\max} \eta_k$ [33], where

$$\kappa_{\max} = \frac{\pi N}{L}, \quad \text{OR} \quad \kappa_{\max} = \frac{\pi}{\Delta x}. \quad (1.8)$$

Corresponding to what had been concluded in [33], the dissipation spectrum is extremely small beyond $\kappa_{\max} \eta_k \geq 1.5$. This leads to a rough estimate of the smallest grid resolution,

$$\frac{\Delta x}{\eta_k} = \frac{\pi}{1.5} \approx 2.1. \quad (1.9)$$

Combining the previous expressions with the help of the expressions given in Chapter 9 of [33], the numerical grid points of a turbulent simulation could be roughly scaled as follows:

$$N \sim 1.6 \frac{l_t}{\eta_k} = 1.6 \text{Re}_t^{3/4} \approx 0.4 \text{Re}_\lambda^{3/2}. \quad (1.10)$$

More generally, the total number of grid points will be scaled as $\text{Re}_t^{3/4}$ [11]:

In Eq. (1.10), Re_λ is the Reynolds number based on the Taylor micro-length scale,

$$\lambda_t = u' \sqrt{\frac{15\nu}{\epsilon}}. \quad (1.11)$$

Equation (1.10) determines the number of grid points N required in each direction for a given Reynolds number Re_t or the limit value of the Reynolds number for a selected number of grid points in each direction.

1.5.2 Resolution of Chemical Scales

The inner flame structure must also be resolved on the computational mesh. In the following, this constraint is discussed for premixed flames since non-premixed flames have no intrinsic thicknesses and require a different treatment [11]. The proper resolution of chemical scales depends strongly on the type of chemical scheme used in the DNS. When simple descriptions

1.5. Spatial Resolution of DNS-DPS

for chemistry are used (one-step, irreversible reaction), calculations show that the resolution of the inner structure of the flame requires at least *ten to twenty* grid points ($Q \simeq 20$). In other words, the flame thickness δ_L should extend beyond $Q \simeq 20$ elementary cells, where

$$\Delta x = \frac{\delta_L}{Q} = \frac{L}{N}. \quad (1.12)$$

Therefore, in terms of flame thicknesses, the size of the computational domain is then given by

$$L \simeq \delta_L N/Q. \quad (1.13)$$

For standard hydrocarbon flames at room temperature, $\delta_L \simeq 0.5$ mm so that a 1024^3 grid would yield a box size of approximately $L \simeq 25$ mm. This condition also leads to an upper limit for the turbulence integral length scale l_t which must be smaller than L to provide converged statistics [11]:

$$\frac{l_t}{\delta_L} < \frac{L}{\delta_L} \leq \frac{N}{Q} \quad (1.14)$$

Another expression may be obtained by replacing δ_L with the diffusive flame thickness, $\delta_\nu = \nu/s_L$. The Damköhler number, $D_a = \tau_t/\tau_c$, compares a flow time scale τ_t and a chemical time scale τ_c . These two time scales may be estimated as $\tau_t = l_t/u'$ and $\tau_c = \delta_\nu/s_L$. The product of the Reynolds number by the Damköhler number is therefore:

$$\text{Re}_t D_a = \frac{l_t^2 s_L}{\delta_\nu \nu} = \left(\frac{l_t}{\delta_\nu} \right)^2, \quad (1.15)$$

leading to the computational grid condition,

$$N/Q > \sqrt{\text{Re}_t D_a}. \quad (1.16)$$

In this manner, the resolution required to resolve the turbulent flame could be computed based on both the Damköhler and the turbulent Reynolds number [11].

1.5.3 Resolution of the spray

As mentioned earlier in this chapter, the spray surface in this dissertation will not be resolved and the DPS approach will be employed. In this approach, the diameter a_k of the largest droplet should be smaller than the grid resolution Δx :

$$\frac{a_k}{\Delta x} < 1.0. \quad (1.17)$$

Of course, this approach does not consider coalescence or breakup of droplets. In summary, **DNS-DPS** have the following spatial scaling limits:

$$\frac{a_k}{\Delta x} < 1, \quad (1.18)$$

$$\frac{\eta_k}{\Delta x} > 1, \quad (1.19)$$

$$\frac{\delta_L}{\Delta x} > 1, \quad (1.20)$$

$$\frac{l_t}{L} < 1, \quad (1.21)$$

$$\kappa_{\max} \eta_k \geq 1.5 \quad (1.22)$$

$$N \geq 1.6 \text{Re}_t^{3/4}, \quad (1.23)$$

$$N/Q > \sqrt{\text{Re}_t D_a}. \quad (1.24)$$

These limits are considered in all simulations carried out in this dissertation.

1.6 Motivation and Dissertation Plan

As mentioned in Sec. 1.4, DNS involving sprays are still a hot research topic and have many questions that need to be answered; (1) the role and behavior of the scalar dissipation rate in turbulent mixing, (2) finding a suitable numerical set-up that is affordable and realistic, (3) having a tool that is able to handle a large domain, a large number of droplets, and, of course, a relatively high Reynolds number. This dissertation attempts to cover all of these issues.

The plan and objective of this dissertation could be summarized as follows: after giving a general introduction and literature survey on direct numerical simulation of spray combustion in Chapter 1, the fundamentals and governing equations of two-phase flows are given in Chapter 2. These governing equations and fundamentals are divided into two parts: (1) the continuous phase (gas), and (2) the discrete phase (liquid droplet).

To cover the third issue discussed in the first paragraph, a powerful DNS tool has been developed. This tool is called DINO, a 3D DNS solver. It was developed during the Ph.D. period in collaboration with selected co-workers. DINO is, in principle, able to simulate different engineering problems in different areas: pure turbulent study, single-phase turbulent combustion, flow in complex geometries, spray combustion, etc. DINO shows excellent parallel efficiency, as demonstrated over different supercomputing machines. High-efficiency computations in terms of CPU time and memory have been conducted with DINO. The algorithms, parallelization, verifications, validations, and possible applications are discussed in detail in Chapter 3.

Chapter 4 deals with the first and second issues discussed in the first paragraph. It introduces and tests affordable and realistic numerical configurations which help investigate the impact of shear on evaporation, mixing, and auto-ignition of liquid n-heptane droplets. It

also examines the flame topology which is characterized by the flame index, mixture fraction, scalar dissipation rate, temperature, and heat release. Thanks to a parametric study, the impact of different parameters on spray evaporation and autoignition is finally quantified.

In Chapter 5, a tool to quantify the flow state is developed. This tool is based on the spectral entropy obtained from solving an eigenvalue problem using as kernel the auto-correlation function of flow velocity. This tool was first derived and then calibrated with a well-defined flow benchmark: homogeneous isotropic turbulence. After the calibration, two different applications were tested using this tool: (1) DNS results obtained for the Taylor-Green vortex benchmark, and (2) results obtained through Large Eddy Simulations (LES) in a blood nozzle.

Even though DINO performs DNS in a very efficient and fast manner, as will be presented in this thesis, most of these applications (see Chapters 3 and 4) require the use of supercomputers/clusters. Due to this fact, several numerical reduction techniques are introduced in Chapter 6. These techniques are divided into three categories, depending on the nature of the reduction: (1) dimensional reduction: a stochastic method called one-dimensional turbulence model; (2) chemical/kinetic reduction: using a tabulation chemistry technique called FPI; (3) post-processing: two modal decomposition techniques are examined; the first is the snapshot proper orthogonal decomposition (SPOD), and the second is the dynamic mode decomposition (DMD). These three approaches are applied only to the gas phase. Therefore, these methods will be applied to and tested in mostly single phase (gas) turbulent reactive flows. These approaches, however, could be combined and applied to spray combustion in a straightforward manner.

This dissertation is closed with a summary in Chapter 7. In this chapter, conclusions concerning all findings and developed tools are given. From the results and current status of this dissertation, several recommendations are provided to improve further the two-phase studies using DINO. Finally, outlook and future plans are briefly discussed.

Chapter 2

Fundamentals and Governing Equations of DNS-DPS

This chapter reviews the governing equations for direct numerical simulation (DNS) and discrete particle simulation (DPS), with clarifications on some of the physical fundamentals of the spray process. First, the governing equations for the gas phase at different regimes are reviewed: compressible, low Mach number, and incompressible flow. Then, fundamental relations of thermodynamics, transport and chemical kinetics are given. Afterwards, different combustion modes (premixed and non-premixed) in laminar and turbulent flows are briefly discussed. Here, the most important characteristic relations for these two modes are given. The second part of this chapter reviews the fundamentals of the spray process: injection, atomization, dispersion, evaporation, and combustion (burning). This chapter is then concluded by reviewing the governing equations of the discrete phase.

2.1 DNS for Different Flow Regimes

The Navier-Stokes equation can be written in three main different forms: *incompressible*, *low-Mach number*, and *compressible*. Selecting the correct form amongst them is based on the application and the validity of the assumptions. Each regime has numerical advantages and disadvantages, depending on the applications as explained in the following.

2.1.1 Compressible Flow Equations

The compressible version of the Navier-Stokes equation is used to simulate flow movement with a relatively high Mach number, $Ma > 0.3$. The total mass conservation (continuity) equation reads

$$\frac{\partial \rho}{\partial t} + \frac{\partial(\rho u_i)}{\partial x_i} = \Gamma_m. \quad (2.1)$$

2.1. DNS for Different Flow Regimes

The mass conservation equation for species k reads

$$\frac{\partial(\rho Y_k)}{\partial t} + \frac{\partial(\rho u_i Y_k)}{\partial x_i} = -\frac{\partial(\rho V_{k,i} Y_k)}{\partial x_i} + \dot{\omega}_k + \Gamma_{m,k}, \quad \text{for } k = 1, 2, \dots, N_s, \quad (2.2)$$

where Y_k is the mass fraction, $V_{k,i}$ is the diffusion velocity, and the reaction rate should fulfill the following constraints:

$$\sum_{k=1}^{N_s} Y_k = 1, \quad (2.3)$$

$$\sum_{k=1}^{N_s} Y_k V_{k,i} = 0, \quad (2.4)$$

$$\sum_{k=1}^{N_s} \dot{\omega}_k = 0, \quad (2.5)$$

where N_s is the total number of species. The equation for the conservation of momentum is written ($i = 1, 2, 3$):

$$\frac{\partial(\rho u_i)}{\partial t} + \frac{\partial(\rho u_i u_j)}{\partial x_j} = -\frac{\partial p}{\partial x_i} + \frac{\partial \tau_{ji}}{\partial x_j} + \rho \sum_{k=1}^{N_s} Y_k f_{k,i} + \Gamma_{u_i}, \quad (2.6)$$

where the viscous tensor τ_{ji} is defined by:

$$\tau_{ji} = -\frac{2}{3}\mu \frac{\partial u_k}{\partial x_k} \delta_{ji} + \mu \left(\frac{\partial u_j}{\partial x_i} + \frac{\partial u_i}{\partial x_j} \right), \quad (2.7)$$

where, x_i , u_i , ρ , and μ are the i -th component of the position vector, i -th component of the gas velocity, total mixture density, and dynamic viscosity of the mixture, respectively.

The equation for the conservation of energy has multiple forms; the most common ones will be presented. The first form is the equation for the total energy e_t , which can be written as

$$\frac{\partial(\rho e_t)}{\partial t} + \frac{\partial(\rho u_i e_t)}{\partial x_i} = -\frac{\partial q_i}{\partial x_i} + \frac{\partial(\sigma_{ij} u_i)}{\partial x_j} + \dot{Q}_s + \rho \sum_{k=1}^{N_s} Y_k f_{k,i} (u_i + V_{k,i}) + \Gamma_e. \quad (2.8)$$

In this equation, the total stress tensor σ_{ij} and the energy flux q_i are

$$\sigma_{ij} = -p\delta_{ij} + \tau_{ij} \quad (2.9)$$

and

$$q_i = \lambda \frac{\partial T}{\partial x_i} + \rho \sum_{k=1}^{N_s} h_k Y_k V_{k,i}, \quad (2.10)$$

respectively. In Eqn. (2.8), \dot{Q}_s represents any heat source (for example, radiative flux, electrical spark, etc.). The fourth term on the right hand side of this equation is the power produced by the volume force f_k on species k . From the relations between the total energy e_t , total enthalpy h_t , and the sensible enthalpy h_s ,

$$h_t = h_s + \sum_{k=1}^{N_s} \Delta h_{f,k}^o Y_k + \frac{1}{2} u_i u_i, \quad (2.11)$$

the equation for sensible enthalpy can be deduced:

$$\begin{aligned} \rho \frac{Dh_s}{Dt} &= \dot{\omega}_T + \frac{Dp}{Dt} + \frac{\partial}{\partial x_i} \left(\lambda \frac{\partial T}{\partial x_i} \right) - \frac{\partial}{\partial x_i} \left(\rho \sum_{k=1}^{N_s} h_{s,k} Y_k V_{k,i} \right) \\ &+ \tau_{ij} \frac{\partial u_i}{\partial x_j} + \dot{Q}_s + \rho \sum_{k=1}^{N_s} Y_k f_{k,i} V_{k,i} + \Gamma_e, \end{aligned} \quad (2.12)$$

where the first term on the right-hand side of this equation represents the heat release due to combustion,

$$\dot{\omega}_T = - \sum_{k=1}^{N_s} \Delta h_{f,k}^o \dot{\omega}_k. \quad (2.13)$$

In Eqns. (2.11) and (2.13), $\Delta h_{f,k}^o$ is the mass enthalpy of formation of species k at a reference temperature T_0 . In CFD, the energy equation is oftentimes coded either in the sensible enthalpy equation or the temperature form,

$$\begin{aligned} \rho C_p \frac{DT}{Dt} &= - \sum_{k=1}^{N_s} h_k \dot{\omega}_k + \frac{Dp}{Dt} + \frac{\partial}{\partial x_i} \left(\lambda \frac{\partial T}{\partial x_i} \right) - \left(\rho \sum_{k=1}^{N_s} C_{p,k} Y_k V_{k,i} \right) \frac{\partial T}{\partial x_i} \\ &+ \tau_{ij} \frac{\partial u_i}{\partial x_j} + \dot{Q}_s + \rho \sum_{k=1}^{N_s} Y_k f_{k,i} V_{k,i} + \Gamma_e, \end{aligned} \quad (2.14)$$

which are more straightforward for coding. On the right hand side of all previous equations (Eqs. (2.1)-(2.14)), the Γ refers to the source terms for mass, momentum, and energy; its value depends on the nature of the source. For spray combustion, the value of Γ will be given later in this chapter.

2.1.2 Low Mach Number Flow Equations

The low Mach number model is derived from the compressible flow equations (Eqs. (2.1)-(2.14)) using asymptotic analysis introduced by Majda and Sethian [34]. Here, the Mach number is assumed to be smaller than 0.3 with the presence of density variation. This analysis is reviewed in a simple manner and can be derived by first writing the momentum equation in one-dimensional form:

$$\rho \frac{\partial u}{\partial t} + \rho u \frac{\partial u}{\partial x} = -\frac{\partial p}{\partial x} + \mu \frac{\partial^2 u}{\partial x^2}. \quad (2.15)$$

Equation (2.15) can be written in dimensionless form using reference length L and speed of sound c_1 in the fresh gas region as

$$\frac{\partial p^*}{\partial x^*} = -\underbrace{\rho^* \frac{\partial u^*}{\partial t^*}}_{\mathcal{O}(\text{Ma})} - \underbrace{\rho^* u^* \frac{\partial u^*}{\partial x^*}}_{\mathcal{O}(\text{Ma}^2)} + \underbrace{\frac{1}{\text{Re}_c} \frac{\partial}{\partial x^*} \frac{\partial u^*}{\partial x^*}}_{\mathcal{O}(\text{Ma}/\text{Re})}, \quad (2.16)$$

where

$$\begin{aligned} \text{Re}_c &= \rho_1 c_1 L / \mu_1, \\ \text{Ma} &= s_L / c_1, \\ u^* &= u / c_1, \\ x^* &= x / L, \\ \rho^* &= \rho / \rho_1, \\ t^* &= c_1 t / L, \\ p^* &= p / (\rho_1 c_1^2), \end{aligned} \quad (2.17)$$

where Re_c and s_L are the acoustic Reynolds number and the flame speed, respectively. In Eq. (2.17), subscript 1 refers to fresh gas quantities. It is obvious from Eq. (2.16) that for high Reynolds number and unsteady flow, the pressure variation is on the order of Ma . In the case of subsonic combustion with very low Ma , the pressure variation is thus negligible. This conclusion allows the assumption that the thermodynamic pressure p_o is a constant value. In this manner, the total pressure p can be decomposed into two separate pressures: the perturbational pressure field \tilde{p} and the ambient thermodynamic pressure p_0 :

$$p(x, t) = p_0 + \tilde{p}(x, t), \quad (2.18)$$

where the low Mach model assumes that $\tilde{p}/p_0 \sim \mathcal{O}(\text{Ma}^2)$ and all thermodynamic quantities are independent of \tilde{p} . Also, this model solves the equation for vorticity and entropy waves, while neglecting the acoustic ones. In the low Mach model, the total mass, the species mass, and the conservation of momentum equations (Eqs. (2.1), (2.2) and (2.6)) for compressible conditions do not change. The changes appear only in the energy, enthalpy, and temperature equations. In the low Mach model, the following terms are negligible:

- total pressure derivative, Dp/Dt , in the energy equation which is mainly thermodynamic,
- viscous heating term, $\tau_{ij}(\partial u_i/\partial x_j)$, which can be neglected because it is of high order in Ma.

Consequently, total energy, sensible enthalpy, and temperature can be defined as

$$\frac{\partial(\rho e_t)}{\partial t} + \frac{\partial(\rho u_i e_t)}{\partial x_i} = -\frac{\partial q_i}{\partial x_i} + \dot{Q}_s + \rho \sum_{k=1}^{N_s} Y_k f_{k,i}(u_i + V_{k,i}) + \Gamma_e, \quad (2.19)$$

$$\begin{aligned} \rho \frac{Dh_s}{Dt} &= \dot{\omega}_T + \frac{\partial}{\partial x_i} \left(\lambda \frac{\partial T}{\partial x_i} \right) - \frac{\partial}{\partial x_i} \left(\rho \sum_{k=1}^{N_s} h_{s,k} Y_k V_{k,i} \right) \\ &+ \dot{Q}_s + \rho \sum_{k=1}^{N_s} Y_k f_{k,i} V_{k,i} + \Gamma_e, \end{aligned} \quad (2.20)$$

$$\begin{aligned} \rho C_p \frac{DT}{Dt} &= -\sum_{k=1}^{N_s} h_k \dot{\omega}_k + \frac{\partial}{\partial x_i} \left(\lambda \frac{\partial T}{\partial x_i} \right) - \left(\rho \sum_{k=1}^{N_s} C_{p,k} Y_k V_{k,i} \right) \frac{\partial T}{\partial x_i} \\ &+ \dot{Q}_s + \rho \sum_{k=1}^{N_s} Y_k f_{k,i} V_{k,i} + \Gamma_e, \end{aligned} \quad (2.21)$$

respectively. Since the acoustic waves are not considered in the low Mach number model, the time step limitation is controlled only by convection and diffusion (and possibly radiation). This allows for an increase in the time step compared to that used in a fully compressible model. This will reduce the total computation time of the simulation. However, in the low Mach number model, the Poisson equation needs to be solved in order to obtain the fluctuating pressure \tilde{p} , which computationally requires additional efforts and special care, as explained later.

2.1.3 Incompressible Flow Equations

The incompressible version of the Navier-Stokes equation is always used to simulate flow which has no (and therefore negligible) density variation; thus solving the temperature equation is not required. The standard application for this model is a cold incompressible flow. In this model, the mass conservation reads

$$\frac{\partial u_i}{\partial x_i} = \Gamma_m, \quad (2.22)$$

2.2. Thermodynamic Relations

and the momentum equation reads simply

$$\frac{\partial u_i}{\partial t} + \frac{\partial(u_i u_j)}{\partial x_j} = -\frac{1}{\rho} \frac{\partial p}{\partial x_i} + \nu \frac{\partial^2 u_i}{\partial x_j^2} + \Gamma_{u,i}. \quad (2.23)$$

As in the low Mach number model, the incompressible version of the Navier-Stokes equation requires the Poisson equation to be solved to obtain the fluctuating pressure.

2.2 Thermodynamic Relations

In the previous sections, different transport and thermodynamic properties appeared. These are reviewed here.

The mass of each species m_k in the mixture, which has total mass m , is represented in mass fraction form as:

$$Y_k = m_k/m. \quad (2.24)$$

However, the mass fraction of the species changes due to chemical reactions, while the mass of each element j is conserved. The mass of each element can be defined as:

$$m_j = \sum_{i=1}^{N_s} \frac{a_{ij} W'_j}{W_i} m_i, \quad \text{for } j = 1, 2, \dots, N_e, \quad (2.25)$$

where a_{ij} , N_e , W'_j , and W_i are the number of atoms of element j in a molecule of species i , total number of elements in the system, the molecular weight of element j , and the molecular weight of species i , respectively. The mass fraction of element j is then

$$\begin{aligned} Z_j &= \frac{m_j}{m} \\ &= \sum_{i=1}^{N_s} \frac{a_{ij} W'_j}{W_i} Y_i \\ &= \frac{W'_j}{W} \sum_{i=1}^{N_s} a_{ij} X_i \quad \text{for } j = 1, 2, 3, \dots, N_e, \end{aligned} \quad (2.26)$$

where X_i is the mole fraction of species i and W is the mean molecular weight of the mixture,

$$W = \left[\sum_{k=1}^{N_s} \frac{Y_k}{W_k} \right]^{-1} = X_i \frac{W_i}{Y_i}. \quad (2.27)$$

It is important to keep the following in mind:

$$\begin{aligned}
 \sum_{i=1}^{N_s} X_i &= 1, \\
 \sum_{i=1}^{N_s} Y_i &= 1, \\
 \sum_{j=1}^{N_e} Z_j &= 1.
 \end{aligned} \tag{2.28}$$

The total pressure for ideal gases can be expressed as

$$p = \sum_{k=1}^{N_s} p_k, \tag{2.29}$$

$$p_k = \rho_k \frac{\mathcal{R}}{W_k} T, \tag{2.30}$$

where $\mathcal{R} = 8.314 \text{ J}/(\text{mole K})$ is the universal gas constant. The total density of the multi-species gas is

$$\rho = \sum_{k=1}^{N_s} \rho_k. \tag{2.31}$$

In this manner, the equation of state can be defined as

$$p = \rho \frac{\mathcal{R}T}{W}. \tag{2.32}$$

The enthalpy of each species h_k and the summation of the sensible and chemical enthalpies of the mixture h are defined as

$$h_k = \underbrace{\int_{T_0}^T C_{p,k} dT}_{\text{sensible}} + \underbrace{\Delta h_{f,k}^0}_{\text{chemical}} \tag{2.33}$$

and

$$h = \sum_{k=1}^N h_k Y_k \tag{2.34}$$

$$\begin{aligned}
 &= \underbrace{\int_{T_0}^T C_p dT}_{\text{sensible enthalpy}} + \underbrace{\sum_{k=1}^{N_s} \Delta h_{f,k}^0 Y_k}_{\text{chemical enthalpy}},
 \end{aligned} \tag{2.35}$$

2.3. Transport Relations

respectively. The energy corresponding to the enthalpy h in the previous equations reads

$$e = h - \frac{p}{\rho}. \quad (2.36)$$

After adding the contribution of the kinetic energy to Eqs. (2.35) and (2.36), the total enthalpy and energy can be written as

$$h_t = h + \frac{1}{2}u_i u_i \quad (2.37)$$

and

$$e_t = e + \frac{1}{2}u_i u_i, \quad (2.38)$$

respectively. In Eq. (2.35), C_p is the heat capacity of the mixture at constant pressure,

$$C_p = \sum_{k=1}^{N_s} C_{p,k} Y_k. \quad (2.39)$$

2.3 Transport Relations

The transport properties, in general, can be collected in three important dimensionless numbers:

(1) The Lewis number Le_k , which is the ratio of the thermal diffusivity coefficient D_{th} to the molecular diffusion coefficient of each species D_k . It compares the diffusion speed of heat and species k :

$$\begin{aligned} Le_k &= \frac{D_{th}}{D_k} \\ &= \frac{\lambda}{\rho C_p D_k}, \end{aligned} \quad (2.40)$$

where λ is the thermal conductivity.

(2) The Prandtl number Pr , which is the ratio of momentum to heat diffusion:

$$\begin{aligned} Pr &= \frac{\nu}{D_{th}}, \\ &= \frac{\nu}{\lambda/(\rho C_p)}, \\ &= \frac{\mu C_p}{\lambda}. \end{aligned} \quad (2.41)$$

(3) The Schmidt number Sc_k , which is the ratio of momentum and molecular diffusion

of the species:

$$\text{Sc}_k = \frac{\nu}{D_k}. \quad (2.42)$$

The previous three dimensionless number are connected by the following relation:

$$\text{Sc}_k = \text{Pr Le}_k. \quad (2.43)$$

2.4 Chemical Kinetic Relations

Any chemical system of N_s species reacts in M reactions [11]:

$$\sum_{k=1}^{N_s} \nu'_{kj} \mathcal{M}_k = \sum_{k=1}^{N_s} \nu''_{kj} \mathcal{M}_k \quad \text{for } j = 1, 2, \dots, M, \quad (2.44)$$

where \mathcal{M}_k is a symbol for species k , ν'_{kj} and ν''_{kj} are the molar stoichiometric coefficients of species k in reaction j . From mass conservation:

$$\sum_{k=1}^{N_s} \nu'_{kj} W_k = \sum_{k=1}^{N_s} \nu''_{kj} W_k \quad \text{for } j = 1, 2, \dots, M. \quad (2.45)$$

The mass reaction rates of species k ,

$$\dot{\omega}_k = \sum_{j=1}^M \omega_{kj} \quad (2.46)$$

$$= W_k \sum_{j=1}^M \nu_{kj} \mathcal{J}_j, \quad (2.47)$$

are the sum of the mass reaction rate of this species in every reaction j ,

$$\dot{\omega}_{kj} = \mathcal{J}_j W_k \nu_{kj}, \quad (2.48)$$

where,

$$\nu_{kj} = \nu''_{kj} - \nu'_{kj}. \quad (2.49)$$

In Eqs. (2.47) and (2.48), \mathcal{J}_j is the progress rate of reaction j ,

$$\mathcal{J}_j = \mathcal{K}_{fj} \prod_{k=1}^{N_s} [X_k]^{\nu'_{kj}} - \mathcal{K}_{rj} \prod_{k=1}^{N_s} [X_k]^{\nu''_{kj}}, \quad (2.50)$$

where $[X_k] = \rho Y_k / W_k$ is the molar concentration of species k . \mathcal{K}_{fj} and \mathcal{K}_{rj} are the forward

2.5. Combustion Modes

and reverse rates of reaction j , which can be modeled using the empirical Arrhenius law:

$$\mathcal{K}_{fj} = A_{fj} T^{\beta_j} \exp\left(-\frac{E_j}{\mathcal{R}T}\right) \quad (2.51)$$

and the equilibrium relation,

$$\mathcal{K}_{rj} = \frac{\mathcal{K}_{fj}}{\left(\frac{p_a}{\mathcal{R}T}\right)^n \exp\left(\frac{\Delta S_j^0}{\mathcal{R}} - \frac{\Delta H_j^0}{\mathcal{R}T}\right)}, \quad (2.52)$$

$$n = \sum_{k=1}^{N_s} \nu_{kj}, \quad (2.53)$$

where A_{fj} , β_j , and E_j , are a pre-exponential constant, temperature exponent, and activation energy, respectively. Δ refers to changes due to species passing from reactants to products in the j -th reaction. H , S , and p_a are the enthalpy, entropy, and the atmospheric pressure, respectively.

2.5 Combustion Modes

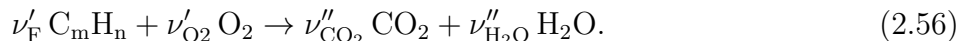
In general, the combustion process can be presented by a simple equation:



where the fuel with the symbol (F) reacts with the oxidizer (symbol O) to generate the combustion product P



In complete combustion of any hydrocarbon fuel $C_m H_n$ the previous equation could be written as



Overall, the combustion process can be categorized into three different modes depending on the mixing of the fuel/oxidizer: premixed, non-premixed (diffusion), and partially-premixed combustion. Each of those can be defined and characterized by several parameters and non-dimensional numbers in laminar and turbulent flow as is described in the following sections.

2.5.1 Premixed Combustion

In premixed combustion, fuel and oxidizer are mixed before entering the place of combustion (chamber), as in the case of an open Bunsen burner: fuel and air are already mixed within

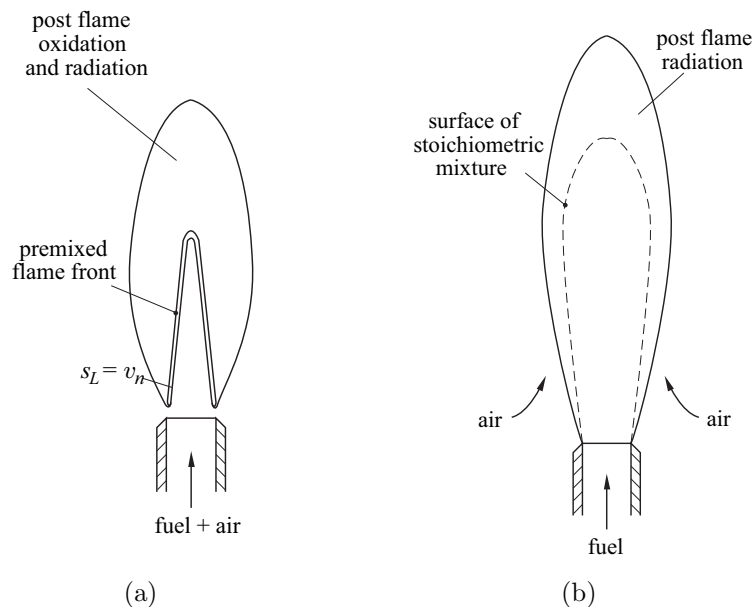


Figure 2.1: Combustion modes: (a) premixed, (b) non-premixed [35].

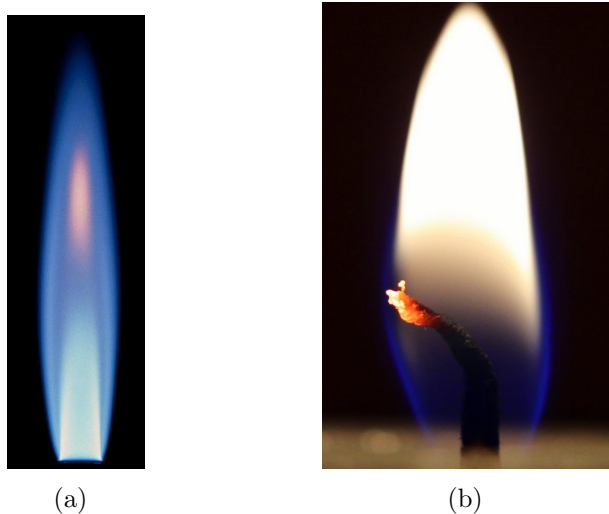


Figure 2.2: Typical color of the flame of different combustion modes: (a) premixed [36], (b) non-premixed [37].

2.5. Combustion Modes

the tube and the gas is ignited downstream as seen in Fig. 2.1(a). A premixed flame front will propagate towards the burner until it finds its steady state position in the form of the well-known Bunsen cone [35]. The fundamental quantity which describes this mode of combustion is the laminar burning velocity (flame speed) s_L . For the steady-state Bunsen cone, the burning velocity therefore must be equal to the flow velocity v_n , normal to the flame front (see Fig. 2.1(a)). Behind the flame front, yet unburnt intermediates, such as CO and H₂, will mix with air entering from outside the chamber and lead to post flame radiation and oxidation [35]. Premixed flames appear with a blue to bluish-green color as seen in Fig. 2.2(a). This blue color is due to the chemiluminescence of some excited species (C₂ and CH radicals). Premixed flames are used whenever intense combustion is required within a small volume. This is the case in household appliances, spark ignition engines, aspirated internal combustion engines, and lean-premixed gas turbine combustion chambers. It can also be found in gas leak explosions. Generally, premixed combustion should be avoided in large combustion devices such as furnaces, since premixing of large volumes of fuel and air would represent a serious safety hazard [35]. In premixed combustion devices, it is important to select the molar-based stoichiometric ratio (air-to-fuel ratio),

$$s_n = \frac{X_O}{X_F} \Big|_{st} = \frac{\nu'_O}{\nu'_F} \quad (2.57)$$

and/or mass-based stoichiometric ratio,

$$s_m = \frac{Y_O}{Y_F} \Big|_{st} = \frac{\nu'_O W_O}{\nu'_F W_F}. \quad (2.58)$$

Usually, the premixed mixture is characterized using the equivalence ratio ϕ . This compares the fuel-to-air ratio in real mixtures with that of the stoichiometric one,

$$\phi = \left(\frac{Y_F}{Y_O} \right) / \left(\frac{Y_F}{Y_O} \right)_{st} \quad (2.59)$$

$$= s_m \frac{Y_F}{Y_O} \quad (2.60)$$

$$= s_m \frac{\dot{m}_F}{\dot{m}_O}, \quad (2.61)$$

where

$$\begin{cases} \phi < 1 & \text{lean mixture,} \\ \phi = 1 & \text{stoichiometric mixture,} \\ \phi > 1 & \text{rich mixture.} \end{cases} \quad (2.62)$$

In premixed combustion, the quantities and variables are often studied as a function of a dimensionless number called progress variable \mathcal{C} . This variable should show monotonic behavior with the combustion process. Frequently, the system temperature T is an example

of this variable:

$$\mathcal{C} = \frac{T - T_u}{T_b - T_u}, \quad (2.63)$$

where subscripts u and b refer to the unburned (fresh) gas and the burned gas regions, respectively. As such, \mathcal{C} will have a value of zero in the fresh gas region and one in the burned gas region. Usually the flame surface location is based on a certain value (threshold) of \mathcal{C} .

In order to describe the laminar premixed flame, two important parameters are required: the laminar flame (burning) speed s_L and the flame thickness δ_L . The flame speed is the velocity at which the laminar flame front propagates normal to itself into the unburned mixture. In the literature, there is a multitude of available definitions; the simplest one is the integral of the burning rate across the flame brush [11]:

$$s_L = -\frac{1}{\rho_u Y_{F,u}} \int_{-\infty}^{\infty} \dot{\omega}_F dx. \quad (2.64)$$

The flame thickness δ_L also has multiple definitions: (1) Based on the thermal or transport properties and called diffusive flame thickness,

$$\begin{aligned} \delta_d &= \frac{D_{th}}{s_L}, \\ &= \frac{\lambda_u}{\rho_u C_p s_L}, \end{aligned} \quad (2.65)$$

or

$$\delta_\nu = \frac{\nu}{s_L}. \quad (2.66)$$

(2) Based on temperature profile,

$$\delta_{th} = \frac{T_b - T_u}{\max(|\frac{\partial T}{\partial x}|)}. \quad (2.67)$$

A more accurate definition for the flame thickness is the one constructed by defining the distance over which the progress variable \mathcal{C} changes from 0.01 to 0.99; this is usually called total flame thickness δ_t [11].

2.5.2 Non-Premixed (Diffusion) Combustion

In non-premixed combustion, no air is mixed with the fuel within the tube of the burner. This may be achieved by using a simple tube or by closing the air inlet in a Bunsen burner. Inherently, only fuel exists in the tube as shown in Fig. 2.1(b). Fuel mixes with the surrounding air by convection and diffusion during combustion. Optimal conditions for combustion

2.5. Combustion Modes

are restricted to the vicinity of the surface of the stoichiometric mixture. This is the surface where fuel and air are locally mixed in a proportion that allows both to be entirely consumed. This leads to the highest flame temperature and to the fastest reaction rates. Since in most cases combustion is much faster than diffusion, the latter is the rate limiting step that controls the entire process. For this reason, flames in which the reactants are initially non-premixed are also called *diffusion flames* [35]. The diffusion flames usually radiate in a bright yellow color as seen in Fig. 2.2(b). This yellow color is caused by radiating soot particles which dominate over the chemiluminescence that is also present at the base of a diffusion flame. Close to the burner, a blue layer appears (see Fig. 2.2(b)) since the local residence time is too short for soot particles to form. An example for non-premixed combustion are diesel engines, where a liquid fuel spray is injected into compressed hot air within the cylinder. It rapidly evaporates and mixes with the air and then auto-ignites under partially premixed conditions. The final stage of combustion occurs under non-premixed conditions [35].

In diffusion flames, the stoichiometry is represented based on mass flow rates in the fuel and air streams which again enter separately. The stoichiometry in this mode of combustion is represented in two different ways: On the one hand there is the local ratio,

$$\phi = s_m \frac{Y_F}{Y_O}, \quad (2.68)$$

which characterizes the local structure of the flames formed when the fuel and oxidizer streams interact. On the other hand, the overall (global) behavior of combustion is represented by the global equivalence ratio,

$$\phi_g = s_m \frac{\text{mass flow rate of the fuel in the first stream}}{\text{mass flow rate of the oxidizer in the second stream}}. \quad (2.69)$$

It is very common to use a passive scalar notation in analysis and post-processing when dealing with diffusion flames. Usually, this passive scalar is the mixture fraction ζ . The simplest form of ζ is the one given for a two-inlet feed system [35]:

$$\zeta = \frac{m_1}{m_1 + m_2}, \quad (2.70)$$

where m_1 and m_2 are the mass of the fuel and air stream, respectively. When single-step kinetic mechanisms are employed, the mixture fraction can be expressed as:

$$\zeta = \frac{s_m Y_F - Y_{O_2} + Y_{O_2,2}}{s_m Y_{F,1} + Y_{O_2,2}}, \quad (2.71)$$

where $Y_{F,1}$ and $Y_{O_2,2}$ are the mass fraction of fuel in the fuel stream and the mass fraction of oxygen in oxidizer stream, respectively. For a stoichiometric mixture, $s_m Y_F = Y_{O_2}$, this passive scalar takes the value of the stoichiometric mixture fraction,

$$\zeta_{st} = \frac{Y_{O_2,2}}{s_m Y_{F,1} + Y_{O_2,2}}, \quad (2.72)$$

where

$$\begin{cases} \zeta < \zeta_{st} & \text{lean mixture,} \\ \zeta = \zeta_{st} & \text{stoichiometric mixture,} \\ \zeta > \zeta_{st} & \text{rich mixture.} \end{cases} \quad (2.73)$$

The flame structure in the diffusion flame is usually represented theoretically in the mixture fraction space, as illustrated in Fig. 2.3, which contains graphs pertaining to the pure mixing in equilibrium with temperature and mass fractions. Another very important parameter in the characterization and modeling of diffusion flames is the scalar dissipation rate,

$$\chi = 2D \left(\frac{\partial \zeta}{\partial x} \right)^2, \quad (2.74)$$

where χ has the dimension of 1/time. It measures the gradients of the mixture fraction (passive scalar) and the molecular of the species towards the flame. It has a direct impact on the combustion process as well as on the mixing, where different scalar dissipation levels lead to different flame structures.

2.6 Turbulent Combustion

The previous section discussed some important concepts for laminar flames. This involves laminar flows, in which the adjacent layers of fluid slide past one another in a “smooth, orderly” manner. The only possible mixing is due to molecular diffusion. The velocity, temperature, and concentration profiles measured in laminar flow with a high-sensitivity instrument will be quite smooth. At a higher Reynolds number, the flow becomes turbulent. In turbulent flows, eddies move randomly back and forth and across the adjacent fluid layers. The flow no longer remains “smooth and orderly”. When the flow entering a flame front is turbulent, the laminar flame mode studied in the previous section is replaced by a regime where turbulence and combustion interact [38]. Turbulent combustion is encountered in most practical combustion systems such as rockets, internal combustion or aircraft engines, industrial burners and furnaces, etc., while laminar combustion applications are almost limited to candles, lighters and some domestic furnaces. Turbulent combustion flow is very complex and requires some description of a characteristic scale. In what follows, the most important scales, which characterize the premixed and non-premixed combustion, are reviewed.

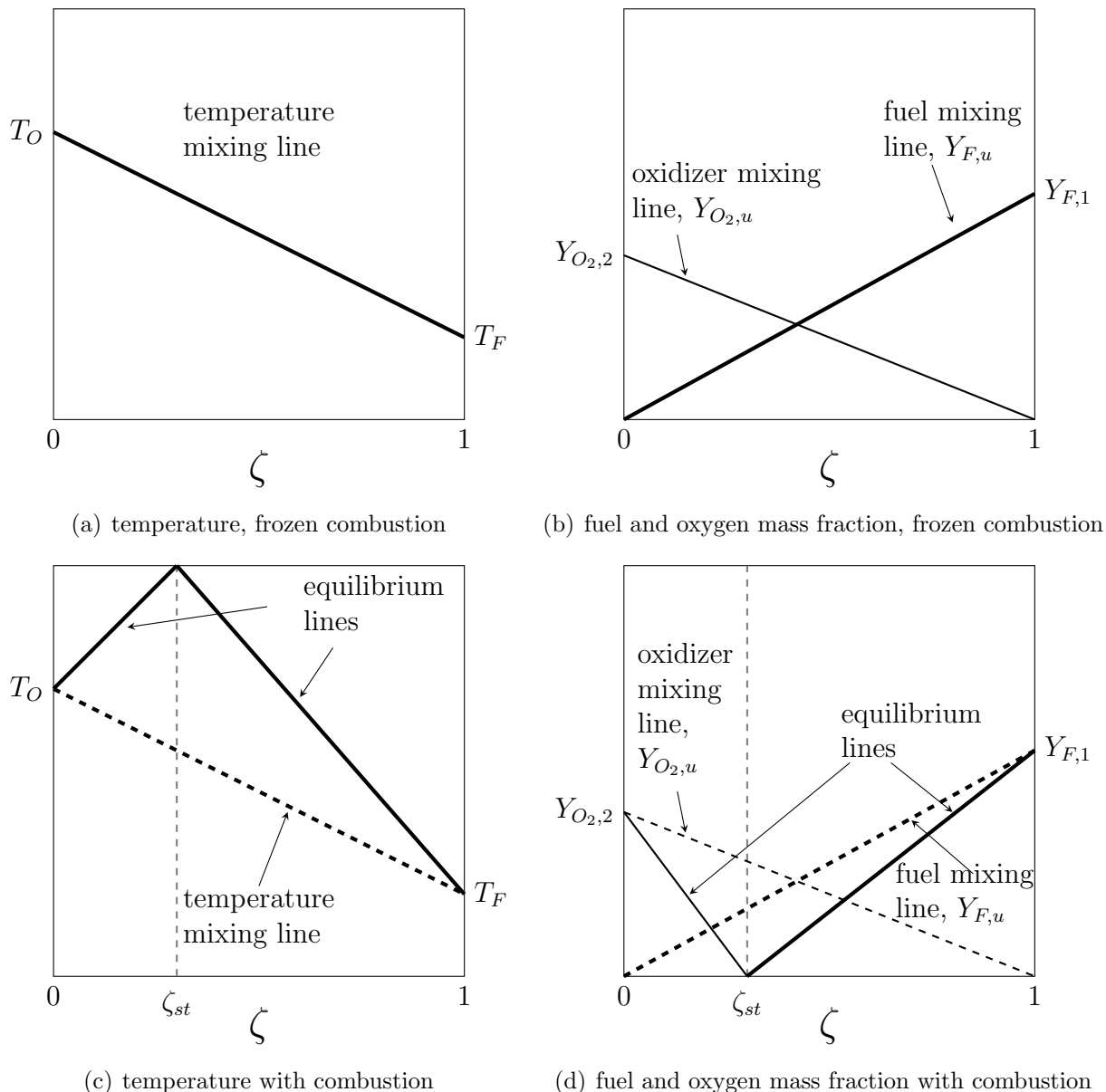


Figure 2.3: Diffusion flame structure in the mixture fraction ζ diagram, for an infinitely-fast and irreversible reaction.

2.6.1 Characterization of Turbulent Premixed Combustion

Turbulent premixed combustion may be described as the interaction between a flame front (thickness δ and speed s_L) and an ensemble of “eddies” representing turbulence. These eddies have sizes ranging from the Kolmogorov (written η_k) to the integral length scale l_t and characteristic speeds ranging from the Kolmogorov velocity u'_k to the integral RMS(u') velocity. If turbulence is supposed to be homogeneous and isotropic, the speed $u(r)$ and the size r of any eddy participating to the turbulence cascade are linked by [11],

$$\epsilon = \frac{u'(r)^3}{r}, \quad (2.75)$$

where ϵ is the local dissipation rate of turbulent kinetic energy. This assumption is useful in imagining how a turbulent flow may interact with a premixed front, because it provides estimates of speed and time variations with r . For example, a typical turbulence time of an eddy of size r is:

$$\tau_f(r) = \frac{r}{u'(r)} = \frac{r^{2/3}}{\epsilon^{1/3}}. \quad (2.76)$$

Comparing this characteristic flow time to a typical premixed flame time scale, $\tau_c = \delta/s_L$, in order to build a reduced number (Damköhler number), $\text{Da}(r) = \tau_f(r)/\tau_c$, suggests scenarios for flame/vortex interaction: for large $\text{Da}(r)$, chemical times are small compared to the eddy time and turbulence is not able to significantly affect the inner flame structure. On the other hand, low values of $\text{Da}(r)$ imply long chemical time scales and a flame strongly modified by turbulent eddies. This number is called the Damköhler number $\text{Da}(r)$ which changes when r goes from the Kolmogorov size η_k to the integral scale l_t . The question here is: which values of r (turbulent eddies) are the most relevant in controlling the flame structure? This question is still unsolved in general and controls many assumptions for developed models. Classical approaches introduce two reduced numbers corresponding to the limiting values of r [11]:

- The Damköhler number Da is defined for the largest eddies and corresponds to the ratio of the integral time scale τ_t to the chemical time scale:

$$\text{Da} = \text{Da}(l_t) = \frac{\tau_t}{\tau_c} = \frac{\tau_f(l_t)}{\tau_c} = \frac{l_t/u'}{\delta/s_L} \quad (2.77)$$

- The Karlovitz number Ka corresponds to the smallest eddies (Kolmogorov) and is the ratio of the chemical time scale to the Kolmogorov time:

$$\text{Ka} = \frac{1}{\text{Da}(\eta_k)} = \frac{\tau_c}{\tau_k} = \frac{\tau_c}{\tau_f(\eta_k)} = \frac{u'(\eta_k)/\eta_k}{s_L/\delta} \quad (2.78)$$

The Karlovitz number could to be written in another form as

$$\text{Ka} = \left(\frac{l_t}{\delta}\right)^{-1/2} \left(\frac{u'}{s_L}\right)^{3/2} = \left(\frac{\delta}{\eta_k}\right)^2 = \frac{\sqrt{\epsilon/\nu}}{s_L/\delta}. \quad (2.79)$$

Since the turbulent Reynolds number based on the integral length scale can be expressed as

$$\text{Re}_t = \frac{u'l_t}{\nu} = \left(\frac{u'}{s_L}\right) \left(\frac{l_t}{\delta}\right), \quad (2.80)$$

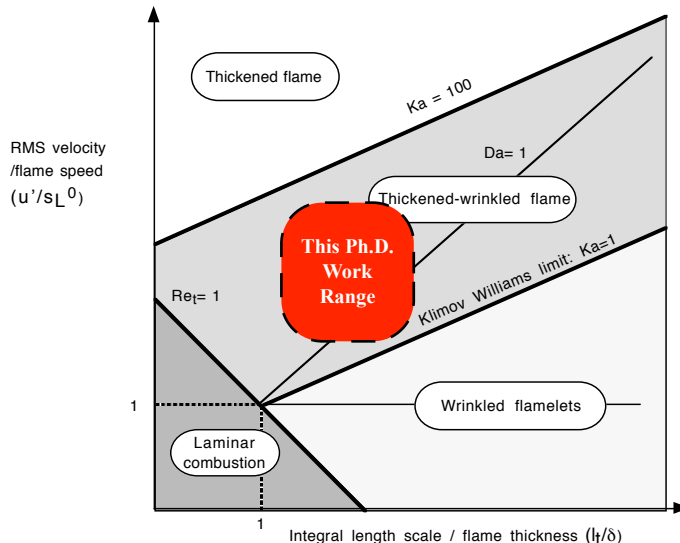


Figure 2.4: Modified turbulent combustion diagram: combustion regimes are identified in terms of length (l_t/δ) and velocity (u'/s_L) ratios (log-log scale) [11].

Re_t can be expressed as a function of the Karlovitz and the Damköhler number as follows:

$$Re_t = Da^2 Ka^2. \quad (2.81)$$

For large Damköhler number values ($Da \gg 1$), chemical times are shorter than the integral turbulence time. Accordingly, turbulence is not able to affect the inner flame structure which remains close to a laminar flame, wrinkled by turbulent motions (“flamelet” limit). In this case, the mean burning rate may be estimated from the burning rate of a laminar flame multiplied by the overall flame surface. On the other hand, when the Damköhler number is low ($Da \ll 1$), the chemical time is larger than the turbulent time. The overall reaction rate is therefore controlled by chemistry, whereas reactants and products are mixed by turbulent motions. This regime is the so-called perfectly stirred reactor. This limiting case is quite easy to model: in this situation, reactants and products are continuously mixed in a time shorter than the chemical time. The mean reaction rate may then be estimated as the reaction rate computed using mean values. These regimes are illustrated in Fig.2.4.

2.6.2 Characterization of Turbulent non-Premixed Combustion

As for turbulent premixed flames, non-premixed combustion regimes have to be identified to support model developments. Compared to premixed flames, regime description is more difficult in turbulent non-premixed combustion. First, reactants have to mix before the reaction; chemical reactions are generally limited by mixing. On the other hand, fast mixing, compared to chemistry, may lead to premixed combustion. The second difficulty arises from the fact that non-premixed flames do not exhibit well-defined characteristic scales: a diffusion flame does not feature a propagation speed and the local flame thickness depends on

flow conditions. The thickness of an unstrained diffusion flame increases with time and such flames have no propagation speed. On the other hand, the thickness of strained flames depends on flow motions and is not an intrinsic flame characteristic. However, in flame/vortex interactions, flame scales can be defined unambiguously [11]. The first important scale is the flame scale, which is defined using the initial conditions of the simulation. The initial flame thickness δ_i is estimated as

$$\delta_i = \left(\frac{1}{|\nabla\zeta|} \right)_{\zeta=\zeta_{st}} = \sqrt{\frac{2\mathcal{D}_{st}}{\chi_{st}}}, \quad (2.82)$$

where χ_{st} is the scalar dissipation rate at the stoichiometric condition $\zeta = \zeta_{st}$ at time $t = 0$ and \mathcal{D}_{st} is the stoichiometric value of the molecular diffusion coefficient. A chemical time scale τ_c is defined from asymptotic theories [11] as

$$\tau_c = 1/\chi_q, \quad (2.83)$$

where χ_q is the scalar dissipation rate at quenching which can be computed in many different ways, the simplest being [11]

$$\chi_q = \frac{\zeta_{st}^2(1 - \zeta_{st})^2}{\tau_c^p}, \quad (2.84)$$

where τ_c^p is simply the flame time corresponding to a premixed stoichiometric flame: $\tau_c^p = \delta/s_L = \mathcal{D}/s_L^2$. This scaling illustrates the link between premixed and diffusion flame parameters: if the stoichiometric speed of the premixed flame is large, the quenching scalar dissipation of the diffusion flame is also large.

The flame velocity is

$$u_f = \delta_i\tau_c. \quad (2.85)$$

The Damköhler number in a diffusion flame can be expressed as

$$\text{Da} = \frac{\tau_f}{\tau_c}, \quad (2.86)$$

where τ_f is the flow time scale which may be taken as a different value:

- in jet flow, $\tau_f = \frac{\text{Jet diameter}}{\text{Jet velocity}}$,
- in a general configuration, $\tau_f = \frac{1}{\chi_{st}}$, and
- in well-characterized turbulent flow, the Kolmogorov time scale or the large eddy turnover time scale is chosen.

After characterizing the non-premixed flame by knowing the above scales and non-dimensional numbers, the combustion regimes can be detected based on Fig. 2.5.

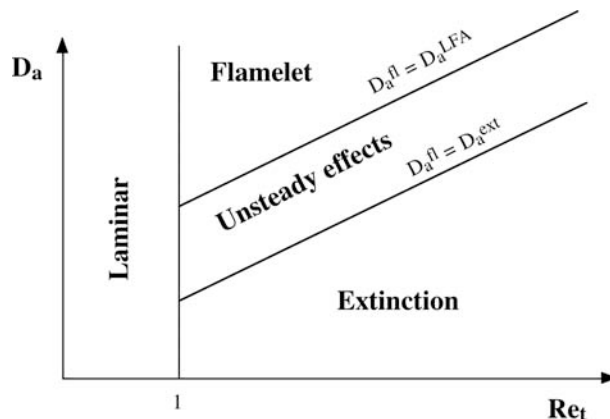


Figure 2.5: Regimes for turbulent non-premixed combustion as a function of the Damköhler number $Da = \tau_t/\tau_c$ (based on the turbulence integral time scale τ_t and the chemical time τ_c) and the turbulent Reynolds number Re_t [11].

2.7 Fundamentals of Droplet and Spray Combustion

Two-phase flows indeed include a number of processes involving a variety of time and length scales. Simplifications must occur in order to be able to reproduce part of these phenomena. The characteristic length scales of an evaporating two-phase flow range from the size of the smallest droplets in the spray (of the order of a micrometer) to the size of the combustion chamber (several centimeters). The characteristic time scales of the flow depend on the size of the droplet, which has a major impact on the inertia and the lifetime of the droplets. A brief overview of the principal processes involving the dispersed phase are reviewed in the following [39].

2.7.1 Injection

The injection system represents one of the essential components of the combustion chamber. The liquid fuel is injected in the form of a cylindrical column or a thin liquid sheet that, due to an aerodynamic destructive effect, is atomized into a cloud of droplets. The characteristics of this cloud, such as the droplet density and size, strongly depend on the injection parameters and the geometry. There are many types of injectors; rotary atomizers, air blast atomizers, pressure atomizers, etc. The characteristics of the spray pattern highly depend not only on the parameters of the injection device, but also on the gaseous flow inside the combustion chamber and the properties of the liquid fuel: the viscosity (directly influencing the droplet size) and the fuel volatility (which impacts the vaporization process) [39], for example.

2.7.2 Atomization

Fuels used in aircraft engines are not sufficiently volatile to be ignited if the surface in contact with the oxidizer is not augmented by pulverization. The liquid sheet exiting the injector

must be atomized into a cloud of droplets. The atomization process can be described as the ensemble of mechanisms that occur in the injection of a high pressure liquid through a small fence. Two different phenomena can be distinguished in this process: the primary atomization which takes place in the region near the orifice and the secondary atomization which usually extends much further as is illustrated in Fig. 2.6, a schematic representation of the main phenomena following the liquid injection [39].

The mechanisms of liquid sheet disintegration have been widely studied. The numerical simulation of the primary atomization process requires the explicit resolution of the Navier-Stokes (NS) equations for both phases (gas and liquid) and the coupling between them through jump relations at the interface. In addition, the position and motion of the interface must be accurately described. DNS of the primary atomization process requires extremely high resolution meshes, since the length scale of the smallest liquid structures can become very small as the liquid ligaments approach their breakup. In general the mesh size is determined by the smallest droplet diameter. At least two to five computational cells per droplet are needed [40]. This feature prevents numerical simulations of the primary atomization at an industrial scale. However, as small droplets are only present at the periphery of the liquid sheet, mesh adaptation techniques can be used to reduce the computational cost. Level-Set and Volume of Fluid (VOF) methods are suitable approaches for this task [41]. Desjardins et al. (2008) [42] developed a level-set method combined with high-order implicit transport schemes to preserve mass conservation. Due to the large range of length and the time scales involved in the process, direct and detailed numerical predictions of the primary atomization process are computationally very expensive and not affordable at large scales. Their application is limited in terms of Reynolds number and geometric complexity [39].

Once the liquid sheet has decomposed into fine liquid ligaments, further disintegration occurs and droplets of different sizes arise due to air entrainment and aerodynamic forces acting on the ligaments. This process is called secondary breakup. Several regimes exist, depending on the Weber number. The Weber number is a dimensionless number relating the aerodynamic forces acting on the droplet to its surface tension. Those two forces have opposite effects on a droplet: the surface tension stabilizes the droplet and the aerodynamic force tends to break it. This is a process of high difficulty in terms of modeling and simulation. Indeed, there are many effects that must be taken into account, such as the droplet deformations prior to breakup and collisions and coalescence which are predominant in this zone of the spray. Indeed, in the secondary breakup zone, the spray is very dense, which increases the probability of collisions between droplets. Numerical studies of this problem may rely on different approaches. DNS using an interface tracking method is out of reach for realistic applications [39].

The spray combustion simulation performed in this dissertation focuses on the diluted regime zone located after the secondary breakup zone. Only diluted flow is considered. Thus, inter-droplet collisions are ignored while two-way coupling with the carrier fluid is considered. In this type of flow, the main physical phenomena are droplet dispersion and evaporation.

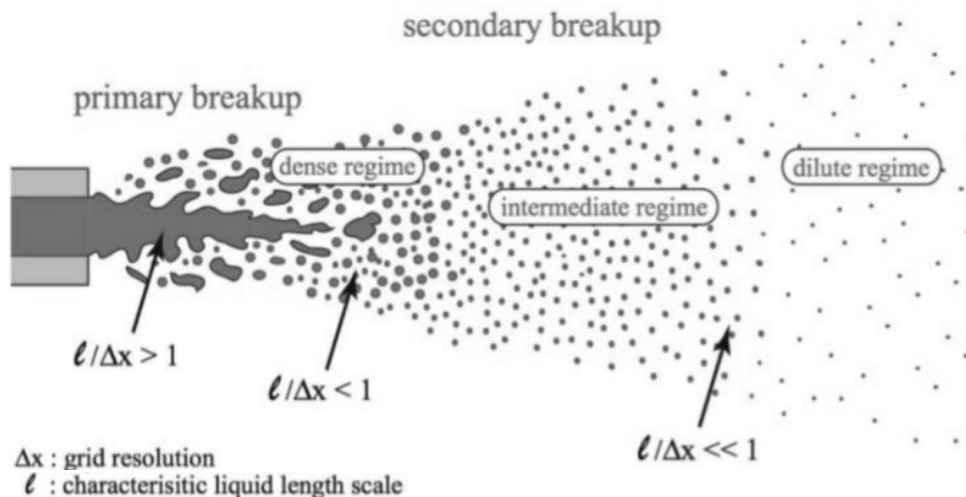


Figure 2.6: Phenomenology of the atomization of a spray [39].

2.7.3 Dispersion and Evaporation

In the diluted regime, dispersion and evaporation become predominant. In this case, droplet trajectories are directly influenced by carrier flow turbulence. However, their response to the gaseous flow depends also on their inertia. The Stokes number (St) relates the characteristic particle response time scale (τ_p) to the characteristic fluid timescale (τ_f), giving a measure of particle inertia. Very inertial particles ($St \gg 1$) have trajectories quite independent from the carrier fluid flow. On the contrary, very low inertial particles ($St \ll 1$) quickly respond to changes in the gaseous flow [39, 43, 44].

There are many models in terms of the vaporization process. The models are mainly based on empirical results from single isolated droplets, which have been modified to include the effects of neighboring droplets, convection, multicomponent fuels, etc. Many parameters have an influence on the vaporization process. Indeed, the characteristics of the fuel, the spray and the carrier flow play an important role and directly influence the evaporation of droplets inside the combustion chamber.

2.7.4 Spray Combustion

The combustion process considered often involves chemical reactions that only take place in the gaseous phase. Thus, the evaporation of liquid fuel droplets is a necessary step for the combustion to take place. However, two main types of combustion exist: single-phase combustion and two-phase combustion. These two regimes depend on the ratio between the characteristic evaporation time and the convection time of the carrier phase. When the characteristic evaporation time of the droplets is very small compared to the convection time, the droplets completely evaporate before reaching the flame front. Combustion taking place in the single-phase regime only depends on the gaseous fuel repartition in the chamber. The gaseous fuel field will, however, depend on the characteristics of the evaporation process and

the dispersion of the droplets. On the other hand, when the evaporation time is longer than the convection time, the flame and spray are coupled. The droplets may reach the flame front and the characteristics of the flame strongly depend on the spray parameters [39]. Two-phase flow combustion has different characteristics than gaseous phase combustion. The characteristics of the flame are modified due to the presence of liquid droplets and strongly depend on the quantity of fuel that has been evaporated before reaching the flame front. Indeed, the gaseous field is modified by the presence of droplets upstream from the flame which may lead to flame instabilities. Note also that the evaporation rate depends, amongst other things, on the concentration of droplets. This may create zones of very high concentration of gaseous fuel as well as very lean zones. The mixing is then different from the case where gaseous fuel is directly injected into the chamber [39]. Réveillon & Vervisch (2005) [17] classified the different modes depending on a dimensionless number, G , which is the ratio between the droplet evaporation rate and the diffusion rate of hot gases within the droplet cloud. When convection is more important than diffusion, G is approximated as follows:

$$G \approx \frac{5 N_k^{2/3}}{S}, \quad (2.87)$$

where N_k is the number of droplets in the cloud and S is a mean droplet spacing parameter linking the characteristic average distance between droplets to the diffusion flame radius.

Figures 2.7 and 2.8, taken from [17], illustrate four distinct modes of spray combustion regimes depending on G . In these figures, for large G , the spray is very dense and diffusion inside the cloud is low, only the droplets located at the periphery of the cloud evaporate. The flame envelopes the entire cloud of droplets. It is referred to as external sheath combustion. For diluted spray regimes, where $G \ll 1$, droplets are far from each other and the evaporation rate increases due to the diffusion of hot gases. Separated flames surround each droplet, which burn individually. Intermediate regimes exist between these two extremes: for G values slightly larger than one, $G > 1$, the flame surrounds the whole cloud of droplets but the diffusion of hot gases is sufficiently high, thus the droplets in the center of the cloud vaporize. When $G < 1$, the center of the cloud burns in an external combustion regime and the droplets located at the periphery burn in an isolated manner.

Réveillon & Vervisch (2005) [17] also provided a different classification based on numerical results of two-dimensional spray flames in counterflow:

- External combustion regime: for low equivalence ratio, the premixed flame completely consumes the fuel (liquid and gaseous), whereas when the equivalence ratio is high, the fuel burns in the diffusion regime.
- Group combustion regime: droplet clusters individually burn on rich premixed flames usually followed by diffusion flames.
- Hybrid combustion regime: intermediate conditions between the external and the group combustion regimes.

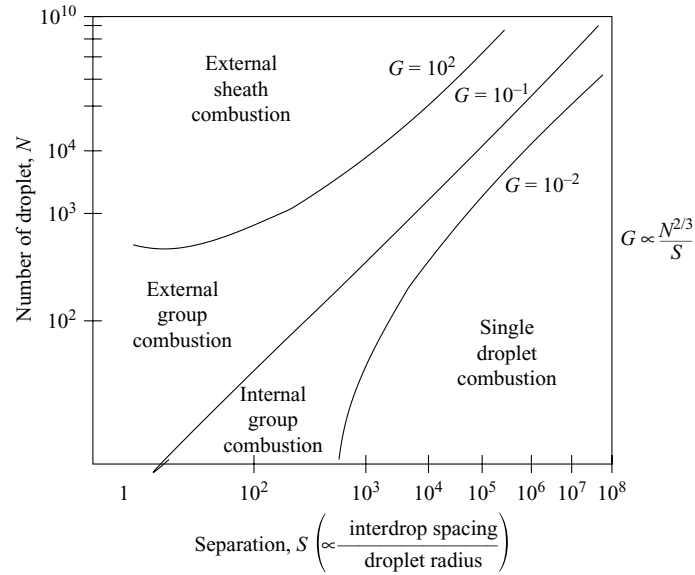


Figure 2.7: Group combustion diagram [17].

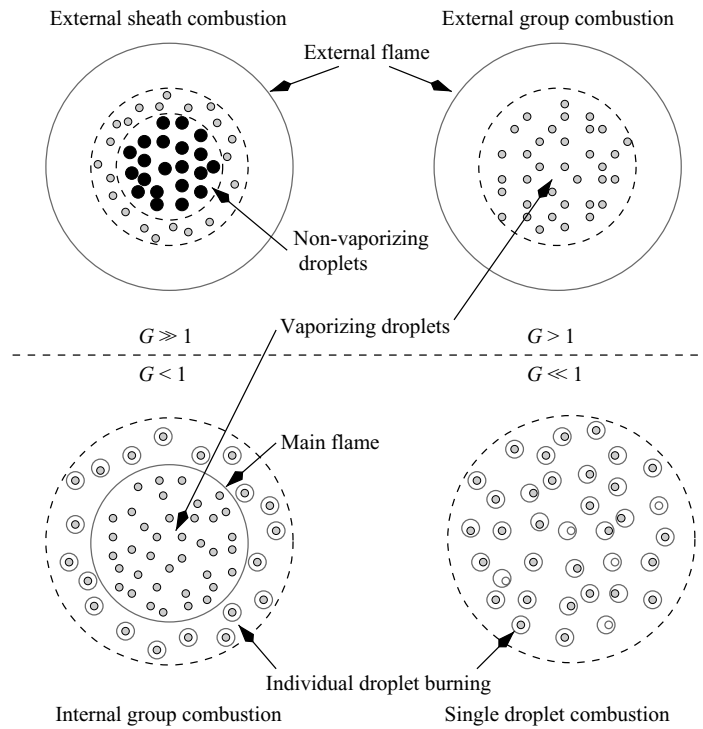


Figure 2.8: Classification of different spray combustion regimes [17].

2.8 Modeling the Evaporation of Fuel Droplets

The process of droplet vaporization is of great importance in many energy systems involving spray combustion such as diesel engines, gas turbines, industrial furnaces, etc. In a general

manner, without accounting for droplet burning at injection, the liquid fuel atomizes into multiple droplets of different sizes, creating a polydisperse spray, the fuel droplets vaporize, the gaseous fuel mixes with the oxidant and then burns. In these kinds of investigations, the prediction of the gaseous fuel concentration is very important for the correct evaluation of critical parameters, such as flame position and heat release [39]. The vaporization of droplets has been widely studied during the past century, experimentally and theoretically. The phenomena taking place in spray evaporation and combustion are very complex. Multiple interactions between the atomization, dispersion, and evaporation of droplets take place at the same time. For this reason, developing models which consider all of these complex phenomena is almost an impossible task. Alternatively, the evaporation of single isolated droplets is studied under different conditions as a first step towards the understanding of the processes in a spray. An isolated droplet represents an ideal model of the physical phenomena involved in the diluted regions of the spray. The vaporization of a single droplet is a process involving momentum, mass and heat transfers in both liquid and gas phases, with coupling at the droplet interface. This kind of study provides the basis for the development of complex spray flow modeling, which may be found in many textbooks [3, 38, 45, 46]. Some of the important evaporation models are listed in the next section.

2.8.1 Existing Evaporation Models

As is introduced in [3, 39], the models of droplet vaporization can be classified into the following six groups with increasing complexity:

1. Constant droplet-temperature model: the droplet surface temperature is uniform and does not change with time; it yields the famous d^2 law.
2. Infinite liquid-conductivity model: the droplet surface temperature is uniform, time-varying, and equal to the temperature inside the droplet.
3. Spherically symmetric transient droplet heating model: it takes into account finite liquid thermal conductivity, but not the recirculation inside the droplets.
4. Effective-conductivity model: takes both finite liquid thermal conductivity and recirculation into account.
5. Vortex model for droplet heating: describes the recirculation inside the droplet in terms of vortex dynamics.
6. Navier-Stokes solution: full exact solution of the Navier-Stokes equations inside the droplet and in the gaseous flow.

The evaporation models can be more precisely classified by independently describing the models used on each of the processes taking place in the vaporization of a droplet. Four main phenomena take place in the evaporation of an isolated droplet [39]:

1. The heat in the gas phase diffuses to the droplet surface;

2.8. Modeling the Evaporation of Fuel Droplets

2. The heat arriving at the droplet surface is diffused into the inside of the droplet;
3. The molecules of fuel detach from the droplet surface due to their increased internal energy (vaporization process);
4. The gaseous fuel diffuses from the droplet surface to the surrounding gas.

Most models assume the diffusion in the gas phase (from and to the droplet surface) to be spherically symmetric. However, some effects due to convection may modify the flow around the droplet. The spherically symmetric model takes into account the convection effects through the Sherwood and Nusselt numbers. Other models include the effect of convection, taking into account the presence of a film around the droplet, introducing correction factors to the spherically symmetric model [47], or completely solving the flow around the droplet [3]. This last option is computationally very expensive. In addition, transport properties are often considered constant between the droplet surface and infinity. Miller et al. (1998) [48] showed that the heat and mass fluxes to the droplet strongly depend on the evaluation of the transport and thermodynamic properties of both the gas and the liquid phase [39].

2.8.2 Evaporation Model for a Single Isolated Droplet

This section reviews the equations used in the evaporation model of Abramzon and Sirignano [47]. In this section and the rest of the dissertation work, infinite conduction in the liquid and spherical symmetry are assumed. In other words, inside the droplet, the thermal conductivity is considered infinitely fast and the temperature is uniform. The gas is considered quasi-stationary, so the thermal and mass transfer in the gaseous phase depend only on the distance to the surface of the droplet.

The Abramzon-Sirignano Evaporation Model

In principle the Abramzon-Sirignano evaporation model [47] is similar to the one developed first by Spalding (1953) [49], with some important corrections. The Spalding model for evaporation does not take into account the existence of a vapor film around the droplet. It does not consider the finite thickness of the thermal and mass boundary layers around the droplet. Taking these layers into account leads to modified expressions for the Sherwood and Nusselt numbers, as will be reviewed in this section [47].

In the Abramzon-Sirignano evaporation model, the mass exchange through the droplet surface may be represented by the fuel mass leaving the surface s :

$$\dot{m}_F = (\pi \rho_g v_k a_k^2)_s, \quad (2.88)$$

where a_k is the diameter of k -th droplet and v_k is the droplet surface regression velocity.

As the mass loss of the droplet due to evaporation is completely converted into gaseous fuel, a simple relationship between mass loss from the droplet surface \dot{m}_k and the mass gain in the gas phase \dot{m}_F can be obtained:

$$\dot{m}_F = \dot{m}_k. \quad (2.89)$$

In this model, the droplet mass loss has the following expressions:

$$\dot{m}_k = -\pi a_k \rho_{g,f} D_{g,f} \text{Sh}_k \ln(1 + \text{B}_{m,k}) \quad (2.90)$$

or

$$\dot{m}_k = -\pi a_k \rho_{g,f} \frac{\lambda_{g,f}}{C_{p,f}^F} \text{Nu}_k \ln(1 + \text{B}_{T,k}), \quad (2.91)$$

where $D_{g,f}$, $\lambda_{g,f}$ are the diffusion coefficient and thermal conductivity of the gas mixture in the film region. Subscripts f , g , and k hereinafter refer to the properties in the film region, gas phase properties, droplet liquid properties, respectively. In Eq. (2.90), $\text{B}_{m,k}$ is the Spalding mass transfer number which can be computed as:

$$\text{B}_{m,k} = \frac{Y_{s,k} - Y_{F,\infty}}{1 - Y_{s,k}}, \quad (2.92)$$

$$Y_{s,k} = \frac{W_F}{W_F + W_O (P_\infty / P_{\text{sat},k} - 1)}, \quad (2.93)$$

where $Y_{s,k}$, $Y_{F,\infty}$, W_O , P_∞ , and $P_{\text{sat},k}$ are the vapor surface mass fraction (saturated vapor mass fraction), fuel mass fraction in the far-field (denoted by the subscript ∞) gas mixture, oxidizer molar mass, far-field pressure, and saturated vapor pressure computed with the Clausius-Clapeyron equation:

$$P_{\text{sat},k} = P_{\text{ref}} \exp \left[-\frac{L_v}{\mathcal{R}} \left(\frac{1}{T_k^s} - \frac{1}{T_{\text{ref}}} \right) \right]. \quad (2.94)$$

In Eq. (2.94), \mathcal{R} , P_{ref} , and T_{ref} are ideal gas constant, reference pressure and temperature, taken here as atmospheric pressure and the boiling temperature of the fuel at this pressure, respectively, while L_v is corrected using the Watson equation,

$$L_v = L_{v,s} \left(\frac{T_{\text{cr}} - T_k}{T_{\text{cr}} - T_{\text{ref}}} \right)^{0.38}. \quad (2.95)$$

Here, $L_{v,s}$ and T_{cr} are the molar latent heat at temperature T_{ref} and the critical temperature of the fuel, respectively.

In Eqs. (2.91), $\text{B}_{T,k}$ is the Spalding heat transfer number, which is computed as a function of $\text{B}_{m,k}$ as follows:

$$B_{T,k} = (1 + B_{m,k})^\theta - 1, \quad (2.96)$$

$$\theta = \frac{C_{p,f}^F \text{Sh}_k \text{Pr}_k}{C_{p,f} \text{Nu}_k \text{Sc}_k}, \quad (2.97)$$

where $C_{p,f}^F$ and $C_{p,f}$ are the fuel vapor and gas mixture specific heats at the film region. Sc, Pr, Sh, and Nu are the Schmidt number for the fuel species, the Prandtl number for the gaseous mixture in the fuel region, the Sherwood number, and the Nusselt number, respectively. These dimensionless numbers are computed, in the Abramzon-Sirignano evaporation model, with the help of the droplet Reynolds number Re_k as follows:

$$\text{Re}_k = \frac{\rho_\infty |\mathbf{U}_\infty - \mathbf{V}_k| a_k}{\mu_f}, \quad (2.98)$$

$$\text{Sc}_k = \frac{\mu_f}{\rho_\infty D_f^F}, \quad (2.99)$$

$$\text{Pr}_k = \frac{\mu_f C_{p,f}}{\lambda_f}, \quad (2.100)$$

$$\text{Sh}_k = 2 + 0.55 \frac{\text{Re}_k^{1/2} \text{Sc}_k^{1/3}}{F(B_{m,k})}, \quad (2.101)$$

$$\text{Nu}_k = 2 + 0.55 \frac{\text{Re}_k^{1/2} \text{Pr}_k^{1/3}}{F(B_{T,k})}, \quad (2.102)$$

and

$$F(B) = (1 + B)^{0.7} \frac{\ln(1 + B)}{B}, \quad (2.103)$$

where \mathbf{U}_∞ and \mathbf{V}_k are, respectively, the velocity vectors of the gas mixture in the far-field and the velocity of the droplet k . The Sherwood number Sh and the Nusselt number Nu are equal to 2 in the case of evaporation in quiescent atmosphere. Due to the interdependence of B_T and Nu, this model requires an iterative method to find the converged value of $B_{T,k}$.

The composition and temperature of the mixture in the film are evaluated by interpolation between their values at the droplet surface and the conditions in the far-field using the one-third rule [27, 47, 48]. This law assumes that the properties of the gaseous mixture in the film around the droplet follow a quasi-stationary evolution. Afterwards, the different thermodynamic properties are calculated at the following temperature and composition [39]:

$$T_f = T_k + \frac{1}{3}(T_\infty - T_k), \quad (2.104)$$

$$Y_{f,k} = Y_{s,k} + \frac{1}{3}(Y_{\infty,k} - Y_{s,k}). \quad (2.105)$$

In order to completely characterize the evaporation process, an equation for the evolution

of the droplet temperature needs to be provided. The total heat rate (Q_k) leaving the droplet are due to the vaporization process and depend directly on the latent heat of vaporization,

$$Q_k = \frac{d}{dt}(m_k h_{s,k}) = -\dot{m}_k L_v, \quad (2.106)$$

$$m_k \frac{dh_{s,k}}{dt} + \dot{m}_k h_{s,k} = -\dot{m}_k L_v, \quad (2.107)$$

where the change of sensible enthalpy can be presented as a function of droplet temperature, $dh_{s,k} = C_{p,k} dT$. This leads to

$$m_k C_{p,k} \frac{dT_k}{dt} = \underbrace{-\dot{m}_k h_{s,k}}_{Q_g^c} - \dot{m}_k L_v \quad (2.108)$$

and

$$Q_g^c = \pi a_k \lambda_f \text{Nu}(T_k - T_\infty) \frac{\ln(B_{T,k} + 1)}{B_{T,k}}. \quad (2.109)$$

Therefore,

$$m_k C_{p,k} \frac{dT_k}{dt} = \pi a_k \lambda_f \text{Nu}(T_k - T_\infty) \frac{\ln(B_{T,k} + 1)}{B_{T,k}} - \dot{m}_k L_v, \quad (2.110)$$

keeping in mind that, when the mass fraction of evaporated fuel at the surface of the droplet, $Y_{s,F}$, approaches 1, the evaporation reaches saturated conditions. Accordingly, the Spalding mass number (Eq. (2.92)) becomes singular. When saturation is reached, the droplet is assumed to be at its saturation point, that is, the evaporation takes place without heating in the liquid and the droplet temperature stays constant.

2.8.3 DNS-DPS Coupling Equation

The coupling between the DNS equations (Navier-Stokes) for the gas phase and the DPS equations for the liquid spray is performed by adding source terms, Γ , to the conservation equations for mass, momentum, and energy (Eqs. (2.1)-(2.14)). The expressions for these source terms can be reviewed as follows:

$$\Gamma_m = -\frac{1}{\mathcal{V}} \sum_k \alpha_k \frac{dm_k}{dt}, \quad (2.111)$$

$$\Gamma_{m,k} = \delta_{k,F} \Gamma_m, \quad (2.112)$$

$$\Gamma_{u_i} = -\frac{1}{\mathcal{V}} \sum_k \alpha_k \frac{d(m_k v_{k,i})}{dt}, \quad (2.113)$$

$$\Gamma_e = -\frac{1}{\mathcal{V}} \sum_k \alpha_k \frac{d(m_k C_{p,K} T_k)}{dt}, \quad (2.114)$$

where \sum_k is the sum over every droplet k inside the volume \mathcal{V} and α is the interpolation weight function which interpolates from Lagrangian to Eulerian space. $\delta_{k,F}$ is the Kronecker delta and is 1 for the fuel species ($k = F$) and 0 otherwise. $v_{k,i}$ is the i -th component of the velocity of the droplet k .

After having reviewed all the equations and models needed for the simulations, it is time developing a suitable computational tool for carrying out corresponding simulations.

Chapter 3

A New DNS Solver: DINO

3.1 Introduction

As discussed in the abstract section, one of the goals of this dissertation is to develop a new DNS solver which considers different aspect needed to investigate turbulent combustion: turbulence, combustion, spray, complex geometry, etc. This kind of solver is difficult to find with the features one needs. In this chapter, the new solver, called DINO, is described in detail. The chapter begins by reviewing the important features in DINO, followed by describing the numerical approaches used in the solver, after which, the parallelization efficiency is discussed, before verifying the code by comparison with analytical solution benchmarks. The chapter concludes with the validation of different parts of the code and some combustions applications. Part of this chapter is based on a publication in Computers and Fluids [50].

3.2 DINO Challenges and Important Features

DINO is a new in-house, Fortran-2003, 3D DNS code developed by the research group under Prof. Dominique Thévenin at the University of Magdeburg “Otto von Guericke”. It began in 2013 as a part of my Ph.D. work. The equations are spatially discretized with a 6th order finite-difference stencil and temporally integrated with the 3rd/4th order Runge-Kutta method. The code is parallelized in two dimensions using the 2DECOMP&FFT library that acts on top of the standard tools: MPI and FFTW. At the beginning of the code development, several challenges and questions faced us as a development group, which can be summarized as follows:

1. Time step restriction due to acoustic waves;
2. Complex treatment of the inflow/outflow boundary condition in compressible solvers;
3. Time step restriction due to the numerical stiffness;
4. Overhead and efficiency of computing the Poisson equation in low-Mach number and incompressible solvers;

3.2. DINO Challenges and Important Features

5. Imposing initial turbulence in an efficient manner;
6. Computing the thermodynamic, kinetic, and transport properties in an accurate way;
7. Treatment of the droplets and of large particles (two-phase flows);
8. Performing DNS for semi-complex geometries.

We (I and the rest of the DNS group, including a collaboration with Felix Dietzsch at T.U. Freiberg) dealt with these challenges as outlined in the following. First, since acoustic waves only appear in fully compressible solvers, DINO is coded using a low-Mach number version of the Navier-Stokes equation (Ch. 2). As such, the time step is no longer controlled by acoustic waves, but by convection, diffusion, and radiation. Additionally, using a low-Mach formulation removes the difficulties of imposing complex inflow/outflow boundary conditions, which appear in classical compressible numerical solvers. In low-Mach number solvers, standard and straightforward inflow/outflow conditions are implemented without any special treatment. The other difficulty is the numerical stiffness resulting from the chemistry; this leads to a small time step (of order of nanoseconds) for the simulation. Therefore, semi-implicit and additive Runge-Kutta techniques are used to solve this issue.

However, one huge overhead still exists: solving the Poisson equation in parallel computations with high-order spatial discretization. It has been found that the standard available solvers, such as HYPRE or ScaLAPACK, though using different orders and different methods (iterative, matrix inverse), still introduce a huge computational overhead. I thus developed an efficient parallelized Poisson solver which is based on FFT for both periodic and non-periodic boundary conditions, but with dedicated pre- and post-processing FFT techniques in the latter case. This Poisson solver is much faster than the other available techniques and delivers of course spectral order. This new Poisson solver completely removes the overhead introduced by any other solver. Combining all previous treatments, an extremely fast DNS code for single phase turbulent reactive flow simulation is obtained.

In DINO, the chemical source terms and the thermodynamic and kinetic properties are computed using the Cantera-1.8 library. The transport properties are computed either with the Cantera library or with the EGLib-3.4 library. The initial turbulent field can be generated by different methods: inverse Fourier transform with analytical energy spectrum (Passot-Pouquet or Von Karman-Pao), the Kraichnan technique, digital filter, or the diffusion technique. The reason for employing different techniques for turbulence in DINO is to maximize the flexibility as a function of boundary type, geometrical configuration, targeted integral length scale, and fluctuation velocity.

Simulating two-phase flow adds a new level of difficulties and raises several questions: What is the nature of the second phase? How will it be treated? Will the surface of the second phase be resolved? Indeed, during the development of this code, two different particles have been considered: solid large particles, and small droplets. Numerically these two particle types are treated in completely different ways. For a large particle, which is usually larger than the grid resolution and Kolmogorov length scale, the surface of this particle must be resolved. This is accomplished by using the direct force immersed boundary method (DF-IBM) to avoid using body-fitted grid techniques. On the other hand, the small particles

(droplets and spray), which are supposed to be smaller than the grid resolution, are treated as a point source (discrete particle simulation, DPS) without resolving the droplet surface or considering breakup or coalescence. The common aspect in both DF-IBM and DPS is the tracking of the particles in Lagrangian space. The properties are exchanged from/into the gas, which is simulated in an Eulerian frame by interpolating between the Eulerian- and Lagrangian-space.

The last issue, which was one of the biggest challenges, is performing DNS in semi-complex geometry. Generally, there are two approaches: (1) using body-fitted grid techniques, or (2) using IBM techniques. The body-fitted grid techniques add complexity to the DNS, especially for the Poisson-Solver. For this reason, DINO was developed using the direct boundary IBM (DB-IBM) technique. In this part of DINO, the complex geometry is implemented by introducing the boundary with stepwise geometry. This is a simple technique which requires a high resolution mesh. As a recommendation, higher-order DB-IBM methods should be implemented in future work. Usually, most of the high-order DB-IBM methods are built on top of the primary stepwise geometry currently implemented.

3.3 Governing Equations

DINO has been conceived from the start as a flexible tool, allowing for a highly accurate investigation of turbulent flows at low and intermediate velocities. Thus, it involves a variety of algorithms, models and equations. It is impossible to discuss everything in great detail. Only the most important aspects will be described in what follows, separating in particular between reacting and non-reacting flows. The low-Mach number approach is used in DINO for reacting flows, since most applications involving chemical reactions and combustion indeed take place at low Mach numbers, $Ma \ll 1$ [11, 50]. For non-reacting flows, incompressible transport equations are considered instead. For both conditions (reacting and non-reacting), either single-phase or two-phase turbulent flows can be described with DINO, as described later. Since DINO relies on external libraries written in dimensional form, it has been written from the start as a dimensional code as well, using SI units.

3.4 Low-Mach Number Formulation for Reacting Flows

In this case, the pressure in the flow is nearly uniform and the coupling between the fluctuating pressure and the density can be neglected. The present formulation is based on an incompressible but dilatable approach, first described for reacting flows by [34]. As discussed in Sec. 2.1.2, pressure is then split into a spatially homogeneous thermodynamic pressure $p(t)$ and a dynamic fluctuating pressure $\tilde{p}(x, t)$, where $\tilde{p}(x, t) \ll p(t)$. The resulting equations still contain vorticity and entropy waves, but acoustic waves have disappeared. Therefore, the timestep is no longer limited by acoustic times, but only by characteristic convection, diffusion or reaction time scales, leading to a considerable speed-up [50, 51].

The conservation equations underlying the low-Mach number approximation for an ideal gas involving N_s chemical components are reviewed in Ch. (2) in standard form. Now, they

3.4. Low-Mach Number Formulation for Reacting Flows

are given in compact form, which helps in coding, as follows:

$$\partial_t(\rho) = -\partial_i(\rho u_i) + \Gamma_m, \quad (3.1)$$

$$\partial_t(\rho u_i) = -\partial_i \tilde{p} + R_{m,i}, \quad (3.2)$$

$$\partial_t(T) = \vartheta + R_T, \quad (3.3)$$

$$\partial_t(Y_k) = \mathfrak{S}_k + R_{Y_k}, \quad (3.4)$$

$$\rho = \frac{pW}{RT}, \quad (3.5)$$

subject to the additional condition for global mass conservation as discussed in Ch. (2):

$$\sum_{k=1}^{N_s} Y_k = 1, \quad (3.6)$$

where ρ , u_i , Γ_m , \tilde{p} , p , T , Y_k , N_s , R and W are the mixture density, i -th-component of flow velocity, mass source term (per unit volume) introduced by the discrete phase, fluctuation pressure, thermodynamic pressure, temperature, k -th species mass fraction, number of species, ideal gas constant, and mixture mean molecular weight, respectively. The right-hand side of the momentum equation, Eq. (3.2), reads using the summation convention of Einstein:

$$R_{m,i} = -\frac{\partial(\rho u_j u_i)}{\partial x_j} + \frac{\partial}{\partial x_j} \left[\mu \left(\frac{\partial u_i}{\partial x_j} + \frac{\partial u_j}{\partial x_i} \right) \right] - \frac{\partial}{\partial x_j} \left[\frac{2}{3} \mu \frac{\partial u_l}{\partial x_l} \right] \delta_{ij} + \Gamma_{u,i}, \quad (3.7)$$

where δ_{ij} , μ , and $\Gamma_{u,i}$ are the Kronecker delta, dynamic, and momentum source term (per unit volume) introduced by the discrete phase, respectively. The right-hand side of the temperature equation, Eq. (3.3), has been split into a stiff term, ϑ , and a non-stiff term, R_T , respectively:

$$\vartheta = -\frac{1}{\rho C_p} \sum_{k=1}^{N_s} h_k \dot{\omega}_k, \quad (3.8)$$

$$R_T = -u_j \frac{\partial T}{\partial x_j} + \frac{1}{\rho C_p} \left[\frac{\partial}{\partial x_j} \left(\lambda \frac{\partial T}{\partial x_j} \right) - \frac{\partial T}{\partial x_j} \sum_{k=1}^{N_s} \rho C_{p,k} Y_k V_{k,j} + \Gamma_e \right]. \quad (3.9)$$

In Eqs. (3.8) and (3.9), C_p , h_k , $\dot{\omega}_k$, λ , $V_{k,j}$, and Γ_e represent the specific heat capacity at constant pressure, specific enthalpy, mass reaction rate, heat diffusion coefficient, j -th component of the species molecular diffusion velocity, and energy source term (per unit volume) introduced by the discrete phase, respectively. The stiff term ϑ involves the reaction rates induced by chemical kinetics and will be integrated in time separately from R_T , leading

to a much faster and more robust integration.

In a similar manner, the right-hand side of the conservation equation for the mass fraction of species k , Y_k (Eq. 3.4), has been split into a stiff term, \mathfrak{S}_k , and a non-stiff term, R_{Y_k} , respectively:

$$\mathfrak{S}_k = \frac{\dot{\omega}_k}{\rho}, \quad (3.10)$$

$$R_{Y_k} = -u_j \frac{\partial Y_k}{\partial x_j} - \frac{1}{\rho} \frac{\partial(\rho Y_k V_{kj})}{\partial x_j} + \Gamma_{m,k}. \quad (3.11)$$

3.4.1 Available Diffusion Velocity Models

To solve the system involving Eqs. (3.9) and (3.11), the molecular diffusion velocity of species k , \mathbf{V}_k , must be modeled appropriately. In order to increase flexibility, three different approaches are implemented in DINO, leading to increasing accuracy but also computational requirements [52]:

1. Unity Lewis numbers;
2. Mixture-averaged diffusion velocities;
3. Multicomponent diffusion velocities.

Additionally, thermal diffusion (Soret term) may be considered for light species, but without the inverse (Dufour) effect. Diffusion due to pressure gradients and to external forces is not relevant for the considered applications and is thus not accounted for.

Unity Lewis Numbers

In that case, it is assumed that the Lewis number of species k , $Le_k = \lambda/(\rho C_p D_k)$ are all identical and equal to unity, meaning that the molecular diffusion velocity of all species is equal to the heat diffusion velocity. Then, the diffusion coefficient of species k , D_k , can be immediately estimated as $D_k = \lambda/(\rho C_p)$ and is identical for all species: $D_k = D$. The diffusion velocity finally reads:

$$\mathbf{V}_k = -D \frac{\nabla Y_k}{Y_k}, \quad (3.12)$$

with X_k the mole fraction of species k . This is simply the Fick's law.

Mixture-Averaged Diffusion Coefficient

Here, following the classical approximation proposed by Hirschfelder and Curtiss, a mixture-averaged diffusion coefficient D_k is first computed for each species k using:

$$D_k = \frac{1 - Y_k}{\sum_{j \neq k} X_j / \mathcal{D}_{jk}}, \quad (3.13)$$

where the \mathcal{D}_{jk} are the binary diffusion coefficients. Then, the diffusion velocity is determined by:

$$\mathbf{V}_k = -D_k \frac{\nabla X_k}{X_k} + \sum_{k=1}^{N_s} D_k \nabla X_k \frac{W_k}{W}, \quad (3.14)$$

The last term in this equation is the correction velocity needed to fulfill mass conservation by molecular diffusion, i.e., $\sum_{k=1}^{N_s} Y_k \mathbf{V}_k = 0$ (Ch. 2), with W_k the molecular weight of species k .

Multicomponent Diffusion Velocity

In many applications the combustion process can not be reduced to a representation of a simple binary mixture. Therefore, the formulation of a species transport law has to account for different transport properties of each species. In general, the multicomponent diffusion process is computed by inverting the species linear transport system [53]:

$$F = L^{00,00^{-1}}, \quad (3.15)$$

with

$$L_{ij}^{00,00} = \frac{16T}{25p} \sum_{k=1}^{N_s} \frac{X_k}{W_i \mathcal{D}_{ik}} \{W_j X_j (1 - \delta_{ik}) - W_i X_j (\delta_{ij} - \delta_{jk})\}. \quad (3.16)$$

The multicomponent diffusion coefficients are then given by

$$D_{ij} = X_i \frac{16TW}{25pW_j} (F_{ij} - F_{ii}). \quad (3.17)$$

Finally, the species diffusion velocities read

$$\mathbf{V}_k = -\frac{1}{X_k W} \sum_{j=1}^{N_s} W_j D_{kj} \nabla X_j. \quad (3.18)$$

In order to evaluate efficiently all multicomponent transport properties, the EGLib library [53, 54] in its version 3.4 has been coupled to DINO. The multicomponent diffusion velocity model has been implemented by Felix Dietzsch at T.U. Freiberg.

Thermal Diffusion

Thermal diffusion (Soret effect) is implemented as an additional term that might be switched on by decision of the user. The corresponding diffusion velocity reads:

$$\mathbf{V}_{kT} = -D_{kT} \frac{\nabla T}{T}. \quad (3.19)$$

Considering that the corresponding computation of D_{kT} is relatively expensive and that this term is only important for light molecular species, the Soret effect is usually only activated for species H and H₂.

3.4.2 Further Transport Coefficients

Additional transport coefficients appear in the equations listed above. The computation of the thermal conductivity λ and of the dynamic viscosity μ relies by default on Cantera 1.8, or alternatively on EGLib 3.4.

3.4.3 Thermodynamic Parameters

All thermodynamic parameters appearing in the previous conservations equations, such as $C_{p,k}$ and h_k are computed by coupling DINO with Cantera 1.8.

3.4.4 Chemical Kinetics

The chemical source terms $\dot{\omega}_k$ appearing in the conservation equations for species are computed by Cantera 1.8 based on detailed reaction schemes from the literature, solving one transport equation for each chemical species appearing in the system. For instance, for one application presented at the end of this chapter (a turbulent ethylene flame), 51 transport equations are taken into account: 46 equations for the 46 species of the reaction mechanism, 3 for momentum, 1 for temperature and 1 Poisson equation (using the equation of state to close the system).

3.5 Incompressible Formulation for Non-Reacting Flows

For non-reacting flows at low Mach numbers, it is better to use fully incompressible flow equations, reducing to mass and momentum conservation, since energy conservation needs not be considered separately. This leads to a faster integration and to a reduction of the memory requirements. Mass conservation in DINO is identical to Eq.(2.22) which was presented in Ch. 2, while the right-hand side of the momentum equation, Eq. (3.7), reduces to,

$$R_{m,i} = -\frac{\partial(\rho u_j u_i)}{\partial x_j} + \mu \frac{\partial^2 u_i}{\partial x_j^2} + \Gamma_{u,i}, \quad (3.20)$$

for a constant dynamic viscosity μ .

3.6 Parallelization Strategy

The parallelization of the code relies on a 2D pencil decomposition using the open-source library 2DECOMP&FFT [55], which has been designed to perform optimized three-dimensional distributed FFTs. This library is called on top of standard MPI and MPI-I/O libraries and includes user-friendly programming interfaces. 2DECOMP&FFT supports large-scale parallel applications on distributed memory systems and shows excellent performance on a variety of existing supercomputers [56, 57]. The library comprises two different possible pencil orientations, x-pencils and z-pencils. DINO has been coded with the x-pencil orientation (Fig. 3.1) in order to minimize the computational time needed for transposing the data as required for non-periodic boundary conditions. Using 2DECOMP&FFT an excellent parallel scaling has been obtained with DINO, as discussed later in Sec. 3.14.1.

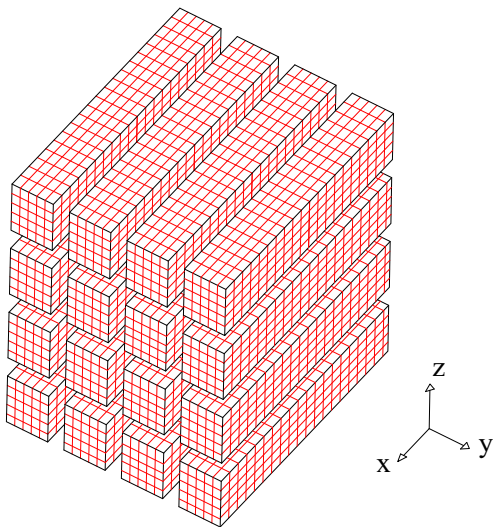


Figure 3.1: 2D domain decomposition with x-pencil orientation.

3.7 Time Integration Schemes

In order to increase flexibility, three different time integration algorithms have been coded in DINO. The final choice of the user should be based on the considered application, on the required accuracy, on the available computational resources and, most important, on the stiffness of the problem, in particular for reacting flows.

The first algorithm is a fully explicit, fourth-order Runge-Kutta method rewritten as a low-storage algorithm [58]. It is the simplest and computationally most efficient algorithm.

It is activated by default for non-reacting cases. However, it suffers from a limited stability for stiff applications. The solution procedure reads:

$$T^{n+1} = T^n + \Delta t (\vartheta^n + R_T^n), \quad (3.21)$$

$$Y_k^{n+1} = Y_k^n + \Delta t (\mathfrak{S}_k^n + R_{Y_k}^n), \quad (3.22)$$

$$\rho^{n+1} = \frac{p W^{n+1}}{\mathbb{R} T^{n+1}}, \quad (3.23)$$

$$(\rho u_i)^* = (\rho u_i)^n + \Delta t R_{m,i}^n, \quad (3.24)$$

$$\nabla^2 \tilde{p}^{n+1/2} = \frac{1}{\Delta t} [\partial_t \rho^{n+1} + \partial_j (\rho u_j)^*], \quad (3.25)$$

$$(\rho u_i)^{n+1} = (\rho u_i)^* - \Delta t \partial_i \tilde{p}^{n+1/2}. \quad (3.26)$$

As documented in Eqs. (3.24)-(3.26), the coupling between continuity and momentum equation is handled by using the pressure-free projection method [59–61]. In this approach the intermediate quantity $(\rho u)^*$ is obtained by solving the momentum equation without pressure gradient (Eq. 3.24). Then, applying the divergence operator to Eq. (3.26) leads to

$$\nabla^2 \tilde{p}^{n+1/2} = \frac{1}{\Delta t} [\partial_i (\rho u_i)^* - \partial_i (\rho u_i)^{n+1}]. \quad (3.27)$$

The Poisson equation is closed by substituting the continuity equation, Eq. (3.1), into Eq. (3.27), leading to the continuity constraint. In Eq. (3.25), a third-order backward finite-difference approximation is used to compute $\partial_t \rho^{n+1}$.

The second algorithm for time integration is based on the split semi-implicit fourth-order Runge-Kutta scheme. In this algorithm the right-hand side of the governing equations for temperature and species are split into non-stiff parts (R_T , R_k) and stiff parts (ϑ , \mathfrak{S}_k), following [62, 63]. The non-stiff parts of T and Y_k are solved using the explicit fourth-order Runge-Kutta solver:

$$T^* = T^n + \Delta t (R_T^n), \quad (3.28)$$

$$Y_k^* = Y_k^n + \Delta t (R_{Y_k}^n), \quad (3.29)$$

$$\rho^* = \frac{p W^*}{\mathbb{R} T^*}. \quad (3.30)$$

The stiff parts are integrated in time by using the implicit solver RADAU-5 [64, 65]. Then,

3.7. Time Integration Schemes

both solutions are added:

$$T^{n+1} = T^* + \Delta t (\vartheta^{n+1}), \quad (3.31)$$

$$Y_k^{n+1} = Y^* + \Delta t (\mathfrak{S}_k^{n+1}), \quad (3.32)$$

$$\rho^{n+1} = \frac{p W^{n+1}}{R T^{n+1}}. \quad (3.33)$$

Finally, momentum conservation and Poisson equation are again integrated using the explicit fourth-order Runge-Kutta method, as explained above (Eqs. (3.24)-(3.26)).

The third possibility for time integration is to use the additive third-order Runge-Kutta method. This non-split semi-implicit Runge-Kutta algorithm is an extension of the Rosenbrock Runge-Kutta approach. In this algorithm the system of equations is solved as follows:

$$d_t \mathbf{Z} = \mathbf{f}(\mathbf{Z}) + \mathbf{g}(\mathbf{Z}), \quad (3.34)$$

$$\partial_t(\rho \mathbf{u}) = \mathbf{f}(\rho \mathbf{u}) - \nabla \tilde{p}, \quad (3.35)$$

where \mathbf{f} and \mathbf{g} are the non-stiff and stiff right-hand side vectors of the equation system, respectively, while \mathbf{Z} is the vector containing the scalar variables $(T, Y_1, Y_2, \dots, Y_{N_s})'$. Then, the solution is obtained through following steps:

$$\mathbf{Z}^{n+1} = \mathbf{Z}^n + \sum_{j=1}^r \alpha_j \mathbf{K}_{\mathbf{z}_j}, \quad (3.36)$$

$$\rho^{n+1} = \frac{p W^{n+1}}{R T^{n+1}}, \quad (3.37)$$

$$(\rho \mathbf{u})^* = (\rho \mathbf{u})^n + \sum_{j=1}^r \alpha_j \mathbf{K}_{\mathbf{u}_j}, \quad (3.38)$$

$$\nabla^2 \tilde{p}^{n+1/2} = \frac{1}{\Delta t} [\partial_t \rho^{n+1} + \nabla(\rho \mathbf{u})^*], \quad (3.39)$$

$$(\rho \mathbf{u})^{n+1} = (\rho \mathbf{u})^* - \Delta t \nabla \tilde{p}. \quad (3.40)$$

Where,

$$\left[\mathbf{I} - \Delta t a_i \mathbf{J} \left(\mathbf{Z}^n + \sum_{j=1}^{i-1} (d_{ij} \mathbf{K}_{\mathbf{z}_j}) \right) \right] \mathbf{K}_{\mathbf{z}_i} = \Delta t \left[\mathbf{f} \left(\mathbf{Z}^n + \sum_{j=1}^{i-1} (b_{ij} \mathbf{K}_{\mathbf{z}_j}) \right) + \mathbf{g} \left(\mathbf{Z}^n + \sum_{j=1}^{i-1} (c_{ij} \mathbf{K}_{\mathbf{z}_j}) \right) \right], \quad (3.41)$$

and

$$\mathbf{K}_{\mathbf{u}_i} = \Delta t \left[\mathbf{f} \left((\rho \mathbf{u})^n + \sum_{j=1}^{i-1} (c_{ij} \mathbf{K}_{\mathbf{u}_j}) \right) \right], \quad \forall \quad i = 1, 2, \dots, r. \quad (3.42)$$

In Eqs. (3.36)-(3.42), r is the number of stages (in DINO, $r = 3$ by default, leading to third order in time) and $\mathbf{J} = \partial \mathbf{g} / \partial \mathbf{Z}$ is the Jacobian matrix of the stiff term, \mathbf{g} . The symbols α_j , a_i , b_{ij} , c_{ij} and d_{ij} designate constant coefficients. The values of these coefficients depend on the retained order. The values used in DINO are listed in Table 3.1 and correspond to the third-order case. More details about the method and its accuracy can be found in [66].

Table 3.1: Coefficients for third-order additive semi-implicit Runge-Kutta integration.

(a_i)			$(b_{ij} = d_{ij})$			(c_{ij})			(α_i)	
a_1	a_2	a_3	b_{21}	b_{31}	b_{32}	c_{21}	c_{31}	c_{32}	$\alpha_1 = \alpha_2$	α_3
0.797097	0.591381	0.134705	$\frac{8}{7}$	$\frac{71}{252}$	$\frac{7}{36}$	1.05893	0.5	-0.375939	$\frac{1}{8}$	$\frac{3}{4}$

Independently from the retained integration procedure, the timestep of the computation can be optionally controlled by three different limiters, separately or in combination: 1) the Courant-Friedrichs-Lewy (CFL) stability criterion, 2) the Fourier stability criterion for diffusive terms, and 3) a dynamic accuracy control obtained through timestep-doubling within the Runge-Kutta procedure, as already used in past DNS codes [58, 67].

3.8 Spatial Discretization

All partial derivatives in space appearing in the conservation equations are discretized using centered, sixth-order finite differences (seven-point stencil), stepwise reduced down to third-order near domain boundaries. The communication across processor boundaries is handled by using the halo-cell communication function included in the 2DECOMP&FFT library.

3.9 Solving the Poisson Equation in Parallel

One of the most difficult issues associated with any low-Mach or incompressible flow solver is to find an efficient way for solving the Poisson equation. Usually, it is solved by explicit iterative methods (Conjugate Gradient CG, Multi-grid, etc.) or more rarely by implicit methods (matrix inversion, spectral methods, or combinations of both). In DINO, the Poisson equation is solved by FFT, even when the boundary conditions of the domain are not periodic.

The developed approach is an extension of that described in [56, 57, 68, 69], where pre- and post-processing was applied both in physical and in wave space. The current algorithm needs only pre- and post-processing in the physical space and for a different purpose. Additional differences result from the fact that the pressure is solved in DINO in a collocated manner and not on a staggered grid.

3.9. Solving the Poisson Equation in Parallel

Suitable pre- and and post-processing steps are applied to the corresponding array before and after calling the parallel FFT subroutine included in 2DECOMP&FFT. All tests have demonstrated that this method delivers a very high order (equivalent spectral accuracy) and is also computationally very efficient compared to existing alternatives. In order to explain the current algorithm it is better to start with classical discrete Fourier transform (\hat{F}_k) for a real sequence F_j , $j = 0, 1, 2, \dots, N - 1$, which is defined by

$$\hat{F}_k = \frac{1}{N} \sum_{j=0}^{N-1} F_j e^{-2\pi j k \sqrt{-1}/N}, \quad k = 0, 1, \dots, N - 1. \quad (3.43)$$

Thanks to Hermitian symmetry, $\hat{F}_k = \hat{F}_{n-k}^*$, with $\hat{F}_N = \hat{F}_0$. The inverse of this transform reads:

$$F_j = \sum_{k=0}^{N-1} F_k e^{2\pi j k \sqrt{-1}/N}. \quad (3.44)$$

This operation is directly applied only for periodic sequences (periodic boundary conditions). These two transforms can then be obtained immediately with 2DECOMP&FFT and FFTW libraries, using FFT and IFFT algorithms, respectively.

Concerning now the implementation in DINO, F_j is first transformed in case of Dirichlet-Dirichlet (DD) boundary conditions using a discrete sine transform (DST),

$$\hat{F}_k = \frac{2}{N} \sum_{j=1}^{N-1} F_j \sin(\pi j k / N). \quad (3.45)$$

In order to obtain the Fourier transform with the standard FFT parallel routines included in 2DECOMP&FFT, the F_j array is extended in a pre-processing step to a temporary, odd symmetry sequence with length of $(2N)$, in the form $(0, F_1, F_2, \dots, F_{N-1}, 0, -F_{N-1}, \dots, -F_2, -F_1)$, where $F_j = -F_{2N-j}$ for $j = 1, N - 1$.

In the same manner, in case of Neumann-Neumann (NN) boundary conditions, a discrete cosine transform (DCT) is used instead:

$$\hat{F}_k = \frac{2}{N} \left[\frac{F_0}{2} + \sum_{j=1}^{N-1} F_j \cos(\pi j k / N) + \frac{(-1)^k F_N}{2} \right], \quad (3.46)$$

The standard FFT routine is applied after extending the array in a pre-processing step into a temporary, even symmetry sequence of length $(2N)$ with the form of $(F_0, F_1, F_2, \dots, F_{N-1}, F_N, F_{N-1}, \dots, F_2, F_1)$, where $F_j = F_{2N-j}$ for $j = 1, N - 1$.

A combination between both boundary conditions is also possible. In the case of a Dirichlet-Neumann (DN) combination, a quarter-wave discrete sine transform (QW-DST) is

suitable:

$$\hat{F}_k = \frac{1}{N} \left[\frac{F_0}{2} + \sum_{j=1}^{N-1} F_j \sin(\pi j(2k-1)/(2N)) + \frac{(-1)^{k-1} F_N}{2} \right], \quad (3.47)$$

Then, a classical FFT routine is again possible, after extending the original sequence to a temporary, odd symmetry sequence with length of $(4N)$ where $(0, F_1, \dots, F_N, F_{N-1}, \dots, F_1, 0, -F_1, \dots, -F_N, -F_{N-1}, \dots, -F_1)$. Similarly, a case with Neumann-Dirichlet (ND) boundary conditions is now transformed with a quarter-wave discrete cosine transform (QW-DCT),

$$\hat{F}_k = \frac{1}{N} \left[\frac{F_0}{2} + \sum_{j=1}^{N-1} F_j \cos(\pi j(2k-1)/(2N)) \right], \quad (3.48)$$

with a standard FFT routine after extending the original sequence to a temporary, even symmetry sequence with length of $(4N)$, in the form $(F_0, F_1, \dots, F_{N-1}, 0, -F_{N-1}, \dots, -F_0, -F_1, \dots, -F_{N-1}, 0, F_{N-1}, \dots, F_1)$.

Finally, the algorithm implemented in DINO for solving the Poisson equation $\nabla^2 p = F$ can be summarized as follows:

1. Pre-processing for sequence F (input to the algorithm), which is a real array of length N , extending its length depending on the boundary conditions;
 - DD: $M = 2N$, $(0, F_1, F_2, \dots, F_{N-1}, 0, -F_{N-1}, \dots, -F_2, -F_1)$;
 - NN: $M = 2N$, $(F_0, F_1, F_2, \dots, F_{N-1}, F_N, F_{N-1}, \dots, F_2, F_1)$;
 - DN: $M = 4N$, $(0, F_1, \dots, F_N, F_{N-1}, \dots, F_1, 0, -F_1, \dots, -F_N, -F_{N-1}, \dots, -F_1)$;
 - ND: $M = 4N$, $(F_0, F_1, \dots, F_{N-1}, 0, -F_{N-1}, \dots, -F_0, -F_1, \dots, -F_{N-1}, 0, F_{N-1}, \dots, F_1)$.
2. Apply standard FFT routine (Eq. 3.43) over M discrete points to obtain \hat{F}_k ;
3. Solve the Poisson equation in wave space, $\hat{p} = -\hat{F}/\kappa^2$;
4. Apply standard IFFT routine (Eq. 3.44) to Fourier transform of the pressure (\hat{p}), obtaining the pressure in the physical space saved in temporary array F (overwritten to save memory);
5. Post-processing for array F by saving the correct part into an array P of length N .

This algorithm has been coded for parallel simulations (parallel FFT) to speed-up the process. Considering for instance a small 3D DNS involving $65 \times 65 \times 32$ grid points parallelized using 16 cores with Dirichlet-Neumann, Neumann-Neumann, and periodic-periodic boundary conditions in x , y , and z direction, respectively, the implemented algorithm is already 6.75 faster than the CG solver implemented in the well-known HYPRE library [70].

3.10 Boundary Conditions in Time and Space

For DNS relying on the low-Mach number or on the incompressible formulation, boundary conditions in space are straightforward [71], at the difference of compressible DNS tools [72]. Standard Dirichlet and Neumann boundary conditions perform well and are stable.

Concerning initial conditions in time, a suitable approximation of real turbulence must usually be generated for DNS. It is then either used directly for time-decaying simulations in the same domain, or it is employed for turbulence injection through an inflow boundary, leading to spatially-evolving turbulence. Both solutions are available in DINO.

To generate the initially needed approximation of the turbulent flow field, four different algorithms are available in the code, so that initial solutions can be obtained for a broad range of integral length scales, turbulence intensities and geometrical configurations. By default, an Inverse Fast Fourier Transform (IFFT) relying either on the Passot-Pouquet spectrum or on the Von Kármán spectrum with Pao correction [67] (see later Eq. 3.74) has been implemented, with help of Felix Dietzsch at T.U. Freiberg, in parallel using 2DECOMP&FFT. As alternatives, the Kraichnan technique [73], digital filtering [74], or random noise diffusion [75] are available as well.

3.11 Grid Stretching

By default, a regular tensor-product grid is generated by DINO. If desirable for the considered application, a static refinement can be applied based on stretching functions (ξ) close to the boundaries (for a better resolution of the boundary layer) or at any place within the domain (e.g., for a better resolution of a mixing region). When applying a static grid refinement, a numerical transformation is applied based on the chain rule [76]. Hence, the derivatives are still computed on a regularly-spaced ($\partial/\partial\xi$) computational grid, and then projected onto the real ($\partial/\partial x$), adapted grid [76]: For the first derivative, the chain rule is computed as follows:

$$\frac{\partial}{\partial x} = \frac{\partial}{\partial \xi} \frac{\partial \xi}{\partial x}, \quad (3.49)$$

and (2) for the second derivative it is computed as:

$$\frac{\partial^2}{\partial x^2} = \frac{\partial}{\partial \xi} \frac{\partial^2 \xi}{\partial x^2} + \frac{\partial^2}{\partial \xi^2} \left(\frac{\partial \xi}{\partial x} \right)^2. \quad (3.50)$$

The transformation function must only be computed once, since it does not change. In that case, it is much easier to keep the equidistant formulation of the derivative computation, and multiply afterwards with the (fixed) transformation function. Tests have shown that it is also slightly faster in terms of computing time.

3.12 Immersed Boundaries

Using two different formulations, the Immersed Boundary Method (IBM) is implemented within DINO. The first one pertains to static immersed boundaries, that will not change in time; this is particularly useful to carry out DNS in complex geometries. This method called direct boundary immersed boundary method (DB-IBM). Considering now moving particles (solid particles, droplets) resolved on the grid, the second usage of IBM is to describe two-phase flows; in this case the direct force immersed boundary method (DF-IBM) is implemented. Both approaches are described in more detail in the next two sections.

3.12.1 DNS in Complex Geometries: DB-IBM

When considering cases with a complex (but currently time-independent) geometry, DINO relies on DB-IBM. The details of the algorithm can be found in [77, 78]. For this purpose, DINO reads the discretized input geometry in 3D as binary values transformed into a boolean variable describing if the corresponding point is within the wall (value: 0) or within the flow (value: 1) as illustrated in Fig. 3.2 . In this manner, even very complex and irregular geometries can be considered in the DNS simulation. In the employed method, there is no interpolation performed at the boundaries which means that this method is zero-order and thus requires very fine mesh. This is a first step towards currently implemented high order methods. Note that the spectral Poisson solver described previously in Sec. 3.9 is compatible with all other features implemented in the code, like those described here.

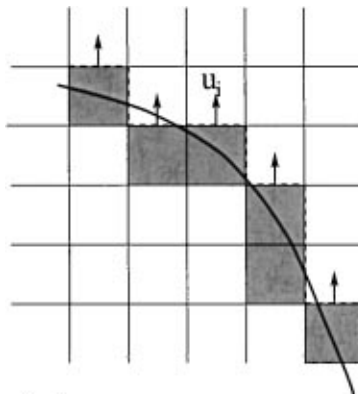


Figure 3.2: Sketch of imposing boundaries into the regular mesh in DB-IBM: stepwise geometry [77].

As an example, Fig. 3.3 shows a patient-specific cerebral aneurysm [79] represented in DINO by using DB-IBM, and instantaneous streamlines obtained in this geometry at peak systole, colored by velocity magnitude.

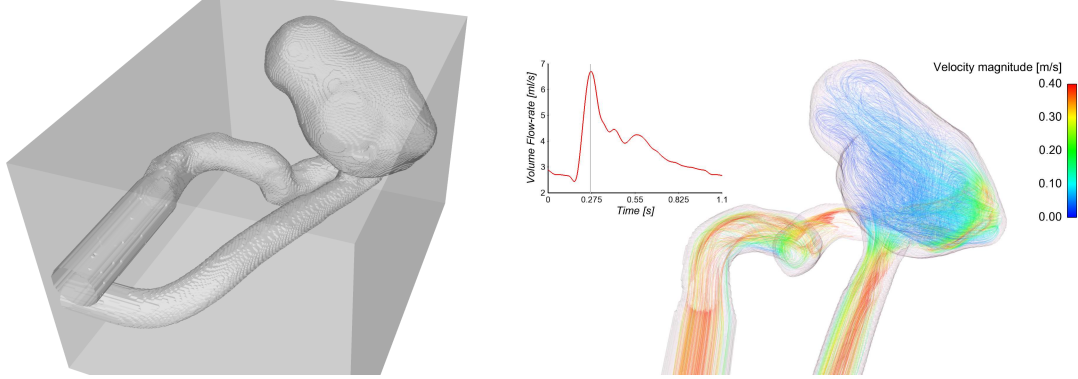


Figure 3.3: Representation of domains with a complex geometry in DINO using DB-IBM. Left: patient-specific cerebral aneurysm [79]. Right: Streamlines colored by velocity magnitude at peak systole.

3.12.2 DF-IBM

The second immersed boundary method implemented in DINO, is the DF-IBM described in [61, 80]. In this method the surface of the immersed body is imposed to the regular grid through a direct force, which is added to the momentum equation (Fig. 3.4).

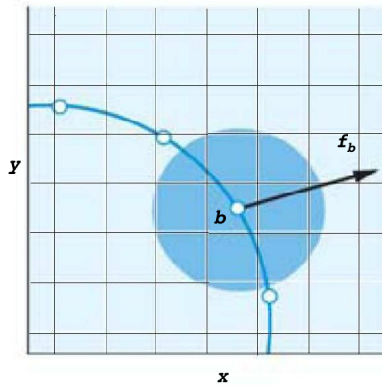


Figure 3.4: Schematic diagram showing the location of the surface force [78].

DF-IBM is usually applied to the moving body cases, because of its simple implementation. In order to explain the concept of DF-IBM, the incompressible Navier-Stokes equation is used in the following form,

$$\frac{\partial \mathbf{u}}{\partial t} + \nabla(\mathbf{u}\mathbf{u}) = -\frac{\nabla p}{\rho} + \frac{\mu}{\rho} \nabla^2 \mathbf{u} + \mathbf{f}_b, \quad (3.51)$$

or,

$$\frac{\partial \mathbf{u}}{\partial t} = \text{RHS} + \mathbf{f}_b. \quad (3.52)$$

This equation is numerically integrated as,

$$\frac{\mathbf{u}^{n+1} - \mathbf{u}^n}{\Delta t} = \text{RHS}^{n+1/2} + \mathbf{f}_b^{n+1/2}, \quad (3.53)$$

where, RHS contains convective, viscous, and the pressure gradient terms. Assuming the body moves with velocity \mathbf{U}_d (desired velocity), the force $\mathbf{f}_b^{n+1/2}$ must fulfill no-slip condition,

$$\mathbf{U}_d^{n+1} = \mathbf{u}^{n+1}. \quad (3.54)$$

Therefore, this force can be computed at the surface of the immersed body as,

$$\mathbf{f}_b^{n+1/2} = -\text{RHS}^{n+1/2} + \frac{\mathbf{U}_d^{n+1} - \mathbf{u}^n}{\Delta t}. \quad (3.55)$$

Computing this force at each time step is straightforward and leads to a low computational overhead. Note that the desired velocity \mathbf{U}_d depends on the geometry of the immersed body and its dynamics.

3.13 Multiphase Flows

Currently, three different multiphase flow scenarios of increasing complexity can be handled by DINO. Until now, the disperse phase involves only spherical particles, though working solutions for resolving spheroids and ellipsoids are available as well [81]:

1. Non-resolved solid particles (also called point particles), suitable to describe particles smaller than the Kolmogorov length scale, which cannot be resolved on the employed DNS grid, as depicted in Fig. 3.5(a).
2. Non-resolved droplets, possibly involving evaporation and chemical reactions. Here, mass and heat exchange between both phases are considered additionally, similar to the approach retained in [50]. Applied to describe the momentum exchange between flow and particles, the Lagrangian point-force approach considers Stokes model for the drag force [43, 44]. The droplet dynamics are determined by knowing its location and velocity:

$$\frac{d\mathbf{X}_k}{dt} = \mathbf{V}_k, \quad (3.56)$$

$$\frac{d\mathbf{V}_k}{dt} = \frac{\mathbf{U}_\infty - \mathbf{V}_k}{\tau_{v,k}}, \quad (3.57)$$

$$\tau_{v,k} = \frac{\rho_L a_k^2}{18\mu_f \left(1 + \frac{1}{6}\text{Re}_k^{2/3}\right)}. \quad (3.58)$$

In Eqs. (3.57) – (3.58), \mathbf{V}_k and \mathbf{U}_∞ are the velocity of the k -th droplet and of the surrounding gas at droplet location. Also, \mathbf{X}_k , ρ_L , Re_k , a_k , μ_f , and $\tau_{v,k}$ are droplet

3.13. Multiphase Flows

position vector, density, Reynolds number, diameter, gas viscosity at the droplet position, and momentum relaxation time scale, respectively. Subscripts ∞ , f are standing for properties of gaseous mixture in the far-field and film regions, respectively.

The evaporation process is computed by using an infinite conduction model inside the droplet and a variable Spalding mass transfer number, $B_{m,k}$ and heat transfer number, $B_{T,k}$ as discussed in Sec. 2.8.2. The equations reviewed in Sec. 2.8.2 are given in form of mass and energy. For coding purpose, it is easier to rewrite them with replacing mass and energy by diameter and temperature, respectively, as follows:

$$m_k = \rho_L \frac{\pi a_k^2}{4}, \quad (3.59)$$

$$\frac{da_k^2}{dt} = -\frac{a_k^2}{\tau_{a,k}}, \quad (3.60)$$

$$\frac{dT_k}{dt} = \frac{1}{\tau_{t,k}} \left[T_\infty - T_k - \frac{B_{T,k} L_{v,s}}{W_F C_{p,f}^F} \left(\frac{T_{cr} - T_k}{T_{cr} - T_{ref}} \right)^{0.38} \right]. \quad (3.61)$$

Mass and heat transfer of the droplet are characterized by two characteristic time scales: evaporation delay ($\tau_{a,k}$) and heating delay ($\tau_{t,k}$),

$$\tau_{a,k} = \frac{Sc_k \rho_L a_k^2}{4Sh_k \mu_f} \frac{1}{\ln(1 + B_{m,k})}, \quad (3.62)$$

$$\tau_{t,k} = \frac{Pr_k C_{p,L} \rho_L a_k^2}{6Nu_k C_{p,f}} \frac{B_{T,k}}{\mu_f \ln(1 + B_{T,k})}. \quad (3.63)$$

In this set of equations, T_k , T_{ref} , T_{cr} , and T_∞ , are the temperature of droplet k , reference temperature, critical temperature, gas temperature in far-field, respectively. Also, Pr , $C_{p,L}$, $C_{p,f}^F$, $C_{p,f}$, Nu , Sc , Sh_c , L_v , W_F and W_O are Prandtl number, specific heat of the liquid droplet, specific heat of the fuel vapor, specific heat of the gas mixture, Nusselt number, Schmidt number, Sherwood number, latent heat of evaporation, molecular weight of fuel and oxidizer, respectively. Definitions and expressions for these dimensionless numbers can be found in Sec. 2.8.2.

3. Fully resolved, moving solid particles. At the difference of the previous approaches, when considering spherical particles noticeably larger than the Kolmogorov length scale, the external surface of the particles can and should be resolved (Fig. 3.5(b)). For this purpose, the DF-IBM described in Sec. 3.12.2 has been employed. Three different collision models are included to describe particle-particle and particle-wall interactions: hard sphere model, lubrication force model, and repulsive force model. These model can be employed as stand alone or in combination, as illustrated in Fig. 3.6.

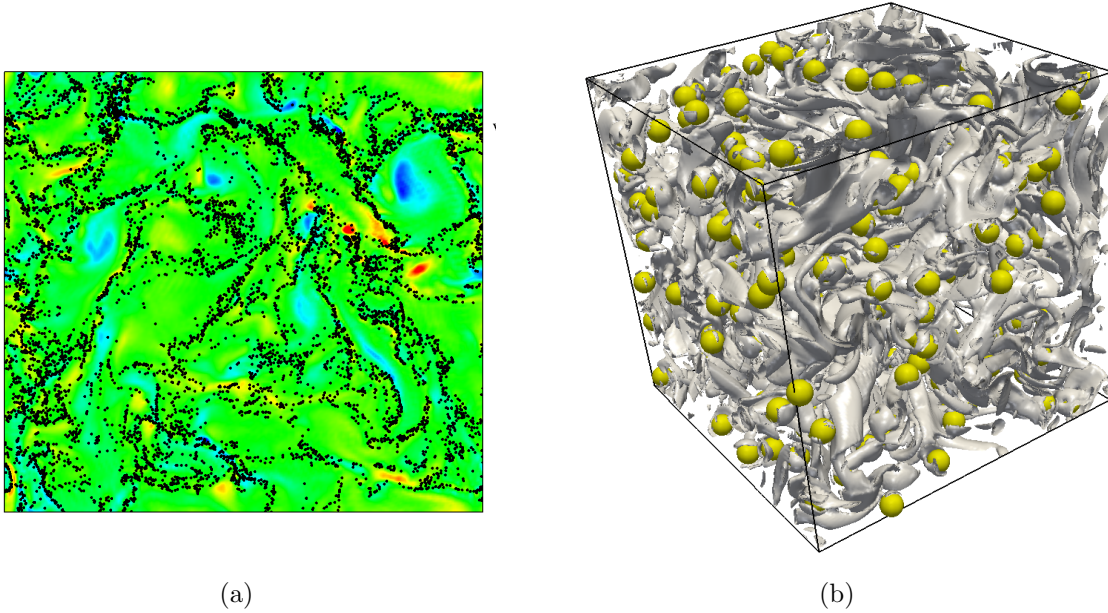


Figure 3.5: Particles in initially homogeneous isotropic turbulence (HIT). (a) Non-resolved spherical particles (ratio diameter/Kolmogorov length scale of 0.1), the color field shows vorticity. (b) Fully resolved solid spherical particles (ratio diameter/Kolmogorov length scale of 20.6), the iso-surface shows the enstrophy of turbulence.

3.14 Code Performance and Verification

3.14.1 Parallel Efficiency

After profiling and optimizing single-processor performance, parallel efficiency has been tested on a variety of machines in order to check portability. In the interest of space, only results obtained with SuperMUC at Leibniz Supercomputing Center in Munich will be discussed. Figure 3.7 shows the strong scalability performance obtained with DINO. This test corresponds to the DNS of a turbulent hydrogen/air flame using a detailed reaction scheme. For this test, the number of processors was varied from 1 024 to 16 384. The obtained parallel efficiency still reaches 85% with 8 192 cores, which is considered as an excellent result for a low-Mach solver. The considerably lower performance with 16 384 cores (74%) is due to the fact that, for this number of cores, two separate islands have to be combined on SuperMUC, leading to large communication overheads.

DINO thus shows a very good parallel efficiency, ensuring efficient computations for up to $O(10^4)$ cores, which is a very satisfactory result for a low-Mach solver, since global operations associated to the Poisson equation severely constrain the parallel performance.

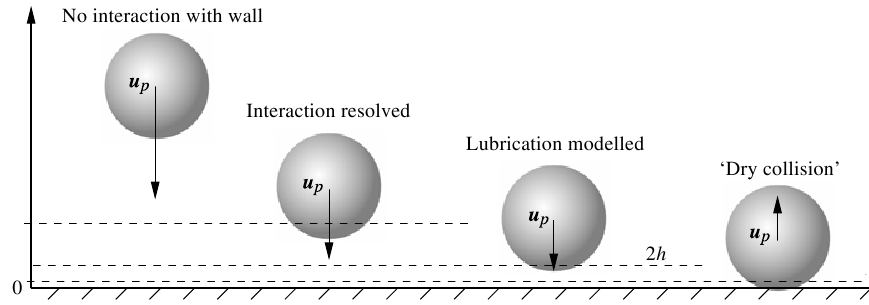


Figure 3.6: Schematic diagram showing the collision mechanism and model ranges [82].

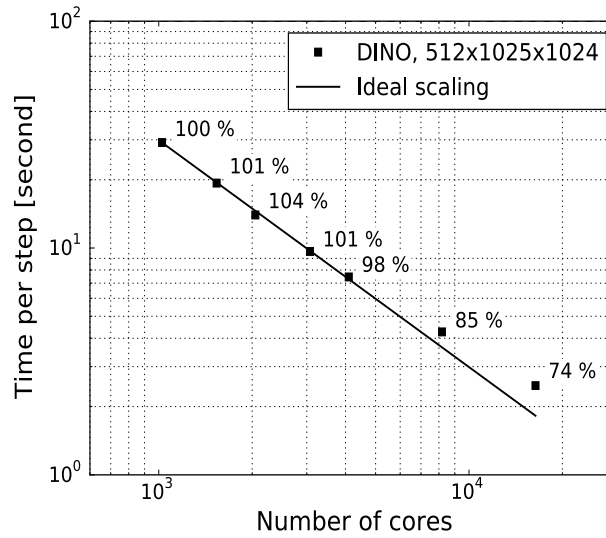


Figure 3.7: Parallel efficiency (strong scaling) of DINO on SuperMUC.

3.14.2 Accuracy and Order

Many benchmarks have been considered during the development of DINO. In the interest of space, it is impossible to document all the corresponding results. In the present section, the most important benchmarks will be discussed.

In order to quantify the accuracy of the solution, the L_2 and L_∞ error norms will be computed:

$$L_2 = \| u^d - U^{\text{ex}} \|_2 = \sqrt{\frac{1}{N} \sum_{n=1}^N |u_n^d - U_n^{\text{ex}}|^2}, \quad (3.64)$$

$$L_\infty = \| u^d - U^{\text{ex}} \|_\infty = \max_{1 \leq n \leq N} |u_n^d - U_n^{\text{ex}}|, \quad (3.65)$$

where u^d and U^{ex} are the numerical and exact analytical solutions, respectively.

Spatial Order: 1D Burgers' Equation

One of the first standard benchmarks is the 1D non-linear Burgers' equation,

$$\frac{\partial u}{\partial t} + u \frac{\partial u}{\partial x} = \nu \frac{\partial^2 u}{\partial x^2}, \quad (3.66)$$

$$u(x, t = 1) = \frac{x}{1 + \exp\left(\frac{x^2 - 0.25}{4\nu}\right)}, \quad 0 < x < 1$$

$$u(x = 0, t) = u(x = 1, t) = 0, \quad t > 0$$

which has an analytical solution [83]:

$$U(x, t) = \frac{x/t}{1 + \exp[x^2/(4\nu t)]\sqrt{t/\exp[1/(8\nu)]}}. \quad (3.67)$$

Figure 3.8 (left) shows the comparison between the time-dependent solution obtained with DINO (black line with circles) and the analytical solution given by Eq. (3.67) (dashed red line) over a domain of one meter discretized with 1025 grid points, with a kinematic viscosity of $0.001 \text{ m}^2/\text{s}$, and a constant timestep of $5 \mu\text{s}$. An excellent agreement is observed.

Error norms below 10^{-9} are obtained when refining the grid. As seen from Fig. 3.8 (right), DINO is found to be, as expected, 6th order in space globally.

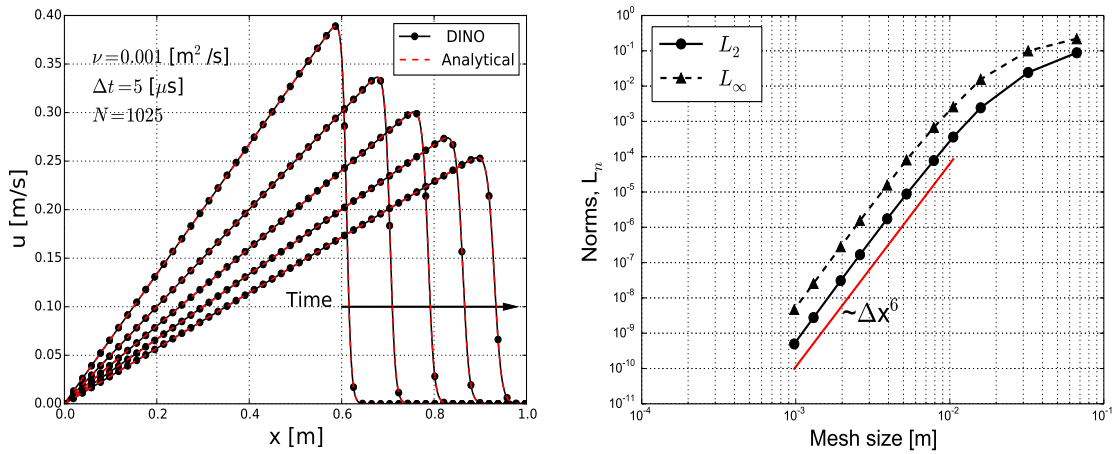


Figure 3.8: Verification and spatial order obtained by solving the one-dimensional Burgers' equation. Left: time-dependent solution for a case with $N = 1025$ grid points. Right: error norms and resulting spatial order of DINO.

Poisson Equation and Spatial Order: 2D Taylor-Green vortex (2D-TGV)

This benchmark considers the two-dimensional Taylor-Green vortex (2D-TGV). The 3D version of this problem will be discussed later for validation. The initial velocity and pressure fields are prescribed at $t = 0$ as follows:

$$\begin{aligned} u(x, y, 0) &= \sin(2\pi x/L) \cos(2\pi y/L), \\ v(x, y, 0) &= -\cos(2\pi x/L) \sin(2\pi y/L), \\ p(x, y, 0) &= \frac{\rho}{24} [\cos(4\pi x/L) + \cos(4\pi y/L)]. \end{aligned} \quad (3.68)$$

The analytical solution reads:

$$\begin{aligned} u(x, y, t) &= u(x, y, 0) \exp^{-8\pi^2 \nu t / L^2}, \\ v(x, y, t) &= v(x, y, 0) \exp^{-8\pi^2 \nu t / L^2}, \\ p(x, y, t) &= p(x, y, 0) \exp^{-16\pi^2 \nu t / L^2}. \end{aligned} \quad (3.69)$$

In the present case, the 2D-TGV is simulated in a periodic square domain with a side length of $L = 1.0$ m, with varying number of grid points (N) and kinematic viscosity (ν) but with a fixed time step ($\Delta t = 0.1$ ms). The error norm L_2 of the velocity field shown in Fig. 3.9 (left) demonstrates that DINO reaches 6th order in space for the solution of the Navier-Stokes equation in 2D as well. Concerning now the Poisson solver, the error norms of the pressure field have been computed based on the analytical solution. Figure 3.9 (right) shows indirectly that the order of convergence for the Poisson solver is much higher than 6th order. In fact, exponential convergence is achieved, as demonstrated in further tests. Due to the interaction between finite-difference and spectral solver in this particular test case (Eq. 3.27), the overall order shown in Fig. 3.9 (right) cannot be better than the 6th order of the finite-difference solution.

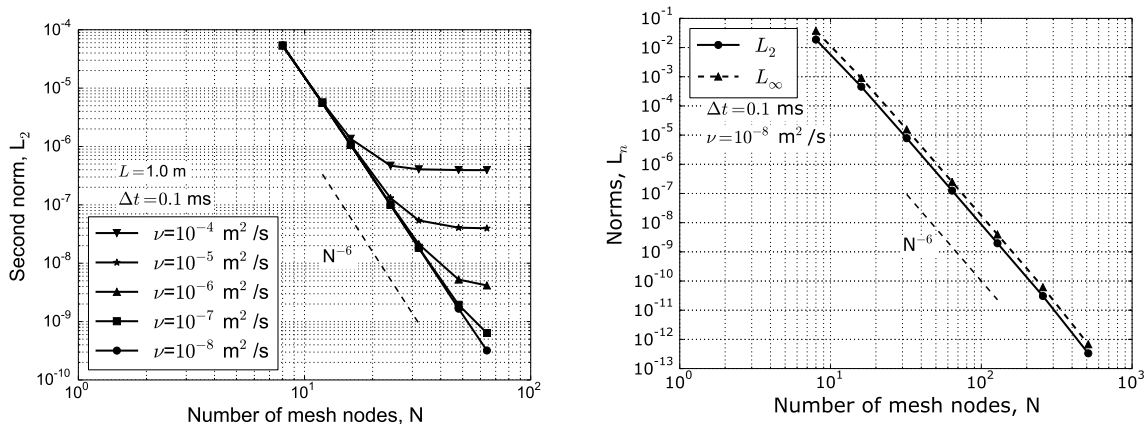


Figure 3.9: Verification and spatial order obtained by solving the 2D Taylor-Green vortex problem. Left: L_2 of velocity field. Right: L_∞ and L_2 of pressure field.

Temporal Order: Wave Equation

To check the temporal order of the time integration algorithm relying on the explicit Runge-Kutta scheme, a hyperbolic, one-dimensional wave equation was considered in a periodic DNS domain:

$$\frac{\partial u}{\partial t} = -c \frac{\partial u}{\partial x}, \quad (3.70)$$

$$u(x, t = 0) = \sin(2\pi x), \quad (3.71)$$

$$(3.72)$$

For this system, the analytical solution is known:

$$U(x, t) = \sin[2\pi(x - ct)]. \quad (3.73)$$

Figure 3.10 (left) shows the comparison between the solution obtained with DINO, u , and the analytical solution, U , at different time instants. The simulation employs 128 grid points, a fixed timestep ($\Delta t = 0.5$ ms), and a fixed wave speed of $c = 0.5$ m/s. In order to obtain the temporal order, both norms are again computed, this time with a fixed number of grid points but changing the timestep. Figure 3.10 (right) shows that the Runge-Kutta procedure delivers as expected an overall 4th-order approximation in time.

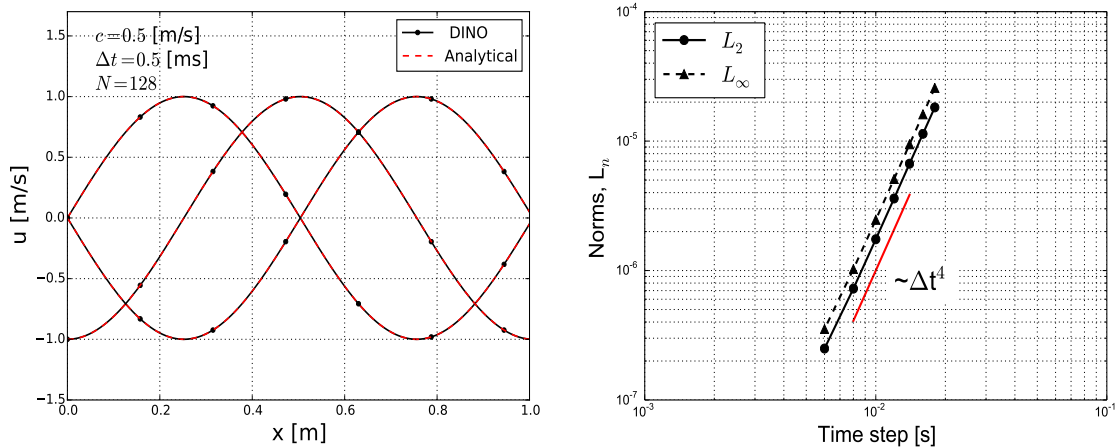


Figure 3.10: Verification and temporal order obtained by solving the one-dimensional wave equation. Left: time-dependent solution. Right: error norms and resulting temporal order of DINO.

3.15 Validation

3.15.1 Lid-Driven Cavity

After checking the proper implementation and accuracy of all major components of DINO, validation tests should involve the whole set of conservation equations for practically relevant cases. One of the most classical test cases for this purpose is the two-dimensional lid-driven cavity for an isothermal incompressible flow. Here, the DINO simulation is performed over a square domain of $L \times L = 1 \text{ m}^2$ discretized with 129×129 grid points. The upper wall velocity is $u_{\text{wall}} = 1.0 \text{ m/s}$, and flow kinematic viscosity $\nu = 10^{-3} \text{ m}^2/\text{s}$. The corresponding Reynolds number is $\text{Re} = u_{\text{wall}}L/\nu = 1000$. For this simulation the adaptive timestep is activated based on the condition $\text{CFL}_{\text{max}} = 0.5$. The results of DINO are compared both to the multigrid solution of Ghia *et al.* [84] as well as to the spectral solver of Botella and Peyret [85]. As can be seen from Fig. 3.11, the results obtained with DINO show an excellent agreement both for the horizontal (u) and vertical velocity (v), respectively.

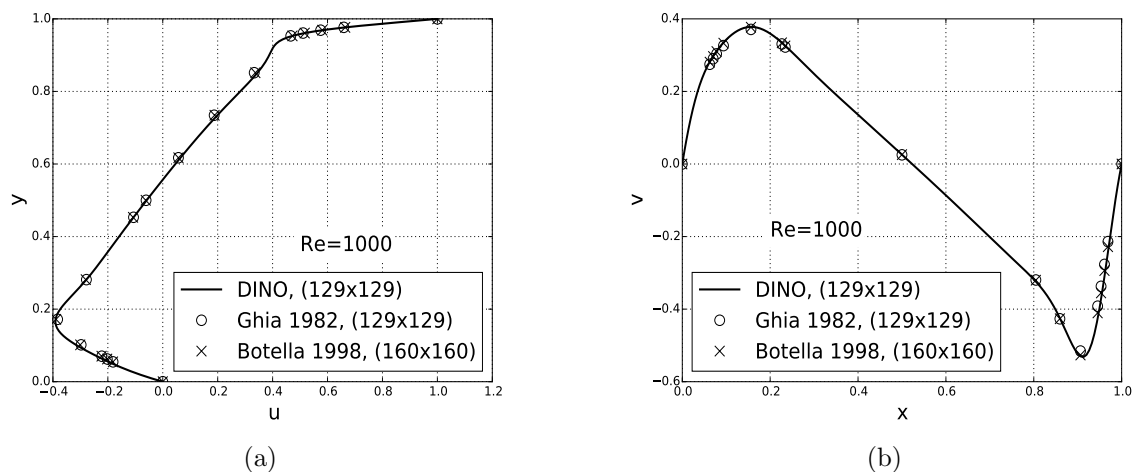


Figure 3.11: Steady-state solution for the two-dimensional lid-driven cavity at $\text{Re} = 1000$. (a) horizontal velocity along the vertical centerline of the cavity. (b) vertical velocity along the horizontal centerline of the cavity.

3.15.2 Homogeneous Isotropic Turbulence (HIT)

For a DNS solver, describing properly turbulence properties is obviously essential. In order to check this feature, one fundamental test case is the decay of homogeneous isotropic turbulence. Validation is done here by comparing the turbulence statistics obtained by DINO with those obtained experimentally behind grid turbulence [86]. The normalized spectrum obtained with DINO for decaying HIT is compared directly with the spectrum from the experiment of Comte-Bellot and Corrsin (1971) at a Taylor Reynolds number of $\text{Re}_\lambda = 71.6$ and

$Re_\lambda = 65.1$. To initiate the simulation, the DNS is started with an analytically prescribed turbulence spectrum $E(\boldsymbol{\kappa})$ following von Kármán with Pao correction (VKP spectrum):

$$E(\boldsymbol{\kappa}) = \frac{3u_e^5}{2\epsilon_e} \frac{[\boldsymbol{\kappa}/\kappa_e]^4}{[1 + (\boldsymbol{\kappa}/\kappa_e)^2]^{17/6}} \exp\left(-\frac{9}{4} \left[\frac{\boldsymbol{\kappa}}{\kappa_d}\right]^{4/3}\right), \quad (3.74)$$

where u_e , ϵ_e , κ_d and κ_e are the spectrum coefficients and $\boldsymbol{\kappa}$ is the wave number vector. Here, values of 0.21, 0.01, 0.08 and 0.018 have been chosen for the spectrum coefficients, respectively, in order to generate initial turbulence in a domain of size $10 \times 10 \times 10 \text{ cm}^3$. After a time $t = 11.2\tau_\eta$, a Taylor-based Reynolds number $Re_\lambda = 71.1$ is obtained and the turbulence properties are compared with the experimental data. Table 3.2 contains also Re_Λ , ϵ , u' , λ_t , Λ , τ_Λ , η_k , and τ_η , which correspond to Reynolds number based on integral length scale, dissipation rate of the kinetic energy, fluctuation velocity root mean square, Taylor length scale, integral length scale, large eddy turn-over time scale, Kolmogorov length scale, and Kolmogorov time scale, respectively.

Table 3.2: Turbulence properties at time $t = 11.2\tau_\eta$

N^3	Re_λ	Re_Λ	ϵ [m^2/s^3]	u' [m/s]	λ_t [mm]	Λ [mm]	τ_Λ [ms]	η_k [mm]	τ_η [ms]
512^3	71.1	336.8	42.52	0.92	3.86	18.3	81.4	0.23	1.1

Figure 3.12 shows the results for the Q-criterion isosurface (Fig. 3.12(a)), and the normalized energy spectrum of the simulation at time $t = 11.2\tau_\eta$ and of the experiments (Fig. 3.12(b)). The comparisons show that the DINO simulation agrees perfectly with the experimental results. It is important to keep in mind that, in this simulation, the ratio of $\eta_k/\Delta x$, where Δx denotes the grid spacing, is larger than unity and the product $\boldsymbol{\kappa}_{max}\eta_k$ is larger than 1.5 during the whole simulation, ensuring that all small flow structures are correctly captured (Sec. 1.5).

3.15.3 3D Taylor-Green Vortex (TGV)

The Taylor-Green vortex (TGV) is a canonical problem in fluid dynamics to study vortex dynamics, laminar to turbulent transition, turbulent decay and energy dissipation. Furthermore, it was retained as one of the central benchmarks in the International Workshops on High-Order CFD Methods [87]. The TGV problem involves different key physical processes found in turbulence and is therefore an excellent testcase for the evaluation of DNS codes. The problem consists of a cubic volume of fluid that contains a smooth initial distribution of vorticity, as shown in Fig. 3.13. As time advances the vortices roll-up, stretch and interact before breaking down. Eventually, viscosity will dissipate all the energy in the fluid and it will come to rest along a well-defined trajectory [88]. Here, results of DINO are compared with simulation results obtained with a pseudo-spectral code using 512^3 grid points [89]. These results are later denoted RLPK. The geometry is a periodic box of dimension of $0 \leq x, y, z \leq 2\pi$ [m], a value kept to facilitate post processing and comparisons with results

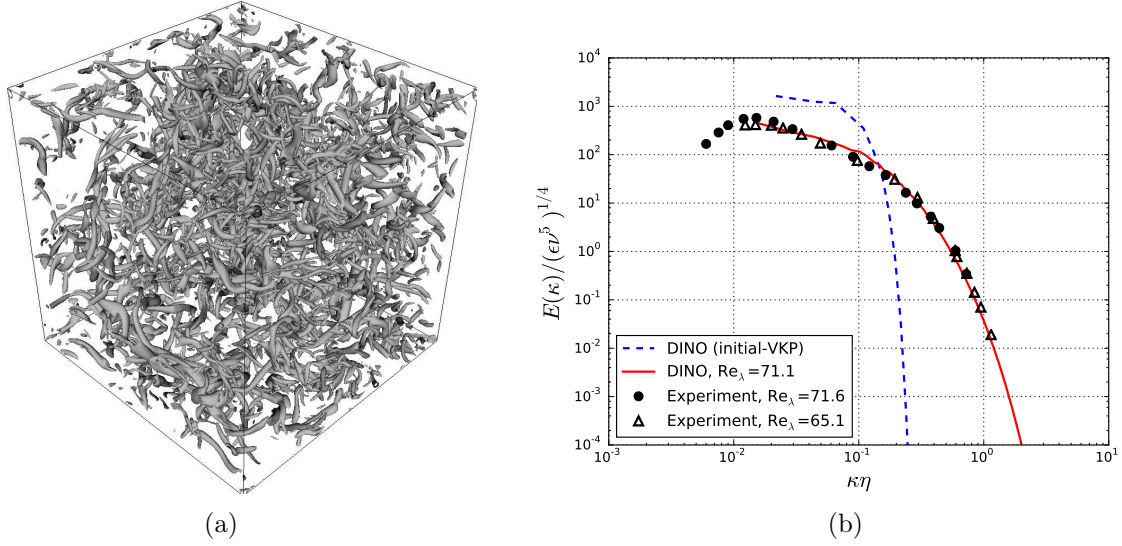


Figure 3.12: Homogeneous isotropic turbulence decaying in time. (a) Q-criterion isosurface (value of $6 \times 10^5 \text{ 1/s}^2$) at time $t = 11.2\tau_\eta$. (b) energy spectrum obtained by DINO compared with experimental results of [86].

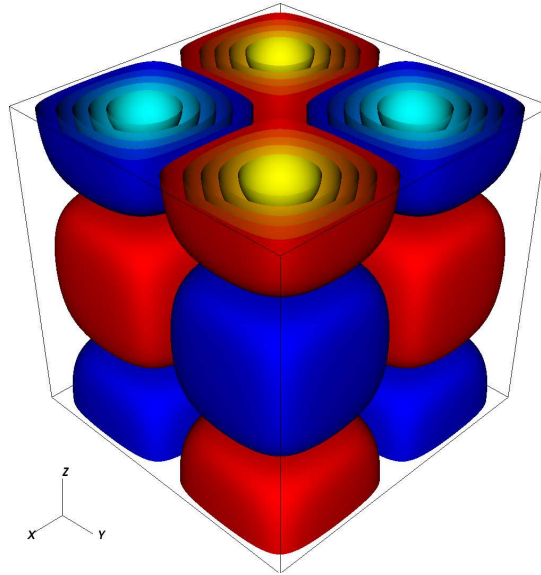


Figure 3.13: isosurface of z-vorticity of 3D-TGV at initial conditions.

from the literature. The initial conditions for TGV are given by the following:

$$u(x, y, z, 0) = u_0 \sin(x/L) \cos(y/L) \cos(z/L), \quad (3.75)$$

$$v(x, y, z, 0) = -u_0 \cos(x/L) \sin(y/L) \cos(z/L), \quad (3.76)$$

$$w(x, y, z, 0) = 0, \quad (3.77)$$

where $u_0 = 1$ m/s and $L = 1$ m are reference velocity and length, respectively. The flow is computed at a Reynolds number ($\text{Re} = u_0 L / \nu$) of 1600. Using 384^3 or 512^3 grid points, the simulation is performed for a duration of $20T_c$, where $T_c = L/u_0$ is the characteristic convective time scale. By solving the Poisson equation, the initial pressure field is obtained. The time evolution of isosurfaces of z -vorticity at different times when using 512^3 grid points is illustrated in Fig. 3.14. Starting from Fig. 3.14(a), the vortices start to roll-up. Then, a breakdown of the coherent structures occurs (Fig. 3.14(b)). Figure 3.14(c) shows the onset of turbulence before decay due to dissipation (Fig. 3.14(d)).

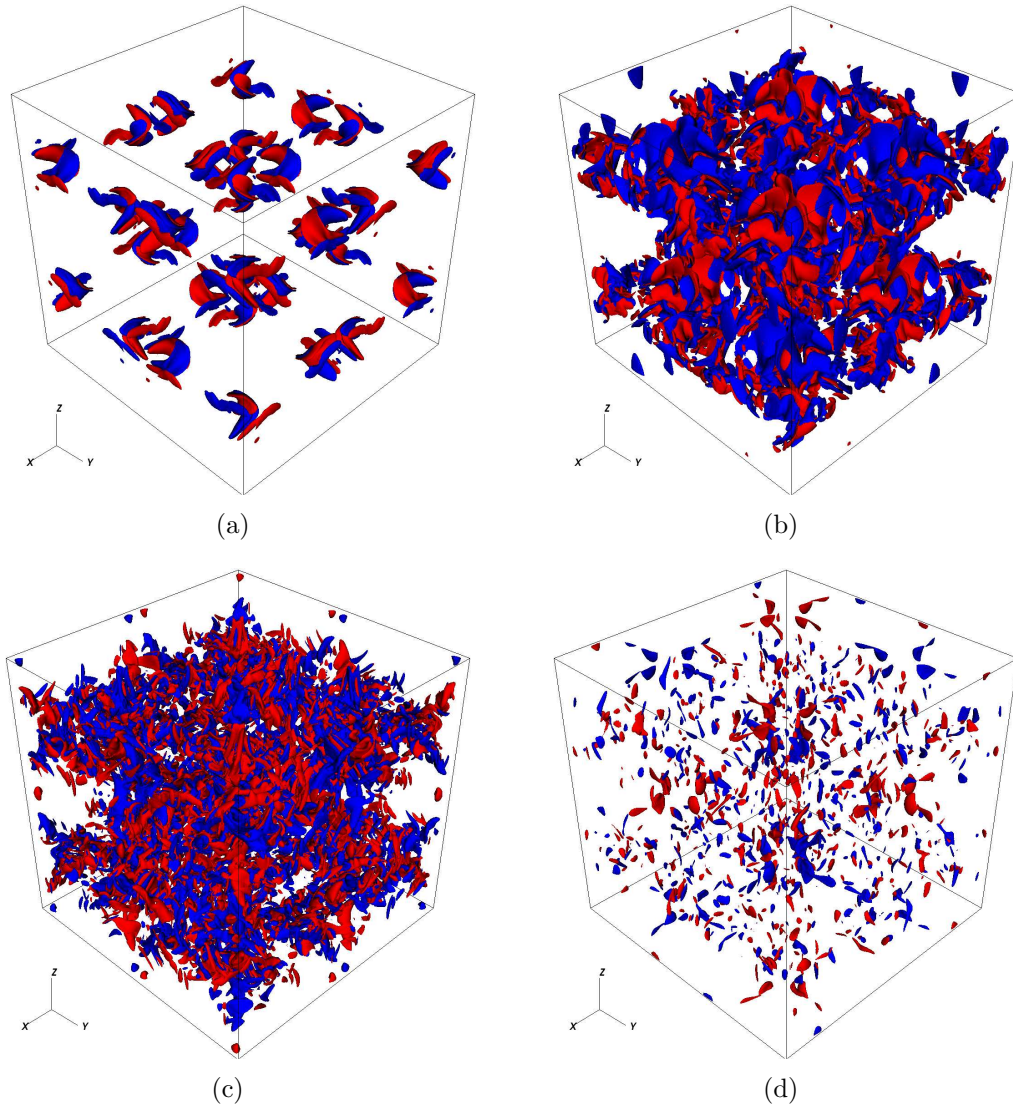


Figure 3.14: Time evolution of isosurfaces of z -vorticity for 3D-TGV using 512^3 grid points at times: (a) $t/T_c = 5.46$ (vortex roll-up), (b) $t/T_c = 8.0$ (coherent structure breakdown), (c) $t/T_c = 12.11$ (turbulence), (d) $t/T_c = 18.55$ (decay), respectively.

3.15. Validation

Figure 3.15 presents the comparison of the DINO results with that of the pseudo-spectral code (RLPK [89]). On the left, the time evolution of kinetic energy

$$KE(t) = \frac{1}{2} \langle u_i u_i \rangle, \quad (3.78)$$

normalized by its initial value is presented, while on the right the evolution of the dissipation rate ϵ (normalized by its maximum value) is shown. For this, ϵ is computed directly from the strain rate tensor, S_{ij} :

$$\epsilon(t) = 2\nu \langle S_{ij} S_{ij} \rangle, \quad (3.79)$$

where $\langle \cdot \rangle$ in Eqs. (3.78) and (3.79) denotes a spatial average. The comparison between DINO and RLPK results shows an excellent agreement. This benchmark proves again the ability of DINO not only to simulate turbulent flows but also transition and dissipation processes.

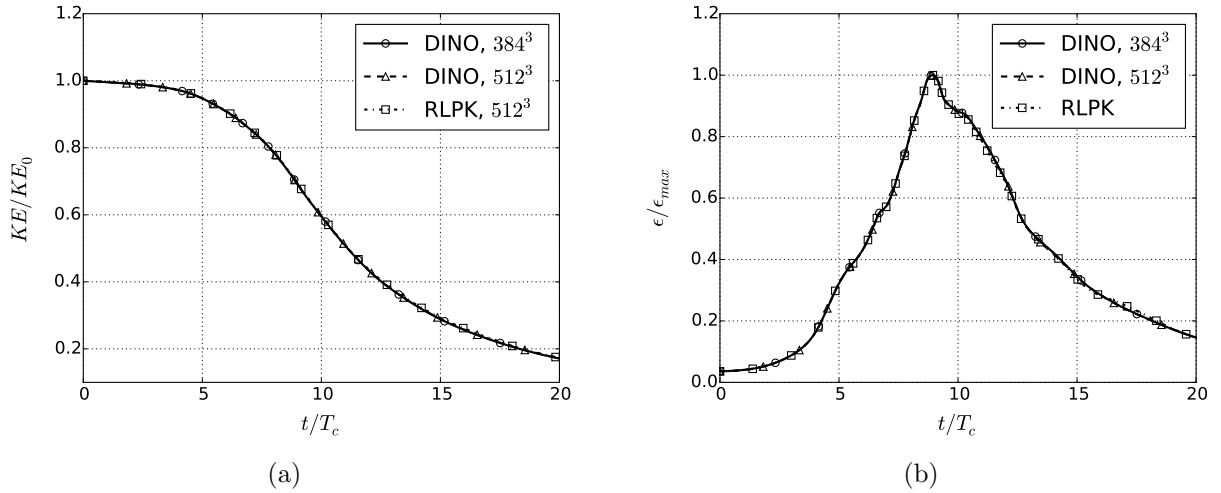


Figure 3.15: Temporal evolution of (a) normalized kinetic energy, and (b) its dissipation rate.

3.15.4 Turbulent Channel Flow

Since resulting features are non-homogeneous and non-isotropic, DNS of a wall-bounded turbulent channel is far more complicated than HIT, but also more interesting for practical purposes. Considering that DINO will ultimately be used to investigate multiphase reacting flows, and keeping in mind that any injection channel and most combustion systems involve walls, it is absolutely necessary to obtain a correct description of such configurations. Near-wall turbulent structures are typically much smaller than in the center of the channel. Hence, using a refined grid near the wall is helpful. As already mentioned in Sec. 3.11, this feature is implemented in DINO, and has been activated for the present test case. In order to check

Table 3.3: Parameters of the turbulent channel flow. Note that the mesh sizes Δx^+ , Δy^+ , Δz^+ are in wall units, and that Δy^+ represents the grid size at the center, the grid being refined close to the walls.

Data	Re_τ	δ	L_x	L_z	N_x	N_y	N_z	Δx^+	Δy^+	Δz^+
DINO	175	0.125 [m]	8δ	4δ	256	193	128	5.4	2.0	5.4
MKM	178	1.00 [-]	$4\pi\delta$	$4\pi\delta$	128	129	128	17.7	4.4	5.9
VK	180	1.00 [-]	$4\pi\delta$	$4\pi\delta$	384	193	192	5.9	2.9	3.9

the accuracy of DINO when employing the developed spectral solver described in Sec. 3.9 on a non-uniform grid, the results obtained for a turbulent channel flow with a friction Reynolds number $Re_\tau \approx 180$ are compared with published DNS databases [90, 91]. These databases were generated with two different spectral codes. Simulation dimensions and parameters considered for DINO and for the databases are summarized in Table 3.3. The current simulation is initiated by using a semi-empirical profile for the turbulent channel flow and adding divergence-free turbulent fluctuations on top of that profile. These initial fluctuations are again generated by IFFT using a VKP spectrum as described in Section 3.10. Compared to initialization with a random noise, preliminary tests have confirmed that this leads to a much faster convergence toward statistically-steady results. The boundary conditions are chosen to be periodic in streamwise and spanwise flow direction, using a uniform grid along both. Along the third direction, wall boundary conditions are used together with near-wall grid refinement. The smallest grid spacing near the wall is $\Delta y_{min}^+ = 1.4$. Turbulence statistics start being collected after reaching statistically steady-state. The mean streamwise velocity in the (dimensional) DINO simulation is 0.83 m/s. Figure 3.16 shows the comparison between DINO, Moser et al. (MKM) and Vreman and Kuerten (VK) concerning mean velocity profile (u^+ , Fig. 3.16(a)), as well as velocity fluctuations and correlations (Fig. 3.16(b)). An excellent agreement is observed, showing that DINO is able to correctly describe turbulence with the spectral Poisson solver, even for wall-bounded flows and using non-uniform grids.

3.15.5 IBM Validation: flow past a circular cylinder

In order to validate the implemented IBM approach, the classical benchmark involving the flow past a circular cylinder has been revisited [92]. The circular cylinder has a diameter of $D_c = 25$ mm. In order to avoid blockage effects, the cylinder is located at $(16D_c, 20D_c)$ within a square domain with side length of $40D_c$. Two different Reynolds numbers ($Re = U_\infty D_c / \nu = 20$ and 40) have been considered by changing the free stream velocity U_∞ while keeping $\nu = 1 \times 10^{-4} \text{ m}^2/\text{s}$. A fine regular grid with 1025×1025 points has been used to discretize the domain. Figure 3.17 depicts the streamlines of the flow around the cylinder with Re equal to 20 (Fig. 3.17(a)) and 40 (Fig. 3.17(b)), using DB-IBM (note that both methods, DB-IBM and DF-IBM, deliver streamlines that cannot visually be distinguished). The drag coefficients obtained by these simulation have been compared with values from the literature in Table 3.4, showing an excellent agreement.

3.15. Validation

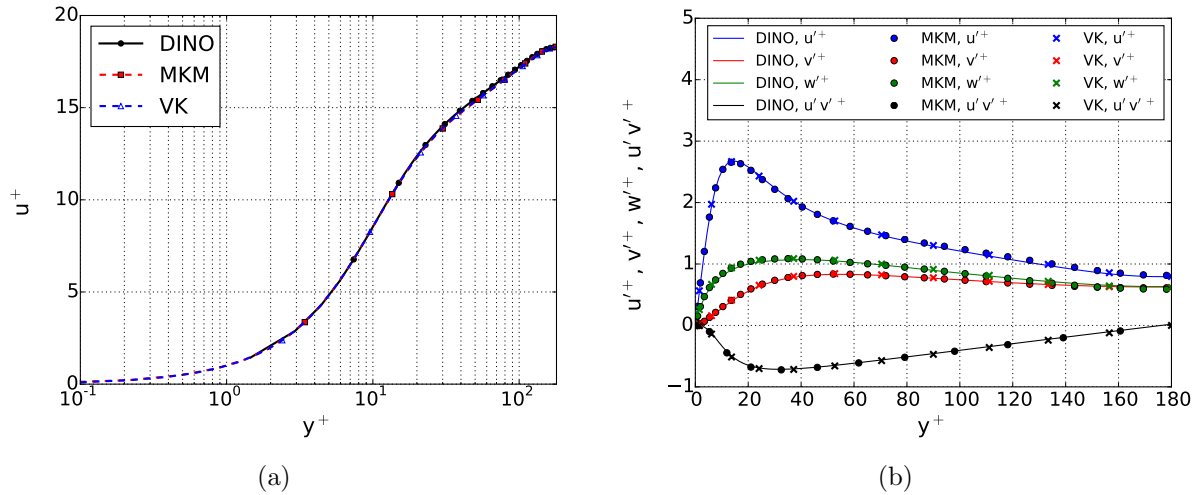


Figure 3.16: Comparison between DINO, Moser et al. (MKM) and Vreman and Kuerten (VK) concerning the turbulent channel flow at $Re_\tau \simeq 180$. (a) mean velocity. (b) velocity fluctuations and correlations.

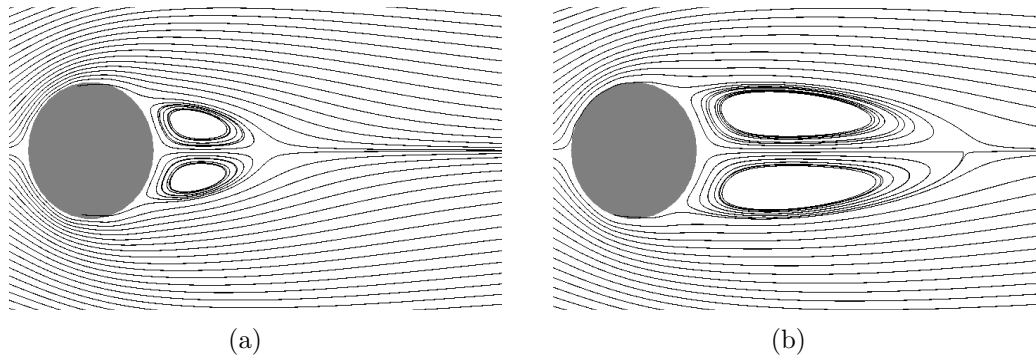


Figure 3.17: Streamlines of flow past a circular cylinder using DB-IBM at (a) $Re = 20$, and (b) $Re = 40$.

3.15.6 Chemistry and Transport

After successfully completing the validation of DINO for turbulent non-reacting incompressible flows, and keeping in mind that DINO shall be also used to investigate reacting configurations, it is necessary to check that all models employed to describe the properties needed for such cases (chemical kinetics, thermodynamic parameters and transport properties) are indeed working accurately. For this purpose, comparisons with experimental measurements will be carried out for configurations of growing complexity.

Table 3.4: Comparison of the drag coefficient C_d obtained by IBM in DINO with literature values.

Reference	Re=20	Re=40
Body-fitted grid [93]	2.045	1.522
Body-fitted grid [94]	2.111	1.574
IBM [92]	2.144	1.589
DINO, DF-IBM	2.140	1.597
DINO, DB-IBM	2.104	1.581

Ignition Delay

The first comparison allows one to check the correct implantation of the kinetic terms, showing that the coupling between DINO and Cantera 1.8 is working properly. Additionally, the efficiency of the time integration for stiff processes can be assessed. For this purpose, the ignition delay of a reacting mixture is computed in a zero-dimensional simulation, comparable to an experiment involving a homogeneous mixture. In such a case, all gradients appearing in the equations are zero, and the integration proceeds only in time, leading to very fast computations.

Since many different fuels are important for research and practical applications, two different combustibles have been considered here, both burning in air: 1) C_2H_4 (ethylene); 2) C_7H_{16} (n-heptane). Different reaction mechanisms are available as a database in the literature to describe oxidation of these fuels. Established mechanisms have been retained for this validation, as summarized in Table 3.5.

Table 3.5: Reaction mechanisms employed to compute ignition delays.

Mixture	Mechanism	Number of species	Number of reactions
C_2H_4 /Air	UCSD-2003 [95]	39	173
	UCSD-2005[95]	46	235
	Luo et al.[96]	32	206
C_7H_{16} /Air	Patel et al. [97]	29	52
	Liu et al. [98]	44	114

Figure 3.18(a) shows the results obtained with DINO concerning ignition delay for ethylene combustion, compared to a variety of published experimental data [99–101]. Please note that experimental results have been obtained under different conditions. Therefore, following a standard procedure in this case, the results of Fig. 3.18(a) have been scaled by the oxygen concentration in the mixture. A very good agreement is obtained, in particular with the most complex mechanism [95]. However, the computational time associated to the mechanism of [96] is considerably shorter, while an acceptable agreement is still observed.

Figure 3.18(b) shows the ignition delays obtained for n-heptane in air, compared to published experimental data [102]. Again, the most complex mechanism [98] leads to an excellent agreement with the experiments, while the noticeably smaller (and thus computationally faster) mechanism of [97] still leads to an acceptable prediction, at least qualitatively.

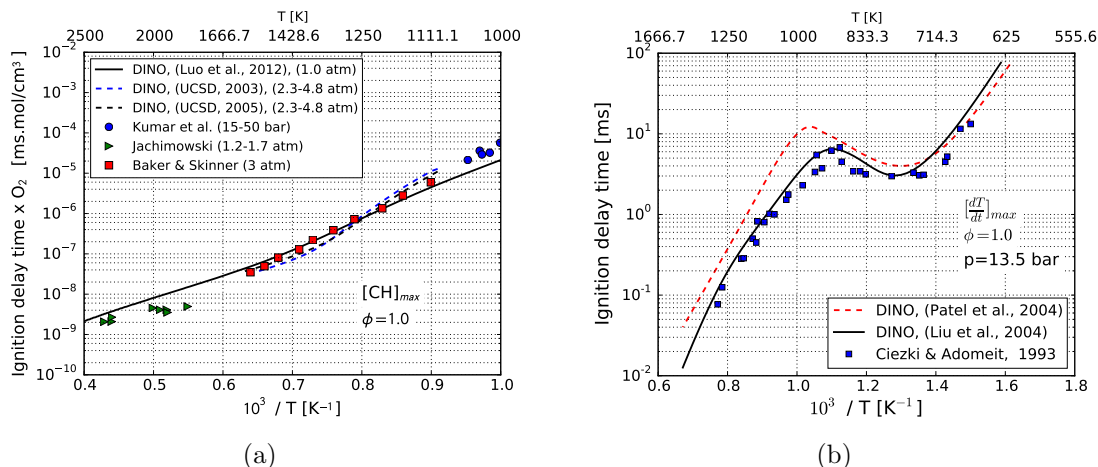


Figure 3.18: Ignition delay obtained with DINO compared with experimental results. (a) C_2H_4/Air . (b) C_7H_{16}/Air . Note that the data have been scaled by the oxygen concentration in the left figure.

All results in this section have been obtained by using the split, semi-implicit Runge-Kutta time integration relying on RADAU-5 (see Sec. 3.7). A fast but stable time integration has been obtained for all conditions.

Laminar Flame Speed

Together with the ignition delay previously discussed, the laminar flame speed S_L observed when burning a fully premixed system (also called in what follows fresh gas), leading to so-called burnt gas conditions, is considered as the key quantity to properly describe gaseous reacting flows. This property can be easily computed using dedicated routines like those implemented in Chemkin or Cantera. However, when using an unsteady solver like DINO, a proper computation of S_L must first be implemented.

Assuming that a quasi steady-state has been obtained with DINO, all time derivatives are zero ($\partial_t(\cdot) = 0$). Since the position of the flame is fixed within the computational domain under such conditions, and following [11], it can also be assumed that the momentum in the fresh gas mixture (subscript 1) and in the burnt mixture (subscript 2) are constant and equal to $(\rho_1 S_L)$, where S_L is the (at first unknown) laminar flame speed. Consequently, by integration of the species equation (Eq. (3.4)), the following equation is obtained to compute the laminar flame speed out of corresponding DNS simulations:

$$S_L = \frac{\int_1^2 \dot{\omega}_k dx - \rho V_k Y_{k1} + \rho V_k Y_{k2}}{\rho(Y_{k2} - Y_{k1})}. \quad (3.80)$$

This equation delivers one value for each species (index k). Following values are the average obtained when considering the obtained values of S_L for all reactants and products. In order to achieve steady-state conditions with DINO, an initially planar premixed flame

configuration is initiated in a one-dimensional domain, with a fresh gas mixture on one side and the corresponding burned gas composition (separately computed beforehand with Cantera 1.8) on the other side of the domain, first without any underlying velocity. Realistic flame profiles progressively develop, after starting the simulation. After a prescribed number of iterations, a first estimation of the flame speed is computed using Eq. (3.80). In order to stabilize the reaction front within the computational domain, the computed value is then prescribed in the simulation as fixed velocity inlet. This procedure is repeated iteratively until the updated flame speed computed using Eq. (3.80) remains constant within $\pm 5\%$. Using this approach, a quasi steady-state can be obtained, with a stable flame established at a fixed position within the one-dimensional domain.

Figure 3.19 shows the comparison of the numerically obtained flame speeds with experimental measurements for ethylene. The integration in time relies on the additive semi-implicit Runge-Kutta method (see Sec. 3.7). Different independent experimental results have been involved in the comparison [103–105]. Figure 3.19 shows that DINO reproduces with an excellent accuracy the laminar flame speed of ethylene flames when using as reaction mechanisms either UCSD-2005 or Luo *et al.* The third scheme (UCSD-2003) shows noticeable deviations and will not be considered further.

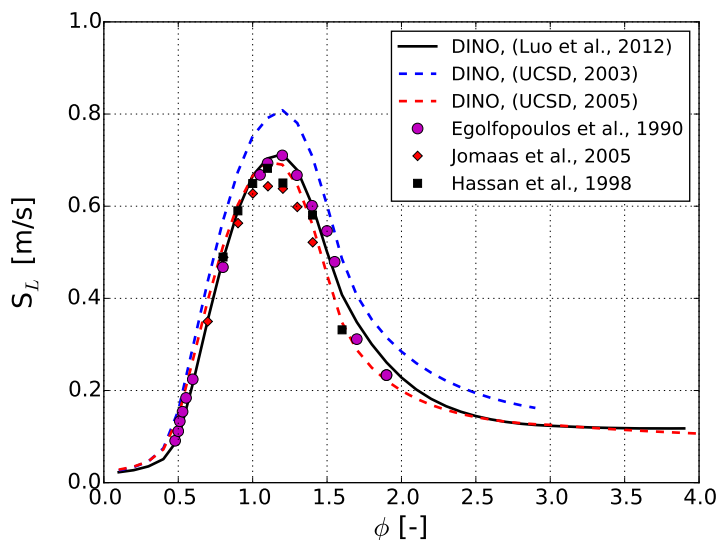


Figure 3.19: Comparison of numerically obtained laminar flame speeds with experimental measurements for ethylene/air flames.

Concluding Sec. 3.15.6, DINO coupled with Cantera 1.8 and Eglib 3.4 is able to represent accurately the key properties controlling combustion, even for complex fuels, provided corresponding reaction schemes are available in the scientific literature. Thanks to the implicit time-integration solvers, stiff systems can be treated in a stable but accurate manner. Until now, up to 53 species and up to 325 reactions (GRI-Mech 3.0 [106]) have been successfully considered in DINO, as will be discussed later.

3.16 First Application Examples

In this section, two gas-phase turbulent combustion applications will be discussed, before considering two-phase flows in the next chapter. Many researchers pay much attention to the jet configuration, because it allows them to investigate essential phenomena in turbulent combustion, such as turbulent mixing, transport, and flame-turbulence interaction. Additionally, it mimics many practical applications, such as engines, furnaces, gas turbines, etc. Here, two numerical configurations will be examined in terms of robustness and feasibility: (1) spatially-evolving jet; (2) temporally-evolving jet.

3.16.1 Spatially-Evolving Jet

In this test, the burned gases are injected into fresh (unburned) premixed gases at stoichiometric conditions. The direct application of this configuration is to examine safety and to assess the risk of the burning mixture escaping due to a failure/crack and thus entering into a fresh premixed gas region at a temperature of 300 K. Two mixtures are tested here: H_2/air and $\text{C}_2\text{H}_4/\text{air}$. Both of the mixtures are injected at the same conditions and injection temperature. The numerical settings are summarized as follows: The length of the numerical domain in the streamwise direction is 0.8 cm, in the spanwise direction 0.6 cm, and in the crosswise direction 0.2 cm. This domain is discretized over 25 million grid points while keeping a grid resolution of 15 μm in each direction. The fresh gases are injected with a jet speed of 170 m/s through a rectangular slot with a width of 0.28 mm and an injection temperature of 1300 K. Periodic boundary conditions are used in the span- and crosswise directions, whereas the streamwise direction has inflow and outflow boundary conditions. It was found that at these conditions, the H_2/air mixture is injected with a jet Reynolds number of 2500, whereas the $\text{C}_2\text{H}_4/\text{air}$ mixture is injected with a jet Reynolds number of 3360. Figures 3.20 and 3.21 show the time evolution of the iso-surfaces of heat release (red) and Q-criterion (gray), and the 2D-cut plane of the temperature contour for both cases. The ignition of the H_2/air mixture is observed: heat release and temperature increase. On the other hand, $\text{C}_2\text{H}_4/\text{air}$ mixture evolves without ignition. This is attributed to the fact that, at the same injection conditions, the $\text{C}_2\text{H}_4/\text{air}$ mixture was injected at higher Reynolds number, so that the mixing time scale is faster than the chemistry time scale. This leads to misfire. The situation is reversed for the H_2/air mixture. In addition to these two tests, many cases can be built by changing the controlling parameters (jet speed, injection temperature, jet width, mixture compositions, etc.) to generate a safety map for such configurations, which may help in risk prediction. This configuration also helps in investigating the turbulence mixing and transport. The simulation with $\text{C}_2\text{H}_4/\text{air}$ was conducted on SuperMUC using 2048 processors and consumed 74 000 CPU-hour.

3.16.2 Temporally-Evolving Jet

The spatially-evolving jet configuration is numerically expensive, especially with combustion. Alternatively, a temporally-evolving jet configuration is sometimes used [107–109]. In this configuration, a slab of pre-heated unburned premixed mixture is located in the center

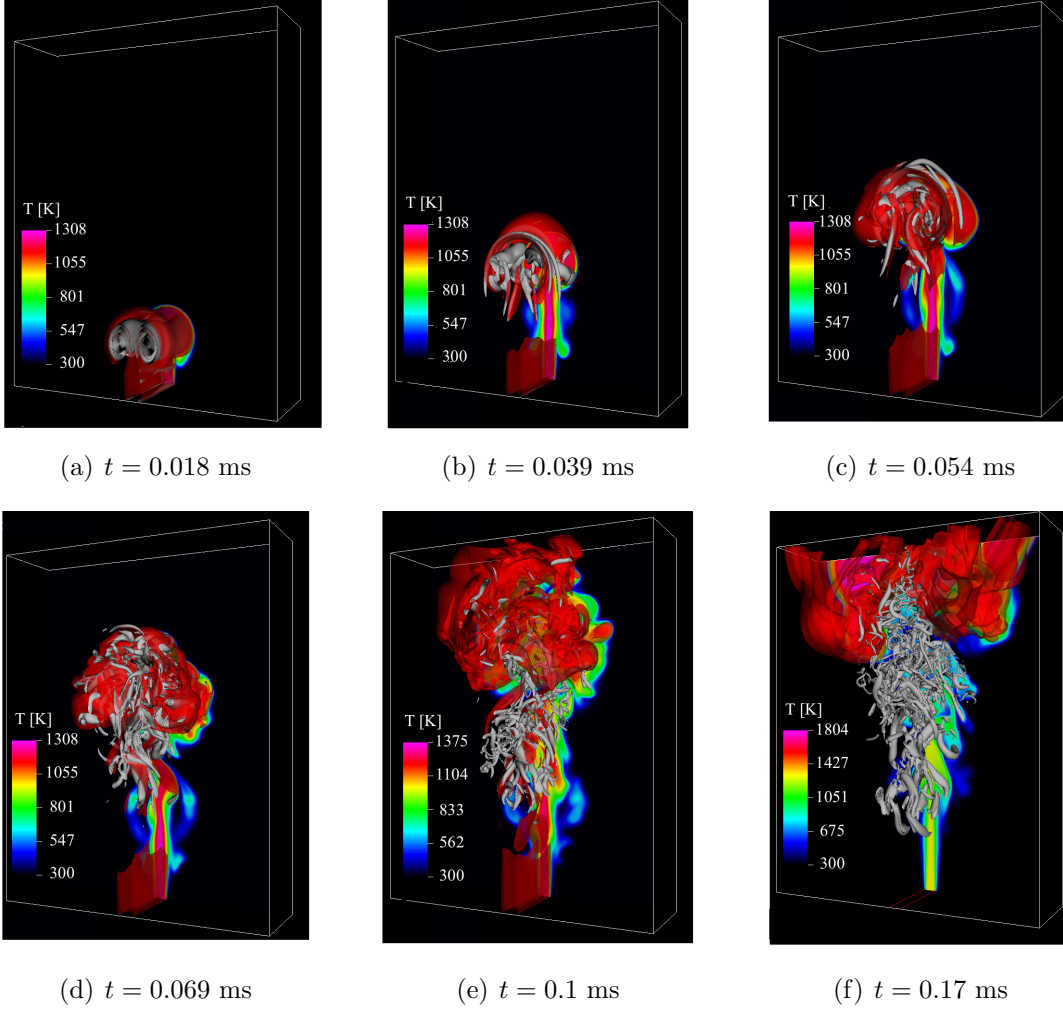


Figure 3.20: Time evolution of spatially-evolving jet of H_2/air mixture. Red and gray isosurfaces represent the heat release and Q -criterion, respectively. The color 2D-cut plane shows the mixture temperature.

(central jet zone) of the computational domain, whereas the left and right slabs (co-flow zones) contain the unburned premixed mixture at a temperature of 300 K. In the computational domain, the middle slab (central jet zone) moves with a jet speed U_j . The surrounding co-flow zone is quiescent. An isotropic turbulent flow field is generated prior to the DNS, and is employed to trigger the turbulence in the central jet zone using a hyperbolic tangent function to filter out the turbulence in the co-flow. In these simulations, the flow is considered periodic in the streamwise and span-wise directions, whereas it has outflow boundary conditions in the crosswise direction. In this section, autoignition of two H_2/air mixtures at stoichiometric conditions will be tested in the same domain and condition, but at different initial jet temperatures. The DNS is performed in domain with dimensions of L_x (streamwise direction) = 0.4 cm, L_y (crosswise direction) = 0.4 cm, and L_z (spanwise direction) = 0.2 cm. This domain is discretized over $n_x = 257$, $n_y = 256$, and $n_z = 128$ grid points, respectively.

3.16. First Application Examples

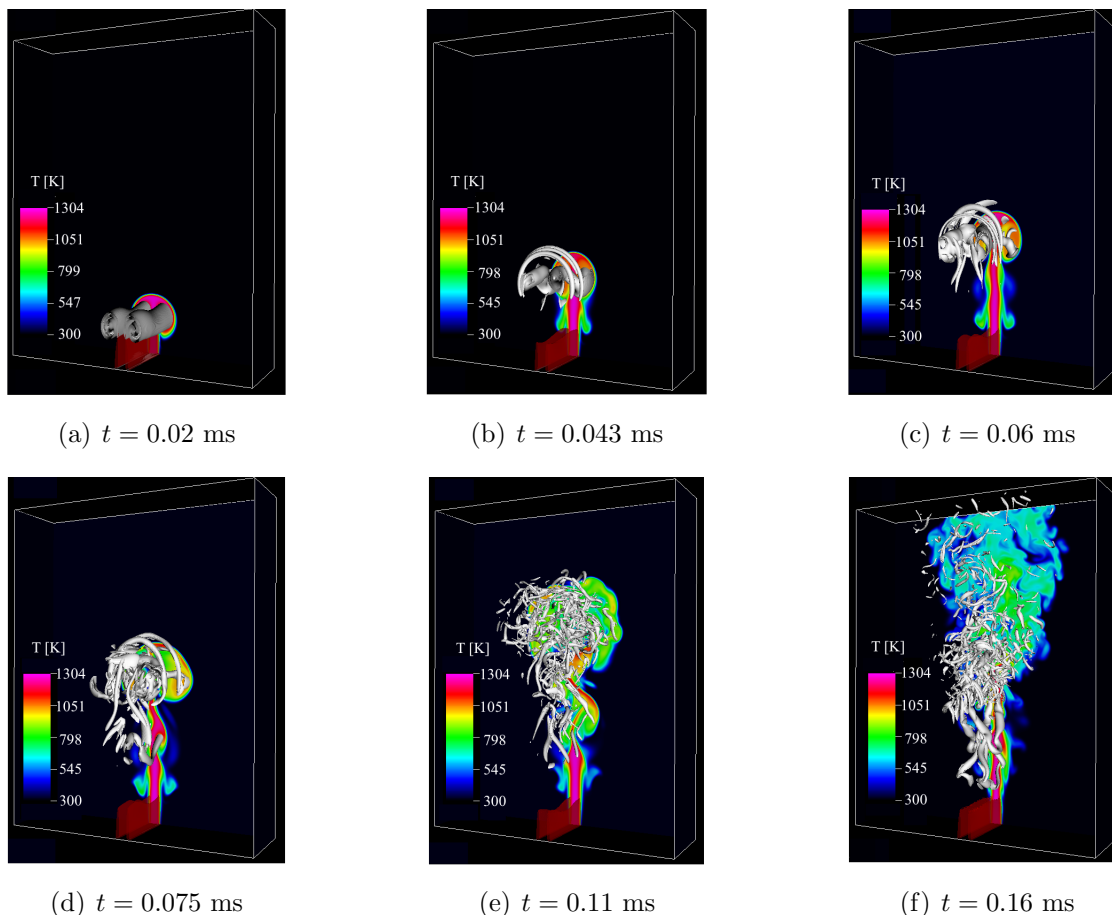


Figure 3.21: Time evolution of spatially-evolving jet of C_2H_4 /air mixture. Red and gray iso-surfaces represent the heat release and Q -criterion, respectively. The color 2D-cut plane shows the mixture temperature.

The middle slab which has a width of 0.04 cm moves with a jet speed of 185 m/s, leading to a jet Reynolds number of about 2500. The first mixture has an initial jet temperature of 1300 K (Fig 3.22), while the second case has an initial temperature of 1500 K (Fig 3.23). As seen in Fig 3.22, the temperature of the mixture decreases and no ignition occurs. This case is suitable to study quenching and turbulence mixing. On the other hand, when the initial temperature is 1500 K, the mixture has sufficient energy to ignite and burn. The temperature increases, as is shown in Fig. 3.23.

These two applications demonstrate DINO's ability to carry out interesting and challenging numerical configurations in a stable and robust manner, opening the door for future studies and simulations involving relatively high Reynolds number with feasible computational time.

It is now time considering the disperse phase, on the way towards spray combustion.

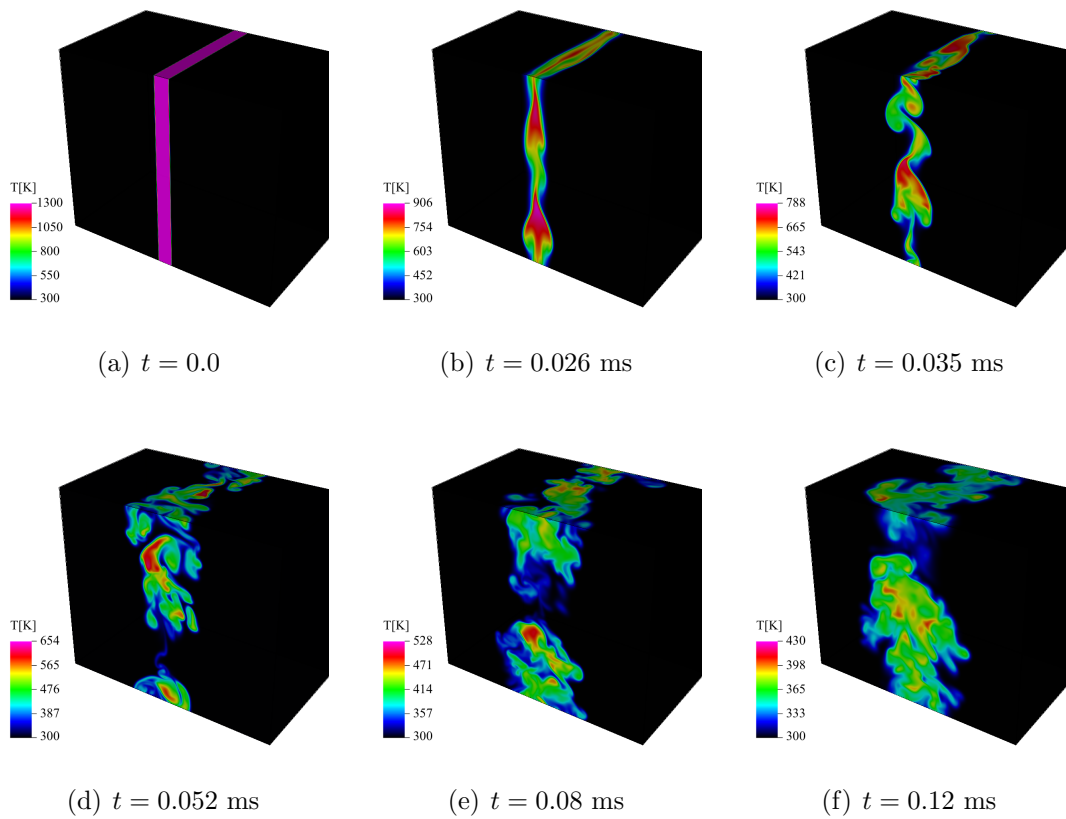


Figure 3.22: Time evolution of temperature of H_2 /air mixture for initial jet temperature of 1300 K.

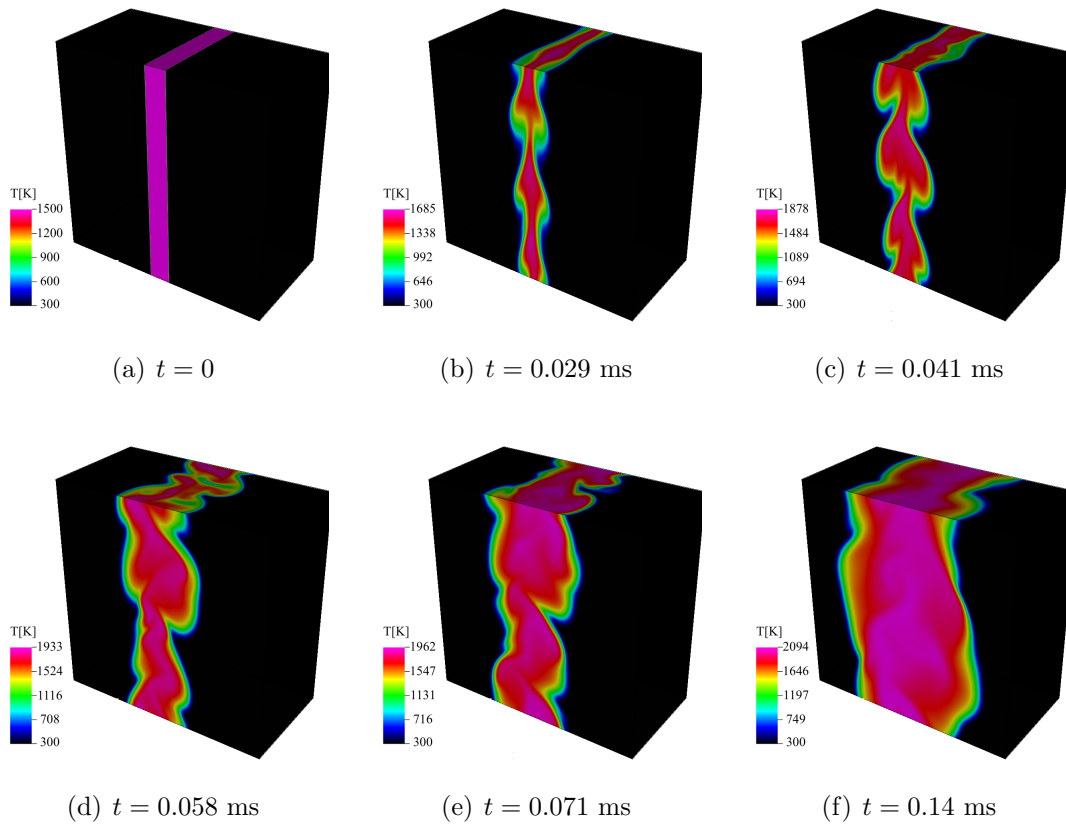


Figure 3.23: Time evolution of temperature of H_2 /air mixture for initial jet temperature of 1500 K.

Chapter 4

Spray and Droplets

4.1 Introduction

In this chapter, DNS of spray combustion are carried out for two purposes: (1) demonstrate the capability of DINO to perform such simulations; (2) answer some of the open questions in the area of spray combustion, as discussed in Sec. 1.4. Two geometries are again considered: (a) temporally-evolving jet, (b) spatially-evolving jet. These configurations are employed here to examine and determine the following: (1) optimal numerical settings, (2) implementation of detailed kinetic schemes and detailed spray properties, (3) impact of physical parameters on spray evaporation and combustion, (4) behavior and role of the scalar dissipation rate in turbulent mixing, (5) safety in terms of autoignition occurrence. Part of this chapter is based on an article published in the Proceedings of the Combustion Institute [110].

4.2 Validation Evaporation Model

The evaporation model introduced by Spalding (1953) [49] and corrected by Abramzon-Sirignano (1989) [47] is used here, as already discussed in Secs. 2.8.2 and 3.13. Before investigating the numerical results, a validation is performed. The most frequent validation benchmark is the evaporation of a single liquid spherical droplet in hot gas. Experimental [111] and numerical [39] results of this benchmark are available. Chauveau et al. (2008) [111] performed experimental measurements concerning the evaporation of a single n-heptane droplet. In their experiments, an n-heptane droplet with an initial diameter $a_{k,0} = 800 \mu\text{m}$, suspended by quartz fibers, evaporates in a quiescent N_2 atmosphere at different gas temperatures and under microgravity conditions. Sierra (2012) [39] used CERFACS' code (AVBP) to compute this case. She exposed a single n-heptane droplet, placed in the middle of a cubic domain, to hot gas. Here, this benchmark is revisited to validate the implemented evaporation model. In this simulation, a single n-heptane droplet with a diameter of $500 \mu\text{m}$ is placed in the center of a cubic periodic domain with a size of 10 cm^3 . This domain is discretized over 16^3 grid points to maintain a grid resolution larger than the droplet diameter (non-resolved approach, DPS). As in the experimental work [111], the domain is filled with

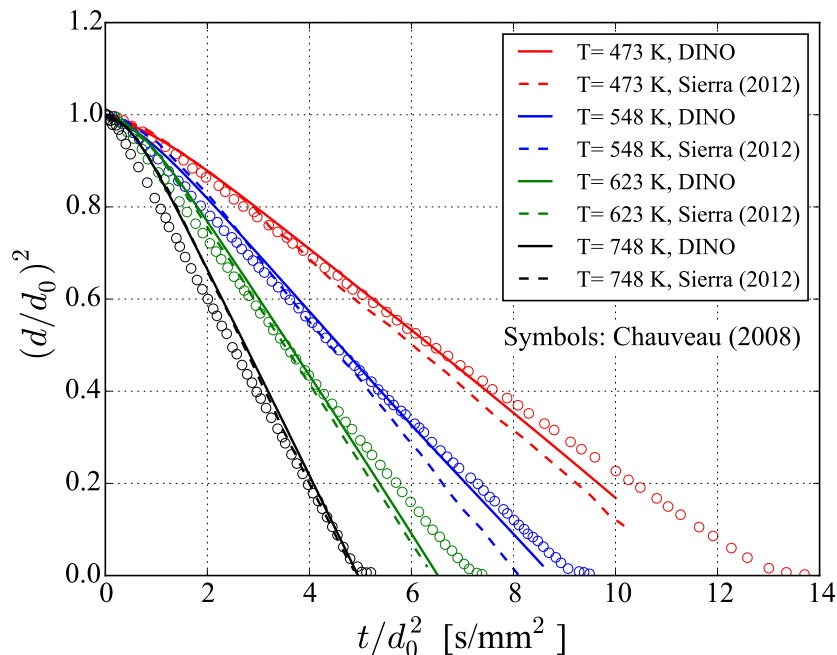


Figure 4.1: Time evolution of diameter of single n-heptane droplet: validation of the evaporation model. The symbols represent the experimental work of Chauveau et al. (2008) [111]; dashed lines represent the simulation result computed by Sierra (2012) [39]; the solid lines represent DINO simulations.

N_2 at atmospheric pressure and four different gas temperatures are tested: 473, 548, 623, and 748 K. In DINO simulations, the detailed kinetic mechanism developed by Patel et al. [112] is used (29 species and 52 elementary reactions); the droplet has an initial temperature of 300 K. Figure 4.1 shows the temporal evolution of the droplet diameter versus time. It compares the DINO results with both the experimental [111] and the numerical work [39]. It is obvious that DINO is closer to the experimental curves for all cases. This is attributed to the fact that Sierra computed the transport and thermodynamic properties from empirical relations implemented in AVBP, while DINO uses Cantera-1.8 directly.

This figure demonstrates that the evaporation model is implemented in the correct way and delivers results which are very close to those acquired by experiments. The small deviations may appear due to model assumption and simplifications, as discussed in Sec. 2.8.2, or due to measurement uncertainties.

4.3 Temporally-Evolving Jet

This part investigates spray evaporation and autoignition in a temporally-evolving jet. The impact of shear on evaporation and spray autoignition mechanisms is quantified by comparing droplets evolving in a high-speed jet flow or in a nearly quiescent environment. Comparisons are based on the topology of the reaction fronts, as characterized by the mixture fraction,

scalar dissipation rate, flame index, as well as fields of temperature and heat release. The impact of the local equivalence ratio and droplet diameter have been investigated by varying these two parameters.

4.3.1 Numerical Setups

Spray in a temporally-evolving jet is considered here, using a domain with dimensions of $L_x = 2.4$ mm, $L_y = 6.4$ mm, $L_z = 6.4$ mm, discretized over $96 \times 256 \times 256$ grid points for spanwise, transverse, and streamwise directions, respectively, keeping a fixed grid resolution of $25 \mu\text{m}$. The numerical setup is illustrated in Fig. 4.2. The domain is periodic in streamwise and spanwise directions while it has outflow boundary conditions in transverse direction. In Fig. 4.2 the black spheres represent schematically the monodispersed droplets that are randomly distributed in the central jet region, with a width H of 0.7 mm and a jet velocity U_j . The droplets always have an initial temperature $T_{k,0}$ of 300 K. These droplets are placed in a central slab of air with a uniform initial temperature $T_{\infty,0}$, and pressure $P_{\infty,0}$, of 1500 K and 5 bar, respectively. In Fig. 4.2, U_{co} represents the velocity of the gaseous coflow. Kinetic terms are computed by relying on Cantera 1.8 with a skeletal kinetic mechanism for n-heptane, which contains $N_s = 29$ species and 52 elementary reactions, as described in [112].

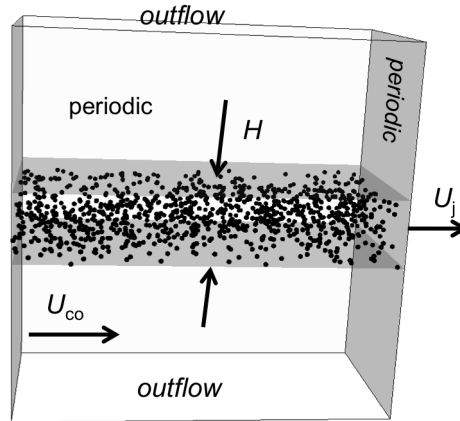


Figure 4.2: Numerical configuration.

In the current work, two different configurations are considered: 1) droplets in a fast temporal jet (Case A); 2) droplets in a nearly quiescent atmosphere (Case B). In Case A, the velocity of the gaseous jet is equal to the initial velocity of the droplets (always set to 100 m/s), while in Case B, the jet velocity equals the coflow velocity (5 m/s). Case B is directly inspired by the work of Wang and Rutland (2007) [27] who used 2D DNS to investigate the ignition of a jet spray in a similar flow. For Case A, the turbulence is triggered by initializing a homogeneous isotropic turbulent flow field, which has an integral length scale Λ of 0.2 mm and a fluctuation velocity u' of 0.4 m/s. The corresponding droplets' Stokes number based on the Kolmogorov time scale is 1.43. All turbulence length scales are well resolved in this simulation, keeping the ratio of Kolmogorov length scale, η_k , to grid resolution, Δx , larger

4.3. Temporally-Evolving Jet

than unity, with $\eta_k/\Delta x = 2.67$. This is sufficient to properly resolve all chemical species as well in this case. The turbulence signals are filtered using a top-hat filter, and are imposed only in the middle of the domain (central slab, containing the droplets). Following [27], no turbulence is initially added in Case B. For both cases, the ratio $a_k/\Delta x$ stays below 0.6, which is an acceptable value for DNS-DPS of spray combustion [27, 28, 31]. The simulation conditions for case A have been chosen to mimic combustion in ICE, except for the pressure, which is kept low, following again [27, 113].

4.3.2 Results and Discussion

Direct comparisons between Case A and Case B will be discussed first, with keeping the initial local equivalence ratio $\phi(t=0)$ of the mixture in the central jet zone equal to 2 and a droplet diameter of 10 μm . In the second part of this section, a parametric study will be performed for Case A by choosing different values for the local equivalence ratio ϕ (0.5, 1, 2), droplet diameter a (10, 13, 16 μm), and jet velocity U_j (25, 50, 75, 100 m/s).

Following [26], auto-ignition is defined as the time and location where the local maximum temperature rises by 400 K over the initial gas temperature. The autoignition delay time τ_g is found to be identical for Case A and Case B ($\tau_g = 0.165$ ms, for $\phi = 2$ and $a = 10$ μm); it is always noticeably shorter than the evaporation delay time, τ_a , equal to 0.27 ms in Case A and 0.29 ms in Case B. Consequently, only the results at $t \approx \tau_g$ will be discussed in details in what follows, together with a discussion concerning the temporal evolution of scalar dissipation rate. For the analysis, three key quantities will be computed. First, the elemental mixture fraction ζ_z (also called Bilger's mixture fraction [30, 114]) for a generic hydrocarbon fuel C_mH_n , with Fu denoting fuel and Ox the oxidizer:

$$\zeta_z = \frac{\beta - \beta_{\text{Ox}}}{\beta_{\text{Fu}} - \beta_{\text{Ox}}}, \quad (4.1)$$

$$\beta = \sum_{i=1}^{N_s} \left(\frac{a_{C,i}}{m} + \frac{a_{H,i}}{n} - \frac{a_{O,i}}{(m+n/4)} \right) \frac{Y_i}{W_i}, \quad (4.2)$$

where $a_{j,i}$ denotes the number of atoms of element j in species i . Second, the scalar dissipation rate, based on the thermal diffusion coefficient λ ,

$$\chi = 2\mathcal{D} (\nabla\zeta_z)^2 = \frac{2\lambda}{\rho C_p} (\nabla\zeta_z)^2. \quad (4.3)$$

Third, Takeno's flame index [115] in its normalized version [6],

$$\xi_p = \frac{1}{2} \left(1 + \frac{\nabla Y_{\text{Fu}}}{|\nabla Y_{\text{Fu}}|} \cdot \frac{\nabla Y_{\text{Ox}}}{|\nabla Y_{\text{Ox}}|} \right), \quad (4.4)$$

which is used to detect burning mode and flame topology, where ξ_p is 0 for a nonpremixed, and 1 for a premixed local combustion mode, respectively. Although interesting alternatives have been derived to compute the flame index when using complex kinetic schemes [116, 117],

the validity of the classical form of Takeno flame index (Eq. 4.4) for simulations involving detailed kinetics has been checked recently [118–120].

Evaporation-Ignition Scenarios

Even though Case A and Case B show the same autoignition delay time, the scenarios of evaporation and ignition clearly differ. Figure 4.3 shows an isosurface of temperature ($T = 1800$ K) and droplets (black spheres). In Case A (Fig. 4.3(a)), which has a very high shear in the gas flow near the jet boundaries, mixing is enhanced and the evaporating droplets start early to disperse along the side of the jet. The mixture fraction in the gas phase increases in two different zones: 1) the central jet area, where evaporation mainly occurs, leading to a decrease in temperature, due to evaporation (Zone I), (2) along the sides of the jet, due to convection and mixing (Zone II). A sample of Zone II is shown in Fig. 4.4(a). Due to an increasing mixture fraction in this region and local high temperatures, the ignition of the spray occurs in a pocket-like manner. These pockets are surrounded by evaporating droplets, which are the source for further fuel in the gaseous phase. Different flame types are observed around this region, as shown by Takeno’s flame index: lean premixed flames (solid thick gray lines, $\xi_p \simeq 1$), and nonpremixed flames (dashed thick gray lines, $\xi_p \simeq 0$), supporting findings of [17]. In Case B (Fig. 4.3(b)), even though evaporation starts in the absence of any turbulence, a weak wavy motion develops until time $t = \tau_g$ due to species diffusion and flame propagation in an inhomogeneous mixture. As seen in Fig. 4.4(b), the evaporation occurs only in the central jet region for Case B, as expected. Finally, ignition occurs at the jet boundaries, similar to observations from [17, 32]. Again, both premixed and nonpremixed flames are observed simultaneously. Later on (not shown), the burning zone propagates towards the jet core, where evaporation and fuel consumption first reach completion. This scenario should also be considered when developing or improving models to describe spray combustion in jet flows.

Statistics

The Probability Density Function (PDF) of ζ_z is depicted in Fig. 4.5. Here, $\zeta_{z,st}$ corresponds to the stoichiometric mixture fraction ($\zeta_{z,st} = 0.062$ for the n-heptane/air mixture). At the ignition time, $t = \tau_g$, the maximum values of ζ_z are around 0.17 in Case A and 0.25 in Case B, respectively. Compared to Case B, the lean mixture ($\zeta_z < \zeta_{z,st}$) is very predominant in Case A. The occurrence of stoichiometric conditions ($\zeta_z = \zeta_{z,st}$) is also more pronounced in Case A than in Case B, whereas Case B shows also very rich conditions.

Figures 4.6, 4.7, and 4.8 show scatter plots of temperature, heat release, and scalar dissipation rate versus mixture fraction, respectively. In all these figures, the scatter points are colored black to represent nonpremixed flames ($\xi_p \simeq 0$), and white to denote premixed flames ($\xi_p \simeq 1$), respectively. Figure 4.6 demonstrates that, in Case A (Fig. 4.6(a)) the ignition (high temperatures) occurs predominantly in the lean mixture region ($\zeta_z \leq \zeta_{z,st}$). Both burning modes, premixed and nonpremixed are observed on both sides of the stoichiometric conditions, confirming Fig. 4.4(a). However, almost no reaction takes place in the evaporation region (since $T_\infty < T_{\infty,init}$ at high values of ζ_z). In Case B, (Fig. 4.6(b)) ignition occurs

4.3. Temporally-Evolving Jet

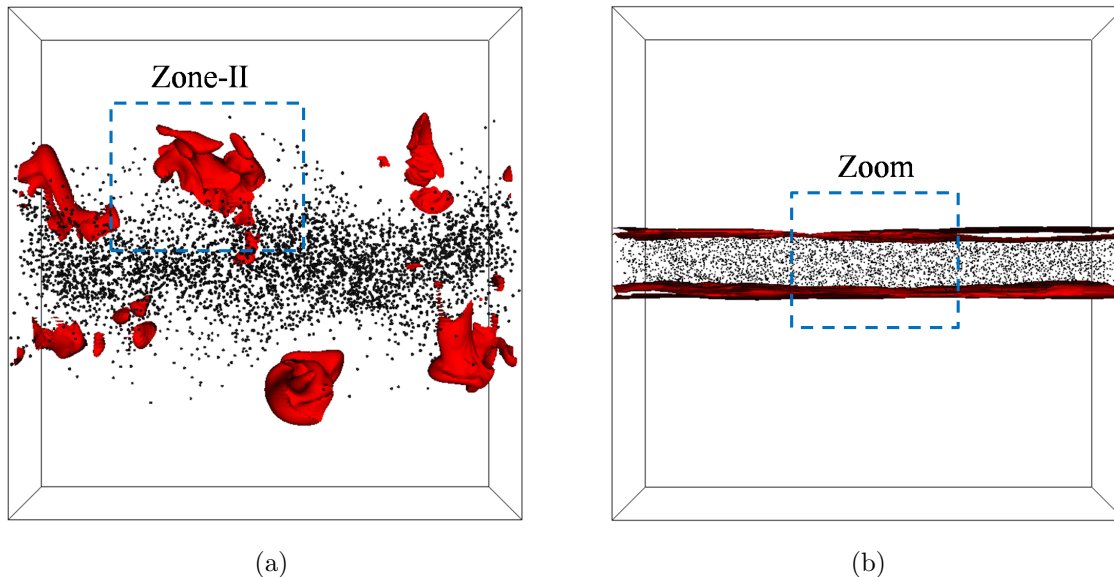


Figure 4.3: Isosurface of temperature ($T = 1800$ K) at time $t = \tau_g$ for both configurations: (a) Case A, (b) Case B. The spheres represent the droplets (size multiplied by factor 10 for visualization purpose). The windows enclosed within blue dashed lines are discussed in the next figure.

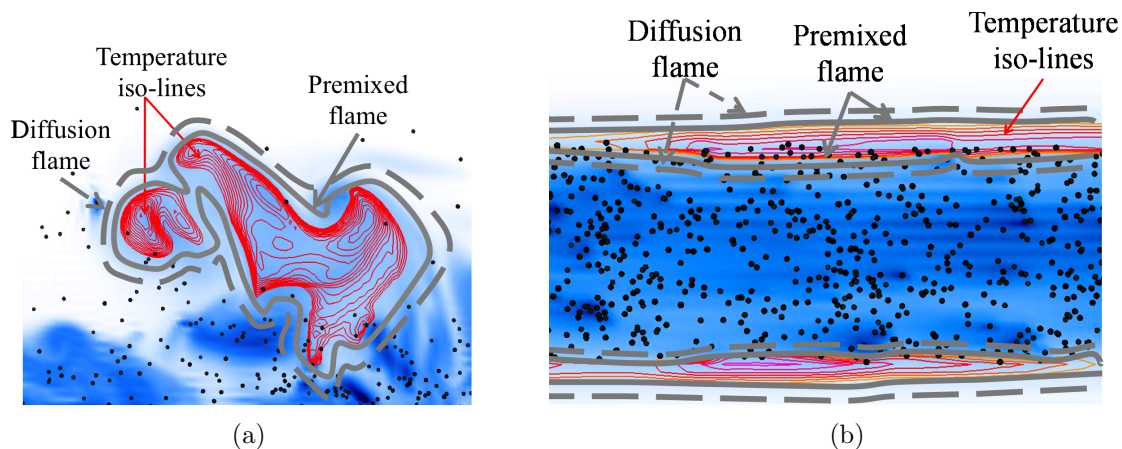


Figure 4.4: Two-dimensional cuts through Fig. 4.3 (blue dashed rectangles): (a) Case A, (b) Case B. The thin isolevels show the temperature with values between 1800 K and 2600 K at time $t = \tau_g$. The background represents the mixture fraction, increasing from white ($\zeta_z = 0$) to blue ($\zeta_z = 0.2$). Solid thick gray lines represent premixed flames ($\xi_p \simeq 1$), while dashed thick gray lines represent nonpremixed flames ($\xi_p \simeq 0$).

mostly for stoichiometric and slightly rich mixtures. Once again, premixed and nonpremixed combustion modes are observed and coexist, with an additional nonpremixed flame at lean conditions (top left part of Fig. 4.6(b)). At the same time, a premixed reaction zone appears

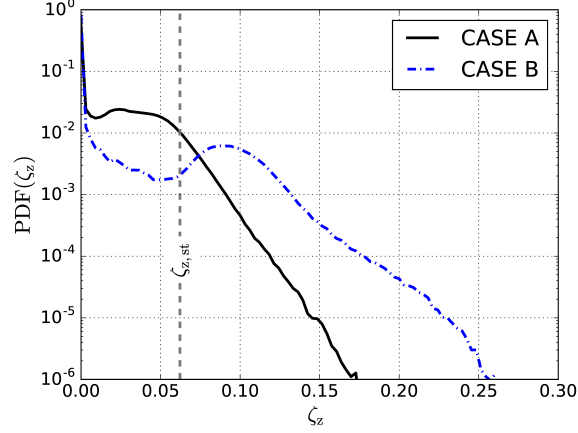


Figure 4.5: Normalized probability density function of mixture fraction at ignition time, $t = \tau_g$.

in the evaporation area, associated with the propagation of the burning zone towards the jet core, as already discussed in the previous section.

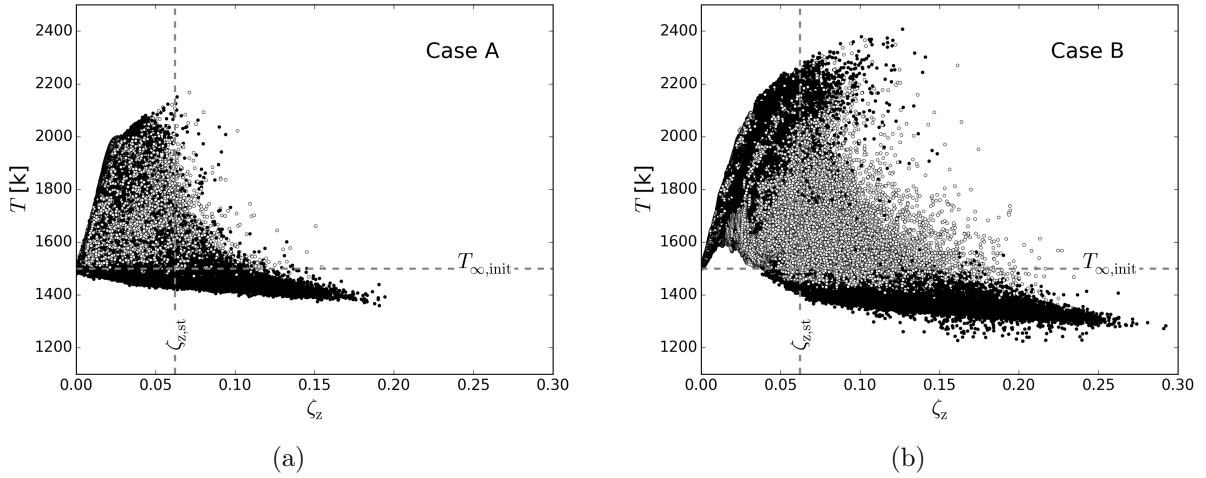


Figure 4.6: Scatter plot of temperature versus mixture fraction at ignition time, $t = \tau_g$: (a) Case A, (b) Case B. Black and white dots represent nonpremixed ($\xi_p \simeq 0$), and premixed ($\xi_p \simeq 1$) flames, respectively.

The scatter plot for heat release in Case A (Fig. 4.7(a)) shows a clear maximum value around stoichiometric conditions in premixed mode. On the other hand, peak heat release is found for Case B at rich conditions, with similar contributions of premixed and nonpremixed flames (Fig. 4.7(b)).

The scalar dissipation rate χ is an essential parameter, which appears in most combustion models. Looking at the scatter plot of χ for both cases (Fig 4.8), completely different behaviors are observed. For Case A (Fig. 4.8(a)), a relatively high dissipation rate is observed at an almost constant level for a broad range of ζ_z (from 0 to 0.17), associated predominantly

4.3. Temporally-Evolving Jet

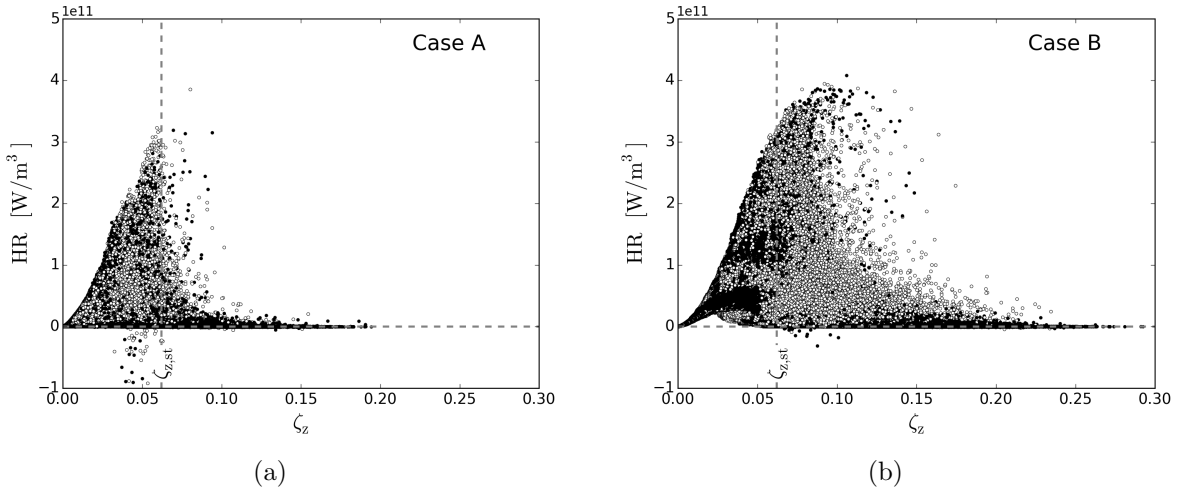


Figure 4.7: Scatter plot of heat release versus mixture fraction at ignition time, $t = \tau_g$. (a) Case A, (b) Case B. Black and white dots represent nonpremixed ($\xi_p \simeq 0$), and premixed ($\xi_p \simeq 1$) flames, respectively.

with the nonpremixed burning mode, as a consequence of the faster evaporation. Conversely, in Case B, peak values of χ are typically twice those found in Case A, and are observed only near stoichiometry and in the slightly rich region, $\zeta_z \geq \zeta_{z,st}$. Additionally, the peak values of χ are now found in premixed flames (Fig. 4.8(b)).

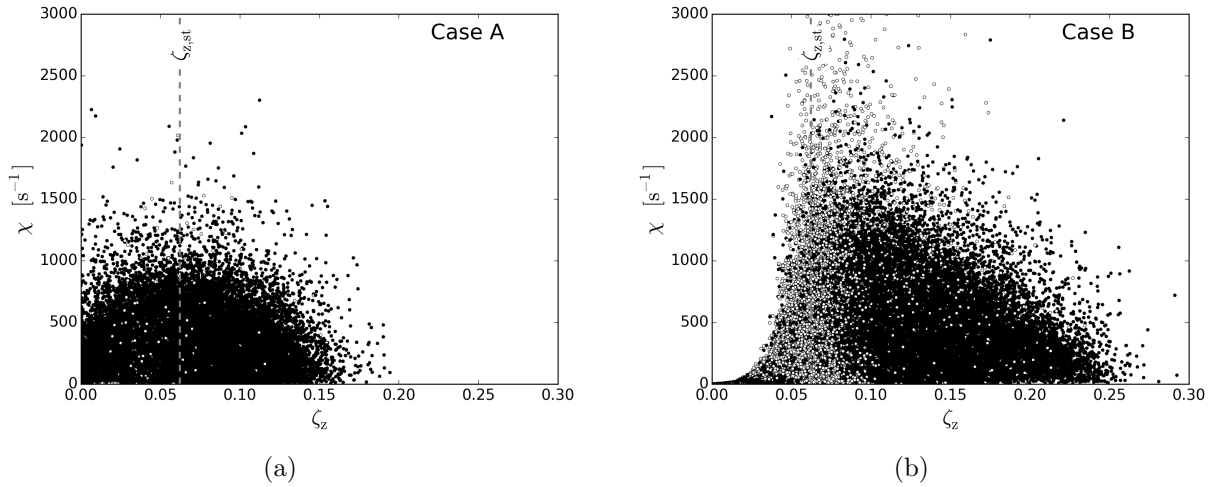


Figure 4.8: Scatter plot of scalar dissipation rate versus mixture fraction at ignition time, $t = \tau_g$. (a) Case A, (b) Case B. Black and white dots represent nonpremixed ($\xi_p \simeq 0$), and premixed ($\xi_p \simeq 1$) flames, respectively.

In order to investigate the role of scalar dissipation, the time evolution of $\langle \chi | \zeta_z \rangle$ (conditional mean of scalar dissipation) versus mixture fraction is depicted in Fig. 4.9. In Case A, $\langle \chi | \zeta_z \rangle$ shows monotonic behavior, increasing with ζ_z (neglecting statistically non-significant

fluctuations for high values of ζ_z); while the values of $\langle \chi | \zeta_z \rangle$ decrease slightly with time due to turbulence decay and dilatation. In Case B (no turbulence imposed), $\langle \chi | \zeta_z \rangle$ behaves differently. In particular, two peaks appear, a large one for rich, a small one for lean conditions. With time, the peak at lean condition moves towards stoichiometry ($\zeta_z \rightarrow \zeta_{z,st}$), where ignition occurs (see Figs. 4.6(b) and 4.8(b)). At $t > \tau_g$, this peak fades away, again due to dilatation. These different behaviors show how challenging it is to derive general models for scalar dissipation rate in spray flames.

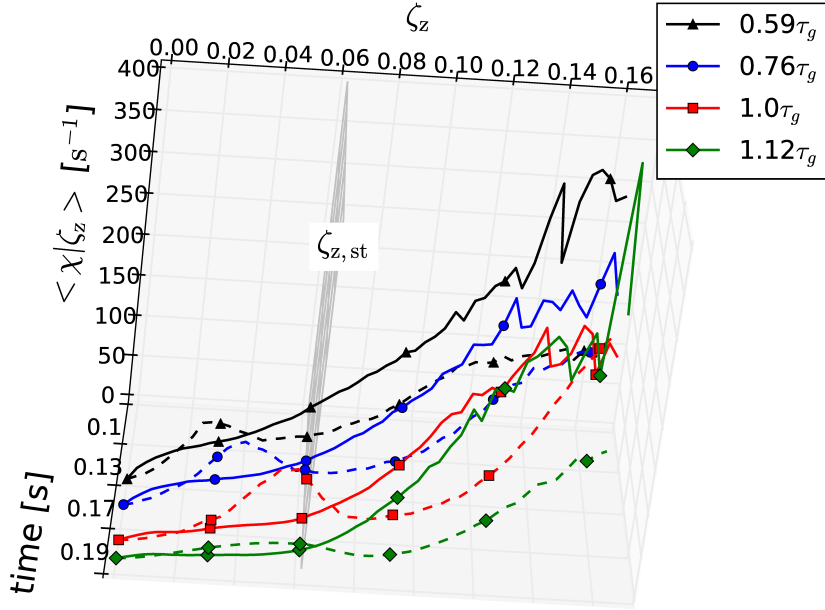


Figure 4.9: Time evolution for conditional mean of scalar dissipation rate versus mixture fraction; where the solid lines and dashed lines represent Case A and B, respectively.

To conclude this section, it is clear that spray evaporation and ignition mechanisms depend highly on the imposed shear in the gas phase; very different results were found in the high-speed jet compared to the nearly quiescent environment. Since the relative importance of shear can be easily changed in the temporally-evolving jet, this configuration appears to be particularly promising for canonical studies; for instance for parametric studies, as discussed in the next section. Systematic investigations of evaporation, mixing, and ignition are possible, while computational costs are much lower than in a comparable, spatially-evolving jet.

Parametric Study

This section focuses only on Case A, with a fast central jet that contains droplets. Three parameters are varied: the local equivalence ratio in the jet ($\phi = 0.5, 1, 2$), the droplet diameter ($a = 10, 13, 16 \mu\text{m}$) and the jet velocity ($U_j = 25, 50, 75, 100 \text{ m/s}$). Figure 4.10 first shows the impact of ϕ (for $a = 10 \mu\text{m}$) on volume-averaged gas temperature. When

4.3. Temporally-Evolving Jet

the equivalence ratio is increased, the average temperature and n-heptane mass fraction (not shown here) increase as well in a monotonous manner and show very similar profiles in time. In fact, increasing ϕ at constant droplet diameter means simply increasing the number of droplets in the numerical domain. As a consequence, the evaporation rate increases along with the reaction rate, within the considered range of ϕ and temperatures. This leads to a higher evaporation rate, and to more n-heptane in the gas mixture, available for reaction. While increasing the intensity of the process, changing ϕ has almost no impact on the autoignition delay time and on the fuel consumption time (Fig. 4.10). The situation is

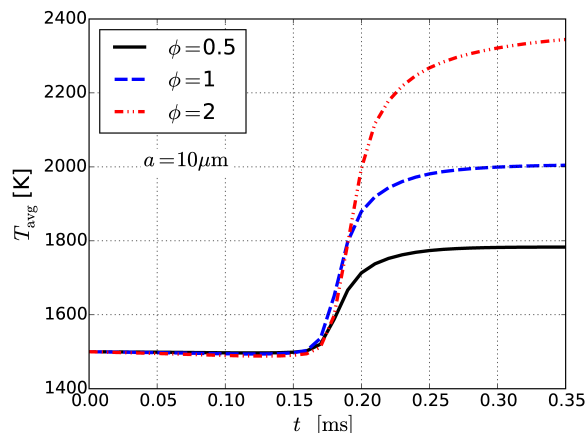


Figure 4.10: Volume-averaged gas temperature versus time for different values of the local equivalence ratio ϕ .

different when changing the diameter of the droplets, a , as shown in Fig. 4.11, while keeping $\phi = 2$. Larger values of the droplet diameter lead to an increasing ignition delay (Fig. 4.11a), since larger droplets need more time to evaporate. Figure 4.11b shows that, when increasing droplet diameter at constant ϕ , the amount of n-heptane found in the gas decreases. This is due to two facts. First, when increasing droplet diameter, the ignition delay time becomes increasingly shorter compared to the evaporation delay time; therefore, the n-heptane fuel in the gas phase is consumed almost immediately, preventing accumulation. Second, larger droplets at the same ϕ mean indeed a lower quantity of droplets with a higher individual mass. As a result, this leads to reduced droplet dispersion in the flow, limiting again evaporation. The impact of droplet diameter found here contradicts that of Wang and Rutland (2007), probably because they simulated “spherical” droplets in a 2D domain, while here 3D is considered. In order to check the impact of shear, jet velocity (Case A) was increased ($U_j = 25, 50, 75, 100$ m/s), corresponding to $Da = 0.31, 0.138, 0.09, 0.07$, respectively; where $Da = \chi_q \tau_j$ is the Damköhler number comparing mixing time scale τ_j and chemical time scale $1/\chi_q$. Here, χ_q and $\tau_j = H/(U_j - U_{co})$ are the scalar dissipation rate at quenching and the jet time scale, respectively. As expected, ignition time τ_g decreases with increasing jet velocity. Figure 4.12 depicts the conditional mean of scalar dissipation rate versus mixture fraction at the ignition time. At low speed, $U_j = 25$ m/s, $\langle \chi | \zeta_z \rangle$ shows the highest values over all ζ_z ; this is because increasing the ignition delay time allows for higher local concentrations of n-heptane in the gas, leading to larger scalar dissipation rates. Increasing the jet velocity

(shear) decreases $\langle \chi | \zeta_z \rangle$ at $\zeta_z \leq \zeta_{z, \text{st}}$, for the same reason. However, for $\zeta_z > \zeta_{z, \text{st}}$, $\langle \chi | \zeta_z \rangle$ mostly increases with jet velocity, due to improved mixing but relatively low temperatures (see Fig. 4.6). To check that the DNS domain is always sufficiently long, the case $U_j^* = 100$ m/s in Figure 4.12 is a repetition with a domain doubled in length, at same grid resolution. Both results are indeed statistically identical, with only spurious variations at large ζ_z due to insufficient data quantity.

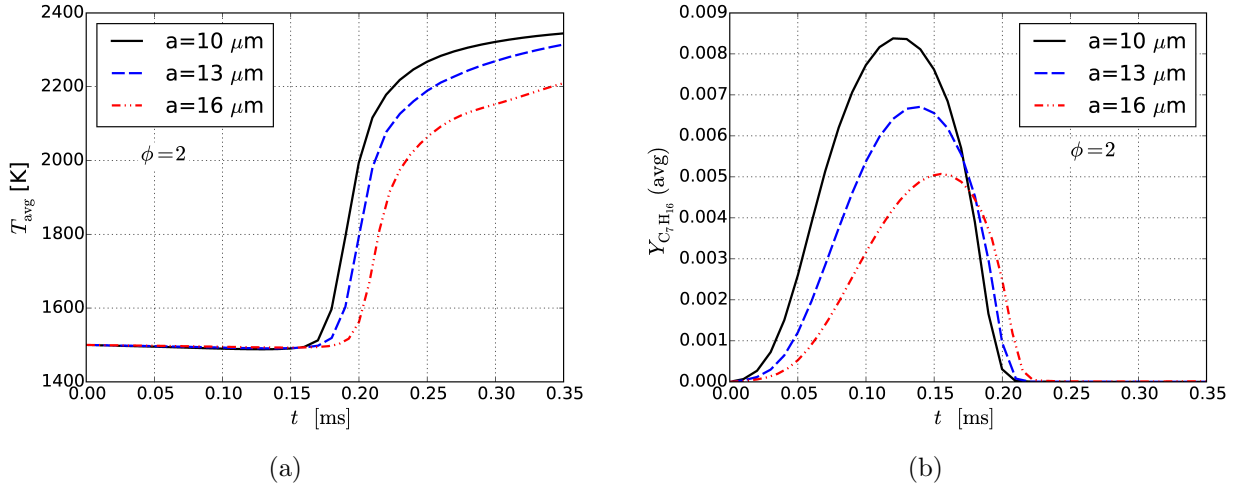


Figure 4.11: Volume-averaged values versus time for different values of the droplet diameter a . (a) Gas temperature. (b) n-heptane mass fraction in the gas.

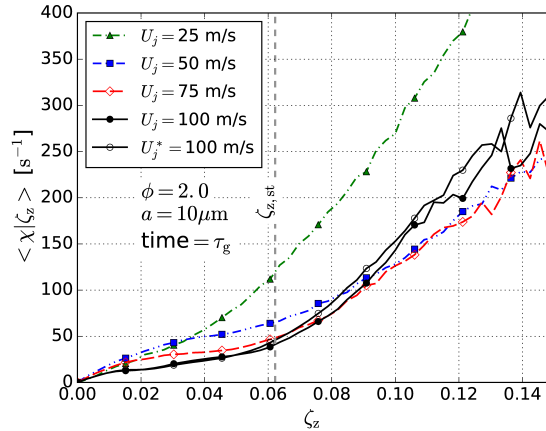


Figure 4.12: Conditional mean of scalar dissipation rate versus mixture fraction at ignition time for different jet velocities. The case with $U_j^* = 100$ m/s is a repetition of $U_j = 100$ m/s, doubling the domain length with same grid resolution.

4.3.3 Conclusions on the Temporally Evolving Jet

In this work, the mechanisms controlling evaporation, mixing, and ignition of a spray in a temporally-evolving jet flow have been investigated by means of 3D DNS. A low-Mach number solver relying on Cantera 1.8 and on a skeletal kinetic mechanism (29 species and 52 elementary reactions describing n-heptane oxidation) were used to this end. In order to quantify the impact of shear, a spray transported in a fast jet has been compared to that evolving in a nearly quiescent flow. These comparisons have revealed that shear in the gas phase indeed has a very significant impact on evaporation, mixing, and ignition scenarios. With high shear, ignition occurs under the retained conditions in a lean mixture, and involves both non-premixed and premixed reaction fronts. Peak heat release is found near stoichiometric conditions in the premixed mode. In the absence of shear, ignition occurs simultaneously over a broad range of conditions, from lean (in the non-premixed mode) to stoichiometric and rich mixtures (involving both non-premixed and premixed combustion fronts). Here, peak heat release is found for a rich mixture involving both combustion modes. Finally, thanks to a parametric study concerning the impact of droplet size, local equivalence ratio, and jet velocity, it has been determined that the autoignition delay time and consumption time depend strongly on the droplet size and jet velocity, yet are almost independent of the local equivalence ratio, at least for the considered conditions.

4.4 Spatially-Evolving Jet

Although, spray in a spatially-evolving jet is a more realistic configuration, it is computationally, more expensive than the temporally-evolving jet for two reasons: (1) It needs a larger domain to correctly follow the spatial evolution, (2) more Lagrangian particles must be tracked. As discussed in the previous chapter, the alternative solution is to use a temporally-evolving jet. However, this setting is not enough to answer all open questions in this area, especially, those concerning spatial evolutions. Because of that, spatially-evolving jet simulations should be ideally combined with temporally-evolving studies. In the following, just preliminary results of spatially-evolving jet simulations are shown; in the future more attention will be paid to this configuration.

4.4.1 Numerical Settings

In a spatially-evolving jet, n-heptane liquid droplets are injected into hot air ($T_0 = 1600$ K) with a speed of 50 m/s through a round inlet with diameter of 0.6 mm. There are three cases, written Case I, Case II, and Case III. The main difference between them is the speed of the surrounding and injected gas. In Case I, the air is initially quiescent. In Cases II and III, hot air is injected with speed of 50 and 70 m/s, respectively. The length of the domain in streamwise direction always 1 cm. However, the lengths of other directions are not constant for all cases. Instead, the resolution is kept constant in all directions and for all cases at $\Delta x = 19.5 \mu\text{m}$. The droplets have initial diameter of 10 μm . Figures 4.13, 4.14, and 4.15 show the time evolution of temperature and the droplets for Cases I, II, and II, respectively.

As it is seen from these figures, the ignition starts at different places and the flame structure is different, depending on the initial condition. In case I, where the air is quiescent, the gas decelerates the droplets, increasing the residence time. The evaporated fuel mixes with the oxidizer and ignites near to the inlet. The ignition starts around the jet edge and envelopes the droplets as it is seen from Fig. 4.13. This can be considered as external group combustion, as illustrated in Figs. 2.7 and 2.8. The behaviors of the spray in Cases II and III are somehow similar, but not identical. In both cases the ignition starts at the same time $t = 0.1$ ms but not at the same place, as seen from Figs. 4.14(a) and 4.15(a), respectively. This is attributed to the fact that the air injected in Case III is faster than in Case II. The ignition starts around the jet, and then spreads to the tip of the jet, surrounding the jet head. The flow in Case III fluctuates more than the other two cases due to increased velocity and turbulence. This set-up is a very good candidate for studying ignition occurrence for safety applications; when ignition and evaporation depend on the initial and running conditions. In the future, more investigations shall be performed with this configuration.

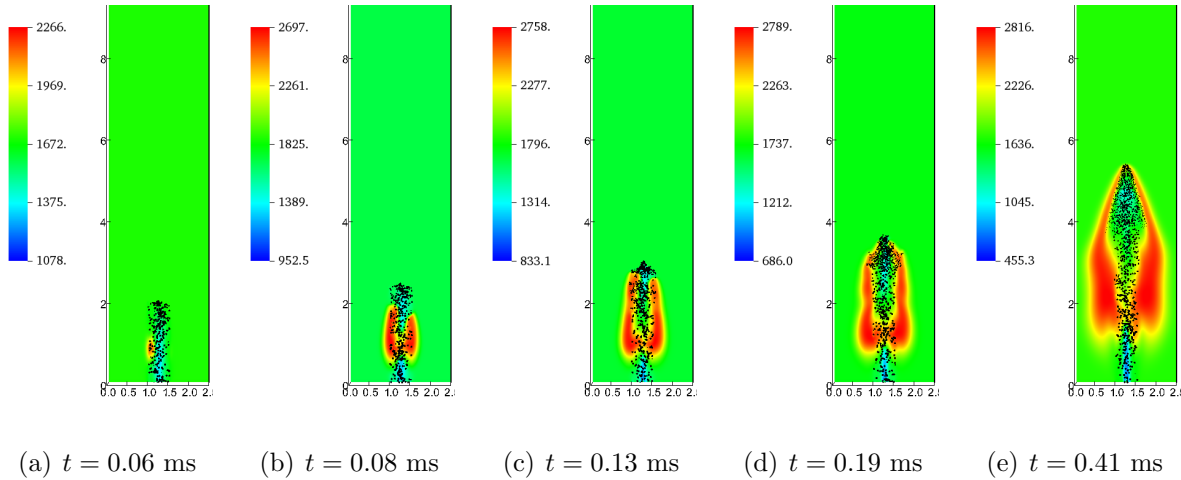


Figure 4.13: Temporal-evolution of 2D-cut plane of gas temperature and droplets for Case I. The size of each droplet is multiplied by 2 for visualization.

Case III can be presented in 3D to show the complete structures of the flow in all directions. The time evolution of a gas temperature iso-volume ($T = 2000$ K) is illustrated in Fig. 4.16. As it can be seen from Fig. 4.16(f), the flow is non-symmetric due to turbulence.

4.4.2 Conclusion on Spatially-Evolving Jet

The numerical setting investigated in this section demonstrates that the behavior and mechanism of spray combustion in a spatially-evolving jet strongly depend on the initial conditions; droplet diameter, surrounding flow speed and temperature, jet diameter, etc. This setting is a very good candidate to study ignition occurrence in safety tests. Furthermore, it would help to investigate different physical phenomena in turbulent spray combustion: mixing, shear, transport, ignition, evaporation, etc.

4.5. General Conclusion

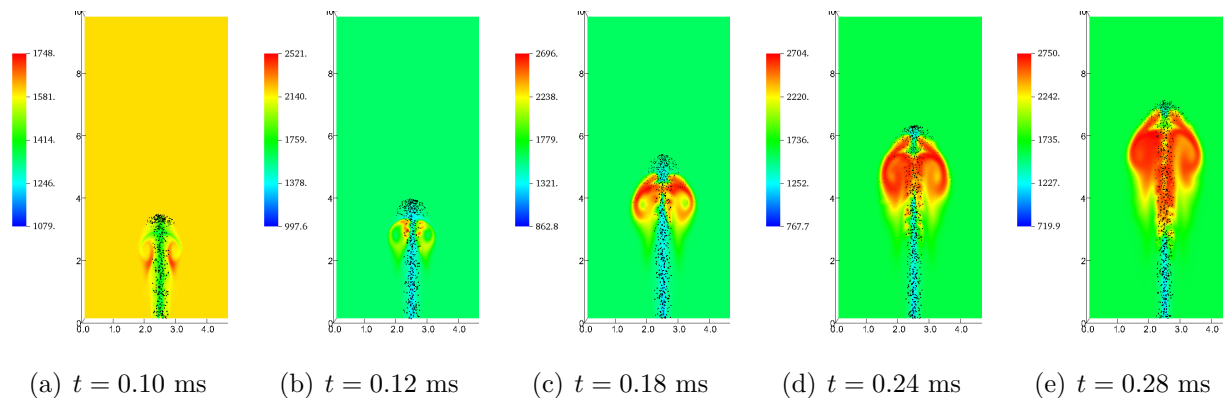


Figure 4.14: Temporal-evolution of 2D-cut plane of gas temperature and droplets for Case II. The size of each droplet is multiplied by 2 for visualization.

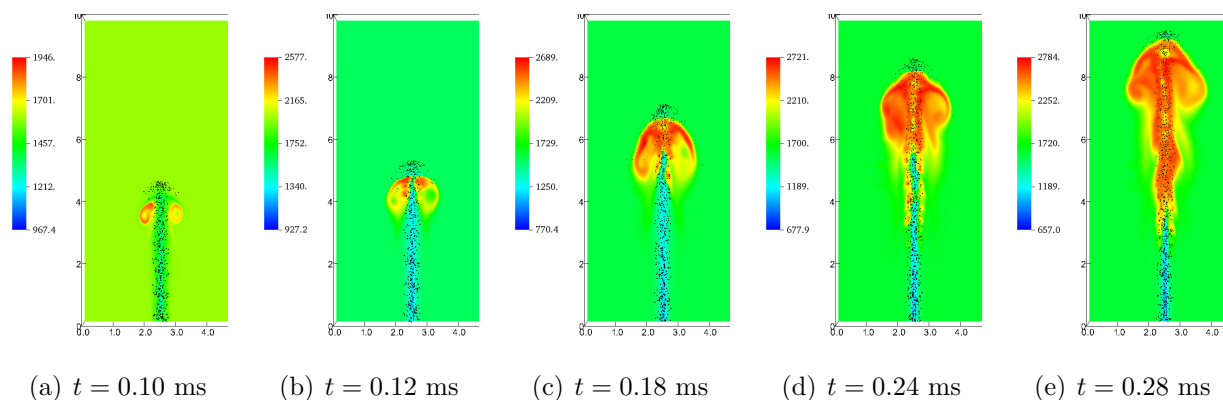


Figure 4.15: Temporal-evolution of 2D-cut plane of gas temperature and droplets for Case III. The size of each droplet is multiplied by 2 for visualization.

4.5 General Conclusion

As a final conclusion, DNS-DPS is found to be a very promising technique for investigating turbulent spray combustion with a high level of accuracy. However, such simulations are still computationally expensive. High-level model reduction techniques would help in studying turbulent spray combustion with shorter computational time, allowing systematic studies. In DNS-DPS, the discrete phase uses the DPS model. Therefore, further reduction on the side of the discrete phase is not possible. The reduction models may only be applied to the continuous (gas) side. For this reason, some model reductions will be tested and developed for the gas side only in Ch. 6. In future, these reduction techniques could be also applied directly to DNS-DPS simulations.

The possibility of using one or the other of these reduction techniques completely depends on the balance between chemistry and turbulence intensity. For this reason, the next chapter introduces a new approach to quantify uniquely the local flow state and the intensity of turbulence.

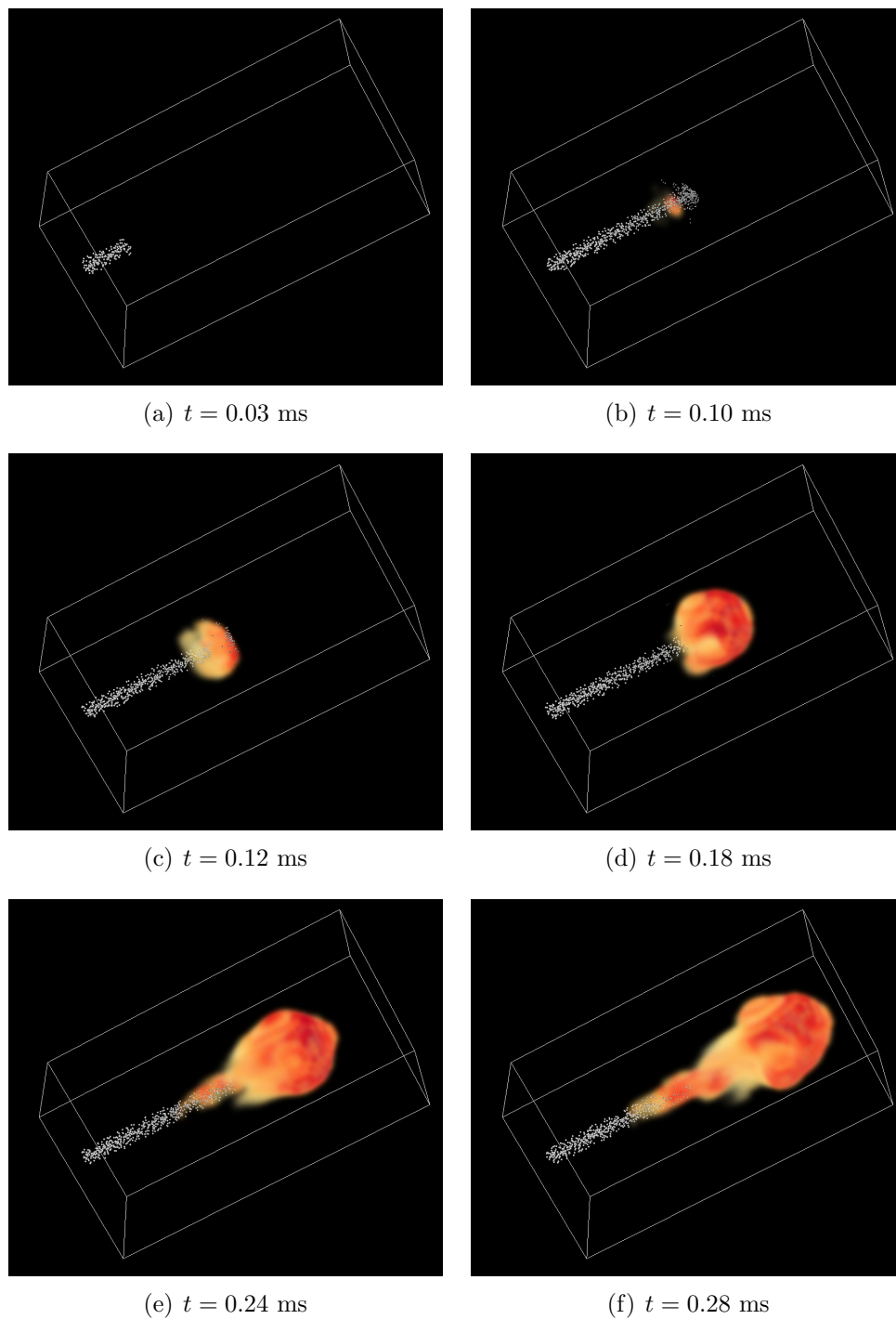


Figure 4.16: Temporal-evolution of iso-volume of gas temperature (value $T = 2000$ K) with droplets for Case III. The size of each droplet is multiplied by 4 for visualization.

Chapter 5

A Tool to Quantify the Flow State: Spectral Entropy

5.1 Introduction

In many practical applications, the flow state changes locally from one location inside the computational domain to another; or in time, for instance before/after ignition. Therefore, different computational concepts/solvers could be applied, e.g., DNS, LES, RANS, hybrid, etc. In this chapter, it is shown that the spectral entropy S_d , obtained by solving the eigenvalue problem for the temporal autocorrelation function, can be used in order to uniquely quantify the flow state and differentiate between laminar, transitional, or turbulent regimes. As such, it delivers a direct measure of turbulence intensity. Consequently, it can be employed to guide hybrid simulations. The first test of this approach relies on DNS for decaying Homogeneous Isotropic Turbulence (HIT) and is performed using DINO for ten different Taylor numbers. Results obtained by analyzing DNS indicate that S_d is an excellent candidate in quantifying turbulence intensity and transition. To verify the robustness of the corresponding analysis, the impact of different resolutions was investigated, revealing that a correct state estimate is still obtained with a coarser spatial or temporal resolution. Finally, to examine the generality of the approach, the entropy thresholds obtained from the DNS analysis were used with the same algorithm to analyze (1) DNS results obtained for the Taylor-Green vortex benchmark at $Re = 1600$ as well as (2) results obtained through Large Eddy Simulations (LES) in a blood nozzle, revealing in both cases a perfect agreement with a traditional, user-based analysis of the flow conditions. Hence, S_d appears to be an excellent quantitative indicator of laminar, transitional, or turbulent flow, allowing an automatic, user-independent analysis of the flow state for a variety of conditions. In principle, it could be used without modification to analyze experimental measurements, as well. Part of this chapter are based on an article submitted to the International Journal of Heat and Fluid Flow.

5.2 History and Literature Survey

Transitional flows are encountered in a variety of practical applications, but transition to turbulence requires further understanding. For instance, there is currently a controversial discussion concerning the possible role of transition in explaining the rupture of arterial vessels and aneurysms [121, 122]. While highly turbulent flows can be properly described using their characteristic energy spectra [33, 123], the appropriate characterization of transitional conditions is far more challenging.

Numerous studies have already been documented in the scientific literature concerning flow transition, see [124–130] to cite a few, illustrating the diversity of paths and processes involved on the way from laminar to turbulent flow and back. However, currently, to the best of the authors’ knowledge, no universal criterion can be found that allows for a direct and user-independent measure of the flow state (either laminar, transitional, or turbulent) based on numerically computed or experimentally measured flow velocity fields. A better understanding of transition and a localization of corresponding conditions could lead to more accurate simulations in connection with wall models, or when using Detached or Large-Eddy Simulations [131, 132]. Additionally, such a criterion is essential to guide hybrid simulations [133], combining in the best possible way different simulation models (possibly laminar flow equations; Reynolds-Averaged Navier-Stokes approach – RANS; Unsteady RANS – URANS; LES; DNS). By identifying the flow state and quantifying the intensity of turbulence, a suitable approach can be implemented in an adaptive manner to combine proper models in space, different regions being computed using different numerical models; or possibly in time, switching between different computational approaches as appropriate. Considering the rapid development of hybrid simulations [134, 135], identifying automatically the most appropriate model is becoming increasingly important. In order to be successful, hybrid simulations should ultimately rely on a user-independent and generally valid indicator of the flow state computed from the simulated flow field, as proposed in this work. Additionally, such an indicator could readily be used to guide in an automatic manner the resolution needed in space and time, so that, starting from a fully resolved computation, grid coarsening and larger time steps could be used for part of the domain or the simulation. Finally, the same approach could also be used to automatically detect regions of interest (e.g., places where transition takes place) when analyzing large datasets.

Proper Orthogonal Decomposition (POD) appears to be a good candidate for detecting transition and analyzing the flow state [136]. After Aubry et al. [137, 138] introduced the idea of using the normalized spectral entropy of the POD eigenvalues to identify changes in flow behavior as a function of the Reynolds number, various works have built on top of the same idea, e.g., [121, 139–142]. In all of these publications, the entropy is a case-dependent value that is used to characterize the flow in a specific configuration. A generalization of the corresponding findings was not attempted.

In general, POD can be performed either with a singular value decomposition [143] or by using the method of Sirovich [144] (also called snapshot POD or SPOD). The latter method is computationally more tractable when considering very large datasets, as obtained, e.g., from DNS. Sirovich’s approach requires that the snapshots should be uncorrelated and linearly

5.3. Governing Equations

independent. Further details concerning both approaches and comparisons between them are described, e.g., by [145–155].

Using the eigenvalue equation of the temporal autocorrelation function as it appears in Sirovich’s original work (Eq. (14) of [144]), a new technique has been derived in this chapter to detect the flow state, but without requiring snapshot independency. In order to calibrate this approach, it should first be applied to well-known flow states. For this purpose, 3D DNS has been conducted, using DINO, for homogeneous isotropic, incompressible, time-decaying turbulence, while increasing in a systematic manner the Taylor Reynolds number from laminar to turbulent conditions through the transition zone. Here, the spatial and temporal resolution requirements associated with the most turbulent case have been kept for all conditions in the DNS. All results have then been analyzed by means of our approach, delivering finally the spectral entropy. In this manner, it is possible to associate the value of the spectral entropy S_d to a specific flow state, and in particular to delineate the transition region or to quantify turbulence intensity based on S_d . Varying in a systematic manner the temporal and spatial resolution employed when post-processing the DNS data, it is possible to quantify the impact of these parameters and the robustness of the analysis. Finally, results obtained from a two-dimensional analysis are compared to the three-dimensional results, since many currently employed experimental measurement techniques only deliver 2D data. Again, the spectral entropy threshold obtained from this analysis can be considered as flow state indicator in any hybrid simulation or used in data post-processing to quantify the flow state, in experiments or simulations. After having derived proper thresholds from these DNS data, two completely different and independent datasets have then been analyzed in the same manner to check the general applicability of the procedure. These two datasets are: (1) a DNS simulation of the classical three-dimensional Taylor-Green vortex (TGV) at a Reynolds number of 1600 (see Sec. 3.15.3); (2) LES computations of a real blood nozzle used by the Food and Drug Administration (FDA) to investigate the accuracy of Computational Fluid Dynamics (CFD) for flows covering laminar, transitional, and turbulent regimes at different values of the Reynolds number [156]. Computing the resulting spectral entropy values at different times (for TGV) or spatial locations (for the FDA nozzle), it is observed that exactly the same thresholds can be successfully applied in all cases to quantify the flow state.

5.3 Governing Equations

The governing equation of an incompressible flow are used to generate the DNS, as reviewed in Sec. 3.5. The derived equations for the spectral entropy are presented in the next section.

5.3.1 Eigenvalue Problem

As mentioned before, the developed method was originally inspired by the SPOD method described in [144], though with a very different purpose and hence conditions. In this section, the notations follow those of [144, 146, 157].

The fundamental idea behind original POD is to decompose each signal $\mathbf{u}(\mathbf{x}, t_k)$ into

orthogonal deterministic functions ϕ (POD spatial modes) and time-dependent coefficients a_k (POD temporal coefficients):

$$\mathbf{u}(\mathbf{x}, t_k) = \sum_{l=1}^{\infty} a_k^l \phi^l(\mathbf{x}). \quad (5.1)$$

Here, superscript l and subscript k refer to the mode number and index of corresponding snapshot (or time step), respectively. The function ϕ denotes the eigenfunction of the Fredholm integral equation

$$\int_{\mathbf{x}} \mathbf{R}(\mathbf{x}, \mathbf{x}') \cdot \phi(\mathbf{x}') d\mathbf{x}' = \lambda \phi(\mathbf{x}). \quad (5.2)$$

The kernel of this eigenvalue problem is the two-point spatial correlation function

$$\mathbf{R}(\mathbf{x}, \mathbf{x}') = \langle \mathbf{u}(\mathbf{x}, t_k) \otimes \mathbf{u}(\mathbf{x}', t_k) \rangle_t, \quad (5.3)$$

where t_k and \mathbf{x} are snapshot time and position vector, respectively. In POD, ϕ is chosen to maximize the value of $\langle |(\mathbf{u}, \phi)|^2 \rangle / \|\phi\|^2$, where $\langle \cdot \rangle_t$, $\langle \cdot \rangle$, (\cdot, \cdot) and $\|\cdot\|$ are time average, spatial average, inner product and norm, respectively. Since the spatial modes ϕ^l are orthonormal to each other, the following equation can be used

$$\phi^l(\mathbf{x}) = \sum_{k=1}^{N_m} a_k^l \mathbf{u}(\mathbf{x}, t_k). \quad (5.4)$$

In order to determine the coefficients a_k , Eq. (5.4) is substituted into Eq. (5.2), resulting in

$$\left(\frac{1}{N_m} \sum_{i=1}^{N_m} \mathbf{u}(\mathbf{x}, t_i) \otimes \mathbf{u}(\mathbf{x}, t_i), \sum_{k=1}^{N_m} a_k \mathbf{u}(\mathbf{x}, t_k) \right) = \lambda \sum_{k=1}^{N_m} a_k \mathbf{u}(\mathbf{x}, t_k), \quad (5.5)$$

where N_m is the total number of snapshots. Sirovich [144] simplified Eq. (5.5) to

$$\sum_{k=1}^{N_m} \frac{1}{N_m} (\mathbf{u}(\mathbf{x}, t_i), \mathbf{u}(\mathbf{x}, t_k)) a_k = \lambda a_i \quad ; \quad i = 1, \dots, N_m. \quad (5.6)$$

However, this simplification is only correct if the snapshots are uncorrelated and linearly independent. Moreover, since Eq. (5.3) is a time-average, it is clear that this formulation was originally derived for statistically steady flows in mind.

Equation (5.6) can be rewritten in symbolic form as:

$$\mathbf{CA} = \lambda \mathbf{A}, \quad (5.7)$$

$$\mathbf{A} = (a_1, a_2, \dots, a_{N_m})^T, \quad (5.8)$$

$$C_{ij} = \frac{(\mathbf{u}(\mathbf{x}, t_i), \mathbf{u}(\mathbf{x}, t_j))}{N_m}. \quad (5.9)$$

5.4. Numerical Approaches and Algorithms

Solving this eigenvalue problem, Eq. (5.7), leads to a total of N_m eigenvalues, written λ^l , and eigenvectors, denoted \mathbf{A}^l ($l \in 1, 2, 3, \dots, N_m$). When using SPOD for data analysis or data compression, it is not always necessary to keep all N_m modes. Then, M represents the number of modes retained in the analysis while N_m still represents the total number of snapshots, i.e., the whole data-set available for the analysis, obviously with $M \leq N_m$.

If the collected snapshots are not uncorrelated and linearly independent, the original signal will not be decomposed correctly by SPOD using Eq. (5.1). However, properly decomposing the signal is not at all the purpose of the present work. Equation (5.6) remains in all cases a valid equation, describing the eigenvalue problem based on the temporal autocorrelation function as kernel. The obtained eigenvalues represent the spectrum of the autocorrelation matrix (\mathbf{C} in Eq. (5.7)). In what follows, these eigenvalues will be used in a standalone manner to quantify the flow state. For this purpose, the two conditions underlying SPOD (uncorrelated snapshots and statistically steady flows) are irrelevant.

5.3.2 Spectral Entropy

In order to characterize the intensity of the turbulence contained in the analyzed velocity field \mathbf{u} , the spectral entropy S_d [158–160], as classically used in information theory, can now be computed. This quantity should allow one to distinguish between different flow regimes, from “highly disordered” (here, meaning turbulence), to “partially ordered” (here, for transition), or “well ordered” (here, for laminar flow).

For the computation of the spectral entropy, the relative energy, P^l first computed based on the corresponding eigenvalue, after ordering them in decreasing order based on λ^l , as:

$$P^l = \frac{\lambda^l}{\sum_{j=1}^M \lambda^j}, \quad (5.10)$$

where $M \leq N_m$ is the number of modes retained in the analysis. Then, the spectral entropy can be determined as:

$$S_d = - \sum_{l=1}^M P^l \ln P^l. \quad (5.11)$$

According to Eq. (5.11), the maximum possible value of S_d is reached when all eigenvalues are equal to each other, i.e., $P^l = 1/M$, and consequently $S_d = \ln(M)$. Physically, this means that the energy is equally distributed over all the M modes. The minimum value of S_d corresponds to the case where the original signal contains only one mode, the first one, meaning that the flow field is steady. Then, $S_d = 0$.

5.4 Numerical Approaches and Algorithms

DINO, in his incompressible version, has been used to perform the DNS. Computing the spectral entropy has been performed as a post-processing step by using an in-house Python

script called PyPODe, which has been originally developed for SPOD analysis and thus contains a solution procedure for Eq. (5.7). In order to follow the steps described in Sect. 5.3.2, the employed algorithm proceeds as follows:

- compute the correlation matrix C , Eq. (5.9);
- solve the eigenvalue problem, Eq. (5.7), to obtain λ^l and \mathbf{A}^l ;
- sort the eigenvalues λ^l in descending order;
- compute the relative energy P^l of each mode;
- deduce the spectral entropy S_d .

5.5 Results and Discussion

In order to check the procedure, the spectral entropy S_d has been first determined for ten different DNS computations associated with increasing values of the Taylor Reynolds number. The retained values span all the interesting flow regimes from laminar to turbulent, as quantified based on Re_λ following for instance [161, 162]. The initial parameters corresponding to each case are listed in Table 5.1. In this table, u' , ϵ , λ_t , η_k , and τ_η are the root mean square of the velocity fluctuations, dissipation rate of the turbulence kinetic energy, Taylor length scale, Kolmogorov length scale, and Kolmogorov time scale, respectively. In Table 5.1, Λ and τ_Λ are the longitudinal integral length scale

$$\Lambda = \frac{\pi}{2 \langle u_1^2 \rangle} \int_0^{\kappa_{\max}} \frac{E(\kappa)}{\kappa} d\kappa, \quad (5.12)$$

and the turbulence eddy turnover time scale,

$$\tau_\Lambda = \frac{\Lambda}{u'}, \quad (5.13)$$

respectively, where in this equation, u_1 , κ , and $E(\kappa)$ are the velocity fluctuation of the turbulence in x-direction, wave number, and the spectrum of the kinetic energy, respectively. Reynolds number based on the Taylor or longitudinal integral length scales are defined as:

$$\text{Re}_\lambda = \frac{u' \lambda_t}{\nu}, \quad (5.14)$$

and

$$\text{Re}_\Lambda = \frac{u' \Lambda}{\nu}, \quad (5.15)$$

respectively.

The time evolutions of the Reynolds number for these cases are shown in Fig. 5.1. It is well-known that the influence of the initial boundary conditions in time (analytical von

Kármán-Pao spectrum, see [?]) can be felt until $t \simeq \tau_\Lambda$ [163]. For this reason, all simulations have been pursued until $t = 3\tau_\Lambda$, the analysis being performed in the time interval of $[\tau_\Lambda, 3\tau_\Lambda]$, as seen in Fig. 5.1. In this manner, possible artifacts associated with the initial conditions are avoided.

5.5.1 Suitable Time Scales for the Entropy Analysis

In our approach, it is important to decide (1) what is the suitable distance in time between two consecutive snapshots entering the analysis, and (2) what the overall time duration for a complete analysis should be. After having answered both questions, the underlying number of snapshots N_m will be determined. The following guidelines have been derived for analyzing the DNS results first, i.e., in a case for which all existing scales in time and space are available in the data. However, the resulting recommendations should also be usable in a more general frame, therefore rough estimates are proposed as well in what follows.

Let us start by considering the minimum time step Δt_{\min}^s between two consecutive snapshots entering the analysis. Clearly, $\Delta t_{\min}^s \rightarrow 0$ would mean that these snapshots contain identical information (and would thus of course be perfectly correlated). Such an analysis would be useless, since the analysis should involve fields that differ from each other. In any turbulent flow, the minimum time interval for which changes in the flow structure are expected is the Kolmogorov time scale, τ_η . Choosing $\Delta t_{\min}^s < \tau_\eta$ would thus lead to a high computational overhead at no benefit, since the analyzed fields would be almost identical. On the other hand, and even if corresponding changes will only occur at small scales in space, two snapshots separated by at least τ_η will be different and thus lead to an interesting analysis. Now, when choosing Δt_{\min}^s much larger than τ_η , the analysis cannot account for small-scale effects and will thus give misleading results at this scale. Nevertheless, such an analysis might still deliver interesting information concerning larger flow scales.

This shows that the distance in time between two consecutive snapshots in a DNS should be chosen at least equal to τ_η , but not much larger than τ_η , if short time-scales are of interest. Later in this work, the condition $\Delta t_{\min}^s \in [\tau_\eta, 2\tau_\eta]$ is retained as a practical range, leading to the fastest possible analysis while still retaining the whole information at all time-scales.

If τ_η is not known a priori, a rough estimation for Δt_{\min}^s to compute the spectral entropy can be obtained instead following:

$$\Delta t_{\min}^s \simeq \frac{\text{smallest resolved length}}{\text{velocity rms}} \simeq \frac{\text{resolution (num./exp.)}}{\text{velocity rms}} = \frac{\Delta x}{u_{\text{rms}}}, \quad (5.16)$$

This estimation will usually lead to values of Δt_{\min}^s slightly below τ_η , as it will be shown for instance in Sect. 5.5.4, and is thus an appropriate, conservative estimate for Δt_{\min}^s .

Now, what should the duration of the whole analysis be? The time distance between the first and the last snapshot (the complete time interval used for the analysis), $\Delta t_{\text{overall}}^s$, should be at least equal to the largest flow time scale of interest, τ_{max}^f . In a turbulent flow, this largest flow time scale is classically given by the turbulence eddy turn-over time, τ_Λ , leading to the condition $\Delta t_{\text{overall}}^s \geq \tau_\Lambda$. However, depending on the problem considered and on the objective of the analysis, $\Delta t_{\text{overall}}^s$ might be in many cases much larger than τ_Λ ; there

Table 5.1: Initial turbulence parameters employed for the ten DNS computations. Please keep in mind that a fixed grid (equidistant grid points $N = 512^3$, needed to resolve properly the most turbulent case) has been used for all conditions.

Re_λ	Re_Λ	ϵ [m ² /s ³]	u' [m/s]	λ_t [mm]	Λ [mm]	τ_Λ [s]	η_k [mm]	τ_η [s]
2.0635	3.6392	0.000565	0.009463	10.9036	19.2298	2.032210	3.856940	0.297520
8.1454	14.365	0.008801	0.037352	10.9036	19.2298	0.514826	1.941280	0.075372
15.205	26.816	0.030668	0.069724	10.9036	19.2298	0.275800	1.420870	0.040378
30.410	53.631	0.122672	0.139448	10.9036	19.2298	0.137900	1.004710	0.020189
46.157	81.404	0.282624	0.211661	10.9036	19.2298	0.090852	0.815503	0.013301
65.163	114.92	0.563292	0.298816	10.9036	19.2298	0.064353	0.686348	0.009421
81.454	143.65	0.880143	0.373520	10.9036	19.2298	0.051483	0.613888	0.007537
100.46	177.17	1.338800	0.460675	10.9036	19.2298	0.041743	0.552776	0.006111
149.88	264.32	2.979810	0.687277	10.9036	19.2298	0.027980	0.452564	0.004096
190.06	335.19	4.791890	0.871547	10.9036	19.2298	0.022064	0.401884	0.003230

is no fundamental upper limit for the value of $\Delta t_{\text{overall}}^s$. Later in this work, when analyzing HIT data derived from DNS in time-decaying turbulence, the condition $\Delta t_{\text{overall}}^s = 2\tau_\Lambda$ is retained.

If τ_Λ is not known, the minimum value of $\Delta t_{\text{overall}}^s$ can be approximately estimated instead by:

$$\Delta t_{\text{overall}}^s \geq \frac{0.2 \text{ (minimum domain length)}}{u_{\text{rms}}} \quad (5.17)$$

where the numerator, 20% of the minimum domain length, is used as an approximation of the integral length scale, following [164, 165].

To summarize, when analyzing HIT data obtained from DNS, appropriate time scales read:

$$\begin{aligned} \tau_\eta &\leq \Delta t_{\text{min}}^s \leq 2\tau_\eta; \\ \Delta t_{\text{overall}}^s &\geq \tau_\Lambda. \end{aligned} \quad (5.18)$$

Considering that τ_η and τ_Λ are not always known, suitable values for the time scales allowing the meaningful computation of spectral entropy can be roughly estimated for such cases as:

$$\begin{aligned} \frac{\Delta x}{u_{\text{rms}}} &\leq \Delta t_{\text{min}}^s \leq 2 \frac{\Delta x}{u_{\text{rms}}}; \\ \Delta t_{\text{overall}}^s &\geq \frac{0.2 \text{ (minimum domain length)}}{u_{\text{rms}}}. \end{aligned} \quad (5.19)$$

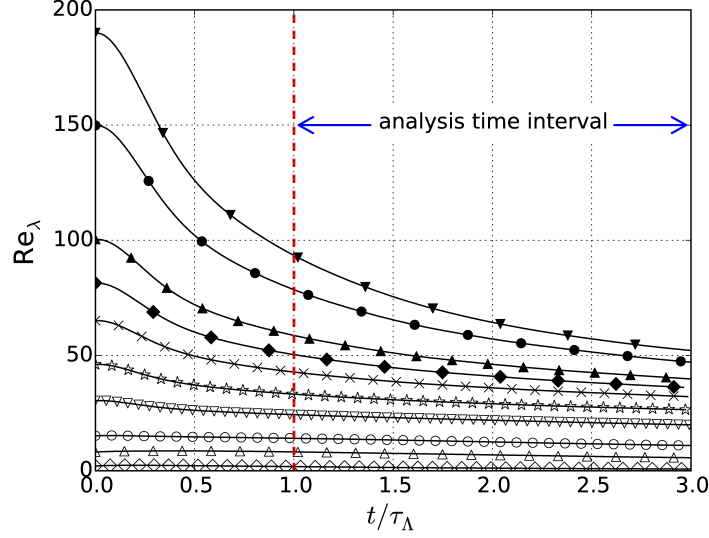


Figure 5.1: Evolution of the Taylor Reynolds number vs. time for all time-decaying DNS simulations. The time interval used for the analysis of the DNS results starts at $t = \tau_\Lambda$ and stops at $t = 3\tau_\Lambda$ for all cases. Values of τ_Λ listed in Table 5.1 are used for normalization.

5.5.2 Using Spectral Entropy as a Measure of Turbulence Intensity

Before returning to the issue concerning suitable time scales, the ten DNS computations from Table 5.1 are first analyzed. Considering an overall duration covering two integral time scales ($\Delta t_{\text{overall}}^s = 2\tau_\Lambda$, see Fig. 5.1), 50 equidistant snapshots are extracted and used in the analysis. Figure 5.2 shows the evolution of spectral entropy versus Taylor Reynolds number when considering all modes ($M = N_m = 50$). The Reynolds number of the horizontal axis is the average Taylor Reynolds number computed in the DNS for the time interval $[\tau_\Lambda, 3\tau_\Lambda]$, used for the analysis as well (see again Fig. 5.1). It is observed in Fig. 5.2 that S_d shows a monotonic behavior when increasing the Reynolds number from laminar conditions to fully turbulent flows. As such, the spectral entropy can be used as a direct measure of turbulence intensity. It can thus be employed to delineate between laminar/quasi-laminar, transitional, and turbulent regimes. In Fig. 5.2, the gray regions correspond roughly to transitional conditions (Re_λ in the range of $[20 - 40]$, following [161, 162]).

The exact values obtained for the spectral entropy S_d are given in Table 5.2. At very low Reynolds number ($\text{Re}_\lambda \leq 20$) the flow remains quasi-laminar, and corresponding values of the spectral entropy are $0 \leq S_d \leq 0.7$. In the intermediate range, corresponding to transition (around $20 \leq \text{Re}_\lambda \leq 40$), the spectral entropy still increases in a monotonous manner up to $S_d \leq 1.1$, but at a lower pace. Finally, under turbulent conditions ($\text{Re}_\lambda \geq 40$), the spectral entropy slowly grows with Re_λ and systematically shows values above 1.1. Analyzing the data more closely, an excellent fit is obtained with a logarithmic function given by $S_d = A \ln(B \text{Re}_\lambda + 1)$, with coefficients $A = 1.089$ and $B = 0.0431$. In the light of these results, the transition between quasi-laminar and turbulent conditions would be roughly

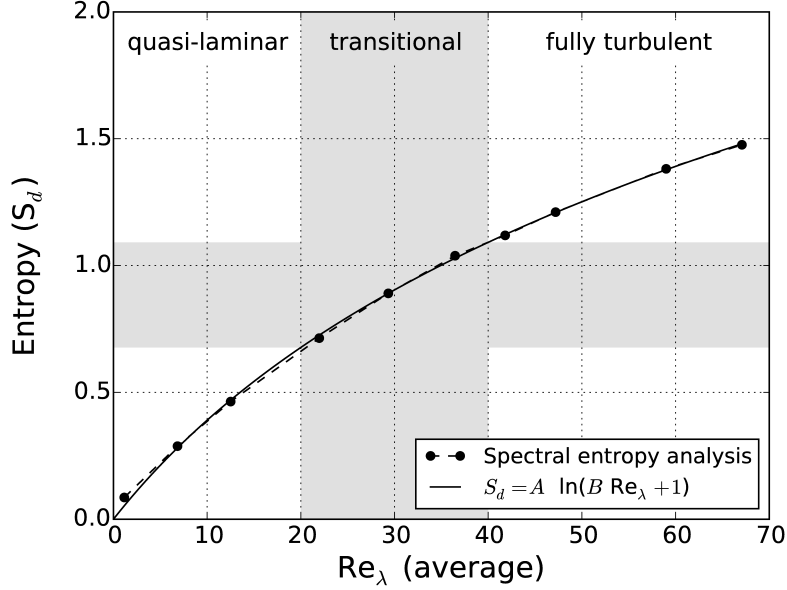


Figure 5.2: Spectral entropy versus average Taylor Reynolds number for all DNS simulations, computed with all modes ($M = N_m = 50$). The dashed line with black dots represents the entropy computed directly from the DNS data. The solid line represents the best curve fitting, with coefficients $A = 1.089$ and $B = 0.0431$. The vertical and horizontal gray regions represent the transitional region in terms of Re_{λ} and of the corresponding entropy values.

associated with $S_d \simeq 1$ (or, if a range is preferred, to values of $S_d \in [0.7 - 1.1]$).

Note that Byrne et al. [121] also used the spectral entropy to quantify the flow stability within patient-specific cerebral aneurysms. In their study of more than 200 different datasets, they concluded that $S_d = 0.0713$ corresponds to stable flows, whereas $S_d = 0.674$ is representative for the onset of unstable flows. The second value indeed corresponds to the beginning of transition in our analysis, confirming the previous discussion.

5.5.3 Impact of Spatial Resolution

It is now important to check how robust S_d might be to estimate the flow state and turbulence intensity. While in DNS all scales must be properly resolved, it is generally impossible to resolve all temporal and spatial scales in experimental measurements. In LES, processes taking place at small scale are modeled and not solved exactly. Could S_d still be used as a robust estimator under such conditions?

In order to answer this question, the analysis has been applied to the same ten cases but decreasing progressively the spatial resolution used during post-processing ($N = 256^3$, 128^3 , 64^3 , 32^3 , 16^3 , 8^3), simply by skipping more and more grid points in a regular manner in the full DNS dataset of 512^3 points. Figure 5.3 shows the corresponding results, and is almost identical to Fig. 5.2. This figure demonstrates that the analysis and the associated computation of S_d do not depend noticeably on the spatial resolution employed during post-processing, at least as long as enough snapshots (here $M = N_m = 50$) are employed. Hence,

Table 5.2: Spectral entropy S_d computed with all modes.

Flow regime	Re_λ	Re_Λ	S_d
quasi-laminar	1.15	1.33	0.09
	6.84	8.80	0.29
	12.51	17.72	0.46
transition	21.97	36.34	0.71
	29.34	54.48	0.89
	36.47	75.01	1.03
turbulent	41.81	92.06	1.11
	47.20	110.85	1.20
	58.99	157.81	1.38
	67.08	195.24	1.48

S_d appears to be a robust estimator of flow state and turbulence intensity, and can also be used to analyze results that are not obtained by DNS, for instance from experiments or using LES, as shown at the end of this work.

5.5.4 Impact of Temporal Resolution

Similar to the issue discussed in the previous section, it is important to now check the required resolution in time. In other words, what is the minimum number of snapshots $N_{m,min}$ needed to correctly predict the flow state? For the results discussed until this point, 50 snapshots have been systematically employed, this value being retained quite arbitrarily. It is time to come back to the discussion of Sect. 5.5.1 in order to obtain a better understanding of how $\Delta t_{overall}^s$, Δt_{min}^s and thus $N_{m,min} = \Delta t_{overall}^s / \Delta t_{min}^s$ should finally be chosen.

Mathematically, a first answer concerning the minimum number of needed snapshots can be proposed by looking at Eq. (5.11), showing that the theoretical upper limit of S_d is $\ln(N_m)$. As a consequence, it is obviously necessary that $\ln(N_m)$ should be larger than the true value of S_d .

Since the true value of S_d is usually not known a priori, and considering that this condition is a necessary but not a sufficient one, a further discussion is needed. Following Sect. 5.5.1, the minimum number of snapshots can be estimated as:

$$N_{m,min} = \frac{\Delta t_{overall}^s}{\Delta t_{min}^s} \simeq \frac{2\tau_\Lambda}{[1-2]\tau_\eta}. \quad (5.20)$$

keeping in mind that the analysis has been carried out over the duration $t \in [\tau_\Lambda, 3\tau_\Lambda]$ for this DNS of time-decaying turbulence (see again Fig. 5.1), so that $\Delta t_{overall}^s = 2\tau_\Lambda$ here.

The resulting minimum numbers of snapshots obtained from Eq. (5.20) for all HIT cases studied by DNS are summarized in Table 5.3. All values of $N_{m,min}$ are represented as a rounded range because of the factor 2 appearing in the denominator of Eq. (5.20). In this

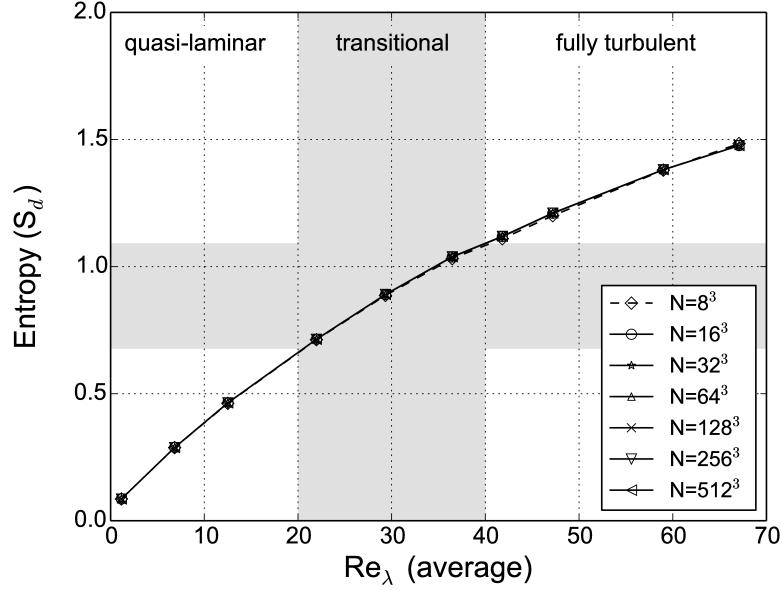


Figure 5.3: Spectral entropy versus average Taylor Reynolds number for all 3D DNS simulations, as a function of the spatial resolution used during post-processing.

table, two different methods have been used to compute $N_{m,\min}$. The first one, shown in bold in the second column, is based on the exact turbulence scales obtained from the simulations, entering Eq. (5.20); the second one is a rough estimate obtained from Eq. (5.19). As observed when comparing both values, Eq. (5.19) delivers a very conservative estimate and will thus lead to additional computational overhead.

The large deviations observed between exact value and estimate mainly result from the fact that Eq. (5.19) is based on the employed grid resolution; in the present DNS, all simulations were performed using a very fine grid resolution, needed only at high Reynolds number, even for the cases with very low Reynolds numbers. This unusual procedure strongly penalizes the estimate from Eq. (5.19), leading to large discrepancies at low values of Re_λ . Keeping this in mind, it is considered that the approximation Eq. (5.19) delivers, in general, a suitable first guess for the minimum number of snapshots needed for the analysis, when characteristic scales are unknown (for instance when considering experiments or LES simulations). Starting from this rough estimate, a refined value can be obtained by changing the employed number of snapshots and checking the outcome.

An independent alternative to check the minimum number of snapshots $N_{m,\min}$ needed for the analysis, is to repeat it with a constant, given spatial resolution (here, the highest resolution with 512^3 grid points has been chosen), but systematically reducing the number of involved snapshots N_m while keeping the same overall time, $\Delta t_{\text{overall}}^s = 2\tau_\Lambda$. This implies that the time interval between two consecutive snapshots Δt_{\min}^s will decrease proportionally to the number of snapshots N_m . Corresponding results are plotted in Fig. 5.4. By comparing Fig. 5.4 and Table 5.3, and considering the highest number of snapshots ($N_m = 50$) as a reference, an excellent agreement is observed:

5.5. Results and Discussion

- Three snapshots are indeed sufficient to obtain the correct value of S_d when $\text{Re}_\lambda < 20$;
- Six snapshots are sufficient for all cases with $\text{Re}_\lambda < 40$;
- Eight snapshots are sufficient when $\text{Re}_\lambda < 50$;
- Ten snapshots are enough for all Reynolds numbers considered in this work, $\text{Re}_\lambda \leq 67$.

It is worth mentioning that a relative error in S_d exceeding 20% is only observed for $N_m = 3$ (a very small number of snapshots) for Reynolds number $\text{Re}_\lambda \geq 30$. This is easy to comprehend, since it is the only case violating the first necessary condition listed at the beginning of this section, $\ln(N_m) \geq S_d$. Here, $\ln(N_m = 3) = 1.099$, a value below that found for S_d in any turbulent flow. It is therefore impossible to analyze in a meaningful manner a turbulent flow with such a small number of snapshots.

To conclude this analysis:

- A small number of snapshots (here, $N_m = 10$ for $\text{Re}_\lambda \leq 67$) are already sufficient to quantify accurately the flow state (quasi-laminar, transitional, or turbulent).
- However, when increasing the turbulence intensity, an increasing amount of snapshots will be necessary to obtain an accurate estimate of the real value of S_d .
- Nevertheless, a small number of snapshots like $N_m = 10$ remain sufficient to delineate between quasi-laminar, transitional, and turbulent conditions in a *qualitative* manner, and this independently of the turbulence intensity.

Going back now to the results discussed in Sect. 5.5.2, it clearly appears that the number of snapshots arbitrarily selected at first, $N_m = 50$, was grossly overestimated. Using so many snapshots for an overall time duration of $\Delta t_{\text{overall}}^s = 2\tau_\Lambda$ leads to a time distance between snapshots far below the Kolmogorov time scale, $\Delta t_{\text{min}}^s \ll \tau_\eta$. Though this is not a real problem, it is a waste of computational resources that should be avoided, since the same information can be obtained using a much smaller data-set as input for the analysis.

5.5.5 2D vs. 3D Analysis

Many experimental measurements access only two-dimensional velocity fields, even if they deliver the three velocity components, for instance when using Stereoscopic Particle Imaging Velocimetry (Stereo-PIV). It is therefore interesting to check if a meaningful two-dimensional analysis of a three-dimensional dataset would be possible. For this purpose, four 2D slices (arbitrarily chosen normal to the z -axis) have been extracted from the 3D DNS dataset (for $z = 0.0$, $z = 0.25L_z$, $z = 0.50L_z$, $z = 0.75L_z$). The results of the analysis using these slices (with three velocity components) are then compared with the values of S_d obtained from the full 3D analysis, as shown in Fig. 5.5.

Obviously, the 2D slices do not contain the entire information concerning the velocity, so that the results are not identical but vary spuriously around the real, 3D value of S_d . However, the obtained variations are quite small (within 10% of each other), highlighting

Table 5.3: Minimum number of snapshots $N_{m,min}$ needed for analyzing the flow state. The bold values in the second column are obtained from the exact DNS scales using Eq. (5.20). In the last column, the estimate values deduced from Eq. (5.19) are presented.

Re_λ (average)	$N_{m,min} = \frac{\Delta t_{overall}^s}{\Delta t_{min}^s}$	
	Exact (Eq. (5.20))	Estimate (Eq. (5.19))
1.15	1-2	20-40
6.84	2-3	44-88
12.51	3-5	53-107
21.97	4-7	62-125
29.34	5-9	66-132
36.47	6-11	69-148
41.81	7-13	71-143
47.20	7-14	73-145
58.99	10-19	75-150
67.08	11-22	76-152

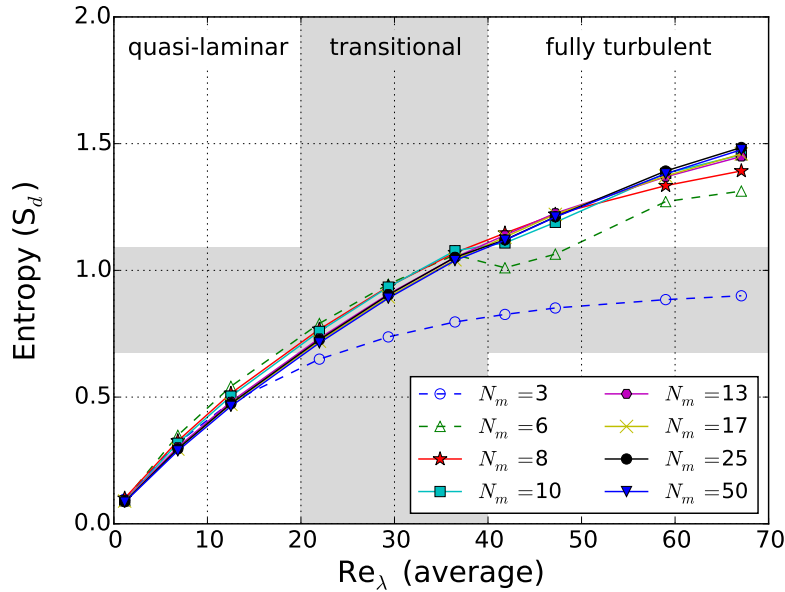


Figure 5.4: Spectral entropy versus average Taylor Reynolds number for all 3D DNS simulations, as a function of the number of snapshots N_m involved in the analysis while keeping the overall time constant, $\Delta t_{overall}^s = 2\tau_\Lambda$.

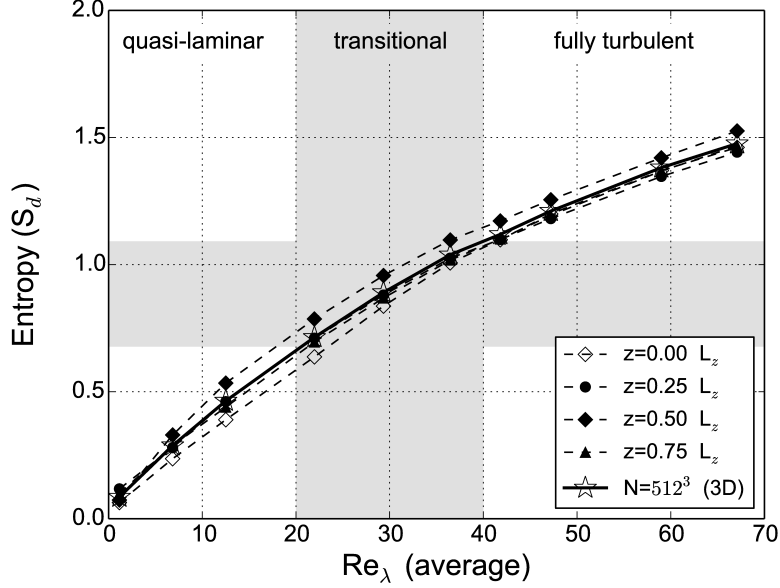


Figure 5.5: Spectral entropy versus average Taylor Reynolds number for all 3D DNS simulations using different 2D slices, compared to the 3D analysis (solid line).

again the robustness of the spectral entropy as an indicator of the flow state. Using $S_d = 1$ as a threshold of transition, separating quasi-laminar from turbulent states, all two-dimensional slices could have been used to correctly predict this condition. Interestingly, the curves fall almost on top of each other for quasi-laminar conditions (which is not surprising), but come also closer to each other at higher turbulence intensity, revealing the increasing homogeneity of turbulence. The largest relative differences are observed within the transition zone.

Finally, it appears that processing two-dimensional slices from a three-dimensional dataset with the approach presented in this work would be sufficient to predict the flow state (laminar, transitional, or turbulent) with an acceptable accuracy for HIT. This would of course not necessarily be the case for flows with strongly anisotropic turbulent features. Nevertheless, due to the isotropic nature of small-scale turbulence, the analysis of slices should still deliver a good approximation in general. Confident in the robustness of the developed approach, two independent application benchmarks can now be considered.

5.5.6 First Benchmark: Three-Dimensional Taylor-Green Vortex (3D-TGV)

As discussed in Sec. 3.15.3, the flow in the 3D-TGV evolves through three regimes: laminar, transition, turbulent. Therefore, it is a perfect candidate to test the validity of spectral entropy. In order to compute the spectral entropy for the time-evolving TGV flow in a meaningful manner, the analysis has been applied for increasing overall time intervals ($t/T_c = [0 - 3], [0 - 5], [0 - 7], [0 - 9], [0 - 11], [0 - 15]$ and $[0 - 18]$), meaning finally that $\Delta t_{\text{overall}}^s \in [3t/T_c, 18t/T_c]$ starting from initialization. In this manner, the different physical processes

described previously are progressively taken into account in the analysis, so that the resulting flow states can be quantified. The number of snapshots N_m involved in the analysis increases proportionally to the time duration.

In order to demonstrate one last time the robustness of the approach, the results obtained when considering more snapshots are summarized in Table 5.4, but show as expected a negligible dependency on this parameter.

The final results are presented in Fig. 5.6(a), which shows the spectral entropy versus time, plotting the value of S_d at the end of the time interval considered for the analysis, $\Delta t_{\text{overall}}^s$. The figure is divided 1) horizontally by a gray region showing the range of S_d corresponding to transition as obtained in Sect. 5.5.2; and 2) vertically by the line $t/T_c = 11$, widely accepted in the TGV scientific literature as the time corresponding to the onset of turbulence, see [88, 166]. As can be seen, Figs. 5.6(a) and 5.6(b) show a perfect agreement between the established vortex dynamics scenario discussed in the scientific literature, Ch. 4, and the entropy threshold obtained in the current study to characterize the flow state.

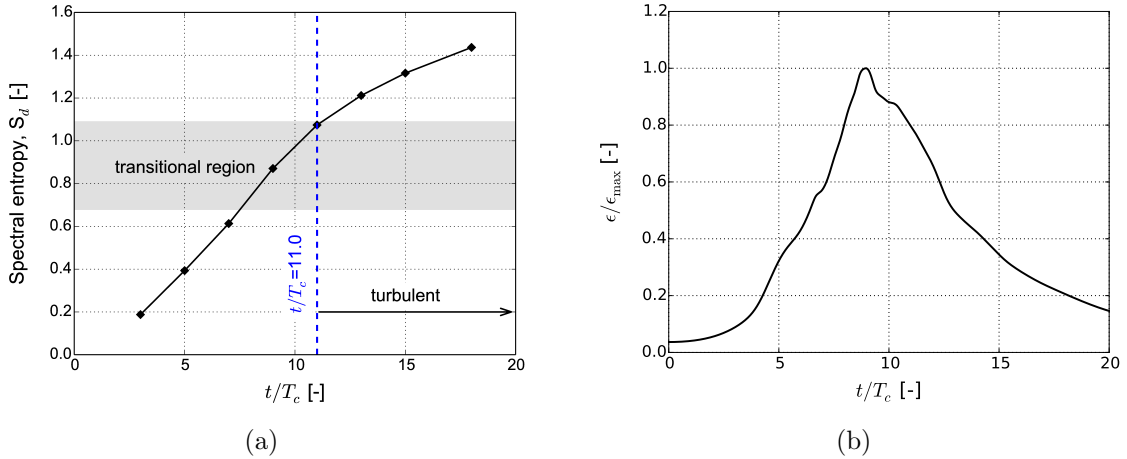


Figure 5.6: Time statistics of 3D-TGV benchmark. (a) Evolution of the spectral entropy S_d computed for increasing values of $\Delta t_{\text{overall}}^s \in [3t/T_c, 18t/T_c]$ starting from initialization, the resulting value of S_d being plotted at the end of the corresponding time interval. (b) Dissipation rate of the kinetic energy computed using DINO simulation.

5.5.7 Second Benchmark: LES of Transitional Flow Within the FDA Nozzle

After having developed a criterion to describe the flow state based on DNS data, it is interesting to check if this approach might be applied to completely different conditions, corresponding to a real application. For this purpose, the same process is now applied to the nozzle benchmark proposed by the U.S. Food and Drug Administration [156]. Corresponding LES data have been obtained at a Reynolds number of 6500 based on the nozzle diameter, as described in [167]. These conditions have been specifically selected since, due to large changes in local diameter, the flow state is expected to be initially laminar, then transition

Table 5.4: Evolution of spectral entropy values for 3D-TGV as function of the number of snapshots N_m .

t/T_c [-]	N_m	S_d
	26	0.1944
[0 – 3]	38	0.1873
	76	0.1875
	32	0.4041
[0 – 5]	63	0.3969
	125	0.3933
	59	0.6203
[0 – 7]	88	0.6167
	175	0.6130
	76	0.8815
[0 – 9]	113	0.8736
	225	0.8705
	92	1.0744
[0 – 11]	138	1.0758
	275	1.0738
	109	1.2143
[0 – 13]	163	1.2129
	325	1.2116
	126	1.3198
[0 – 15]	188	1.3171
	376	1.3161
	151	1.4374
[0 – 18]	226	1.4369
	451	1.4364

to turbulence before re-laminarization occurs. It is therefore particularly suitable to check the threshold values of S_d listed previously. The entire LES data sets are available and will now be post-processed along different planes normal to the main flow direction. The lower part of Fig. 5.7 shows nine spectral entropy values (labeled from 1 to 9) along the corresponding planes depicted in the top part of Fig. 5.7. At each cross-section, all LES mesh cells have been included in the analysis, with all three velocity components.

The obtained results based on S_d fully confirm the statements discussed in [167]. Using $S_d \approx 1$ as an indicator of transition, the FDA nozzle starts from a fully laminar flow ($S_d \approx 0$), undergoes transition to turbulence between sections 3 and 4, just after the sudden expansion, before getting back to laminar conditions around section 8. This shows that the methodology first developed by relying on academic DNS datasets can also be directly employed to analyze realistic flow conditions. The spectral entropy can thus be used as a user-independent indicator of the local flow state (laminar, transitional, or turbulent), either in space or in time, opening the door for hybrid simulations of such cases.

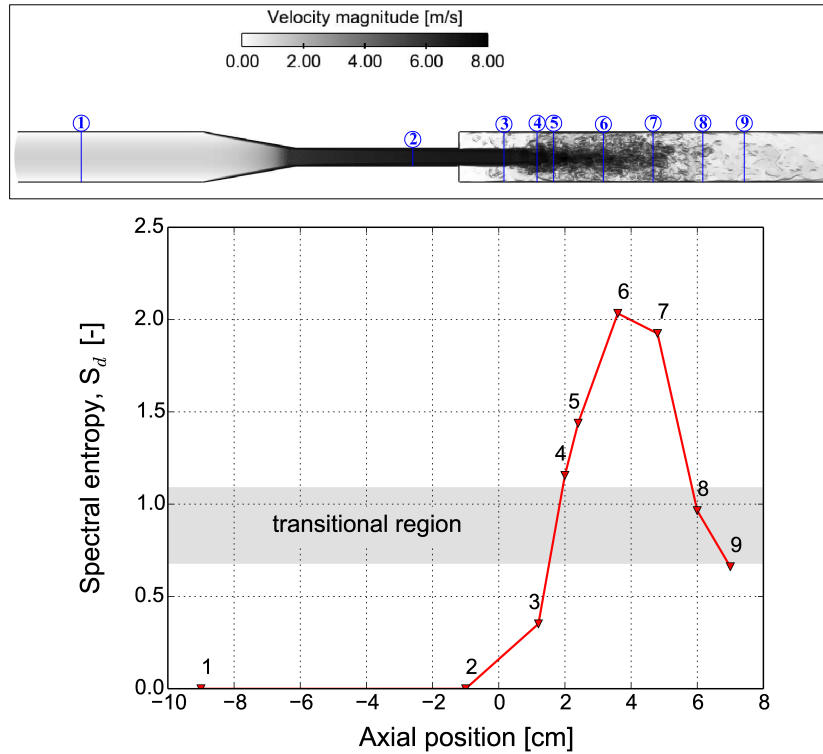


Figure 5.7: Analysis results for the FDA nozzle, with flow from left to right. Top: instantaneous velocity magnitude in a central 2D plane, as obtained by LES; the blue lines with the labels refer to the locations of the analyzed cross-sections. Bottom: spectral entropy S_d obtained at the different cross-sections, the numbers from 1 to 9 corresponding to the labels in the top figure.

5.6 Conclusions

Based on reference DNS datasets obtained at ten different Taylor Reynolds numbers covering all flow regimes from laminar to fully turbulent, the spectral entropy S_d computed from the eigenvalues of the temporal autocorrelation function is proposed as a quantitative indicator of the flow state. It is a user-independent quantity that can be computed in an automatic manner, delivering a single scalar, non-dimensional quantity starting from a three-dimensional, unsteady velocity field. The tests have shown that it is a robust estimator, with only limited impact of the resolution in space and time during post-processing. Additionally, two-dimensional fields appear to be sufficient for determining the flow state, at least under locally isotropic conditions. Therefore, this same estimator could be readily employed to analyze experimental data sets obtained by planar techniques.

The generality of these findings has been successfully challenged by applying the same

5.6. Conclusions

methodology to (1) DNS results of the three-dimensional Taylor-Green vortex benchmark at $Re=1600$ and to (2) LES results of the transitional flow within the FDA benchmark nozzle. Obviously, further tests will be needed to verify the universality of the threshold values for S_d . At the current state of this analysis, $S_d \approx 1$ appears to be a suitable indicator of transition, with $S_d \leq 0.7$ identifying laminar and quasi-laminar conditions, and $S_d \geq 1.1$ denoting turbulent flow. With the help of these thresholds, hybrid CFD codes could locally detect a region with a different flow state and, therefore, determine the proper local solver.

Having now a suitable measure of turbulence intensity, different method suitable for coupling chemistry with a turbulent flow will be describe.

Chapter 6

Model Reduction and Modal Decomposition

6.1 Introduction

As already discussed in previous chapters, the numerical simulation of 3D turbulent combustion, with/without spray, is computationally expensive and requires extremely large supercomputers to carry out the simulation and to save the results, which are several terabytes in size. Therefore, two different approaches are classically utilized to reduce the computational run time and/or size of the output results: (1) reducing the run time using a reliable model along with DNS, (2) reducing the size of the output by saving coarse results, then applying the modal decomposition techniques. In this chapter, two model reduction techniques are used: (a) one-dimensional turbulence model (ODT) which is a stochastic model considered as a spatial reduction, (b) tabulation chemistry (FPI). For the other aspect, two modal decomposition methods are employed to perform post-processing on the coarse resolution result of the well-resolved simulation: (1) proper orthogonal decomposition (POD), and (2) dynamic mode decomposition (DMD). The interest of these modal decomposition methods is to extract the flow structure from coarse resolution results or even from 2D descriptions.

In DNS-DPS simulations, no further reduction is suggested in this dissertation for the discrete phase (liquid droplets). All previously suggested reductions are applied to the continuous phase only. Hence, in this chapter these techniques will be tested and validated only on pure gas applications as well. In future, using these techniques with spray combustion is straightforward and does not require any significant modifications.

6.2 Spatial Reduction: ODT

6.2.1 Objectives

This part investigates the ability of the one-dimensional turbulence model (ODT) to predict occurrence of ignition and ignition probability in a reacting gas mixture submitted to turbulence. Since ODT is computationally very efficient, this would be a major progress for

safety-relevant applications. ODT delivers fast predictions, while still capturing the most relevant physicochemical processes controlling ignition. However, ODT contains some empirical parameters that must be set by comparison with reliable reference data. To set these parameters and check the accuracy of the resulting ODT predictions, they are compared in this chapter with reference data from the DNS. DNS is recognized as the most accurate numerical tool to investigate ignition in turbulent flow. However, it requires enormous computational times, so that it cannot be used for practical safety predictions. As demonstrated in this part, ODT realizations can be used to correctly predict the occurrence of ignition in turbulent premixed flames while saving more than 90% of the required computational time, memory and disk space, thanks to validation and comparison with DNS. Part of this work has been submitted to the International Journal of Physical Chemistry (*Zeitschrift für Physikalische Chemie*).

6.2.2 State of The Art

The physicochemical processes leading to ignition of a reactive mixture have been extensively investigated during the last decades, demonstrating both the importance and the complexity of this issue. Most early studies of ignition phenomena from the point of view of safety analysis could only rely on experimental measurements and simplified theoretical models, like those reported in the seminal book of Lewis and von Elbe [168]. This is due to the fact that ignition is a fully coupled process involving two main aspects: 1) chemistry and 2) heat transfer, both mostly in a turbulent environment. Chemical kinetics describe the evolution of all radicals needed for the onset of ignition. A quantitative investigation taking this point into account can only be realized if all relevant chemical pathways are known, if the corresponding reaction parameters have been determined accurately, and if the available computational power is sufficient to carry out corresponding simulations, involving possibly hundreds or thousands of individual reactions. The challenge associated with this issue hence completely depends on the composition of the considered mixture, in particular on the fuel. Secondly, heat exchange processes with the surroundings will be essential to decide if the ignition event will be successful and lead to a fully developed flame, or if it will fail after a short time. In order to take this aspect into account, all relevant heat exchange paths must be described accurately. A reliable quantitative study then necessitates an excellent description of the local turbulent flow conditions and of all relevant transport properties. The challenges associated with this second aspect depend on the flow conditions (laminar vs. turbulent) and on the retained configuration (premixed vs. non-premixed, possible interaction with surfaces, possible importance of radiative heat transfer, of evaporation...).

In this chapter, only the ignition of premixed systems is considered, so that fuel and oxidizer are always well-mixed in advance. Due to the progress in computing power, simulations taking into account in a realistic manner the surrounding turbulent flow conditions, and thus the convective and conductive heat exchange, became possible in the early nineties. Corresponding results are found for instance in [72, 169] for two-dimensional (2D) flows and/or employing a single-step chemical reaction to describe oxidation. The obtained observations have been discussed further in [10, 11], demonstrating in particular the interest of direct numerical simulations (DNS) to investigate such configurations. Nevertheless, the probabil-

ity of successful ignition could not be considered using DNS and realistic chemical kinetics at this early stage. Later works went a step ahead to consider more realistic kinetics in 2D flows (e.g., [170]) or in 3D conditions but with a simplified kinetic description (one-step chemistry, like for instance in [171–173]). Later DNS studies indeed considered 3D flames with complex kinetic schemes (see e.g., [50, 174, 175]) but did not investigate specifically ignition probability.

DNS is indeed recognized as the most accurate tool to investigate ignition of a premixed system. However, quantifying ignition probability in connection with turbulence requires many realizations, due to the stochastic nature of turbulent coupling. Repeating in a parametric study many DNS in 3D while taking into account complex kinetics is simply impossible on current computers. Therefore, a suitable alternative is needed, possibly in connection with a few isolated DNS simulations. After checking thoroughly the scientific literature, a proper tool appears to be the one-dimensional turbulence model (ODT), which was developed first for cold flows by Kerstein [176]. This model has undergone continual improvement since then. A vector formulation of this model was introduced by Kerstein et al. [177]. Ashurst and Kerstein [178] developed a variable-density formulation, and also introduced a spatial formulation of the model in which all variables evolve along lines in space, invoking standard boundary layer assumptions. This variable-density formulation is crucial for combustion simulations. ODT has been applied for many different combustion systems; Echehki et al. [179] applied the ODT model to turbulent jet diffusion flames. Hewson and Kerstein used the model directly to study syngas flames [180], including a detailed study of flame extinction and reignition [181]. Gupta and Echehki [182] investigated autoignition in spatially-evolving jet diffusion flames. Punati et al. [183] compared ODT with DNS for a temporally-evolving jet diffusion flame. Lignell and Rappleye [184] studied extinction and reignition in spatially-evolving jet flames. Jozefik et al. [185] evaluated the ability of ODT to simulate reactive counterflow flames by comparing with a DNS dataset. Unfortunately, all these interesting studies have considered non-premixed systems, and cannot therefore directly be used for our current objectives.

Very recently, Punati et al. [186] performed ODT simulations of a planar, premixed hydrogen jet flame. They investigated mostly flame propagation processes. They found that standard ODT is not able to reproduce correctly these conditions, and highlighted possible further development.

In this chapter, ODT is used as complement to DNS in order to investigate ignition probability. DNS are first performed for reference cases. After calibrating the ODT parameters with these reference values, it is checked that ODT can indeed be used to evaluate the occurrence of ignition. Based on these findings, ODT could then be used as standalone tool to compute ignition probability for safety-relevant conditions.

Since ignition involves complex kinetic paths, it is absolutely necessary to take into account sufficiently accurate reaction schemes in the numerical analysis. Appropriate kinetic schemes will be considered in this section for propane/air mixture. To the authors' knowledge, it is the first time that ODT is considered in a premixed configuration involving such a complex fuel.

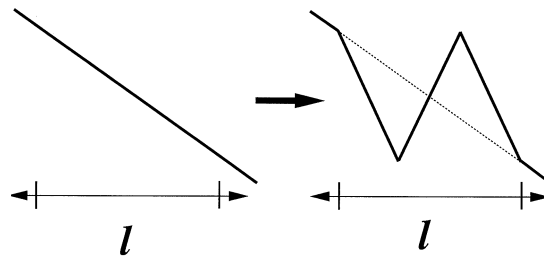


Figure 6.1: A schematic illustration of the triplet map in ODT [179].

6.2.3 Governing Equations

DNS and ODT involve different sets of equations and formulations. DNS are further performed using a low-Mach number solver in DINO; the complete equations are reviewed in Ch. 3. The ODT formulations are described in what follows.

ODT Model Equation

In the low-Mach number DNS solver, the diffusion and advection processes are considered simultaneously. On the other hand, the ODT model handles these processes in two separate, but coupled steps. The following is an explanation of the ODT concept as reviewed in [184]. The diffusive advancement is simulated by solving a one-dimensional form of the Navier-Stokes equation, without advection term nor fluctuation pressure. Instead, the diffusive advancement is implemented using a Lagrangian finite-volume method, in which cell faces move with the mass-average velocity. In the ODT simulation, the cells expand or contract due to flow dilatation arising from heat or mass transfer processes. More details about these diffusive equations and their connection to the Navier-Stokes equation can be found in [184, 187].

The omitted terms are modeled by concurrent mapping events of the scalar fields, corresponding to the turbulent advection processes. Advection processes representing turbulent transport are implemented as discrete eddy events, involving triplet maps that rearrange the fluid domain and mimic the effect of turbulence. These triplet maps occur concurrently with the diffusion processes, and are parameterized by a size l , position y_0 , and time scale τ . The triplet map is implemented, as illustrated in Fig. 6.1, by taking all variable profiles in the eddy region, making three copies, compressing each of them spatially by a factor of three, and replacing the original profiles by the three compressed copies with the middle copy inverted spatially.

The triplet map is conservative of all quantities and it can be defined as

$$f(y) = \begin{cases} 3(y - y_0) & \text{if } y_0 \leq y \leq y_0 + l/3, \\ 2l - 3(y - y_0) & \text{if } y_0 + l/3 \leq y \leq y_0 + 2l/3, \\ 3(y - y_0) - l & \text{if } y_0 + 2l/3 \leq y \leq y_0 + l, \\ y - y_0 & \text{otherwise.} \end{cases} \quad (6.1)$$

The ODT velocity profile evolves through the specification of the occurrences of eddy events. The eddy selection process is stochastic and follows the variable density formulation first introduced in [178], modified as described in [184]. In this formulation, the eddy time scale τ for a candidate eddy (y_0, l) is computed using (1) a measure E_{kin} of the local kinetic energy in the eddy region, and (2) the scaling: $E_{\text{kin}} = 0.5\rho_0 l^3 / \tau^2$, where ρ_0 is a measure of density in the eddy region. The local rate (per square length) of each eddy is

$$\lambda' = \frac{1}{l^2 \tau}, \quad (6.2)$$

and the total rate of all eddies is

$$\Lambda' = \int \int \lambda' dy_0 dl. \quad (6.3)$$

Therefore, the joint PDF of eddy parameters y_0 and l is

$$P(y_0, l) = \lambda'(y_0, l) / \Lambda'. \quad (6.4)$$

Eddy occurrences can be sampled from a Poisson distribution with mean rate Λ' , with y_0 and l parameters sampled from $P(y_0, l)$.

In practice, evaluating $P(y_0, l)$ is prohibitively expensive since it changes continuously as the velocity profile changes. In fact, the time scales of all possible eddies would need to be computed to obtain $P(y_0, l)$, which would then be used to sample the next eddy. But after a single eddy were implemented (and associated diffusive advancement occurs), $P(y_0, l)$ would need to be recomputed. Instead, a thinning process [188] based on the rejection method [189] is used. Eddies are sampled from an analytic approximation to $P(y_0, l)$, denoted $\tilde{P}(y_0, l)$, and accepted with probability

$$Pa = \frac{\Delta t_s}{\tau \tilde{P}(y_0, l) \cdot l^2}. \quad (6.5)$$

$\tilde{P}(y_0, l)$ is modeled as $\tilde{P}(y_0, l) = f(l) \cdot g(y_0)$. The PDF $g(y_0)$ is uniform on the domain $y_0 \leq 0 \leq L_y - 1$, where L_y is the domain length and $f(l)$ is given in [184]:

$$f(l) = \frac{-2l_p}{l^2} \left(\frac{\exp(-2l_p/l)}{\exp(-2l_p/l_{\max}) - \exp(-2l_p/l_{\min})} \right), \quad (6.6)$$

6.2. Spatial Reduction: ODT

where l_p , l_{\min} , and l_{\max} are user-specified most probable, minimum, and maximum eddy sizes, respectively. Values used in the simulations are $l_p/L_y = 0.05$, $l_{\max}/L_y = 1$, and $l_{\min}/L_y = 0.005$. The function $f(l)$ reasonably approximates the shape of the eddy PDF. The accuracy of $f(l)$ only affects the eddy sampling efficiency, which is not the limiting step in the ODT simulations (the diffusive-reactive advancement is). In Eq. (6.5), the time Δt_s between the eddy trials is sampled from a Poisson distribution with mean $\overline{\Delta t_s}$. This mean sample time is initialized as $\overline{\Delta t_s} = 0.1 \overline{Pa} \cdot \overline{\Delta y^2} / \nu n$, where ν is kinematic viscosity, n is the number of grid points, $\overline{\Delta y^2}$ is the average grid size, and \overline{Pa} is a specified average acceptance probability (set to 0.02). $\overline{\Delta y^2} / \nu$ is a diffusive time at the grid cell size (an approximate lower bound on an eddy timescale). The factor $1/n$ allows sampling of this small diffusive scale eddy in all cells (on average). The 0.1 multiplier is a conservative factor. $\overline{\Delta t_s}$ is dynamically adjusted during the simulation to maintain the specified \overline{Pa} .

The eddy time scale τ , which is used to specify the eddy acceptance probability, can be computed as

$$\frac{1}{\tau} = C \sqrt{\frac{2}{\rho_0 l^3} (E_{\text{kin}} - Z E_{\text{vp}})}, \quad (6.7)$$

In this equation, $\rho_0 = l^{-3} \int \rho K(y)^2 dy$ is a measure of the density in the eddy region for variable density flow, with $K(y)$ the kernel function used in the vector formulation of ODT. E_{vp} is a viscous penalty term; it suppresses small eddies that are subject to strong viscous damping and modeled using scaling arguments as $E_{\text{vp}} = 0.5 \bar{\mu}^2 / \bar{\rho} l$, where $\bar{\rho}$ and $\bar{\mu}$ are the average density and viscosity in the eddy region. Finally, the parameters C and Z are adjustable model parameters. For open domains, a restriction must be imposed on the eddy selection process in order to prevent unphysically large eddy events from occurring. Suppression of large eddies is obtained using the elapsed time method, following [179, 180, 184, 187]. The corresponding criterion reads

$$t > \beta \tau. \quad (6.8)$$

It is applied in such a way that the eddies are only allowed if the elapsed time is greater than $\beta \tau$, where β is an adjustable parameter as well. Therefore, there are three significant empirical parameters in ODT that need to be adjusted; C , Z , and β . For this purpose, comparing with reference DNS data is an excellent opportunity.

6.2.4 Numerical Settings

A temporally-evolving planar jet configuration has been considered in this section. The interest of this specific configuration for DNS studies has been discussed in more detail in Ch. 4 [110]; this configuration is ideal for ODT, since it is statically 1D. In this setup, a layer of pre-heated unburned premixed mixture is located in the center (central jet zone) of the computational domain, whereas left and right layers (co-flow zones) contain unburned premixed mixture at a temperature of 300 K. Initial profiles of temperature and major species are illustrated along a 1D-line following the y -direction of the domain, as shown

in Fig. 6.2(a). The comparisons rely on a 3D simulation for DNS, while 1D simulations are sufficient for ODT, both evolving in time. The corresponding comparison is explained schematically in Fig. 6.2(b). In this figure, contours of instantaneous temperature field are presented as a typical output from DNS, whereas the white line represents the ODT line direction. In the 3D DNS domain, the middle slab (central jet zone) moves with jet speed U_j . The surrounding co-flow zone is quiescent. An isotropic turbulent flow field is generated prior to the DNS simulation, and is used to trigger the turbulence in the central jet zone, using a hyperbolic tangent function to filter out the turbulence in the coflow. For DNS simulations, the flow is considered periodic in streamwise direction and spanwise direction, whereas it has outflow boundary conditions in the crosswise direction. The DNS simulation is performed in a domain with dimension of L_x (streamwise direction) = 0.7 cm, L_y (crosswise direction) = 0.5 cm, and L_z (spanwise direction) = 0.25 cm. This domain has been discretized over $n_x = 384$, $n_y = 257$, and $n_z = 128$ grid points, respectively. In ODT simulations, the 1D domain has a length of $L = 0.5$ cm, initially discretized with 256 grid cells. However, it is important to mention that the ODT code used here relies on dynamic mesh adaption [187]. Therefore, the number and size of the cell is adapted automatically based on the underlying eddies' properties.

In this section, a stoichiometric mixture of propane (C_3H_8)/air is employed to examine the ignition occurrence in premixed, sheared turbulent flames. Again, the initial distribution of temperature and major species is illustrated in Fig. 6.2(a). The propane oxidation is described in both DNS and ODT by the GRI-mech 3.0 kinetic mechanism [106], which is implemented by relying on the open-source library Cantera for obtaining all physicochemical and thermodynamic properties. The GRI-mech 3.0 is a well-established, optimized mechanism, built from a compilation of 325 elementary chemical reactions, involving $N_s = 53$ chemical species. This mechanism has been mainly optimized to describe natural gas oxidation. The underlying optimization process did not explicitly include targets relevant to pure propane. However, many studies (e.g., [190, 191]) compared experimental results with numerical ones based on GRI-mech 3.0 for propane flames, and revealed that this mechanism agrees very well with experimental results for propane oxidation.

The DNS simulations, again, have been conducted using DINO. The C++ parallel code developed by Lignell and co-workers [187] is used for the ODT simulations. Both codes have been running on SuperMUC. The parallelization in DNS relies on domain-decomposition implemented with Message-Passing Interface (MPI). For ODT, parallelization is performed by considering simultaneously many different independent realizations; therefore, no communication is required.

6.2.5 Results

In this section four cases will be tested, as documented in Table 6.1. All these cases have the same initial uniform mixture (stoichiometric C_3H_8 /air), but different initial maximum temperature (temperature in the central jet region, see Fig. 6.2(a)). These cases have been selected based on preliminary studies, since autoignition will succeed in two of them ($T_{\max} = 1600$ K, $T_{\max} = 1700$ K) and fail for the other two conditions ($T_{\max} = 1400$ K, $T_{\max} = 1500$ K). Table 6.1 summarizes the properties of these cases for DNS and ODT. There, T_{\max} , ν_j ,

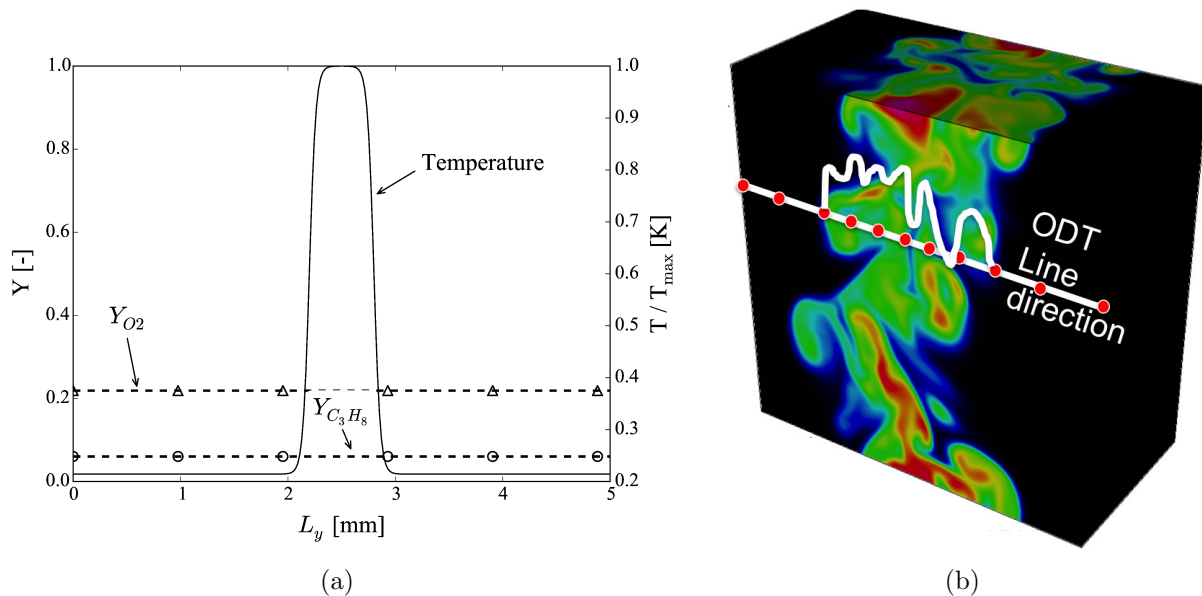


Figure 6.2: Numerical settings; (a) Schematic distribution of initial temperature and major species mass fractions for autoignition tests. (b) Instantaneous DNS result in the 3D domain, showing the temperature field as color contours. The white thick line along the crosswise direction, with a profile plotted along it, represents a typical 1D ODT simulation.

Table 6.1: Initial properties of the four cases considered to investigate autoignition with both DNS and ODT

Case	T_{\max}	U_j [m/s]	ν_j [m ² /s]	Re_j	autoignition occurrence
Case I	1400	130	2.01×10^{-4}	388.06	fails
Case II	1500	150	2.25×10^{-4}	400.00	fails
Case III	1600	180	2.51×10^{-4}	430.00	success
Case IV	1700	200	2.77×10^{-4}	433.21	success

and Re_j are maximum temperature of the mixture, kinematic viscosity, and the Reynolds number in the jet region, respectively. For all cases, $Re_j = U_j H / \nu_j$ is kept around 400, so that turbulence intensity remains similar. In all simulations and cases, the jet width is kept as $H = 0.6$ mm and the kinematic viscosity of the co-flow remains 1.49×10^{-5} m²/s. The time in this section is nondimensionalized using the jet flow time scale $\tau_j = H / U_j$.

Even though the initial profiles for both DNS and ODT are identical, it does not mean that the turbulence-flame interaction processes are exactly the same. To obtain the same turbulence structure and scales, the ODT parameters (C , Z , and β) first need to be tuned in an appropriate manner. After setting the underlying parameters based on DNS as reference data, ODT will be used as standalone tool and compared with the DNS in order to evaluate the possibility of using ODT to generate a probability map for different parameters, opening the door for later systematic studies relevant for safety predictions.

ODT parameter tuning

In the next sections, the ensemble-averaged statistics in DNS are obtained by computing the mean values over the streamwise and spanwise directions. The ensemble-averaged in the ODT is obtained by averaging over 544 independent realizations. This number of realizations is corresponding to the number of processors used simultaneously on SuperMUC machine for ODT simulations (34 nodes \times 16 cores).

Eddy rate parameter C

The eddy rate parameter C plays a very important role in the ODT simulation, since it quantifies turbulent transport. Therefore, it is roughly analogous to the coefficient of an eddy-viscosity model, with the distinction that it tunes the advancement of a temporally- and spatially-resolved unsteady simulation, rather than an ensemble-averaged state [187]. Figures 6.3 - 6.6 show the comparison between DNS and ODT for three different values of C (2.5, 5.0, 10.0), while retaining $\beta = 0.8$ and $Z = 200$. This initial guess for β and Z is obtained based on our own experience and on the observations discussed in [183]. In all cases, $C = 2.5$ leads to ODT temperature profiles in good qualitative agreement with DNS, but with a quantitative difference. For Case I at early simulation times, ODT with $C = 2.5$ gives good agreement with DNS as seen from Fig. 6.3(a); but it increasingly deviates with time (Fig. 6.3(b) and 6.3(c)). A similar behavior is observed for Case II, but with a larger deviation, as seen from Figs. 6.4(a)-6.4(c). Although $C = 2.5$ does not lead to a perfect agreement at all times, it is still sufficient to predict ignition success, which is the central issue of this project.

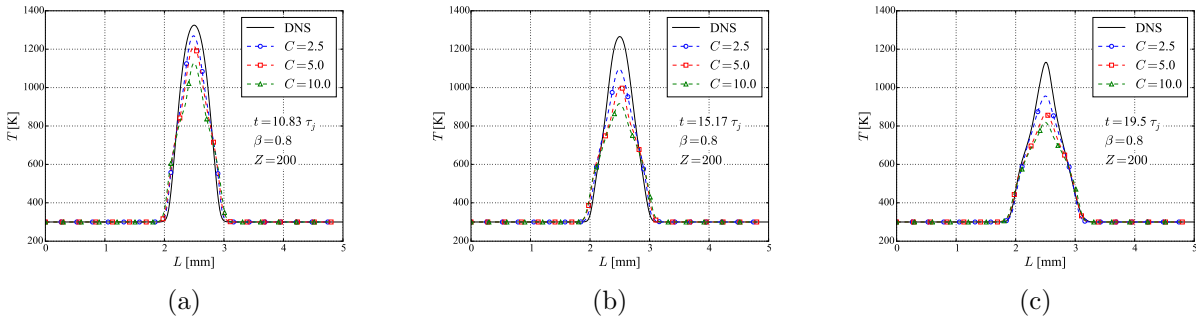


Figure 6.3: Time-evolution of ensemble-averaged temperature of Case I

Unfortunately, Figure 6.5 shows that ODT with these parameters does not predict correctly autoignition for Case III. Nevertheless, it is observed that decreasing the value of C (within chosen range: 2.5 - 10) improves the agreement between ODT and DNS.

On the other hand, decreasing C to 2.5 is sufficient in Case IV to correctly predict successful ignition. The question remains, why ODT fails in Case III but succeeds in Case IV? This is because increasing temperature in Case IV smoothed out the large eddies in the ODT simulation, preventing unphysical diffusion and mixing, which was not the case in Case III. This takes us to the second important parameter, β , which is used to suppress

6.2. Spatial Reduction: ODT

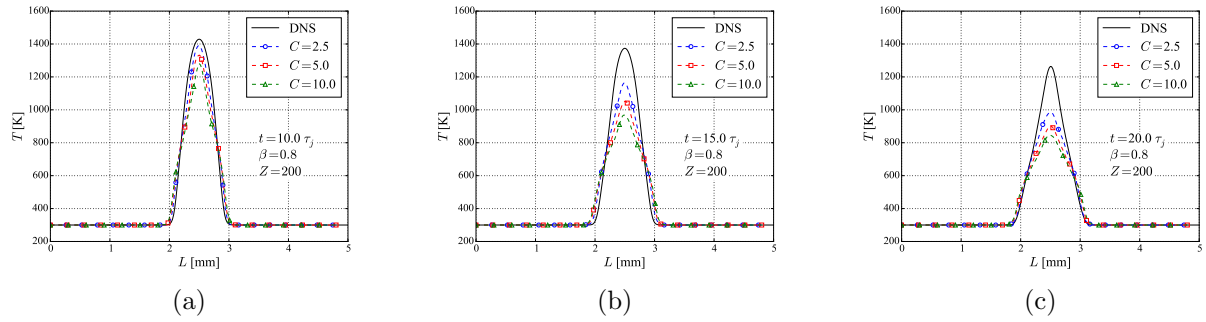


Figure 6.4: Time-evolution of ensemble-averaged temperature of Case II

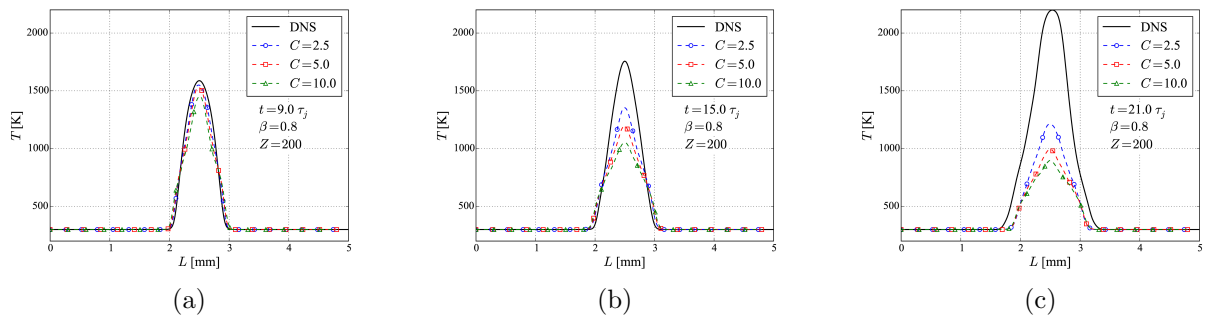


Figure 6.5: Time-evolution of ensemble-averaged temperature of Case III

such unphysical eddies. Before considering β , it is clear that keeping $C = 2.5$ is the best choice among the three values investigated. Considering further tests and after discussing with experienced ODT users, decreasing C further would lead to excessively smooth profiles, which would not reproduce any more the physical reality. Hence, $C = 2.5$ will be kept throughout in what follows.

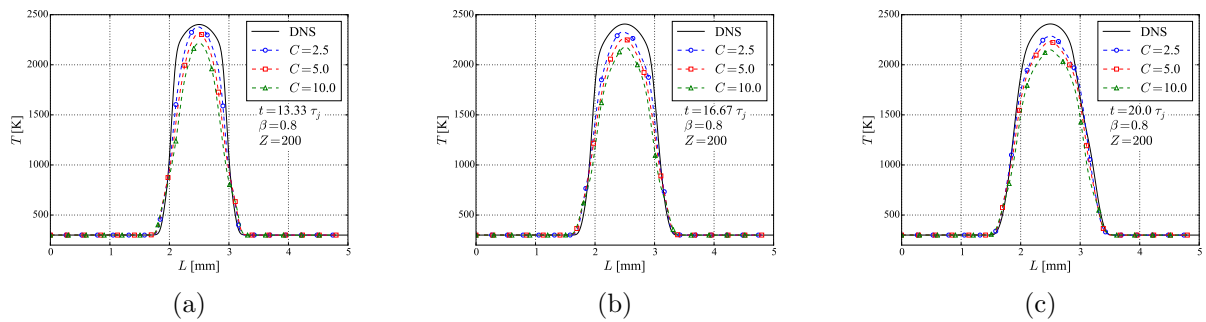


Figure 6.6: Time-evolution of ensemble-averaged temperature of Case IV

Large-eddy suppression parameter β

In this study, a strong large-eddy suppression mechanism is required to prevent unphysically large eddies from occurring in open domains, as already discussed before. These large eddies can have a strong impact on overall turbulent entrainment and mixing rates. The impact of β on the temperature profile is checked by choosing values of $\beta = 0.8, 1.0, 1.2, 1.5$, while keeping $C = 2.5$ and $Z = 200$. The results are illustrated in Figs. 6.7-6.10. It is observed that increasing β gives a better agreement with DNS simulations for the temperature profile. Looking closer at Case I, it is found that at early times (Figs. 6.7(a) and 6.7(b)) ODT with $\beta = 1.5$ shows best comparison to DNS. Later (Fig. 6.7(c)) DNS profiles are found between curves of $\beta = 1.5$ and $\beta = 1.2$. In Case II, ODT with $\beta = 1.5$ is always the best choice (Fig. 6.8); still, ODT with $\beta = 1.2$ is close to the DNS results.

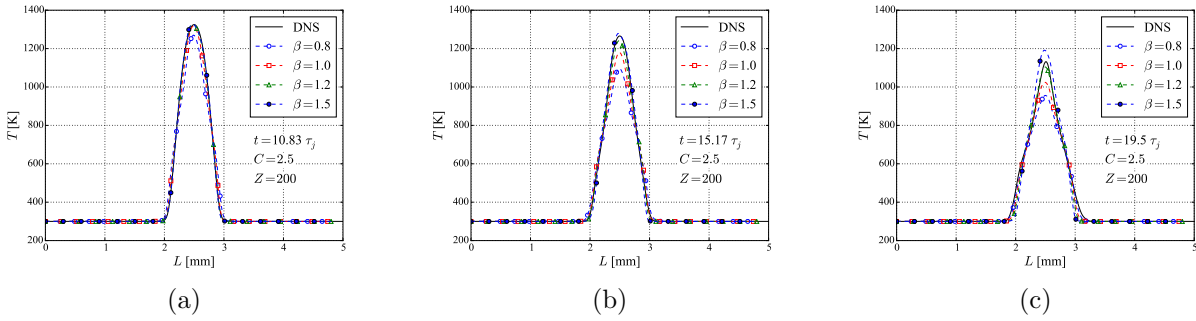


Figure 6.7: Time-evolution of ensemble-averaged temperature of Case I

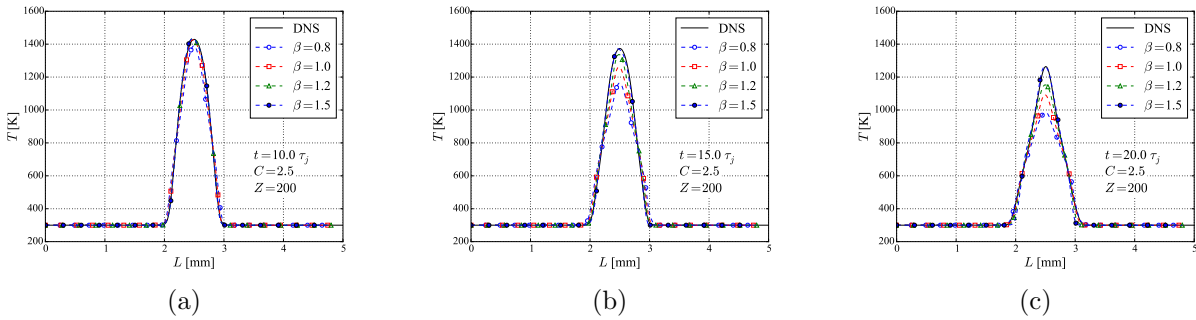


Figure 6.8: Time-evolution of ensemble-averaged temperature of Case II

As discussed in the previous section, the third case (Case III) is the most critical one, since choosing wrong parameters for ODT will lead to a wrong prediction concerning ignition success. Looking at Fig. 6.9, it is found that ODT with $\beta = 1.2$ and 1.5 both predict autoignition correctly. However, ODT with $\beta = 1.2$ underestimates the temperature profile at later times (Fig. 6.9(c)). It is also seen that ODT with $\beta = 0.8$ and 1.0 underpredicts the temperature profile and leads to the wrong prediction.

6.2. Spatial Reduction: ODT

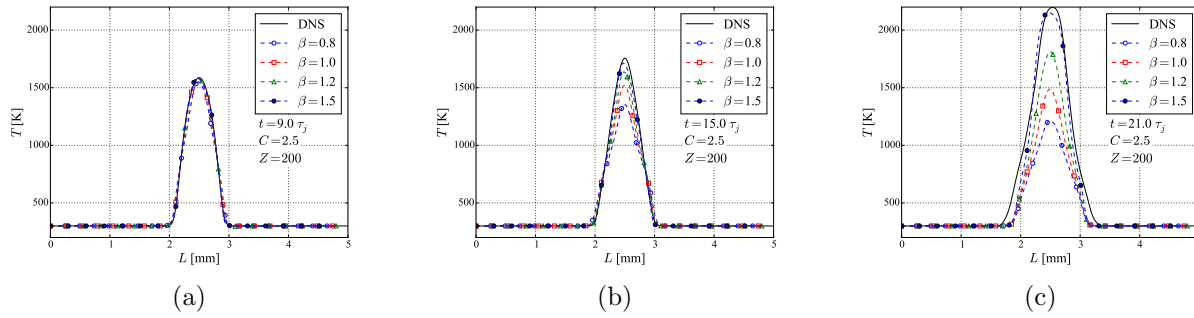


Figure 6.9: Time-evolution of ensemble-averaged temperature of Case III

As discussed before, Case IV has a high temperature, which is smoothing out large eddies, decreasing turbulent mixing. Therefore, changing $\beta = 1.0$ to 1.2 and 1.5 does not change much the observations in this case.

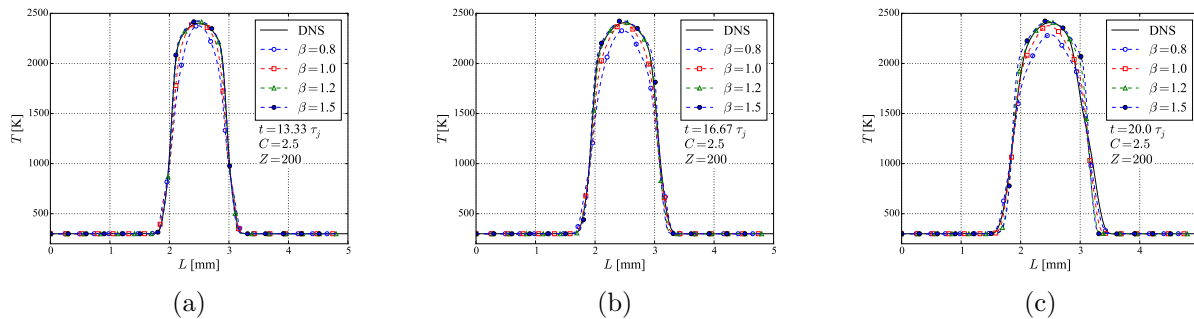


Figure 6.10: Time-evolution of ensemble-averaged temperature of Case IV

In summary, choosing a value of β between 1.2 and 1.5 while keeping $C = 2.5$ leads to an excellent agreement between ODT and DNS, leading to correct predictions of ignition occurrence or failure for the tested conditions.

Viscous penalty parameter Z

The viscous penalty parameter Z is used to suppress small eddies. Usually, Z has a very small impact compared to the other two parameters (C and β). This is confirmed for Cases I, II and IV in Figs. 6.11, 6.12, and 6.14, respectively. Changing Z from 10 to 200 (while keeping $C = 2.5$ and $\beta = 1.5$) does not change in any noticeable way the temperature profiles or the occurrence of ignition. However, a slight impact of Z is observed in Case III (Fig. 6.13), where ODT with $Z = 200$ shows a much better agreement compared to that generated by ODT with $Z = 10$. Hence, $Z = 200$ will be used for all further simulations.

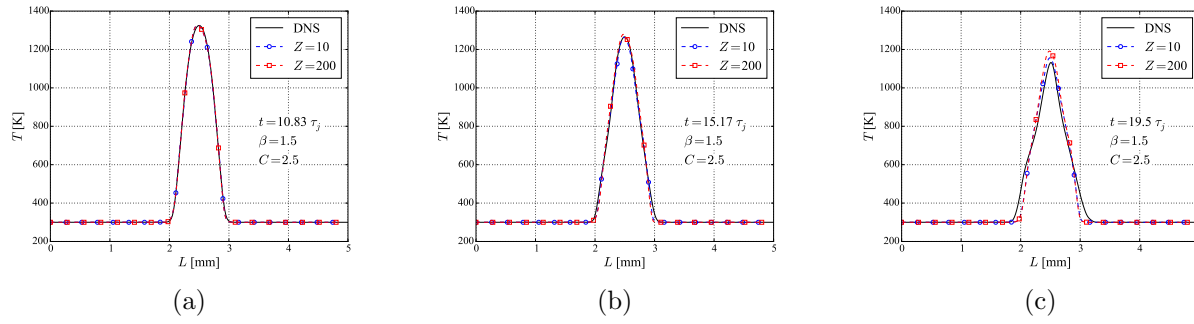


Figure 6.11: Time-evolution of ensemble-averaged temperature of Case I

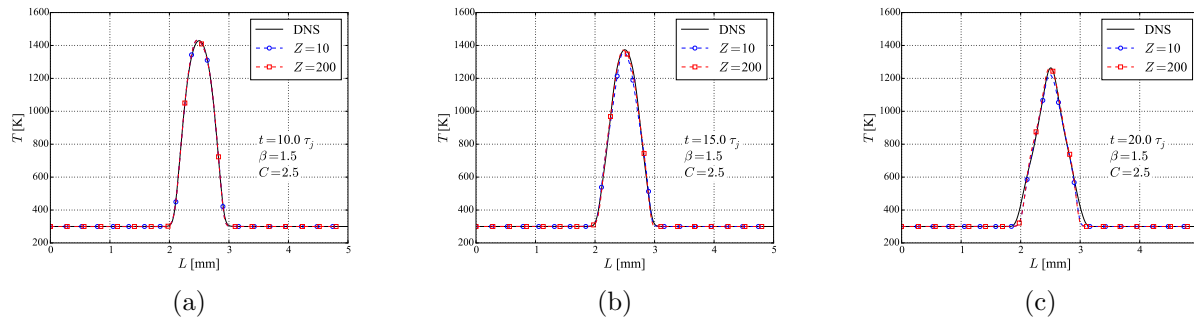


Figure 6.12: Time-evolution of ensemble-averaged temperature of Case II

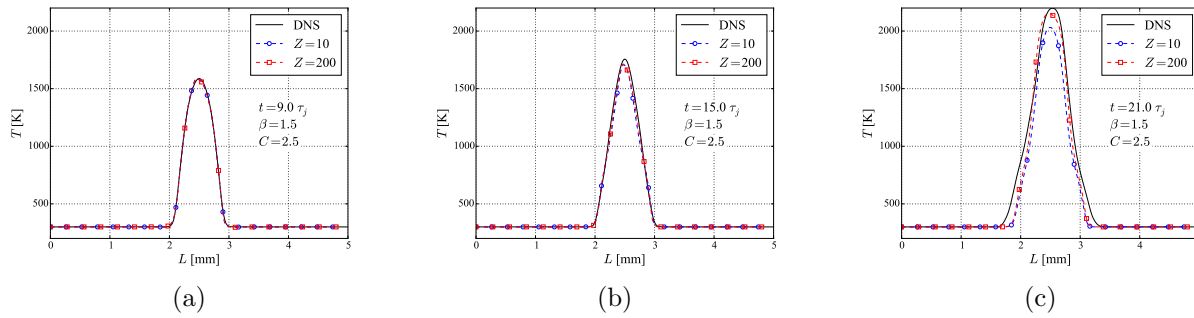


Figure 6.13: Time-evolution of ensemble-averaged temperature of Case III

ODT versus DNS

After completing the adjustment of all ODT parameters, it is now time to have a deeper look at the ODT simulations, and see how many details can be obtained from ODT.

ODT realization with the full DNS domain

Figures 6.15-6.18 show instantaneous profiles of the temperature field in the DNS and ODT domain. These figures demonstrate the similarity between the outputs of DNS and ODT. In

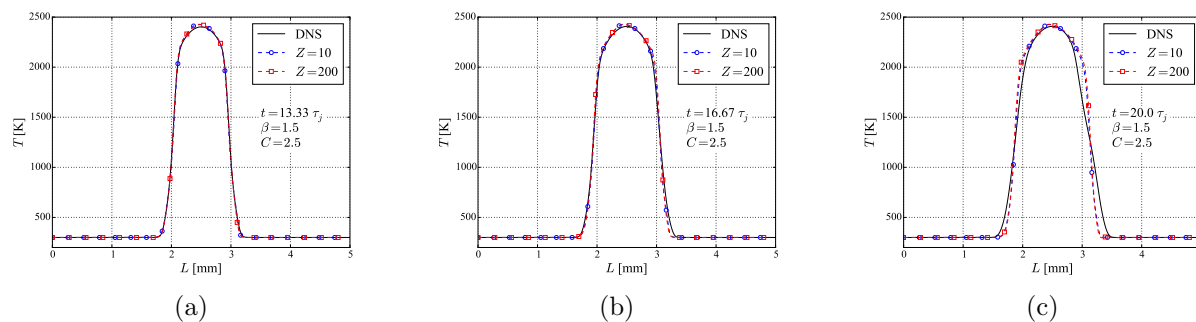
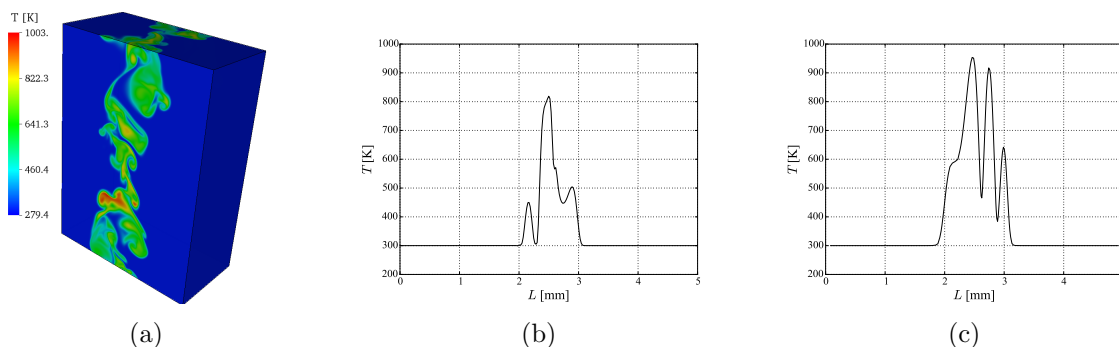


Figure 6.14: Time-evolution of ensemble-averaged temperature of Case IV

order to facilitate comparison, a line along the crosswise direction of the DNS domain is taken (Figs. 6.15(b), 6.16(b), 6.17(b), and 6.18(b)) and is qualitatively compared to a single ODT realization (Figs. 6.15(c), 6.16(c), 6.17(c), and 6.18(c)) using the preset parameters, $C = 2.5$, $\beta = 1.5$, and $Z = 200$. These comparisons demonstrate the qualitative ability of ODT to capture the evolution of turbulent eddies and turbulent mixing for all cases. Note that the axis scales used in subfigures (b) and (c) are always the same: this is a direct comparison. However, it is not sufficient to judge the ability of ODT from such instantaneous figures and isolated, random realizations. Therefore, scatter plots have been generated to support further discussions.

Figure 6.15: Instantaneous temperature profile at $t = 32.6\tau_j$ for Case I: (a) Contours of DNS, (b) line taken along the crosswise direction of DNS domain, (c) An ODT realization selected randomly.

Scatter plot of heat release

This section discusses the ability of ODT to reproduce the heat release scatter plot as function of temperature, since heat release and temperature are essential parameters in safety-relevant applications. The ODT results are obtained by keeping $C = 2.5$, $\beta = 1.5$, and $Z = 200$ for all cases, except for Case IV, for which the influence of β will be discussed further. Again, the axis scales used for DNS and ODT are always identical.

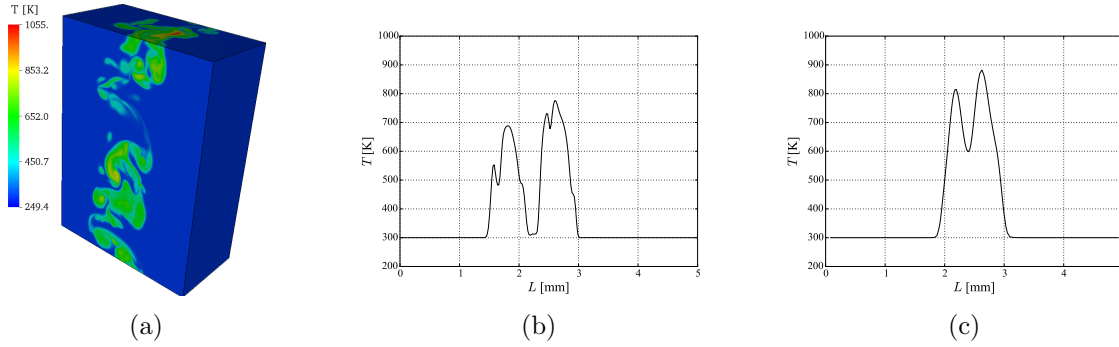


Figure 6.16: Instantaneous temperature profile at $t = 37.5\tau_j$ for Case II: (a) Contours of DNS, (b) line taken along the crosswise direction of DNS domain, (c) An ODT realization selected randomly.

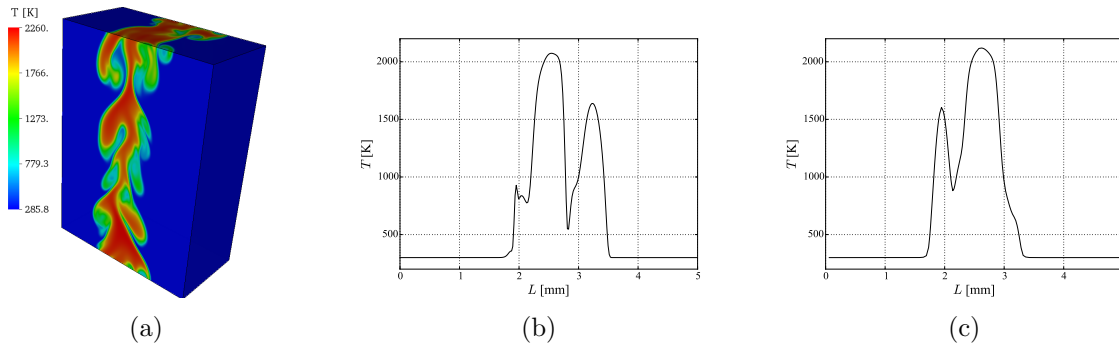


Figure 6.17: Instantaneous temperature profile at $t = 27.27\tau_j$ for Case III: (a) Contours of DNS, (b) line taken along the crosswise direction of DNS domain, (c) An ODT realization selected randomly.

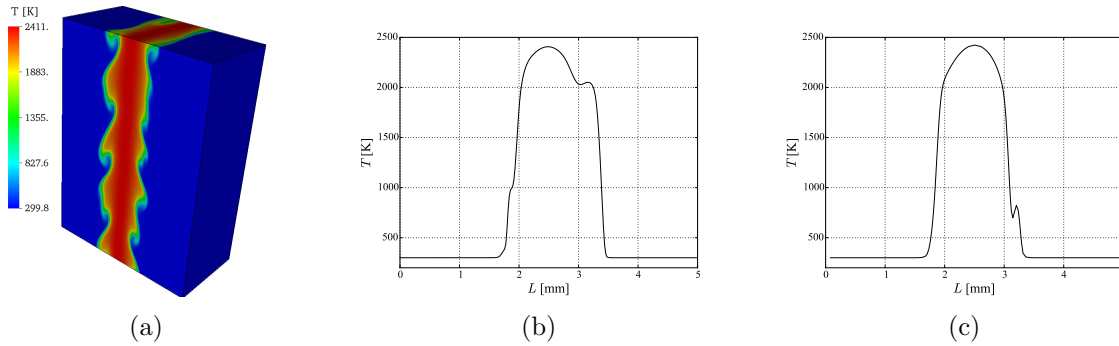


Figure 6.18: Instantaneous temperature profile at $t = 20.69\tau_j$ for Case IV: (a) Contours of DNS, (b) line taken along the crosswise direction of DNS domain, (c) An ODT realization selected randomly.

For Case I (Fig. 6.19), ODT leads at early times to an underestimation of heat release (Figs. 6.19(a) and 6.19(b)); the dispersion of the initial distribution is too small. With

growing time, the structure of heat release is represented by ODT with increasing accuracy. At later times, $t = 15.2\tau$ and $t = 19.5\tau$, ODT reproduces the heat release scatter plot of DNS with a very good agreement, with only a slight over-prediction at temperatures around 800-1000 K.

Case II shows a slightly different behavior, as it is seen from Fig. 6.20. At early stages (Figs. 6.20(a) - 6.20(b)) the dispersion of ODT is not sufficient and does not reproduce correctly heat release at high temperature ($T > 1400$ K); this may be due to a delay of the onset of eddies in ODT model. However, ODT later starts to agree extremely well with DNS; nearly identical structures are finally observed (Figs. 6.20(g) and 6.20(h)).

Figure 6.21 demonstrates that Case III is very well reproduced by ODT; the left and right columns show good agreement at all times.

Regarding finally Case IV, it has been previously discussed that changing β from 1.0 to 1.5 did not impact noticeably the temperature (see again Fig. 6.10). Testing first ODT with $\beta = 1.5$, the obtained heat release scatter plot is very regular (Figs. 6.22(c), 6.22(f), 6.22(i), and 6.22(l)); the obtained dispersion is much too small compared to DNS results (Figs. 6.22(a), 6.22(d), 6.22(g), and 6.22(j)). Changing the value of β to 1.2, the scatter plots are in much better agreement with the DNS reference.

As a conclusion of this section, it is observed that ODT is able to reproduce with a very good accuracy the heat release and temperature profiles for four different reference cases computed by DNS. Considering both temperature and heat release, the optimal ODT parameters for this problem are found to be $C = 2.5$, $\beta = 1.2$, and $Z = 200$. Using these parameters, ODT is able to properly distinguish between successful or failed ignition.

6.2.6 Advantages and Drawbacks of ODT

After adjusting the free parameters C , Z , and β , ODT becomes an extremely fast computational approach. The longest DNS simulation in this study consumed 73,728 CPU-hours on SuperMUC; for comparison, the longest ODT simulation required 1,500 CPU-hours on the same machine, but for 544 realizations; one single ODT computation takes only a few minutes. The same observation applies for the required storage disk space. DNS always stores 3D data, whereas ODT saves 1D profiles. While the largest DNS simulation produced 500 GB of data, 500 realizations of ODT required only 5 GB. Replacing completely DNS by ODT, for the current conditions and Reynolds number, would save 97.9% of computational time and 99% of storage disk space. Even when considering very complex kinetic mechanisms, ODT could still be employed on a standard PC, without any need for a dedicated supercomputing system. This would make systematic safety-relevant studies possible. It is important to keep in mind that this comparison is case-dependent; it depends on the Reynolds number and the conditions under test [192].

Overall, ODT appears to be an excellent tool to predict ignition probability for safety applications. In a few hours of computing time, a parametric study is possible with ODT, after tuning the model parameters by comparisons with DNS. This is the only drawback of ODT; reference cases are needed (experiment or DNS) in order to fit the three free parameters for the specific configuration considered in the study.

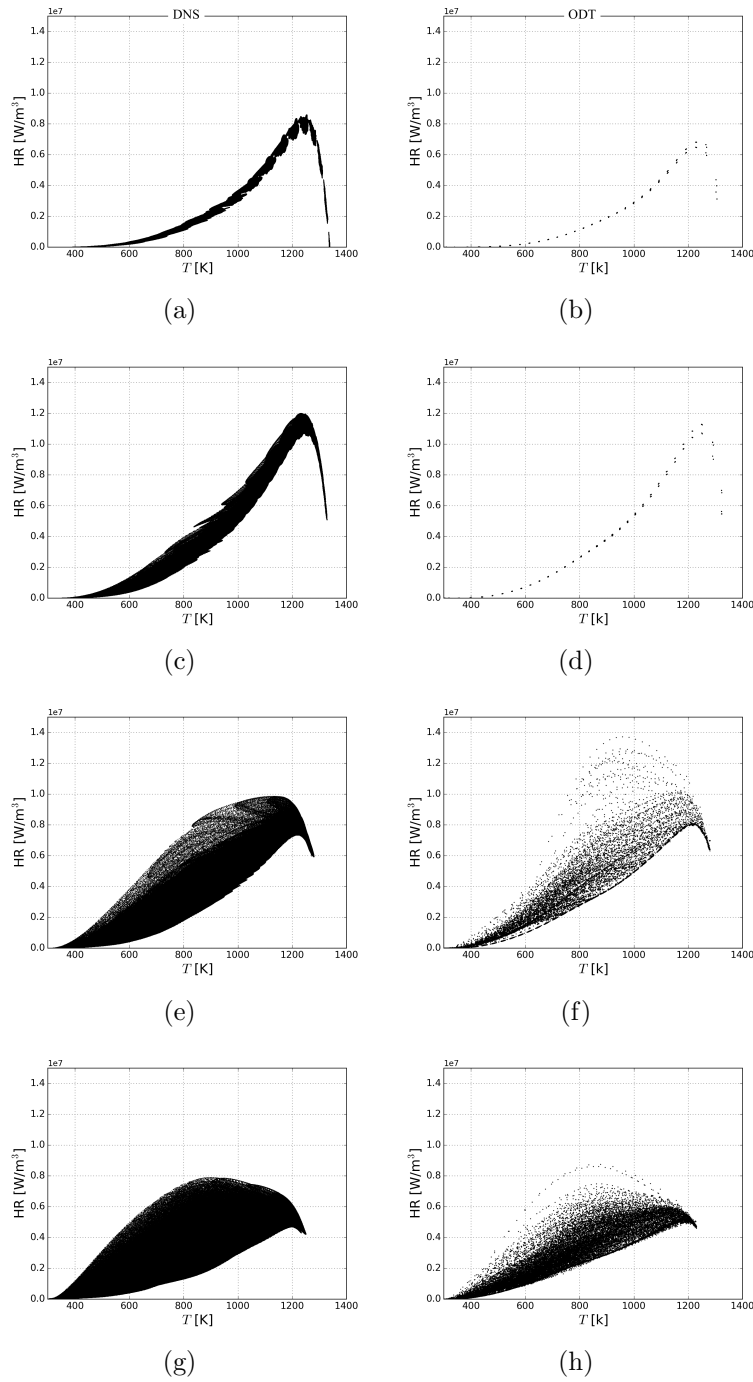


Figure 6.19: Time-evolution of scatter plot of heat release versus temperature for Case I. Left column represents the DNS. Right column represents ODT. Time from top to bottom: $t = 6.5 \tau_j$, $10.8 \tau_j$, $15.2 \tau_j$, and $19.5 \tau_j$.

6.2. Spatial Reduction: ODT

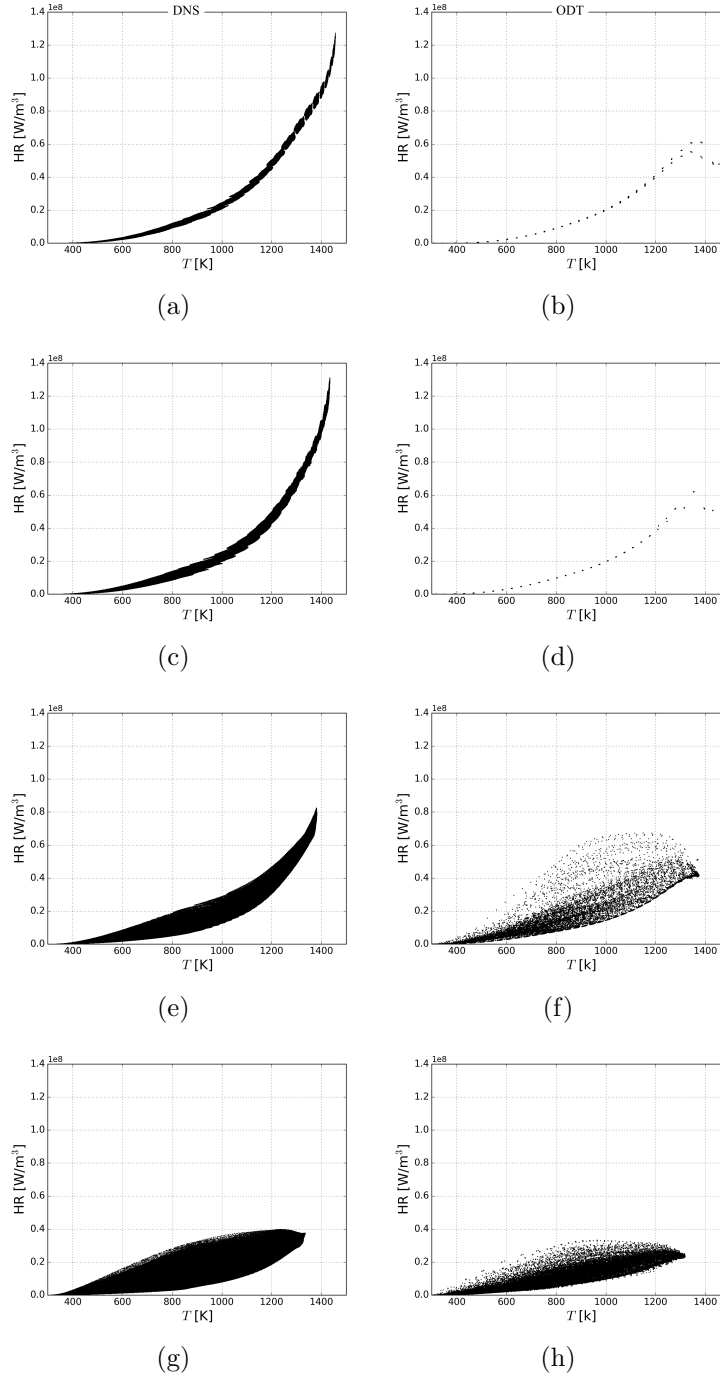


Figure 6.20: Time-evolution of scatter plot of heat release versus temperature for Case II. Left column represents the DNS. Right column represents ODT. Time from top to bottom: $t = 7.5 \tau_j$, $10.0 \tau_j$, $15.0 \tau_j$, and $20.0 \tau_j$.

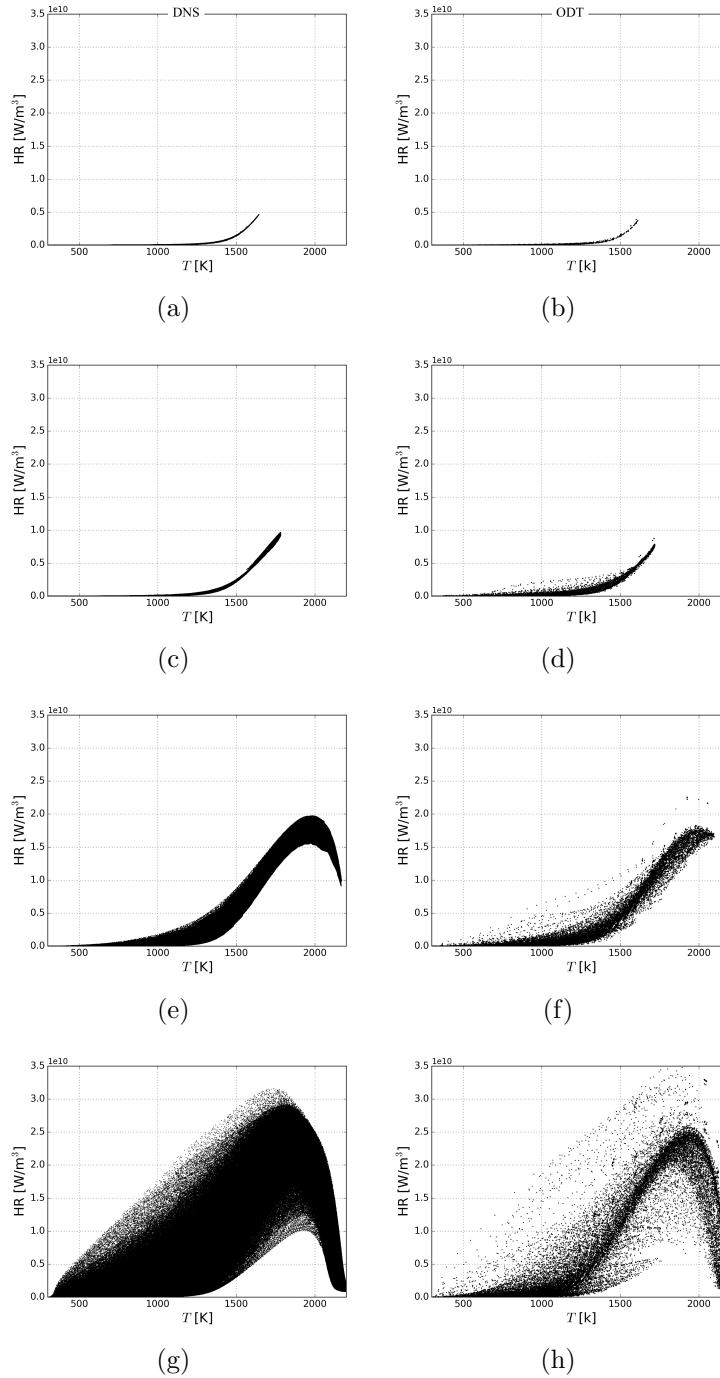


Figure 6.21: Time-evolution of scatter plot of heat release versus temperature for Case III. Left column represents the DNS. Right column represents ODT. Time from top to bottom: $t = 9.0 \tau_j$, $12.0 \tau_j$, $15.0 \tau_j$, and $21.0 \tau_j$.

6.2. Spatial Reduction: ODT

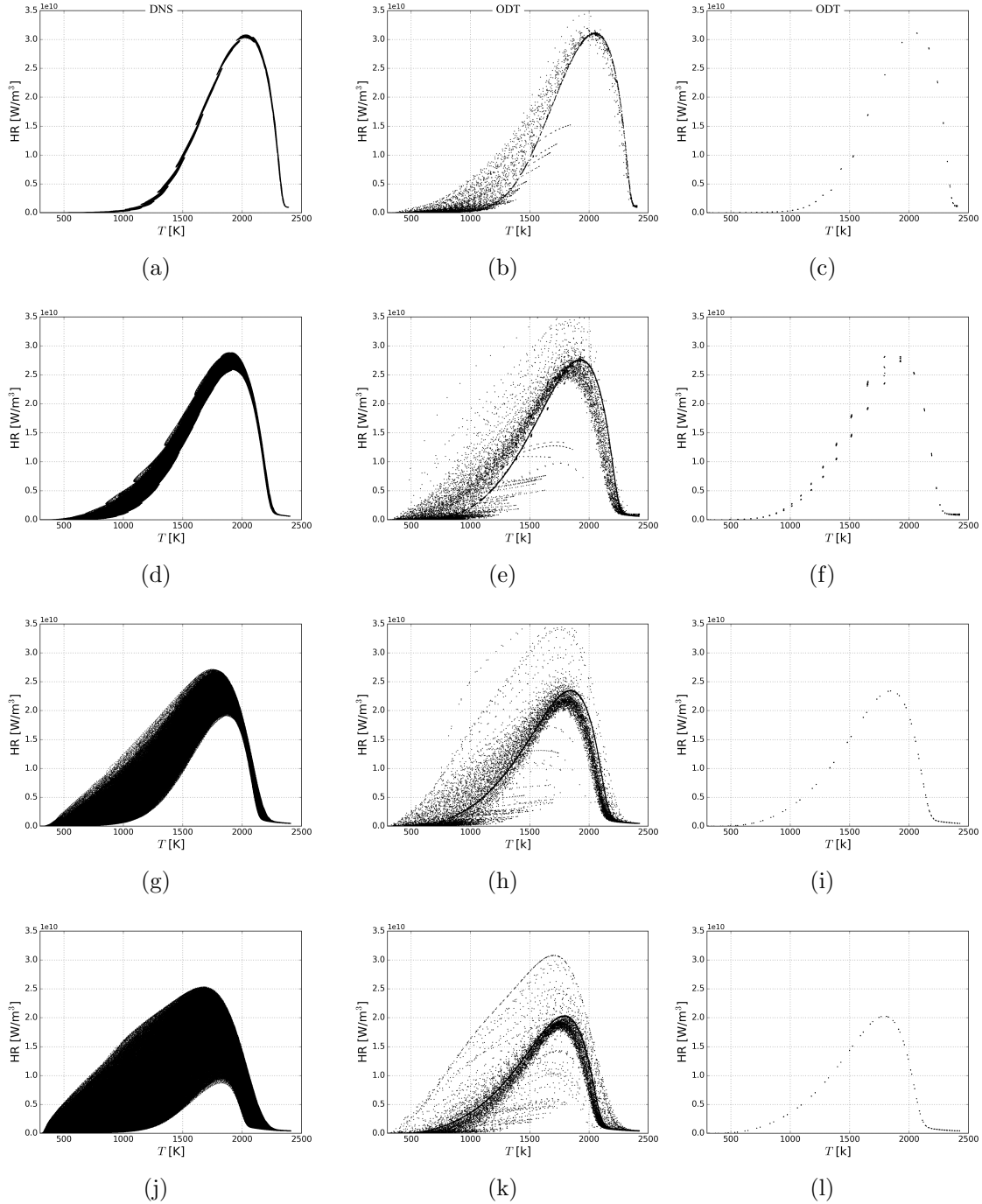


Figure 6.22: Time-evolution of scatter plot of heat release versus temperature for Case IV. Left column represents the DNS. Second column represents ODT with $\beta = 1.2$. Last column represents ODT with $\beta = 1.5$. Time from top to bottom: $t = 10.0 \tau_j$, $13.3 \tau_j$, $16.7 \tau_j$, and $20.0 \tau_j$.

6.2.7 Conclusions on ODT

This study has shown that ODT is able to predict success or failure of autoignition for a premixed flame in turbulent shear flow. A temporally-evolving planar jet configuration has been used for that purpose, comparing ODT results with DNS observations in a systematic manner. These comparisons show that ODT can predict temperature and heat release for a variety of initial conditions involving different temperatures and jet velocities both qualitatively and quantitatively. After fitting the three free parameters of the model, ODT is able to correctly predict the occurrence of autoignition with extremely short computational times and negligible disk space requirements. This opens the door for the generation of ignition probability maps for safety-relevant applications. Compared to a systematic DNS study, ODT saves more than 90% of computational resources.

6.3 Tabulation Chemistry: FPI

This section focuses on the probability of autoignition of an ethylene/air mixture by comparing detailed chemistry and tabulated chemistry.

6.3.1 Objectives

Here, we evaluate the implementation of tabulated chemistry (FPI) in the DINO code and examine its capability to simulate premixed turbulent jet flames. The evaluation is first performed by comparing the obtained flame structure in a 1D planar laminar premixed flame and the required computational efforts associated with tabulated chemistry with results produced by a detailed chemistry approach relying on Cantera. Then, a simulation of a turbulent jet flame using FPI is compared with that using detailed chemistry.

6.3.2 State of The Art

The tabulated chemistry approach called FPI relies on detailed chemistry evaluations as first described by Gicquel et al. [193] as an extension of intrinsic low-dimensional manifolds technique [194]. The capability of FPI to provide accurate predictions at low computational costs has been demonstrated for many combustion applications, e.g., [195–198]. This makes FPI one of the most promising reduced models for laminar and turbulent combustion applications. The advantage of FPI becomes even more important with complex mixtures, e.g., methane, ethylene, diethyl ether, n-heptane, etc. In the current section, combustion of a turbulent ethylene/air mixture is of particular interest. Resolving all turbulence and flame scales in a DNS using detailed chemistry (solving all reaction and species equations during the simulation) leads to unacceptable computational times. The current study evaluates and discusses the behavior of FPI concerning combustion of ethylene/air mixtures, comparing the obtained accuracy and the required computational time associated to a detailed chemistry DNS (relying on Cantera) with those obtained with FPI. To the authors' knowledge, a comparison between detailed chemistry and FPI has never been provided yet for such a complex fuel in a DNS.

6.3.3 FPI Principle

The FPI approach relies on a pre-tabulated detailed chemistry solution, usually based on one-dimensional laminar premixed flames. In this approach, every thermodynamic/physical/chemical quantity, φ , is expressed as a function of two independent variables: mixture fraction, Y_z , and progress variable, Y_c :

$$\varphi^{FPI} = \varphi(Y_z(\phi), Y_c). \quad (6.9)$$

Here, Y_z describes the state of the mixture through the equivalence ratio ϕ . Hence, it should be based on a suitable combination of non-reactive species. In this study, Y_z is simply equal to the nitrogen mass fraction, Y_{N_2} . On the other hand, Y_c must show a monotonic behavior

representing the overall process of the chemical reactions. Here, the progress variable has been chosen as a combination of CO and CO₂, following [199, 200]:

$$Y_c = Y_{CO_2} + \alpha Y_{CO}, \quad \alpha \geq 0. \quad (6.10)$$

6.3.4 Numerics

In order to evaluate the FPI behavior for an ethylene/air system, a 1D look-up table has been generated by using an in-house Fortran code based on Cantera version 1.8. The table is computed starting from a skeletal mechanism developed by Luo et al. [96] that contains 32 species and 206 reactions. In this study, Y_z , Y_c , and all species mass fractions Y_k , mole fractions X_k , mixture-averaged diffusion coefficients D_k , and mass production rates $\dot{\omega}_k$ are saved into an FPI table. The temperature, density, dynamic viscosity, specific heat, and thermal conductivity of the mixture are stored in the same table, as well. This table is generated under the unity Lewis number assumption.

All comparisons have been performed using DINO. DINO can handle both techniques: detailed chemistry (based on Cantera) or tabulated chemistry (based on FPI tables). In the case of detailed chemistry, 211 conservation equations are finally solved: the low-Mach number Navier-Stokes equations, Poisson equation for pressure, temperature, and 32 species equations, with the system being closed by the equation of state. On the other hand, in the case of FPI, only six equations need to be solved: again, the low-Mach number Navier-Stokes equations, Poisson equation for pressure, and two conservation equations for Y_z and Y_c , using the equation of state to close the system.

6.3.5 Results

FPI with 1D Planar Premixed Flame

In this section, comparisons concerning laminar 1D planar premixed flames for stoichiometric conditions, $\phi = 1$, are presented. Figure 6.23 shows the relation between different species mass fraction combination (progress variable) versus the temperature.

Figures 6.24 and 6.25 show the comparison between detailed chemistry (Cantera, red line) and tabulated chemistry (FPI, dashed black line) in terms of temperature and heat release for an ethylene/air mixture at two different values for α in Eq. (6.10). These figures reveal that the FPI simulations are able to reproduce the correct flame structure. Under current mixture conditions, the results with $\alpha = 0$ reproduce the flame structure perfectly for a 1D laminar flame.

FPI with Planar Spatially-Evolving Jet

Herein lies a similar case, in concept, to that discussed in Sec 3.16.1, where the burned gases are injected into the fresh premixed mixture. Again, this is an application for safety prediction, where the burned gases may escape through a crack to the fresh unburned premixed mixture. A schematic diagram of the combustion system and the DNS domain is illustrated in Fig. 6.26.

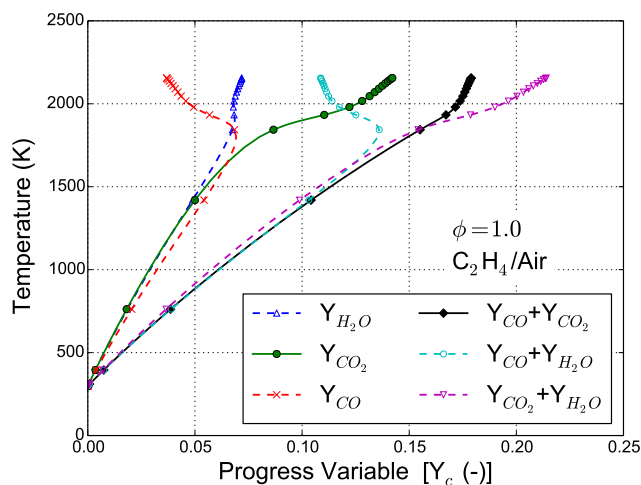


Figure 6.23: Temperature versus different possible progress variables.

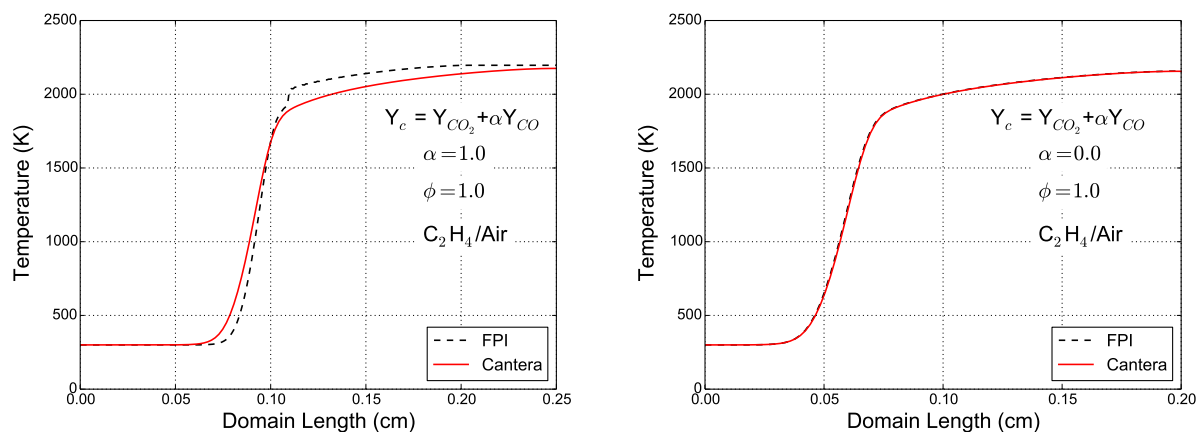


Figure 6.24: Comparison of FPI with detailed chemistry: temperature.

The numerical settings for this simulation may be summarized as follows: the pre-cooled burned gases of the ethylene/air mixture are injected with a speed of 110 m/s through a planar nozzle with a width of 0.28 mm; these burned gases are injected at a temperature of 1100 K into a fresh premixed ethylene/air mixture at temperature of 300 K; this leads to a initial jet Reynolds number of 2020. The domain lengths in all directions are 8 mm in streamwise direction, 6 mm in crosswise direction, and 2 mm in span-wise direction. This domain is computationally discretized over 25 million grid points to maintain the grid resolution at $15.6 \mu\text{m}$ in all directions. The kinetic scheme developed by Luo et al. [96] is used during the detailed chemistry simulation, and to generate the FPI table. Again this mechanism has 32 species and 206 elementary reactions.

Figure 6.27 shows the temporal revolution of the temperature iso-surface for both the detailed kinetic simulation and the FPI simulation. This figure demonstrates that the FPI

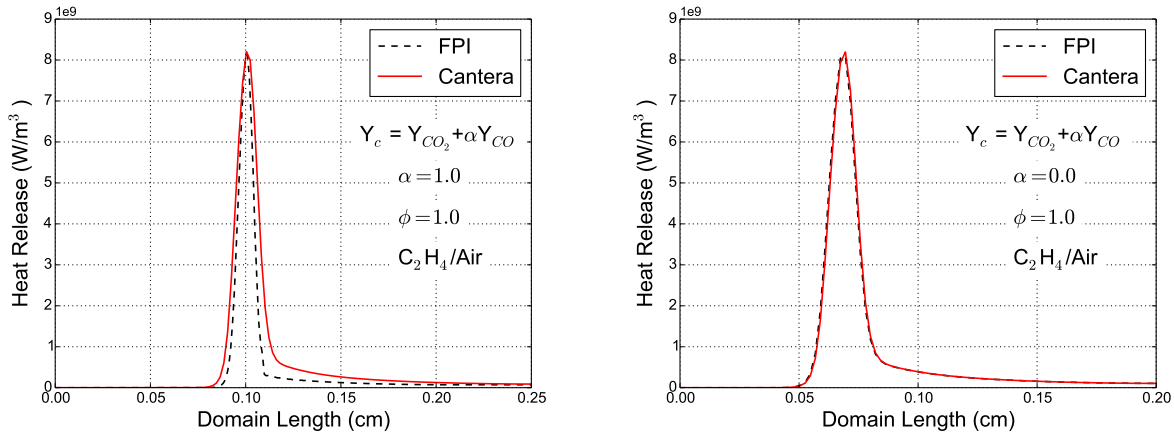


Figure 6.25: Comparison of FPI with detailed chemistry: heat release.

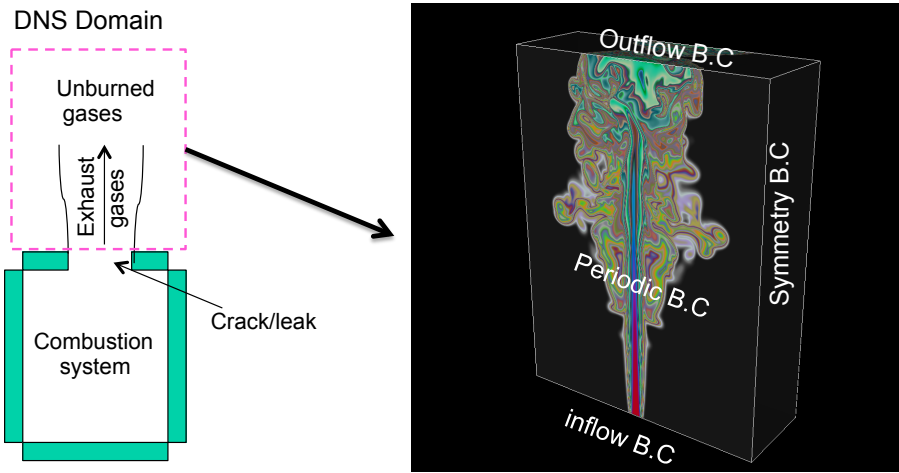


Figure 6.26: Schematic diagram shows the burned gases escape from combustion system and illustrate the considered DNS domain. The iso-surfaces in the right-hand side figure represents the temperature at different levels.

simulation shows excellent agreement with the detailed chemistry simulation in low turbulence regions; slight deviations appear in high-turbulence regions.

In order to gain a full picture of these deviations, averaged values taken over the span-wise direction are collected at different lines along the stream-wise direction, as is illustrated in figure 6.28.

Averaged temperature and velocity at these locations are presented in Figs 6.29, and 6.30, respectively. As is seen in Figs. 6.29(a), 6.29(b), 6.30(a), and 6.30(b), the temperature and stream-wise velocity of the FPI simulation show very good agreement with those of the detailed chemistry simulation up to a distance of $y/H \leq 15$. These results are at weak turbulence regions. At higher locations, $y/H > 15$ (Figs. 6.29(c), 6.29(d), 6.30(c), and 6.30(d)), the mixing increases and the flow becomes more turbulent. At these locations, FPI

6.3. Tabulation Chemistry: FPI

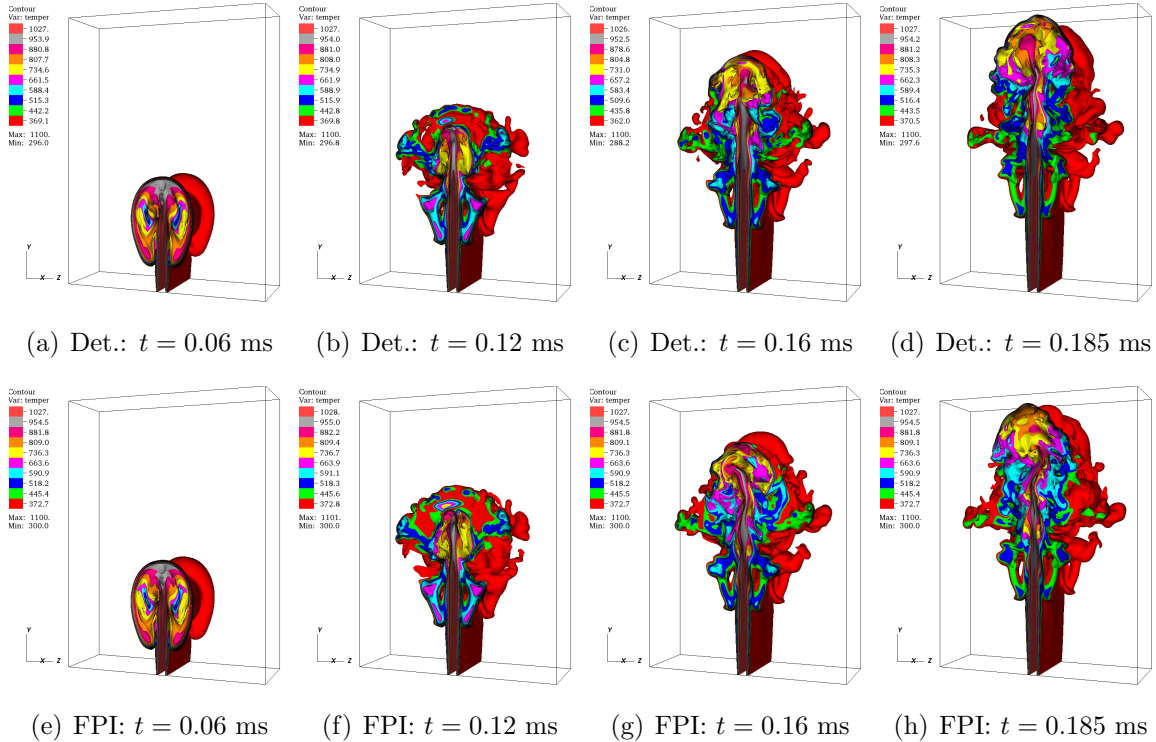


Figure 6.27: Temporal revolution of temperature iso-surface for both detailed (Det.) chemistry simulation (Top) and FPI one (bottom).

and detailed chemistry show more deviations from one another. This is attributed to the fact that the one-dimensional FPI table is applicable to weak turbulent flow, but for stronger turbulent flow, a higher dimensional table is required.

6.3.6 Conclusions on FPI

In the 3D simulations, the FPI simulation consumed 5 900 CPU-hours, whereas the detailed kinetic simulation consumed 59 000 CPU-hours. As a general conclusion, the FPI tabulation technique produces acceptable results in DINO and saves 90% of the CPU time required for detailed kinetic simulations. As for future recommendations, two- and three-dimensional FPI tables should be implemented as in [201, 202] to capture the cases involving strong turbulence

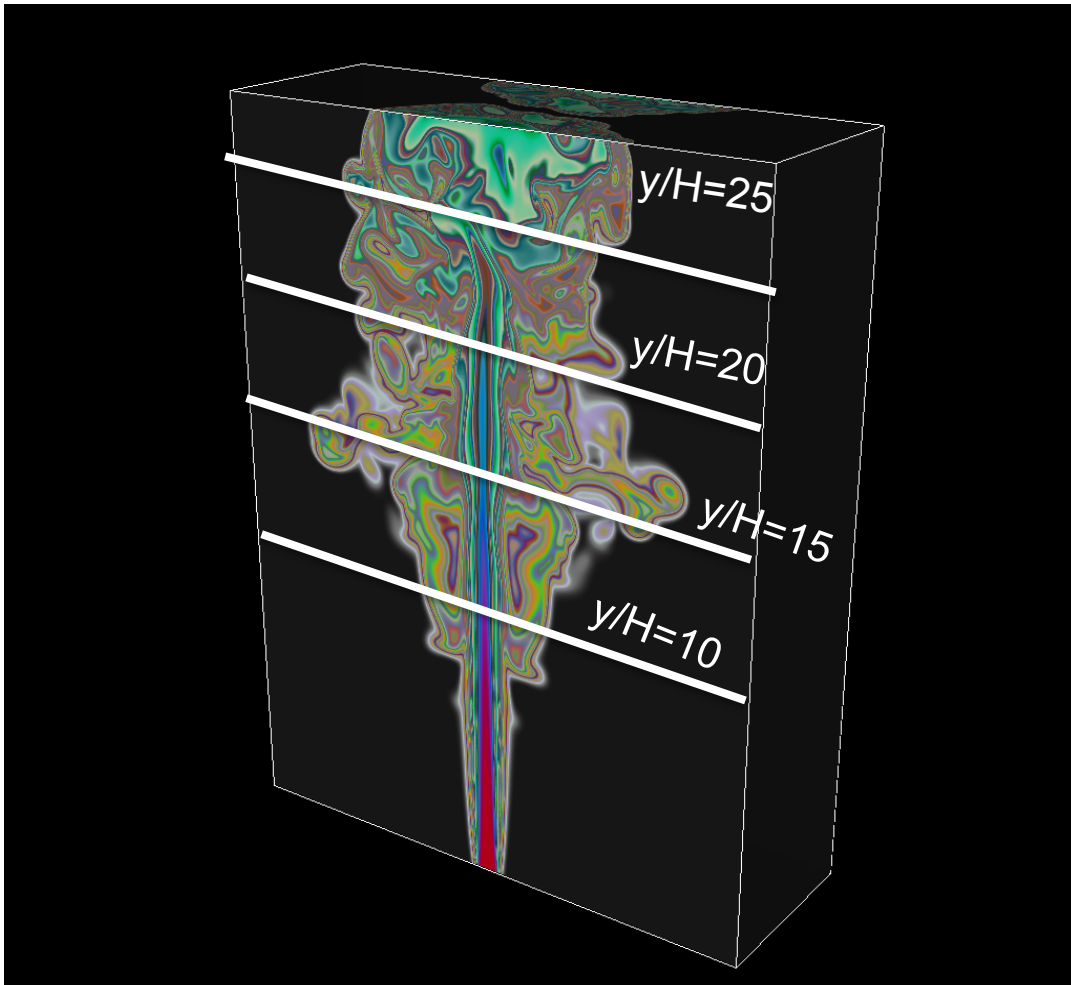


Figure 6.28: Schematic diagram showing the places where the averages are computed. Average is computed over spanwise direction at 4 different locations along the streamwise direction; $y/H = 10, 15, 20$, and 25 . H is the jet width, and y is the length along the streamwise direction.

6.3. Tabulation Chemistry: FPI

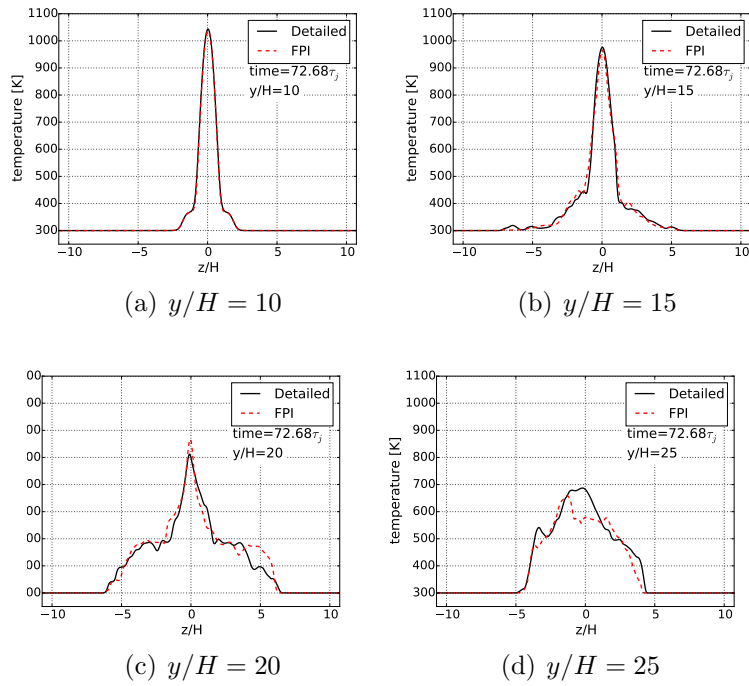


Figure 6.29: Ensemble-average temperature collected over spanwise direction at 4 different location along the streamwise direction.

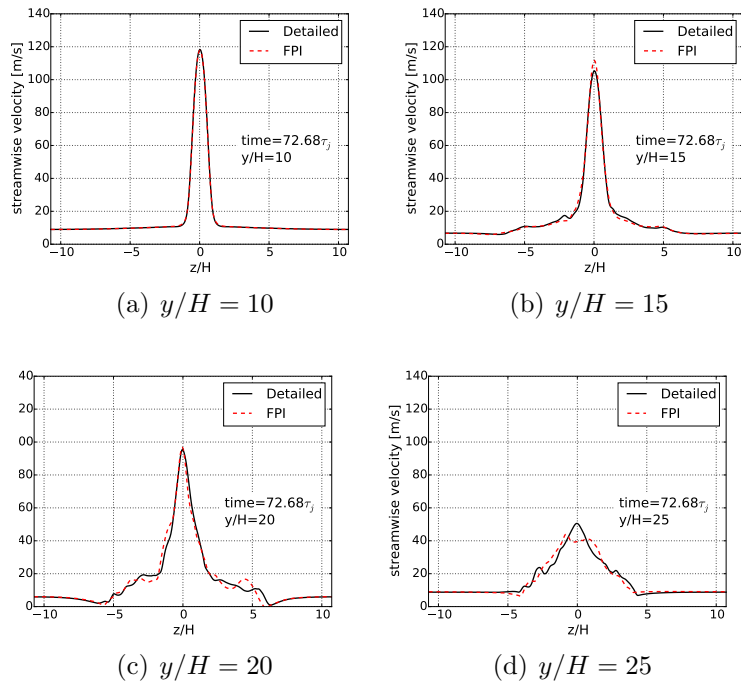


Figure 6.30: Ensemble-averaged streamwise velocity collected over spanwise direction at 4 different location along the streamwise direction.

6.4 Post-Processing Analysis: DMD vs SPOD

6.4.1 Objectives

The objective of this section is to show the advantage of using the modal decomposition in post-processing and in analyzing turbulent coherent structures. To accomplish this, the turbulent structures in a channel flow and in a mixing jet are investigated using Dynamic Mode Decomposition (DMD) and Snapshot Proper Orthogonal Decomposition (SPOD, see also Ch. 5). The analyzed data sets have been generated by DNS at high Reynolds numbers. In the channel flow, the occurrence of turbulent superstructures (e.g. very large scale structures) will mainly be examined. The jet case is employed to investigate mixing in turbulent jet flow. In both cases, DMD and SPOD, analyses are compared to test their performance concerning the analysis of complex flow and to highlight the complementarity between these two approaches. In both cases, coarse resolution outputs are saved from well-resolved DNS simulations. The modal decomposition analysis is then carried out, showing the ability of these techniques to extract important turbulent features from coarse output. This leads to a large amount of saved disc space and makes the analysis of an extraordinarily large domain possible.

6.4.2 Fundamentals of SPOD and DMD

In principle, SPOD and DMD are designed to define the coherent structure of turbulence, but in two different ways. In the following, the basic equations for each of them are defined.

In **SPOD**, each signal (here, flow velocity) can be decomposed, as already described in Ch. 5, into temporal parts a and spatial parts ϕ ,

$$\mathbf{u}(\mathbf{x}_i, t_j) = \mathbf{u}_j = \sum_{m=1}^M a_m(t_j) \phi_m(\mathbf{x}_i), \quad (6.11)$$

where the eigenfunctions ϕ_m are called spatial modes and a_m is the temporal coefficient. The ϕ_m and a_m are completely determined after solving the eigenvalue problem

$$\mathbf{C}\mathbf{v}_i = \lambda_i \mathbf{v}_i, \quad \text{for } i = 1, 2, \dots, N, \quad (6.12)$$

where λ_i and \mathbf{v}_i are the eigenvalue and eigenvectors of the i -th mode, respectively. The entries of \mathbf{C} describe the covariance of two snapshots at different moments in time, $\mathbf{C} = C_{ij} = (\mathbf{u}_i, \mathbf{u}_j)$. This matrix \mathbf{C} is similar to the temporal autocorrelation function, which is statistically second-order, and λ_i represents the energy associated to the i -th mode.

The basics of **DMD** is to assume that the snapshots are generated by a linear, discrete time model,

$$\mathbf{u}_{j+1} = \mathbf{A}\mathbf{u}_j. \quad (6.13)$$

It is assumed that the snapshots become linearly dependent for an increasing number of snapshots, so that snapshot \mathbf{u}_N can be constructed by a linear combination of all previous

snapshots,

$$\mathbf{u}_N = \sum_{j=1}^{N-1} c_j \mathbf{u}_j. \quad (6.14)$$

The previous relation can be also written as:

$$[\mathbf{u}_2 \dots \mathbf{u}_N] = \mathbf{A}[\mathbf{u}_1 \dots \mathbf{u}_{N-1}] = \tilde{\mathbf{U}}\tilde{\mathbf{C}} + \mathbf{r}\mathbf{e}^T, \quad (6.15)$$

where in this equation, $\tilde{\mathbf{U}} = [\mathbf{u}_1, \dots, \mathbf{u}_{N-1}]$ is the reduced data matrix, $\mathbf{e} = [0, 0, \dots, 1]$ is the unit vector, \mathbf{r} is the residual error, and $\tilde{\mathbf{C}}$ is the companion matrix,

$$\tilde{\mathbf{C}} = \begin{bmatrix} 0 & 0 & \dots & 0 & c_1 \\ 1 & 0 & \dots & 0 & c_2 \\ 0 & 1 & \dots & 0 & c_3 \\ \vdots & \vdots & \ddots & \vdots & \vdots \\ 0 & \dots & 0 & 1 & c_{N-1} \end{bmatrix},$$

where the entries c_i are computed such that the error is minimized (least-square problem). As in SPOD, after obtaining $\tilde{\mathbf{C}}$, an eigenvalue problem is solved,

$$\tilde{\mathbf{C}}\tilde{\mathbf{v}}_i = \tilde{\lambda}_i\tilde{\mathbf{v}}_i, \quad \text{for } i = 1, 2, \dots, N-1. \quad (6.16)$$

After obtaining the eigenvalue $\tilde{\lambda}$ and eigenvectors $\tilde{\mathbf{v}}_i$, the DMD modes and temporal amplitudes can be obtained [203]. In DMD, the eigenvalues and eigenvectors are complex numbers. The frequency f_i and growth (or decay) rate σ_i of the DMD is obtained by logarithmic mapping of the eigenvalues;

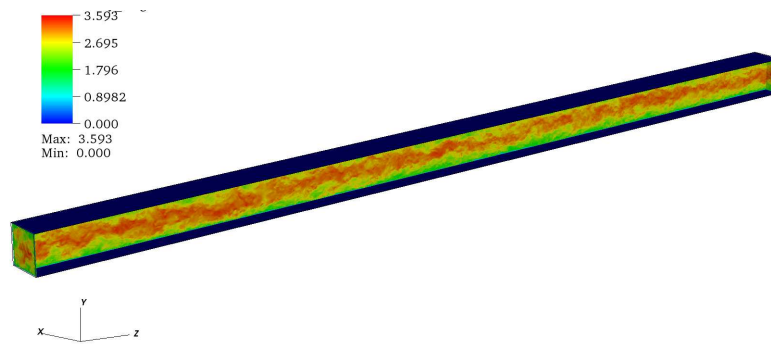
$$f_i = \frac{\Im[\ln(\tilde{\lambda}_i)]}{2\pi\Delta t}, \quad (6.17)$$

$$\sigma_i = \frac{\Re[\ln(\tilde{\lambda}_i)]}{\Delta t}. \quad (6.18)$$

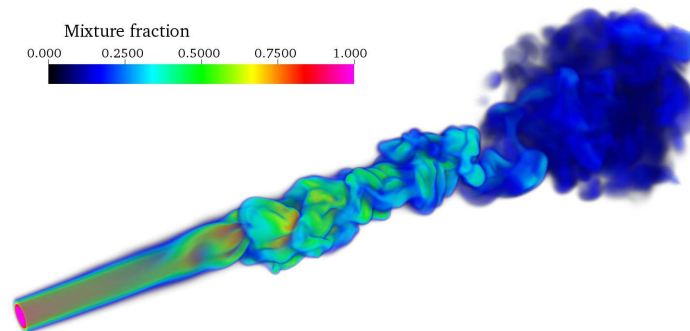
The main difference between SPOD and DMD is that SPOD is based on an energy ranking of orthogonal structures computed from a correlation matrix of the snapshot. This leads to two possible drawbacks: (1) the energy content is not necessarily the correct measure to rank the flow structures; (2) valuable information may be lost since only second-order statistics are used as a basis for the decomposition. Additionally, POD allows mixing between scale and frequency at each mode, while DMD separately provides one growth rate and frequency for each mode. In DMD, the dynamic modes are non-orthogonal; they can be sorted by frequency, growth rate, or mode norm. SPOD and DMD also differ in the computational requirements. In the following examples, it was found that computing the DMD decomposition is six times slower than for POD.

6.4.3 Numerical Settings

DNS have been conducted to simulate two different cases: (1) turbulent flow in a square-shaped channel with a bulk Reynolds number of 20 000 in a domain of size $H \times 20H \times H$, where H is the height of the channel; this domain was discretized with more than 400 million grid points; (2) mixing of hydrogen with air in a turbulent jet flow at a jet Reynolds number of 2 600, simulated with about 70 million grid points in a domain of size $7.5d_j \times 30d_j \times 7.5d_j$, where d_j is the jet diameter. All simulations were performed using DINO. The results of these DNS were then analyzed with the in-house Python script called PyPODE which was developed during this Ph.D. work. PyPODE was coded on top of the modred-1.0.2 package [204] and contains both DMD [205] and SPOD [144] algorithms. Figures 6.31(a) and 6.31(b) show 2D-planes of velocity magnitude in the turbulent channel and the iso-volume of the mixture fraction in the jet, respectively.



(a)



(b)

Figure 6.31: (a) 2D cuts showing instantaneous velocity magnitude in the highly turbulent channel flow. (b) Iso-volume of instantaneous mixture fraction in the turbulent jet.

6.4.4 Results and Analysis

In this section, the analysis of jet flow and turbulent channel flow using both SPOD and DMD will be discussed. In the following, the first mode (which represents the mean value) is removed and not included in the spectrum or to show the spatial modes. The modal decomposition analysis is performed for coarse outputs of a well-resolved simulation; only 75% of the computational grid points are written to the disk. In this manner, 25% of disk space is saved by using modal decomposition. It could even use a coarser outputs and still obtain important information.

Jet flow As in many turbulent mixing processes, the turbulent jet has three different ranges of scale responsible for the entire turbulence dynamics [206]: (1) smallest scales that are responsible for molecular mixing; (2) large-scale flow structures describe the entrainment stage that is responsible for the engulfment of large pockets of irrotational fluid species into the turbulent flow region; (3) intermediate range of scales, which are responsible for the subsequent kinematic stirring process responsible for the large interfacial surface generation between the mixed species.

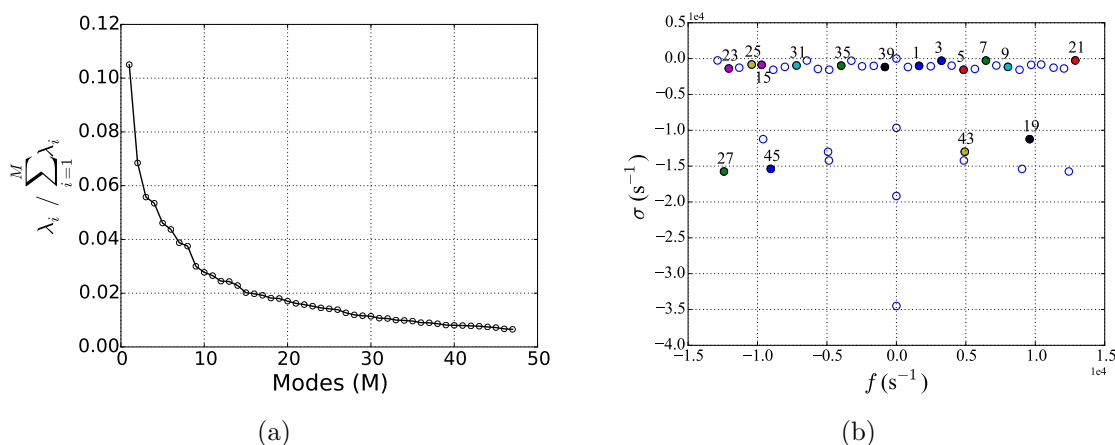


Figure 6.32: Modal spectrum of the mixing jet case. (a) eigenvalue of SPOD. (b) spectrum of DMD.

Figure 6.32(a) shows the eigenvalue (spectrum) of SPOD versus the number of modes. From this figure, it is obvious that the first modes (most energetic modes) are the most dominant, with a rapid energy decrease (exponential decay). By comparison, the logarithmic mapping of the DMD eigenvalues can be represented as growth (decay) rate versus frequency, as seen in Fig. 6.32(b). In this figure, the numbers represent the numbering of the modes and are not ordered; one could sort them based on the frequency in order to identify the most dominant modes. Figure 6.33 shows the iso-surfaces of the spatial modes: the top row is the SPOD and the bottom row is the DMD. From the first five modes (Figs. 6.33(a)-6.33(e) and Figs. 6.33(h)-6.33(l)) in both SPOD and DMD, it is clear that the most dominant structures appear in the original shear layer and progressively extend toward the transition region. The first four modes are quite similar in topology, while the fifth mode shows a

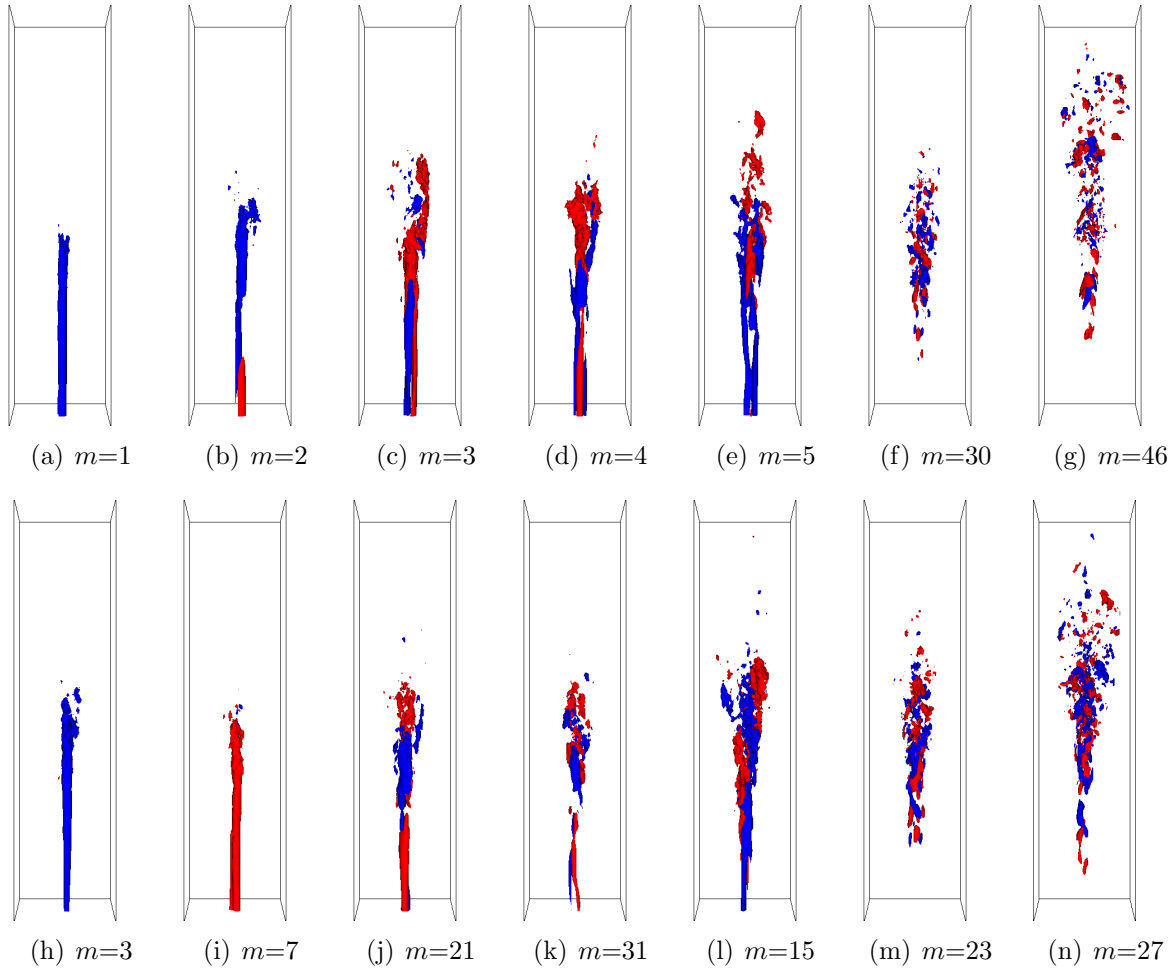


Figure 6.33: Iso-surfaces of the spatial modes in the mixing jet, colored by the sign of streamwise velocity (positive or negative); each mode is normalized by its local maximum. Red and blue iso-surfaces represent the values of 0.5 and -0.5 , respectively. Top: SPOD. Bottom: DMD.

difference between SPOD and DMD. In DMD (Fig.6.33(m)), broader structures appear at the head of the jet, which may have been lost in SPOD (Fig.6.33(e)) due to its intrinsic limitation to second-order. Figures 6.33(f) and 6.33(m) illustrate that SPOD and DMD show qualitatively similar intermediate modes. At high frequency in DMD, Fig. 6.33(n) shows the fastest and smallest structure revealed by the dynamics modes. It still shows a structure which is similar to the largest mode in SPOD (Fig 6.33(g)), even if it is known that this cannot be directly interpreted in terms of a physical structure.

In conclusion, the SPOD, which is computationally six times faster than DMD, is able to properly extract the most energetic modes and their corresponding coherent structures. In cases where the interest is set on low-order structures or on specific frequency regions, DMD would probably be the proper choice.

Channel flow In a very long turbulent channel flow at high Reynolds numbers ($Re \geq 20\,000$), long meandering velocity fluctuations with both positive and negative streamwise velocity are sometimes observed [207]. These velocity fluctuations appear in the log-law and lower wake regions of the turbulent boundary layer and are named superstructures. In the present work, possible superstructures are tracked with SPOD and DMD.

As usual, the spectrum of modal decomposition should be presented first (Figs. 6.34(a) and 6.34(b)). Again, the first dominant spatial modes could be represented in an isolated manner based on the given spectrum. Figure 6.35 shows that SPOD (Figs. 6.35(a)-6.35(f)), and even more so DMD (Figs. 6.35(g)-6.35(l)), reveal the presence of very long meandering velocity fluctuations, with both positive and negative streamwise velocities. These might be superstructures, in agreement with the definition of [207]. However, it is in this case difficult to find a qualitative similarity between the POD and DMD modes. This is attributed to the fact that the number of snapshots employed for the analysis is not sufficient. In future work, a larger number of snapshot must be taken into account. From these preliminary results, it appears that DMD might play an essential role in following the dynamics of superstructures; SPOD may most likely only be used for very energetic superstructures.

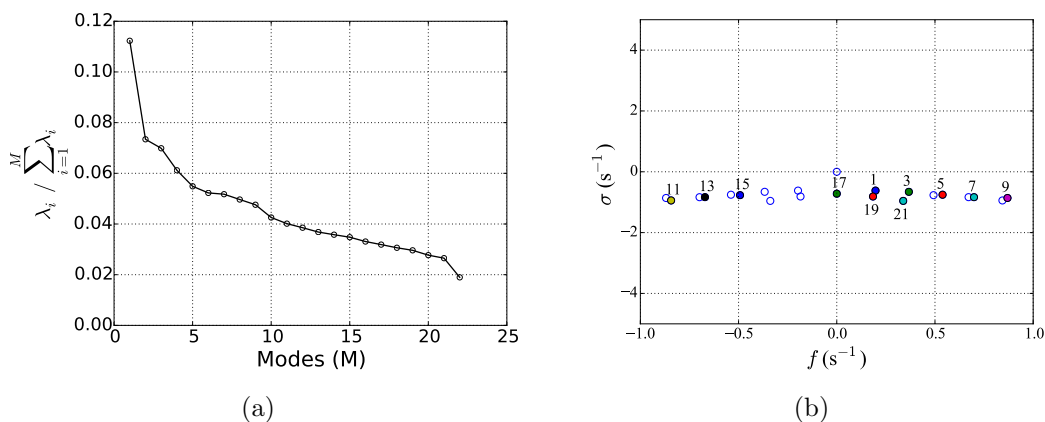


Figure 6.34: Modal spectrum of the channel flow case. (a) eigenvalue of SPOD. (b) spectrum of DMD

6.4.5 Conclusions on Modal Decomposition

Turbulent structures and mixing in a long turbulent channel flow and in a mixing jet have been investigated with both SPOD and DMD modal decomposition methods. It has been found that in the mixing jet case, both SPOD and DMD qualitatively deliver very similar information concerning dominant structures and modes. In the turbulent channel flow at high Reynolds number, DMD seems to be more suitable for identifying and tracking possible superstructures. However, in both cases, SPOD computations were found to be about six times faster than the corresponding DMD analysis. Additionally, SPOD and DMD should be retained as complementary methods for the same analysis, taking advantage of both

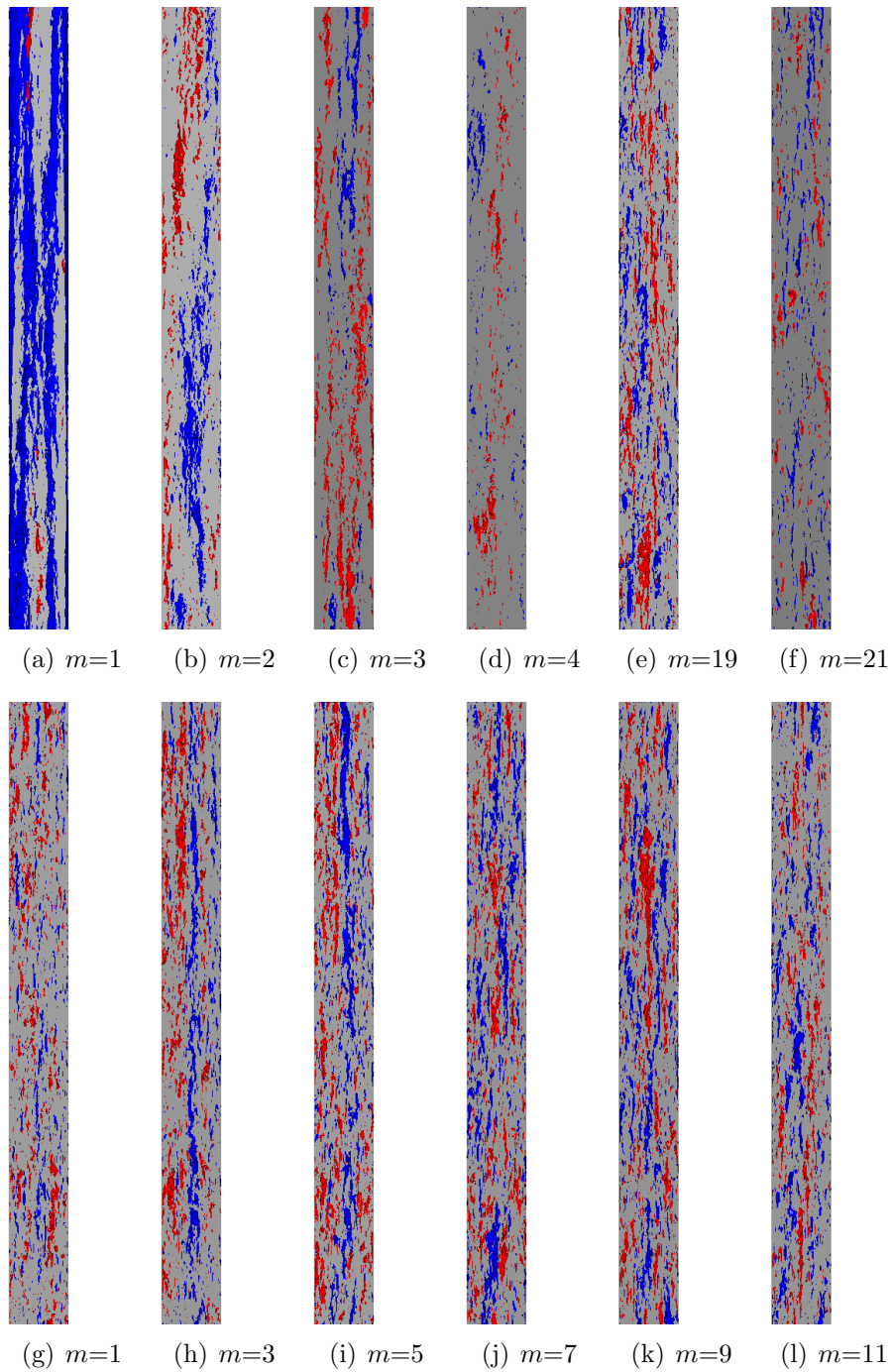


Figure 6.35: Iso-surfaces of the spatial modes in the channel flow close to the wall (part of the domain), colored by the sign of streamwise velocity (positive or negative); each mode is normalized by its local maximum value. Red and blue iso-surfaces represent the values of 0.5 and -0.5 , respectively. Top: POD. Bottom: DMD.

approaches. As a final conclusion, using modal decomposition is very useful to describe the turbulence dynamics and scales with the possibility of reducing the required storage disk space.

6.5 Conclusion

During this Ph.D. work, different reduction techniques and analysis methods have been implemented and tested. All show specific advantages and limitations. Future work will be necessary to check, in a systematic manner, the best possible conditions for DNS of spray combustion.

Chapter 7

Conclusions and Outlook

7.1 Conclusion

As is well-known in the DNS community, DNS of turbulent combustion requires a computationally parallelized solver that can efficiently scale over large machines (supercomputers), as well as a large amount of disk space. Additionally, for relatively large DNS, the size of the total output may reach several terabytes. Copying such data from supercomputers to a local machine sometimes necessitates more time than that required for the simulation itself. All of these are challenges that the modern DNS of combustion faces.

This dissertation discussed all of the tools required in order to perform and analyze DNS of turbulent flows and spray combustion. After discussing the fundamentals of turbulent spray combustion and reviewing the governing equations, a new DNS tool, called DINO, has been developed. DINO offers a solution to a great deal of problems facing researchers who concern themselves with DNS of turbulent combustion. It is sixth-order in space and fourth-order in time. DINO is a low-Mach number solver. Therefore, the time step allowed in DINO's simulations is larger than that required in similar, fully compressible solvers. This is owed to the time step in the low-Mach number formulation being controlled by diffusion and convection instead of by the acoustic wave time scale, which is generally extremely small (order of nanoseconds). DINO possesses a new tool to compute the Poisson equation in an efficient way. This tool is based on a standard FFT library, and is even applicable for non-periodic boundary conditions. DINO exhibits excellent scalability on different machines, which assists in conducting large simulations in an acceptable time. Verification and validation have been carried out to evaluate the efficiency and capability of DINO. Two important turbulent combustion numerical settings have been tested, namely temporally- and spatially-evolving jets demonstrating DINO's ability to carry out such complex flow simulations. After having a strong DNS solver in DINO, which deals with turbulent gas flows, a second part, which deals with the discrete phase, has been implemented and validated. This second part, called discrete particle simulation (DPS), considers non-resolved liquid droplets or solid particles. In DPS, the discrete phase is tracked in Lagrangian space. Exchanges of mass, momentum, and heat transfer between the continuous phase and discrete phase are accomplished via interpolation from Eulerian to Lagrangian spaces. For fully resolved

particles, the surface of each particle is resolved using the direct force immersed boundary method (DF-IBM). In DINO, a complex geometry can be implemented with a regular grid using the direct boundary immersed boundary method (DB-IBM).

A detailed evaporation model has been used in spray combustion simulations. This model was first validated. Then, two different applications were investigated and examined: (1) spray in temporally-evolving jet, and (2) spray in spatially-evolving jet. These investigations have revealed that shear in the gas phase indeed has a very significant impact on evaporation, mixing, and ignition scenarios. With high shear, ignition occurs under the retained conditions in a lean mixture, and involves both non-premixed and premixed reaction fronts. Peak heat release is found near stoichiometric conditions in the premixed mode. In the absence of shear, ignition occurs simultaneously over a broad range of conditions, from lean (in the non-premixed mode) to stoichiometric and rich mixtures (involving both non-premixed and premixed combustion fronts). Here, peak heat release is found for a rich mixture involving both combustion modes. Thanks to a parametric study concerning the impact of droplet size, local equivalence ratio, and jet velocity, it has been found that the autoignition delay time and consumption time depend strongly on the droplet size and jet velocity, yet are almost independent of the local equivalence ratio, at least for the considered conditions.

As is common in turbulent flow, it is very useful to quantify the flow state locally and globally. For this reason, a new tool has been developed to quantify the flow state: laminar, transitional, or turbulent. This tool is based on the spectral entropy S_d obtained from solving an eigenvalue problem, with the auto-correlation function of the flow velocity as kernel. This tool was first derived and then calibrated with a well-defined flow benchmark: homogeneous isotropic turbulence. After the calibration, two different applications were tested using this tool: (1) DNS results obtained for the Taylor-Green vortex benchmark at $Re = 1600$ as well as (2) results obtained through Large Eddy Simulations in a blood nozzle, revealing in both cases a perfect agreement with a traditional, user-based analysis of the flow conditions. Hence, S_d appears to be an excellent quantitative indicator of laminar, transitional, or turbulent flow, allowing an automatic, user-independent analysis of the flow state for a variety of conditions. With its help, one can acquire the nature of any general flow during the simulation or during the post-processing step, opening the door for a more efficient use of large-scale and hyper simulations.

The last part of this dissertation considered the possible reduction of the computational efforts in terms of computational time and disk storage space. Two techniques were suggested and examined to reduce the running computational time, along with another two for storage space reduction. The first two techniques are the one-dimensional turbulence model (ODT) and tabulation chemistry (FPI). ODT is a stochastic method which mimics the effect of 3D turbulence in 1D simulations by resolving most of the physics involved; more than 90% of the run time is saved by using this technique. The FPI technique is a kind of chemical-kinetic reduction; in this technique, the thermodynamics, kinetics, and transport properties are tabulated as a function of a progress variable instead of computing them at each time step during the simulation. With this technique, 90% of the computational time required for a detailed simulation can be avoided. The other two techniques examined in order to reduce the required disk space are the snapshot proper orthogonal decomposition (SPOD)

and dynamic mode decomposition (DMD). With the help of these methods, post-processing can be conducted for coarse output of a well-resolved simulation and still capture all of the dynamics and scales of turbulence.

The main contributions and novelties contained in this dissertation are listed below.

Novelties and main contributions:

- Development of a new DNS tool which can accurately handle many different physical phenomena in reactive and non-reactive two-phase turbulent flows;
- Development of a method to quantify the flow state and detect transition to turbulence;
- Using of the temporally-evolving jet configuration for the first time in 3D DNS of spray combustion;
- Proving for the first time that the one-dimensional turbulence model can be used to test the occurrence of auto-ignition in premixed propane/air mixtures;
- Development of a new tool which can perform modal decomposition (SPOD and DMD) as a post-processing technique to reduce the required disk storage space and to analyze the turbulence dynamics and scales.

7.2 Outlook and Recommendations

In future work, several developments could be carried out to increase further the efficiency of DNS. Corresponding recommendations are listed as follows:

1. Implementing a multi-block technique in DINO, which would help in simulating complex geometries while maintaining the efficiency of the original solver. It should be kept in mind that doing this is a very large modification of the solver.
2. Improving the order of DB-IBM since, in the current version of DINO, DB-IBM is based on a zero-order method; necessitating extremely fine grids locally.
3. Improving the FPI tabulation method implemented in DINO since, in this version, it is based on the unity Lewis number assumption. Additionally, a 2D or 3D table would increase the accuracy of FPI-DNS simulations in highly turbulent flows.
4. Combining in an optimal manner SPOD and DMD analysis.
5. These would allow further systematic studies of spray combustion, on the way towards nanoparticle synthesis in spray flames.

Bibliography

- [1] Porsche direct injection engine, <http://www.autos.ca/auto-tech/auto-tech-direct-versus-port-fuel-injection/>.
- [2] Combustion wire spray application, <http://www.syntheticcoatings.ie/Page.asp?PageID=9>.
- [3] W.A. Sirignano. *Fluid dynamics and transport of droplets and sprays*. Cambridge University Press, New York, USA, 2nd edition, 2010.
- [4] An example of domestic spray atomization, <http://www.bedbugguide.com/bed-bugs-spray-a-way-to-prevent-and-eliminate-bed-bugs/>.
- [5] ARCHIE-WeSt supercomputer centre: spray combustion scenario, <https://www.archie-west.ac.uk/projects/computational-fluid-dynamics/the-cfd-development-of-non-premixed-dual-fuel-combustion-diesel-engine-injected-by-high-pressure-gas-in-the-cylinder-chamber/>.
- [6] J. Réveillon, C. Pera, and Z. Bouali. Examples of the potential of DNS for the understanding of reactive multiphase flows. *Int. J. Spray Combust. Dyn.*, 3 (1):63–92, 2011.
- [7] S.A. Orszag and G.S. Patterson. Numerical simulation of three-dimensional homogeneous isotropic turbulence. *Phys. Rev. Lett.*, 28:76–79, 1972.
- [8] R.S. Rogallo. Numerical experiments in homogeneous turbulence. Technical Report TM81315, NASA, 1981.
- [9] P. Givi. Model free simulations of turbulent reactive flows. *Prog. Energy Combust. Sci.*, 15:1–107, 1989.
- [10] T. Poinso, S. Candel, and A. Trouvé. Applications of direct numerical simulation to premixed turbulent combustion. *Prog. Energy Combust. Sci.*, 21(6):531–576, 1996.
- [11] T. Poinso and D. Veynante. *Theoretical and numerical combustion*. Aquaprint, Bordeaux, France, 3rd edition, 2011.
- [12] J.J. Riley and G.S. Patterson. Diffusion experiments with numerically integrated isotropic turbulence. *Phys. Fluids*, 17:292–297, 1974.

-
- [13] F. Mashayek, F.A. Jaber, R.S. Miller, and P. Givi. Dispersion and polydispersity of droplets in stationary isotropic turbulence. *Int. J. Multiphase Flow*, 23(2):337–335, 1997.
- [14] R.S. Miller and J. Bellan. Direct numerical simulation and subgrid analysis of a transitional droplet laden mixing layer. *Phys. Fluids*, 12 (3):650–671, 2000.
- [15] F. Mashayek. Direct numerical simulations of evaporating droplet dispersion in forced low mach number turbulence. *Int. J. Heat Mass transfer*, 41(17):2601–2617, 1998.
- [16] R.S. Miller and J. Bellan. Direct numerical simulation of a confined three-dimensional gas mixing layer with one evaporating hydrocarbon-droplet-laden stream. *Phys. Fluids*, 384:293–338, 1999.
- [17] J. Réveillon and L. Vervisch. Analysis of weakly turbulent dilute-spray flames and spray combustion regimes. *J. Fluid Mech.*, 537:317–347, 2005.
- [18] F. Mashayek. Numerical investigation of reacting droplets in homogeneous shear turbulence. *J. Fluid Mech.*, 405:1–36, 2000.
- [19] P. Domingo, L. Vervisch, and J. Réveillon. DNS analysis of partially premixed combustion in spray and gaseous turbulent flame-bases stabilized in hot air. *Combust. Flame*, 140:172–195, 2005.
- [20] J. Réveillon and F.X. Demoulin. Evaporating droplets in turbulent reacting flows. *Proc. Combust. Inst.*, 31:2319–2326, 2007.
- [21] A.P. Wandel, N. Chakraborty, and E. Mastorakos. Direct numerical simulations of turbulent flame expansion in fine sprays. *Proc. Combust. Inst.*, 32:2283–2290, 2009.
- [22] L. Fréret, O. Thomine, J. Réveillon, S. de Chaisemartin, F. Laurent, and M. Massot. On the role of preferential segregation in flame dynamics in polydisperse evaporating sprays. In *Proceedings of the Summer Program 2010, Center for Turbulence Research*. Stanford University, 2010.
- [23] A. Fujita, H. Watanabe, R. Kurose, and S. Komori. Two-dimensional direct numerical simulation of spray flames - Part 1: Effects of equivalence ratio, fuel droplet size and radiation, and validity of flamelet model. *Fuel*, 104:515–525, 2013.
- [24] T. Kitano, T. Nakatani, R. Kurose, and S. Komori. Two-dimensional direct numerical simulation of spray flames - Part 2: Effects of ambient pressure and lift, and validity of flamelet model. *Fuel*, 104:526–535, 2013.
- [25] T. Kitano, J. Nishio, R. Kurose, and S. Komori. Effects of ambient pressure, gas temperature and combustion reaction on droplet evaporation. *Combust. Flame*, 161:551–564, 2014.

Bibliography

- [26] Y. Wang and C.J. Rutland. Effects of temperature and equivalence ratio on the ignition of n-heptane fuel spray in turbulent flow. *Proc. Combust. Inst.*, 30:893–900, 2005.
- [27] Y. Wang and C.J. Rutland. Direct numerical simulation of ignition in turbulent n-heptane liquid-fuel spray jets. *Combust. Flame*, 149:353–365, 2007.
- [28] A. Neophytou, E. Mastorakos, and R.S. Cant. Complex chemistry simulations of spark ignition in turbulent sprays. *Proc. Combust. Inst.*, 33:2135–2142, 2011.
- [29] A. Neophytou, E. Mastorakos, and R.S. Cant. The internal structure of igniting turbulent sprays as revealed by complex chemistry DNS. *Combust. Flame*, 159:641–664, 2012.
- [30] G. Borghesi, E. Mastorakos, and R.S. Cant. Complex chemistry DNS of n-heptane spray autoignition at high pressure and intermediate temperature conditions. *Combust. Flame*, 160:1254–1275, 2013.
- [31] H. Wang, K. Luo, and J. Fan. Effects of turbulent intensity and droplet diameter on spray combustion using direct numerical simulation. *Fuel*, 121:311–318, 2014.
- [32] T. Jin, K. Luo, Q. Dai, and J. Fan. Direct numerical simulation on supersonic turbulent reacting and non-reacting spray jet in heated coflow. *Fuel*, 164:267–276, 2016.
- [33] S.B. Pope. *Turbulent Flows*. Cambridge University Press, Cambridge, UK, 2000.
- [34] A. Majda and J. Sethian. The derivation and numerical solution of the equations for zero Mach number combustion. *Combust. Sci. Technol.*, 42:185–205, 1985.
- [35] N. Peters. https://www.princeton.edu/cefrc/Files/2010%20Lecture%20Notes/Norbert%20Peters/Peters_Summerschool_reference.pdf, 2010.
- [36] Premixed flame colors, <http://www.slideshare.net/grovervijayk/model-lesson-on-parts-of-flame-by-vijay-grover>.
- [37] Non-premixed flame colors, http://www.phikwadraat.nl/candle_flame/.
- [38] K.K. Kuo. *Principles of Combustion*. John Wiley & Sons, Inc., New York, 1986.
- [39] P.S. Sierra. Modeling the dispersion and evaporation of sprays in aeronautical combustion chambers. Ph.D. thesis, Institut National Polytechnique de Toulouse, 2012.
- [40] M. Gorokhovski and M. Herrmann. Modeling primary atomization. *Ann. Rev. Fluid Mech.*, 40(5):343–366, 2008.
- [41] T. Menard, S. Tanguy, and A. Berlemont. Coupling level set/VOF/ghost fluid methods: Validation and application to 3d simulation of the primary break-up of a liquid jet. *Int. J. Multiphase Flow*, 33(5):510–524, 2007.

-
- [42] O. Desjardins, V. Moureau, and H. Pitsch. An accurate conservative level set/ghost fluid method for simulating turbulent atomization. *J. Comput. Phys.*, 227(18):8395–8416, 2008.
- [43] A. Abdelsamie and C. Lee. Decaying versus stationary turbulence in particle-laden isotropic turbulence: Turbulence modulation mechanism. *Phys. Fluids*, 24:015106, 2012.
- [44] A. Abdelsamie and C. Lee. Decaying versus stationary turbulence in particle-laden isotropic turbulence: Heavy particle statistics modifications. *Phys. Fluids*, 25:033303, 2013.
- [45] F.A. Williams. *Combustion theory*. The Benjamin/Cummings Publishing Company, Inc., 2nd edition edition, 1985.
- [46] K.K. Kuo. *Principles of combustion*. John Wiley & Sons, Inc., 2nd edition edition, 2005.
- [47] B. Abramzon and W. A. Sirignano. Droplet vaporization model for spray combustion calculations. *Int. J. Heat Mass Transfer.*, 32(9):1605–1618, 1989.
- [48] R.S. Miller, K. Harstad, and J. Bellan. Evaluation of equilibrium and non-equilibrium evaporation models for many-droplet gas-liquid flow simulations. *Int. J. Multiphase Flow*, 24(6):1025–1055, 1998.
- [49] D.B. Spalding. The combustion of liquid fuels. In *Proceeding of the Fourth Symposium on Combustion*, pages 847–864, Baltimore, MD, 1953. Combustion Institute.
- [50] A. Abdelsamie, G. Fru, T. Oster, F. Dietzsch, G. Janiga, and D. Thévenin. Towards direct numerical simulations of low-Mach number turbulent reacting and two-phase flows using immersed boundaries. *Comput. Fluids*, 131:123–141, 2016.
- [51] J.D. Charentenay, D. Thévenin, and B. Zamuner. Comparison of direct numerical simulations of turbulent flames using compressible or low-Mach number formulations. *Int. J. Numer. Meth. Fluids*, 39:497–515, 2002.
- [52] R. Hilbert, F. Tap, H. El-Rabii, and D. Thévenin. Impact of detailed chemistry and transport models on turbulent combustion simulations. *Prog. Energy Combust. Sci.*, 30:61–117, 2004.
- [53] A. Ern and V. Giovangigli. Multicomponent transport algorithms. Lecture Notes in Physics Monographs, Berlin, Heidelberg, Springer. 24, 1994.
- [54] A. Ern and V. Giovangigli. Fast and accurate multicomponent transport property evaluation. *J. Comput. Phys.*, 120(1):105–116, 1995.
- [55] N. Li and S. Laizet. 2DECOMP&FFT - a highly scalable 2D decomposition library and FFT interface. In *Cray User Group 2010 conference*, Edinburgh, UK, 2010.

Bibliography

- [56] S. Laizet, E. Lamballais, and J.C. Vassilicos. A numerical strategy to combine high-order schemes, complex geometry and parallel computing for high resolution DNS of fractal generated turbulence. *Comput. Fluids*, 39:471–484, 2010.
- [57] S. Laizet and N. Li. Incompact3d: A powerful tool to tackle turbulence problems with up to $O(10^5)$ computational cores. *Int. J. Numer. Meth. Fluids*, 67:1735–1757, 2011.
- [58] W.H. Press, S.A. Teukolsky, W.T. Vetterling, and B.P. Flannery. *Numerical recipes in FORTRAN*. Cambridge University Press, New York, US, 2nd edition, 1992.
- [59] J. Kim and P. Moin. Application of a fractional-step method to incompressible Navier-Stokes equations. *J. Comput. Phys.*, 59:308–323, 1985.
- [60] D. Brown, R. Cortez, and M. Minion. Accurate projection methods for the incompressible Navier-Stokes equations. *J. Comput. Phys.*, 168(2):464–499, 2001.
- [61] F. Lucci, A. Ferrante, and S. Elghobashi. Modulation of isotropic turbulence by particles of Taylor-length-scale size. *J. Fluid Mech.*, 650:5–55, 2010.
- [62] H.N. Najm, P.S. Wyckoff, and O.M. Knio. A semi-implicit numerical scheme for reacting flow. I. Stiff chemistry. *J. Comput. Phys.*, 143:381–402, 1998.
- [63] O.M. Knio, H.N. Najm, and P.S. Wyckoff. A semi-implicit numerical scheme for reacting flow. II. Stiff, operator-split formulation. *J. Comput. Phys.*, 154:428–467, 1999.
- [64] E. Hairer and G. Wanner. *Solving ordinary differential equations II: Stiff and differential-algebraic problems*. Berlin, Springer-Verlag, 2nd revised edition, 1999.
- [65] J. Caudal, B. Fiorina, B. Labégorre, and O. Gicquel. Modeling interactions between chemistry and turbulence for simulations of partial oxidation processes. *Fuel Process. Technol.*, 134:231–242, 2015.
- [66] X. Zhong. Additive semi-implicit Runge-Kutta methods for computing high speed non equilibrium reactive flows. *J. Comput. Phys.*, 128:19–31, 1996.
- [67] D. Thévenin, F. Behrendt, U. Maas, B. Przywara, and J. Warnatz. Development of a parallel direct simulation code to investigate reactive flows. *Comput. Fluids*, 25(5):485–496, 1996.
- [68] J. W. Cooley, P.A.W. Lewis, and P.D. Welsh. The fast Fourier transform algorithm: Programming considerations in the calculation of sine, cosine and Laplace transforms. *J. Sound Vib.*, 12:315–337, 1970.
- [69] P.N. Swarztrauber. Symmetric FFTs. *Math. Comput.*, 47:323–346, 1986.
- [70] HYPRE-library, http://computation.llnl.gov/project/linear_solvers/software.php.

-
- [71] D. Thévenin, O. Gicquel, J. de Charentenay, R. Hilbert, and D. Veynante. Two- versus three-dimensional direct simulations of turbulent methane flame kernels using realistic chemistry. *Proc. Combust. Inst.*, 29:2031–2039, 2003.
- [72] M. Baum, T. Poinso, and D. Thévenin. Accurate boundary conditions for multicomponent reactive flows. *J. Comput. Phys.*, 116(2):247–261, 1995.
- [73] R.H. Kraichnan. Diffusion by a random velocity field. *Phys. Fluids*, 13:22–31, 1970.
- [74] M. Klein, A. Sadiki, and J. Janicka. A digital filter based generation of inflow data for spatially developing direct numerical or large eddy simulation. *J. Comput. Phys.*, 186:625–665, 2002.
- [75] A. Kempf, M. Klein, and J. Janicka. Efficient generation of initial-and inflow-conditions for transient turbulent flows in arbitrary geometries. *Flow Turb. Combust.*, 74:67–84, 2005.
- [76] J.D. Anderson. *Computational fluid dynamics: the basics with applications*. McGraw-Hill, New York, US, 1995.
- [77] E.A. Fadlun, R. Verzicco, P. Orlandi, and J. Mohd-Yusof. Combined immersed-boundary finite-difference methods for three-dimensional complex flow simulations. *J. Comput. Phys.*, 161:35–60, 2000.
- [78] R. Mittal and G. Iaccarino. Immersed boundary methods. *Annu. Rev. Fluid Mech.*, 37:239–261, 2005.
- [79] D.A. Steinman, Y. Hoi, P. Fahy, L. Morris, M.T. Walsh, N. Aristokleous, A.S. Anayiotos, Y. Papaharilaou, A. Arzani, S.C. Shadden, P. Berg, G. Janiga, and et al. Variability of computational fluid dynamics solutions for pressure and flow in a giant aneurysm: the ASME 2012 Summer Bioengineering Conference CFD Challenge. *J Biomech Eng.*, 135:021016, 2013.
- [80] M. Uhlmann. An immersed boundary method with direct forcing for the simulation of particulate flows. *J. Comput. Phys.*, 209:448–476, 2005.
- [81] A. Eshghinejadfard, A. Abdelsamie, G. Janiga, and D. Thévenin. Direct-forcing immersed boundary lattice Boltzmann simulation of particle/fluid interactions for spherical and non-spherical particles. *Particuology*, 25:93–103, 2016.
- [82] T. Kempe and J. Fröhlich. Collision modelling for the interface-resolved simulation of spherical particles in viscous fluids. *J. Fluid Mech.*, 709:445489, 2012.
- [83] B. Inanand and A.R. Bahadir. Numerical solution of the one-dimensional Burgers’ equation: Implicit and fully implicit exponential finite difference methods. *J. Phys.*, 81(4):547–556, 2013.

- [84] U. Ghia, K.N. Ghia, and C.T. Shin. High-resolutions for incompressible flows using Navier-Stokes equations and a multigrid method. *J. Comput. Phys.*, 48:387–411, 1982.
- [85] O. Botella and R. Peyret. Benchmark spectral results on the lid-driven cavity flow. *Comput. Fluids*, 27(4):421–433, 1998.
- [86] G. Comte-Bellot and S. Corrsin. Simple Eulerian time correlation of full and narrow band velocity signals in isotropic turbulence. *J. Fluid Mech.*, 48(2):273–337, 1971.
- [87] Z.J. Wang, K. Fidkowski, R. Abgrall, F. Bassi, D. Caraen, A. Cary, H. Deconinck, R. Hartmann, K. Hillewaert, H. Huynh, N. Kroll, G. May, P.-O. Persson, B. van Leer, and M. Visbal. High-order CFD methods: current status and perspective. *Int. J. Numer. Meth. Fluids*, 72:811–845, 2013.
- [88] J.R. DeBonis. Solutions of the Taylor-Green vortex problem using high-resolution explicit finite difference methods. *AIAA paper*, 2013. 2013–0382.
- [89] W.M. van Rees, A. Leonard, D.I. Pullin, and P. Koumoutsakos. A comparison of vortex and pseudo-spectral methods for the simulation of periodic vortical flows at high Reynolds numbers. *J. Comput. Phys.*, 230:2794–2805, 2011.
- [90] R. Moser, J. Kim, and M.N. Mansour. Direct numerical simulation of turbulent channel flow up to $Re_\tau = 590$. *Phys. Fluids*, 11(4):943–945, 1999.
- [91] A.W. Vreman and J.G.M. Kuerten. Comparison of direct numerical simulation databases of turbulent channel flow at $Re_\tau = 180$. *Phys. Fluids*, 26:015102, 2014.
- [92] X.D. Niu, C. Shu, Y.T. Chew, and Y. Peng. A momentum exchange-based immersed boundary-lattice Boltzmann method for simulating incompressible viscous flows. *Phys. Lett. A*, 354:173–182, 2006.
- [93] S.C.R. Dennis and G.-Z. Chang. Numerical solutions for steady flow past a circular cylinder at Reynolds numbers up to 100. *J. Fluid Mech.*, 42(3):471–489, 1970.
- [94] X.D. Niu, Y.T. Chew, and C. Shu. Simulation of flows around an impulsively started circular cylinder by Taylor series expansion- and least squares-based lattice Boltzmann method. *J. Comput. Phys.*, 188:176–193, 2003.
- [95] Chemical kinetic mechanism for combustion applications, Center for energy research (Combustion division), University of California at San Diego, <http://web.eng.ucsd.edu/mae/groups/combustion/mechanism.html>.
- [96] Z. Luo, C.S. Yoo, E.S. Richardson, J.H. Chen, C.K. Law, and T. Lu. Chemical explosive mode analysis for a turbulent lifted ethylene jet flame in highly-heated co-flow. *Combust. Flame*, 159:265–274, 2012.
- [97] A. Patel, S. Kong, and R. Reitz. Development and validation of a reduced reaction mechanism for HCCI engine simulations. *SAE Technical Paper 2004-01-0558*, 2004. DOI:10.4271/2004-01-0558.

-
- [98] S. Liu, J.C. Hewson, J.H. Chen, and H. Pitsch. Effects of strain rate on high-pressure nonpremixed *n*-heptane autoignition in counterflow. *Combust. Flame*, 137:320–339, 2004.
- [99] C.J. Jachimowski. An experimental and analytical study of acetylene and ethylene oxidation behind shock waves. *Combust. Flame*, 29:55–66, 1977.
- [100] J.A. Baker and G.B. Kinner. Shock-tube studies on the ignition of ethylene-oxygen-argon mixtures. *Combust. Flame*, 19:347–350, 1972.
- [101] K. Kumar, G. Mittal, C.-J. Sung, and C.K. Law. An experimental investigation of ethylene/O₂/diluent mixtures: Laminar flame speeds with preheat and ignition delays at high pressures. *Combust. Flame*, 153:343–354, 2008.
- [102] H.K. Ciezki and G. Adomeit. Shock-tube investigation of self-ignition of *n*-heptane-air mixtures under engine relevant condition. *Combust. Flame*, 93(4):421–433, 1993.
- [103] F.N. Egolfopoulos, D.L. Zhu, and C.K. Law. Experimental and numerical determination of laminar flame speeds: mixtures of C₂-hydrocarbons with oxygen and nitrogen. *Proc. Combust. Inst.*, 23:471–478, 1990.
- [104] G. Jomaas, X.L. Zheng, D.L. Zhu, and C.K. Law. Experimental determination of counterflow ignition temperatures and laminar flame speeds of C₂-C₃ hydrocarbons at atmospheric and elevated pressures. *Proc. Combust. Inst.*, 30:193–200, 2005.
- [105] M.I. Hassan, K.T. Aung, O.C. Kwon, and G.M. Faeth. Properties of laminar premixed hydrocarbon/air flames at various pressures. *J. Propul. Power*, 14(4):479–488, 1998.
- [106] G.P. Smith, D.M. Golden, M. Frenklach, N.W. Moriarty, B. Eiteneer, M. Goldenberg, C.T. Bowman, R.K. Hanson, S. Song, W.C. Gardiner, Jr., V.V. Lissianski, and Z. Qin. GRI-Mech 3.0 (1999); http://www.me.berkeley.edu/gri_mech/.
- [107] E.R. Hawkes, R. Sankaran, J.C. Sutherland, and J.H. Chen. Scalar mixing in direct numerical simulations of temporally evolving plane jet flames with skeletal CO/H₂ kinetics. *Proc. Combust. Inst.*, 32:1633–1640, 2007.
- [108] A. Scholtissek, F. Dietzsch, M. Gauding, and C. Hasse. In-situ tracking of mixture fraction gradient trajectories and unsteady flamelet analysis in turbulent non-premixed combustion. *Combust. Flame*, 2016. DOI: 10.1016/j.combustflame.2016.07.011.
- [109] F. Hunger, M. Gauding, and C. Hasse. On the impact of the turbulent/non-turbulent interface on differential diffusion in a turbulent jet flow. *J. Fluid Mech.*, 802:R5, 2016.
- [110] A. Abdelsamie and D. Thévenin. Direct numerical simulation of spray evaporation and autoignition in a temporally-evolving jet. *Proc. Combust. Inst.*, 36(2):2493–2502, 2017.

Bibliography

- [111] C. Chauveau, F. Halter, A. Lalonde, and I. Gokalp. An experimental study on the droplet vaporization: Effects of heat conduction through the support fiber. 2008. ILASS-EUROPE Conference, Como. Italy.
- [112] A. Patel, S.C. Kong, and R.D. Reitz. Development and validation of a reduced reaction mechanism for HCCI engine simulations. *SAE Technical Paper*, 2004-01-0558, 2004.
- [113] Z. Bouali, C. Pera, and J. Réveillon. Numerical analysis of the influence of two-phase flow mass and heat transfer on n-heptane autoignition. *Combust. Flame*, 159:2056–2068, 2012.
- [114] R.W. Bilger, S.H. Stårner, and R.J. Kee. On reduced mechanisms for methane-air combustion in nonpremixed flames. *Combust. Flame*, 80 (2):135–149, 1990.
- [115] H. Yamashita, M. Shimada, and T. Takeno. A numerical study on flame stability at the transition point of jet diffusion flames. *Proc. Combust. Inst.*, 26:27–34, 1996.
- [116] B. Fiorina, O. Gicquel, L. Vervisch, S. Carperntier, and N. Darabiha. Approximating the chemical structure of partially premixed and diffusion counterflow flames using FPI flamelet tabulation. *Combust. Flame*, 140:147–160, 2005.
- [117] E. Knudsen and H. Pitsch. A general flamelet transformation useful for distinguishing between premixed and non-premixed modes of combustion. *Combust. Flame*, 156:678–696, 2009.
- [118] Y. Mizobuchi, J. Shinjo, S. Ogawa, and T. Takeno. A numerical study on the formation of diffusion flame islands in a turbulent hydrogen jet lifted flame. *Proc. Combust. Inst.*, 30:611–619, 2005.
- [119] D.O. Lignell, J.H. Chen, and H.A. Schmutz. Effects of Damköhler number on flame extinction and reignition in turbulent, non-premixed flames using DNS. *Combust. Flame*, 158:949–963, 2011.
- [120] D.A. Rosenberg, P.M. Allison, and J.F. Driscoll. Flame index and its statistical properties measured to understand partially premixed turbulent combustion. *Combust. Flame*, 162:2808–2822, 2015.
- [121] G. Byrne, F. Mut, and J. Cebral. Quantifying the large-scale hemodynamics of intracranial aneurysms. *Am. J. Neuroradiol.*, 35:333–338, 2014.
- [122] J. Mikhal and B.J. Geurts. Immersed boundary method for pulsatile transitional flow in realistic cerebral aneurysms. *Comput. Fluids*, 91:144–163, 2014.
- [123] H. Tennekes and J.L. Lumley. *A first course in turbulence*. Cambridge: MIT press, Cambridge, UK, 1972.
- [124] R. Akhavan, R.D. Kamm, and A.H. Shapiro. An investigation of transition to turbulence in bounded oscillatory Stokes flows. Part 1. Experiments. *J. Fluid Mech.*, 225:395–422, 1991.

-
- [125] B. Eckhardt. Turbulence transition in pipe flow: Some open questions. *Nonlinearity*, 21:1–11, 2008.
- [126] L.M. González, M. Ahmed, J. Kühnen, H.C. Kuhlmann, and V. Theofilis. Three-dimensional flow instability in a lid-driven isosceles triangular cavity. *J. Fluid Mech.*, 675:369–396, 2011.
- [127] M. Hino, M. Sawamoto, and S. Takasu. Experiments on transition to turbulence in an oscillating pipe flow. *J. Fluid Mech.*, 75:193–207, 1976.
- [128] S. Kefayati and T.L. Poepinga. Transitional flow analysis in the carotid artery bifurcation by proper orthogonal decomposition and particle image velocimetry. *Med Eng. Phys.*, 35:898–909, 2013.
- [129] S.E. Lee, S.-W. Lee, P.F. Fischer, H.S. Bassiouny, and F. Loth. Direct numerical simulation of transitional flow in a stenosed carotid bifurcation. *J. Biomech.*, 41(11):2551–2561, 2008.
- [130] P. Wulf, C. Egbers, and H.J. Rath. Routes to chaos in wide-gap spherical Couette flow. *Phys. Fluids*, 11(6):1359–1372, 1999.
- [131] E. Bou-Zeid, C. Meneveau, and M. Parlange. A scale-dependent Lagrangian dynamic model for large eddy simulation of complex turbulent flows. *Phys. Fluids*, 17:025105, 2005.
- [132] C. Meneveau. Transition between viscous and inertial-range scaling of turbulence structure functions. *Phys. Rev. E.*, 54(4):3657–3663, 1996.
- [133] L. Davidson and S. Dahlström. Hybrid RANS-LES: An approach to make LES applicable at high Reynolds number. *Int. J. Comput. Fluid Dyn.*, 19(6):415–427, 2005.
- [134] L. Davidson and S.-H. Peng. Embedded large-eddy simulation using the partially averaged Navier-Stokes model. *AIAA J.*, 51(5):1066–1079, 2013.
- [135] P. Sagaut, S. Deck, and M. Terracol. *Multiscale and multiresolution approaches in turbulence, LES, DES and hybrid RANS/LES methods: applications and guidelines*. Imperial College Press, London, 2nd edition, 2013.
- [136] J. Delville, L. Ukeiley, L. Cordier, J.P. Bonnet, and M. Glauser. Examination of large-scale structures in a turbulent plane mixing layer. Part 1. Proper orthogonal decomposition. *J. Fluid Mech.*, 391:91–122, 1999.
- [137] N. Aubry, M.-P. Chauve, and R. Guyonnet. Transition to turbulence on a rotating flat disk. *Phys. Fluids*, 6:2800–2814, 1994.
- [138] M. Ullmann, U. Prüfert, J. Seidel, O. Ernst, and C. Hasse. Application of proper orthogonal decomposition methods in reactive pore diffusion simulations. *Can. J. Chem. Eng.*, 92:1552–1560, 2014.

- [139] K. Bhaganagar and V. Juttijudata. Turbulent time-events in channel with rough walls. *Theor. Comput. Fluid Dyn.*, 26:583–589, 2012.
- [140] D. Freire, S. Kahan, C. Cabeza, G. Sarasúa, and A.C. Marti. The formation of coherent structures within turbulent fountains in stratified media. *Eur. J. Mech. B-Fluid*, 50:89–97, 2015.
- [141] N. Furuichi, Y. Takeda, and M. Kumada. Spatial structure of the flow through an axisymmetric sudden expansion. *Exp. Fluids*, 34:643–650, 2003.
- [142] P. Hasal, J.-L. Montes, H.-C. Boisson, and I. Fořt. Macro-instabilities of velocity field in stirred vessel: Detection and analysis. *Chem. Eng. Sci.*, 55:391–401, 2000.
- [143] J.L. Lumley. The structure of inhomogeneous turbulent flows. In A.M Iaglom and V.I. Tatarski, editors, *Atmospheric Turbulence and Radio Wave Propagation*, pages 221–227. Nauka and Moscow, 1967.
- [144] L. Sirovich. Turbulence and the dynamics of coherent structures. Part 1: Coherent structures. *Q. Appl. Math.*, 45(3):561–571, 1987.
- [145] P. Arányi, G. Janiga, K. Zähringer, and D. Thévenin. Analysis of different POD methods for PIV-measurements in complex unsteady flows. *Int. J. Heat Fluid Flow*, 43:204–211, 2013.
- [146] N. Aubry. On the hidden beauty of the proper orthogonal decomposition. *Theor. Comput. Fluid Dyn.*, 2:339–352, 1991.
- [147] N. Aubry, R. Guyonnet, and R. Lima. Spatio-temporal analysis of complex signals: Theory and applications. *J. Statist. Phys.*, 64(3/4):683–739, 1991.
- [148] G. Berkooz, P. Holmes, and J.L. Lumley. The proper orthogonal decomposition in the analysis of turbulent flows. *Annu. Rev. Fluid Mech.*, 25:539–575, 1993.
- [149] A. Cammilleri, F. Gueniat, J. Carlier, L. Pastur, E. Memin, F. Lusseyran, and G. Artana. POD-spectral decomposition for fluid flow analysis and model reduction. *Theor. Comput. Fluid Dyn.*, 27:787–815, 2013.
- [150] Ph. Debesse, L. Pastur, F. Lusseyran, Y. Fraigneau, C. Tenaud, C. Bonamy, A. V. G. Cavalieri, and P. Jordan. A comparison of data reduction techniques for the aeroacoustic analysis of flow over a blunt flat plate. *Theor. Comput. Fluid Dyn.*, pages 1–22, 2015.
- [151] S. Gamard, W.K. George, D. Jung, and S. Woodward. Application of a “slice” proper orthogonal decomposition to the far field of an axisymmetric turbulent jet. *Phys. Fluids*, 14:2515–2522, 2002.
- [152] L. Kapitza, O. Imberdis, H. Bensler, J. Willand, and D. Thévenin. An experimental analysis of the turbulent structures generated by the intake port of a DISI-engine. *Exp. Fluids*, 48(2):265–280, 2010.

-
- [153] M. Manhart. Vortex shedding from a hemisphere in a turbulent boundary layer. *Theor. Comput. Fluid Dyn.*, 12:1–28, 1998.
- [154] M. Manhart and H. Wengle. Spatiotemporal decomposition of a fully inhomogeneous turbulent flow field. *Theor. Comput. Fluid Dyn.*, 5:223–242, 1993.
- [155] M. Manhart, H. Wengle, P. Schmid, and H. Werner. Eigenmode decomposition of the turbulent shear layer above a square rib. *Appl. Sci. Res.*, 51:359–364, 1993.
- [156] S.F.C. Stewart, E.G. Paterson, G.W. Burgreen, P. Hariharan, M. Giarra, V. Reddy, S.W. Day, K.B. Manning, S. Deutsch, M.R. Berman, M.R. Myers, and R.A. Malinuskas. Assessment of CFD performance in simulations of an idealized medical device: results of FDA’s first computational inter laboratory study. *Cardiovasc. Eng. Technol.*, 3(2):139–160, 2012.
- [157] P. Holmes, J.L. Lumley., and G. Berkooz. *Turbulence, coherent structures, dynamical systems and symmetry*. Cambridge University Press, New York, 1996.
- [158] P. Grassberger and I. Procaccia. Estimation of the Kolmogorov entropy from a chaotic signal. *Phys. Rev. A*, 28:2591–2593, 1983.
- [159] L.K. Isaacson. Spectral entropy, empirical entropy and empirical exergy for deterministic boundary layer structures. *Entropy*, 15:4134–4158, 2013.
- [160] G.E. Powell and I.C. Percival. A spectral entropy method for distinguishing regular and irregular motion of Hamiltonian systems. *J. Phys. A: Math. Gen.*, 12(11):2053–2071, 1979.
- [161] D. Lohse. Crossover from high to low Reynolds number turbulence. *Phys. Rev. Lett.*, 73(24):3223–3226, 1994.
- [162] J.B. Perot. Determination of the decay exponent in mechanically stirred isotropic turbulence. *AIP Adv.*, 1:0221041/1–18, 2011.
- [163] C. Rutland, J. Ferziger, and S. El-Thary. Full numerical simulations and modeling of turbulent premixed flames. *Proc. Combust. Inst.*, 23:621–627, 1990.
- [164] P.L. Carroll and G. Blanquart. A proposed modification to Lundgren’s physical space velocity forcing method for isotropic turbulence. *Phys. Fluids*, 25:105114, 2013.
- [165] C. Rosales and C. Meneveau. Linear forcing in numerical simulations of isotropic turbulence: Physical space implementations and convergence properties. *Phys. Fluids*, 17:095106, 2005.
- [166] M.E. Brachet, D.I. Meiron, S.A. Orszag, B.G. Nickel, R.H. Morf, and U. Frisch. Small-scale structure of the Taylor-Green vortex. *J. Fluid Mech.*, 130:411–452, 1983.
- [167] G. Janiga. Large eddy simulation of the FDA benchmark nozzle for a Reynolds number of 6500. *Comput. Biol. Med.*, 47:113–119, 2014.

Bibliography

- [168] B. Lewis and G. von Elbe. *Combustion, Flames and Explosions of Gases*. Academic Press Inc, Orlando, Florida 32887, 3rd edition, 1987.
- [169] T. Hasegawa, A. Arai, S. Kadowaki, and S. Yamaguchi. Autoignition of a turbulent premixed gas. *Combust. Sci. Tech.*, 84:1–13, 1992.
- [170] C.F. Kaminski, J. Hult, M. Aldén, S. Lindenmaier, A. Dreizler, U. Maas, and M. Baum. Spark ignition of turbulent methane/air mixtures revealed by time-resolved planar laser-induced fluorescence and direct numerical simulations. *Proc. Combust. Inst.*, 28(1):339–405, 2000.
- [171] J. Hult, S. Gashi, N. Chakraborty, M. Klein, K. Jenkins, R. Cant, and C. Kaminski. Measurement of flame surface density for turbulent premixed flames using PLIF and DNS. *Proc. Combust. Inst.*, 31:1319–1326, 2007.
- [172] M. Klein, N. Chakraborty, and R.S. Cant. Effects of turbulence on self-sustained combustion in premixed flame kernels: A direct numerical simulation (DNS) study. *Flow Turb. Comb.*, 81:583–607, 2008.
- [173] N. Chakraborty, E. Mastorakos, and S. Cant. Effects of turbulence on spark ignition in inhomogeneous mixtures: A direct numerical simulation (DNS) study. *Combust. Sci. Tech.*, pages 293–317, 2007.
- [174] R. Sankaran, E.R. Hawkes, J.H. Chen, T. Lu, and C.K. Law. Structure of a spatially developing turbulent lean methane/air Bunsen flame. *Proc. Combust. Inst.*, 31:1291–1298, 2007.
- [175] A.J. Aspden, M.S. Day, and J.B. Bell. Three-dimensional direct numerical simulation of turbulent lean premixed methane combustion with detailed kinetics. *Combust. Flame*, 166:266–283, 2016.
- [176] A.R. Kerstein. One-dimensional turbulence: Model formulation and application to homogeneous turbulence, shear flows, and buoyant stratified flows. *J. Fluid Mech.*, 392:277–334, 1999.
- [177] A.R. Kerstein, W.T. Ashurst, S. Wunsch, and V. Nilse. One dimensional turbulence: vector formulation and application to free shear flows. *J. Fluid Mech.*, 447:85–109, 2001.
- [178] W.T. Ashurst and A.R. Kerstein. One-dimensional turbulence: Variable-density formulation and application to mixing layers. *Phys. Fluids*, 17:025107–1–025107–26, 2005.
- [179] T. Echekki, A.R. Kerstein, T.D. Dreeben, and J.-Y. Chen. One-dimensional turbulence simulation of turbulent jet diffusion flames: model formulation and illustrative applications. *Combust. Flame*, 125:1083–1105, 2001.
- [180] J.C. Hewson and A.R. Kerstein. Stochastic simulation of transport and chemical kinetics in turbulent CO/H₂/N₂ flames. *Combust. Theor. Model.*, 5(4):669–697, 2001.

-
- [181] J.C. Hewson and A.R. Kerstein. Local extinction and reignition in nonpremixed turbulent CO/H₂/N₂ jet flames. *Combust. Sci. Tech.*, 174:35–66, 2002.
- [182] K.G. Gupta and T. Echehki. One-dimensional turbulence model simulations of autoignition of hydrogen/carbon monoxide fuel mixtures in a turbulent jet. *Combust. Flame*, 158:327–344, 2011.
- [183] N. Punati, J.C. Sutherland, A.R. Kerstein, E.R. Hawkes, and J.H. Chen. An evaluation of the one-dimensional turbulence model: Comparison with direct numerical simulations of CO/H₂ jets with extinction and reignition. *Proc. Combust. Inst.*, 33:1515–1522, 2011.
- [184] D.O. Lignell and D. Rappleye. One-dimensional-turbulence simulation of flame extinction and reignition in planar ethylene jet flames. *Combust. Flame*, 159:2930–2943, 2012.
- [185] Z. Jozefik, A.R. Kerstein, H. Schmidt, S. Lyra, H. Kolla, and J.H. Chen. One-dimensional turbulence modeling of a turbulent counterflow flame with comparison to DNS. *Combust. Flame*, 162:2999–3015, 2015.
- [186] N. Punati, H. Wang, E.R. Hawkes, and J.C. Sutherland. One-dimensional modeling of turbulent premixed jet flames-comparison to DNS. *Flow Turb. Combust.*, 97:913–930, 2016.
- [187] D.O. Lignell, A.R. Kerstein, and E.I. Monson. Mesh adaption for efficient multiscale implementation of one-dimensional turbulence. *Theor. Comput. Fluid Dyn.*, 27(3):273–295, 2013.
- [188] P.A. Lewis and G.S. Shedler. Simulation of nonhomogeneous Poisson processes by thinning. *Naval Res. Logistic Q.*, 26:403–413, 1979.
- [189] A. Papoulis and S.U. Pillai. *Probability, Random Variables, and Stochastic Processes*. McGraw-Hill, New York, 4th edition, 2002.
- [190] N.S. Titova, P.S. Kuleshov, and A.M. Starik. Kinetic mechanism of propane ignition and combustion in air. *Combust. Explos. Shock Waves*, 47(3):249–264, 2011.
- [191] GRI-Mech 3.0, <http://combustion.berkeley.edu/gri-mech/version30/text30.html#propane>.
- [192] D.O. Lignell, G.C. Fredline, and A.D. Lewis. Comparison of one-dimensional turbulence and direct numerical simulations of soot formation and transport in a nonpremixed ethylene jet flame. *Proc. Combust. Inst.*, 35:1199–1206, 2015.
- [193] O. Gicquel, N. Darabiha, and D. Thévenin. Laminar premixed hydrogen/air counterflow flame simulations using flame prolongation of ILDM with differential diffusion. *Proc. Combust. Inst.*, 28:1901–1908, 2000.

- [194] U. Maas and S.B. Pope. Simplifying chemical kinetics: Intrinsic low-dimensional manifolds in composition space. *Combust. Flame*, 88:239–264, 1992.
- [195] P.K. Jha and C.P.T. Groth. Tabulated chemistry approaches for laminar flames: Evaluation of flame-prolongation of ILDM and flamelet methods. *Combust. Theor. Model.*, 16:31–57, 2011.
- [196] J.B. Michel, O. Colin, and D. Veynante. Comparison of differing formulations of the PCM model by their application to the simulation of an auto-igniting H₂/air jet. *Flow. Turbul. Combust.*, 83:33–60, 2009.
- [197] J.B. Michel, O. Colin, C. Angelberger, and D. Veynante. Using the tabulated diffusion flamelet model ADF-PCM to simulate a lifted methane-air jet flame. *Combust. Flame*, 156:1318–1331, 2009.
- [198] L.-H. Dorey, N. Bertier, L. Tessé, and F. Dupoirieux. Soot and radiation modeling in laminar ethylene flames with tabulated detailed chemistry. *C. R. Mécanique*, 338:756–769, 2011.
- [199] B. Fiorina, R. Baron, O. Gicquel, D. Thévenin, S. Carpentier, and N. Darabiha. Modelling non-adiabatic partially premixed flames using flame-prolongation of ILDM. *Combust. Theor. Model.*, 7:449–470, 2003.
- [200] A. Najafi-Yazdi, B. Cuenot, and L. Mongeau. Systematic definition of progress variables and intrinsically low-dimensional flamelet generated manifolds for chemistry tabulation. *Combust. Flame*, 159:1197–1204, 2012.
- [201] V. Bykov and U. Maas. The extension of the ILDM concept to reaction-diffusion manifolds. *Combust. Theor. Model*, 11(6):839–862, 2007.
- [202] R. Schießl, V. Bykov, U. Maas, A. Abdelsamie, and D. Thévenin. Implementing multi-directional molecular diffusion terms into reaction diffusion manifolds (REDIMs). *Proc. Combust. Inst.*, 36:673–679, 2017.
- [203] O. Frederich and D.M. Luchtenburg. Modal analysis of complex turbulent flow. In *7th Int Symposium. on Turbulence and Shear Flow Phenomena (TSFP-7)*, Ottawa, Canada, 2011.
- [204] MODRED 2.0.1 package, <http://pythonhosted.org/modred/index.html>.
- [205] P.J. Schmid. Dynamic mode decomposition of numerical and experimental data. *J. Fluid Mech.*, 656:5–28, 2010.
- [206] P.E. Dimotakis. The mixing transition in turbulent flows. *J. Fluid Mech.*, 409:69–98, 2000.
- [207] N. Hutchins and I. Marusic. Evidence of very long meandering features in the logarithmic region of turbulent boundary layers. *J. Fluid Mech.*, 579:1–2, 2007.



Abouelmagd Abdelsamie

Curriculum Vitae

Contact Information

Address Laboratory of Fluid Dynamics and Technical Flows,
University of Magdeburg "Otto von Guericke",
Universitätsplatz 2,
D-39106 Magdeburg, Germany
E-mail abouelmagd.abdelsamie@ovgu.de
Website <https://www.lss.ovgu.de/lss>

Personal Information

Birth-date March 28th 1985
Birth-place Cairo, Egypt
Citizenship Egyptian

Research Interests

- Direct numerical simulation (DNS) of multiphase turbulent flow and spray combustion
- Immersed boundary method (IBM) for moving boundaries in turbulent flow
- Low-Mach number reactive flow and Poisson solvers algorithms
- One Dimensional Turbulence model in combustion
- Modal decomposition of turbulent flow: DMD and POD

Education

2012–present **PhD student in group of Prof. Dominique Thévenin**, *University of Magdeburg, "Otto von Guericke", Germany.*
2009–2011 **Masters of Science in Mechanical Engineering**, *Yonsei University, South Korea.*
2002–2007 **Bachelor of Science in Mechanical Engineering**, *Helwan University, Egypt.*

Masters Thesis

Title *Decaying against stationary turbulence: physical modulation mechanisms in particle-laden isotropic turbulence*

Description (Investigation of turbulence modulations by solid sphere particles using Direct Numerical Simulation with pseudo-spectral flow solver, written in Fortran90)

Experience

2012-Present **PhD student.**

Laboratory of Fluid Dynamics and Technical Flows,
University of Magdeburg "Otto von Guericke", Magdeburg, Germany.

2011-2012 **Teaching Assistant.**

- Fundamentals of Fluid Mechanics course,
- Fundamentals of Gas Dynamics course,
- Fundamentals of Heat Transfer course,

Helwan University, Elmataria, Egypt.

2009–2011 **Master Student.**

Laboratory of Turbulence and Environmental Flow Physics,
Yonsei University, Seoul, South Korea.

2007–2009 **Research Assistant.**

Laboratory of Thermodynamics,
Helwan University, Elmataria, Egypt.

Awards

2012 Best Master's Thesis of the year, Prize from Korean Society of Mechanical Engineers (KSME), South Korea.

Journal publications

A. Abdelsamie and D. Thévenin. Direct numerical simulation of spray evaporation and autoignition in a temporally-evolving jet. *Proc. Combust. Inst.* **36**(2):2493–2502, 2017

C. Chi, G. Janiga, **A. Abdelsamie**, K. Zähringer, T Turányi, D. Thévenin. DNS study of the optimal chemical markers for heat release in syngas flames. *Flow Turbul. Combust.* **98**(4): 1117–1132, 2017

A. Abdelsamie, G. Fru, T. Oster, F. Dietzsch, G. Janiga and D. Thévenin. Towards direct numerical simulations of low-Mach number turbulent reacting and two-phase flows using immersed boundaries. *Comput. Fluids*, **131**:123–141, 2016

R. Schießl, V. Bykov, U. Maas, **A. Abdelsamie** and D. Thévenin. Implementing multi-directional molecular diffusion terms into Reaction Diffusion Manifolds (REDIMs). *Proc. Combust. Inst.* **36**: 673–679, 2017

A. Eshghinejadfard, **A. Abdelsamie**, G. Janiga and D. Thévenin. Direct-forcing immersed boundary lattice Boltzmann simulation of particle/fluid interactions for spherical and non-spherical particles. *Particuology*, **25**:93–103, 2016.

A. Abdelsamie and D. Thévenin. Direct numerical simulations of turbulent spray combustion: behavior of scalar dissipation rate. *At. J. Technol. Eng.* 2016, accepted for publication.

A. Abdelsamie and C. Lee. Decaying versus stationary turbulence in particle-laden isotropic turbulence: Heavy particle statistics modifications, *Phys. Fluids*, **25**: 033303, 2013.

A. Abdelsamie and C. Lee. Decaying versus stationary turbulence in particle-laden isotropic turbulence: Turbulence modulation mechanism, *Phys. Fluids*, **24**:015106, 2012.

Proceedings, Abstracts, Symposium, Workshops

A. Abdelsamie and D. Thévenin. Direct numerical simulations of turbulent spray combustion: behavior of scalar dissipation rate. In: Twelfth International Conference of Fluid Dynamics (ICFD12), Cairo, Egypt, 19-20 December, accepted for presentation, 2016.

A. Abdelsamie, G. Janiga, C. Chi and D. Thévenin. Turbulence structure analysis of DNS data using DMD and SPOD: mixing jet and channel flow. In: iTi Conference on Turbulence VII, Bertinoro, Italy, September 7-9, poster presentation, 2016.

A. Abdelsamie and D. Thévenin. Direct numerical simulation of n-heptane droplets igniting in a turbulent flow. In: 9th International Conference on Multiphase Flow, Firenze, Italy, 2016.

C. Chi, G. Janiga, **A. Abdelsamie**, K. Zähringer, T. Turányi and D. Thévenin. DNS study of the optimal chemical markers for heat release in syngas flames. In: 36th International Symposium on Combustion, Seoul, Korea, The Combustion Institute, poster presentation, 2016.

A. Abdelsamie and D. Thévenin. Modulation of isotropic turbulence by resolved and non-resolved spherical particles. In: Direct and Large-Eddy Simulation IX, (J. Fröhlich, H. Kuerten, B.J. Geurts and V. Armenio, Eds.), Springer, 621-629, 2015.

A. Abdelsamie and D. Thévenin. Direct Numerical Simulation of burning n-heptane droplets: auto-ignition and turbulence modulation mechanisms. In: Direct and Large-Eddy Simulation X, Limassol, Cyprus, Paper 152, 2015.

A. Abdelsamie and D. Thévenin. Auto-ignition probability of ethylene/air mixture: Comparison between detailed chemistry and tabulated chemistry. In: 5th International Workshop on Model Reduction in Reacting Flows, Cottbus, Germany, 2015.

A. Abdelsamie and D. Thévenin. Comparison between ODT and DNS for ethylene/air auto-ignition. In: 15th International Conference on Numerical Combustion, Avignon, France, 24, 2015.

A. Abdelsamie and D. Thévenin. Direct numerical simulation of the auto-ignition of turbulent ethylene/air mixtures. In: 15th International Conference on Numerical Combustion, Avignon, France, 42, 2015.

P. Berg, **A. Abdelsamie** and G. Janiga. Possible transitional flow in a giant intracranial aneurysm: finite volume approach versus Direct Numerical Simulation. In: 4th International Conference on Computational and Mathematical Biomedical Engineering-CMBE2015, (P. Nithiarasu and E. Budyn, Eds.) Cachan, France, 567-570, 2015.

G. Janiga, G. Fru, **A. Abdelsamie** and D. Thévenin. Probability of hotspot ignition in turbulent hydrogen-air mixtures using Direct Numerical Simulations. In: 7th European Combustion Meeting (ECM 2015), Budapest, Hungary, P3-81/1-6, 2015.

R. Schießl, V. Bykov, U. Maas, **A. Abdelsamie** and D. Thévenin. The (mis)alignment of diffusive fluxes in turbulent combustion: DNS analysis and treatment in the Reaction-Diffusion Manifold (REDIM) model. In: 7th European Combustion Meeting (ECM 2015), Budapest, Hungary, P4-63/1-6, 2015.

A. Abdelsamie and D. Thévenin. Modulation of turbulent properties in a spray flame burning n-Heptane using Direct Numerical Simulation. In: 35th Symposium (International) on Combustion, San Francisco, Poster presentation, 2014.

P. Berg, **A. Abdelsamie**, G. Janiga and D. Thévenin. Large Eddy Simulation in intracranial aneurysms: should transition be considered in numerical modeling? In: 11th World Congress on Computational Mechanics, Barcelona, Spain, (Oñate, E., Oliver, X. and Huerta, A., Eds.), Paper MS233A-2, 2014.

A. Eshghinejadfard, **A. Abdelsamie**, T. Oster and D. Thévenin. Impact of the collision model for fully resolved particles interacting in a fluid. In: ASME 2014 Fluids Engineering Summer Meeting (FEDSM2014), Chicago, Illinois, Paper FEDSM2014-21447, 2014.

A. Abdelsamie, T. Chittipotula, C. Lee and Thévenin D. Stationary and decaying turbulence modulation by finite-size fully resolved particles. In: 8th International Conference on Multiphase Flow, Jeju, South Korea, oral presentation, 2013.

A. Abdelsamie and Thévenin D. Turbulence modulation by fully resolved particles using immersed boundary methods. In: Joint EUROMECH/ERCOFTAC Colloquium on Immersed Boundary Methods, Leiden, The Netherlands, 145-147, 2013.

P. Berg, **A. Abdelsamie**, H. Yu, G. Janiga and D. Thévenin. Multi-phase blood flow modeling in intracranial aneurysms considering possible transition to turbulence. In: ASME Summer Bioengineering Conference, Oregon, USA, SBC2013-14289, poster presentation, 2013.

P. Berg, **A. Abdelsamie**, H. Yu, G. Janiga and D. Thévenin. Multi-phase blood flow modeling in intracranial aneurysms considering possible transition to turbulence. In: 8th International Symposium on Turbulence and Shear Flow Phenomena, Poitiers, France, oral presentation, 2013.

T. Oster, G. Fru, **A. Abdelsamie** and D. Thévenin. On-the-fly processing and feature extraction of flame and flow properties obtained by Direct Numerical Simulation. In: SIAM International Conference on Numerical Combustion, Dallas, Texas, oral presentation, 2013.

A. Abdelsamie, C. Lee and D. Thévenin. Two-way interactions in particle-laden isotropic turbulence: physical mechanisms and numerical approaches. In: 13th Workshop on Two-Phase Flow Predictions, (Sommerfeld, M., Ed.), Halle-Merseburg, Germany, 1-10, 2012.

A. Abdelsamie and C. Lee. Physical perspectives on the investigation of two-way interaction in particle-laden isotropic turbulence, 64th Annual Meeting of the APS Division of Fluid Dynamics, Baltimore, Maryland, U.S.A., November 20-22, 2011

A. Abdelsamie and C. Lee. Turbulence modulation in particle-laden isotropic turbulent flow, KSME (Korean Society of Mechanical Engineers), South Korea, April 15-16, 2011.

A. Abdelsamie and C. Lee. Particle dispersion in isotropic turbulence under lift forces, The 6th National Congress on the Fluid Engineering, Busan, South Korea, August 18-20, 2010.

Technical Skills

Programming: FORTRAN, C/C++, Python, and MATLAB/Octave

Good command of: Message Passing Interface (MPI), Open Multiprocessing (OpenMP), and FFTW libraries

PostProcessing/Visualization: Visit, Paraview, Tecplot, gnuplot, and matplotlib

Operating Systems: Linux/Unix, mac-OS, Microsoft Windows family and very good experience with HPC

Computer-Aided Design: Gambit, Icem-Ansys, Autocad 2002-2007

Standard CFD: ANSYS-Fluent, OpenFoam

 Languages

Arabic **Native language**
English **Very Good**
German **Basic command**

.....

Date

.....

Signature